Laser Ranging Interferometry for Future Gravity Missions: Instrument Design, Link Acquisition and Data Calibration

Vom Fachbereich Produktionstechnik

der

UNIVERSITÄT BREMEN

zur Erlangung des Grades
Doktor-Ingenieur
genehmigte

Dissertation

von

M.Sc. Filippo Ales

1. Gutachter: Prof. Dr. rer. nat. Claus Braxmaier
Fachbereich Produktionstechnik

2. Gutachter: Prof. Dr. rer. nat. Gerhard Heinzel
Albert Einstein Institute (AEI), Universität Hannover

Tag der mündlichen Prüfung: 13 Januar 2017

Ich erkläre: "Ich habe die vorgelegte Dissertation selbständig und ohne unerlaubte fremde Hilfe und nur mit den Hilfen angefertigt, die ich in der Dissertation angegeben habe. Alle Textstellen, die wörtlich oder sinngemäß aus veröffentlichen Schriften entnommen sind, und alle Angaben, die auf mündlichen Auskünften beruhen, sind als solche kenntlich gemacht."

Filippo Ales
Immenstaad, 13 April 2016

Abstract

The Gravity Recovery and Climate Experiment (GRACE) Follow-On mission, successor of the GRACE mission, is intended to be launched in late 2017 in order to provide continuity of data for the study of Earth's mass distribution and for climate research. Together with the primary ranging instrument, the Microwave Instrument (MWI), the GRACE Follow-On platform embeds a secondary ranging instrument, the Laser Ranging Instrument (LRI), as a technology demonstrator. The LRI is going to be the first intra-satellite laser ranging interferometer and aims to improve the actual range measurement accuracy of the MWI by a factor of 20. Although the GRACE Follow-On mission is yet to be launched, the scientific community is already performing studies for a next generation low-low satellite-to-satellite tracking mission which uses a laser instrument as the primary metrology device. The presented study aims to improve the design solution adopted for the LRI of GRACE Follow-On in terms of instrument layout, algorithms for the laser link acquisition and techniques for mitigating the range measurement noise.

The first part of this work describes viable layout solutions of an heterodyne interferometer employed for intra-satellite range metrology and the major noise contributions which degrade the overall ranging accuracy of the instrument. Together with the optical layout of the instrument, novel design concepts of the instrument's subsystems are also considered. Precisely, a phasemeter designed to autonomously acquire and track a heterodyne signal with low Signal-to-Noise Ratio (SNR) in a frequency band that spans from 1 MHz to 25 MHz is presented. Particular attention is also dedicated to the mathematical modeling of the steering mirror dynamics and to the enhancement of its pointing performance by means of feedforward control.

Before addressing their metrology target, space missions which employ laser instruments (often) require an intermediate phase dedicated to the acquisition of the laser signal. The complexity of this process can vary according to the layout of the instrument and to the mission environment. In the second part of this work, solutions for autonomously acquiring the laser signal are analyzed and put in relation with the boundary constraints of the acquisition problem. The acquisition algorithms presented and the robustness of their design is verified mainly using numerical simulations. Experimental tests have also been performed for validating the simulation hypothesis and verifying their compliancy to a realistic mission scenario. The laser link simulator developed specifically for this study is also described in detail.

The last part of this work describes a calibration algorithm developed for minimizing, during data postprocessing, the noise due to the tilt-to-piston coupling which represents one of the highest contributors to the overall measurement noise. The algorithm is conceived such that it can retrieve the effect of the noise within the measurement using either the residual attitude jitter of the two satellites or dedicated calibration maneuvers, with the former concept analyzed more in detail. The calibration algorithm is tested using the simulated range measurement of a GRACE Follow-On like mission and the Level-1B data products of the GRACE mission. The outcome of the calibration process is also described.

Zusammenfassung

Die GRACE Follow-On Mission, Nachfolger der GRACE Mission, soll Ende 2017 starten, um die Kontinuität der Daten über die Masseverteilung der Erde und für die Klimaforschung zu gewährleisten. Neben dem primären Mikrowelleninstrument wird GRACE Follow-On als Technologiedemonstrator über das erste Intra-Satelliten Laser-Ranging Interferometer verfügen. Ziel dieses Interferometers ist eine Verbesserung der Leistung der aktuellen Entfernungsmessung von GRACE um einen Faktor 20. Obwohl die GRACE Follow-On Mission noch nicht gestartet ist, arbeiten Wissenschaftler bereits an der nächste Generation von Laserinstrumenten zur Metrologie zwischen Satelliten auf niedrigen Erdorbits. Hauptthema der vorgestellten Doktorarbeit ist die Weiterentwicklung und Optimierung des aktuellen LRI Instrumentenkonzepts, welches auf GRACE Follow-On integriert wurde. Dazu werden der Entwurf des Instrumentes, Algorithmen zur Herstellung der Laserverbindung und Techniken zur Reduktion des Längenmessrauschens untersucht.

Der erste Teil dieser Arbeit befasst sich mit der Beschreibung von alternativen optischen Ausführungen eines Heterodyninterferometers für Intra-Satelliten Abstandsmessungen, dem Messprinzip und der dominanten Rauschbeiträge, die die Gesamtgenauigkeit des Instruments limitieren. Neben dem optischen Layout des Instruments werden neuartige Konzepte der einzelnen Subsysteme ebenfalls berücksichtigt. Insbesondere wird ein Phasendetektor vorgestellt, der das autonome Erfassen und Verfolgen eines heterodynen Signals mit niedrigem SNR in einem Frequenzband zwischen 1 MHz und 25 MHz erlaubt. Besondere Sorgfalt wird auch auf die mathematische Modellierung der Kippspiegeldynamik und deren Verbesserung durch eine Feedforward-regelung verwandt.

Üblicherweise ist bei Missionen, die ein Laser-Instrument zur Abstandsmessung einsetzen, vor dem Betrieb der eigentlichen optischen Metrologie eine Prozedur zur Signalaquisition erforderlich. Die Komplexität dieses Prozesses hängt nicht nur vom Layout des Instruments ab, sondern auch von möglichen Störeinflüssen der Umgebung. Daher werden im zweiten Teil dieser Arbeit Methoden zur autonomen Erfassung des Lasersignals analysiert und mit den Anforderungen an die Akquisition verglichen. Die vorgestellten Akquisitionsalgorithmen und deren Robustheit werden hauptsächlich anhand numerischer Simulationen überprüft. Darüber hinaus wurden experimentelle Tests durchgeführt, um die Annahmen der Simulationen zu validieren und ihre Kompatibilität mit einem realistischen Missionsszenario zu prüfen. Ein speziell für diese Studie entwickelter "Laser Link Simulator" wird im Detail beschrieben.

Der letzte Teil dieser Doktorarbeit beschreibt einen Kalibrierungsalgorithmus zur Minimierung des Rauschens aufgrund der Kopplung zwischen Kippwinkel und optischer Pfadlänge bei der Nachprozessierung der Daten. Diese Rauschquelle stellt einen der größten Beiträge zum gesamten Messrauschen dar. Der Algorithmus ist so konzipiert, dass er die Wirkung des Rauschens innerhalb der Messung mit zwei unterschiedlichen Methoden erfassen kann: entweder über das verbleibende Lagerauschen der beiden Satelliten, oder über spezielle Kalibrierungsmanöver, wobei die erste Methode hier detaillierter analysiert wird. Der Kalibrierungsalgorithmus wurde durch simulierte Längenmessungen von einer GRACE Follow-On-ähnlichen Mission und die Level-1B Daten der GRACE Mission getestet. Die Ergebnisse dieses Kalibrierungsprozesses werden ebenfalls beschrieben.

Contents

List of Acronyms

ADC Analog-to-Digital Converter

AOCS Attitude and Orbit Control System

ASD Amplitude Spectral Density

CCD Charge-Coupled Device

CCR Corner Cube Retroreflector

CDF Cumulative Distribution Function

CoM Center of Mass

CRS Coordinate Reference System

DFFT Discrete Fast Fourier Transform

DPLL Digital Phase-Locked Loop

DWS Differential Wavefront Sensing

LISA Laser Interferometer Space Antenna

eLISA evolved Laser Interferometer Space Antenna

FPGA Field Programmable Gate Array

GNC Guidance Navigation and Control

GPS Global Positioning System

GRACE Gravity Recovery and Climate Experiment

KBR K-Band Ranging

LEO Low Earth Orbit

LO Local Oscillator

LoS Line of Sight

LPF Low-Pass Filter

LRI Laser Ranging Instrument

LTI Linear Time Invariant

MWI Microwave Instrument

NCO Numerically Controlled Oscillator

NPRO Non-Planar Ring Oscillator

NSF Noise Shape Function

PDF Probability Density Function

PI Proportional-Integral

PID Proportional-Integral-Derivative

QPD Quadrant-PhotoDiode

RSS Root of Sum of Squares

RX Received

SM Steering Mirror

SNR Signal-to-Noise Ratio

STR Star Tracker

TMA Triple Mirror Assembly

TPC Tilt-to-Piston Coupling

TX Transmitted

USO Ultra-Stable Oscillator

WPD Wavelet Packet Decomposition

Chapter 1

Introduction

Laser technology for spaceborne applications has been principally employed, up to date, for communication purposes. The Semiconductor-laser Inter-satellite Link EXperiment (SILEX) [1], the laser communication terminal operated as secondary payload on-board the TerraSAR-X and the Near Field InfraRed Experiment (NFIRE) satellites [2, 3], or the most recent Lunar Laser Communication Demonstration (LLCD) mounted on board the Lunar Atmosphere and Dust Environment Explorer (LADEE) [4] are just some examples of missions and payloads that use high-rate optical links for data communication. The technology reliability shown by these missions brought laser communications to be a viable candidate to radio communications. Indeed, long-duration mission which rely on optical communication as the European Data Relay System (EDRS) with the second generation laser communication terminal [5] or the Laser Communication Relay Demonstration (LCRD) [6] have been recently put in orbit (the first EDRS payload has been launched in 2016 on-board Eutelsat 9B) or are planned to be launched in the near future.

In the last decades, laser interferometers have become also one of the key technologies for the instruments appointed in the detection of gravitational waves [7]. The measurement principle that is used for ground-based gravitational wave observatories such as LIGO [8] (which has recently proofed the existence of gravitational waves [9]), Virgo [10] and GEO 600 [11] can be also applied to space-based observatories [12, 13, 14, 15, 16] in order to extend the actual measurement spectrum to the low-frequencies (due to the curvature of the Earth, the arm-length of a ground-based observatory is limited to a few kilometers, thus the observable gravitational waves are in the high frequency spectrum - typically from tenths of Hz to kHz). Indeed, the absence of a gravity gradient related to the Earth's geology and the possibility of increasing the arm-length of the interferometer (thus amplifying the strain resolution) permits the observation of gravitational waves emitted by large massive systems.

The design of a space-based interferometer such as the evolved Laser Interferometer Space Antenna (eLISA) (conceived to detect gravitational waves in the frequency spectrum that goes from 0.1 mHz to 1 Hz [17]) resembles the Michelson interferometer although the practical realization is closer to a Doppler tracking system in which the metrology target is the change of frequency in the signal received from a distant satellite [18]. The actual baseline concept for the eLISA mission (which is inherited from the former joint venture NASA-ESA mission Laser Interferometer Space Antenna (LISA)) is to have a master satellite which sends light to two slave satellites distant one million kilometers and receives in turn light from them. The received light is combined with an on-board reference light signal and the relative frequency difference is stored. The beat signal, recorded on each of the three satellites, is afterwards recombined using the time-delay interferometry technique [19, 20] for evaluating changes in baseline separation of the proof masses (which have to be free-falling) carried on board each satellite.

In order to verify the readiness of some of the fundamental technologies for a LISA-like mission, the mission LISA Pathfinder has been launched in December 2015 [21, 22]. The primary goal of LISA Pathfinder is to verify the possibility of maintaining proof-masses in

free-fall [23] through a drag-free control system [24]. The drag-free control system measures the relative motion of the proof-masses with an optical metrology device [25, 26] and actuates a set of micro-Newton thrusters [27] in order to maintain them in free-fall. By the time of writing, the mission has successfully released the two proof-masses of its primary payload, the LISA technology package, has entered science mode and has successfully passed the in-orbit commissioning review.

A research field where laser interferometry can also play a key role is in the monitoring of spatial and temporal variations of the Earth's gravitational field. The gravity field is composed of a variety of signals which are related not only to the solid Earth but also to short-term dynamic trends (i.e. water mass variation and transportation) which are essential for the understanding of the Earth's climate processes and their changes. Satellite gravimetry observations are fundamental for the study of the climate since they allow to perform global monitoring (and thus have a global picture of mass redistribution) which is impossible to perform via in situ or regional investigations.

In the last decade, climate monitoring through satellite gravimetry has been carried out by the GRACE mission [28, 29] and by the Gravity field and steady-state Ocean Circulation Explorer (GOCE) mission [30, 31]. The GRACE mission consists of a satellite pair separated by a distance of $\approx$ 200 km and placed in a quasi-polar orbit ($\approx$ 89° of inclination). The gravitational potential is retrieved by continuously measuring the distance variation between the satellites through a microwave link which has a range accuracy of $\approx$ 2 µm. With this constellation, it is possible to obtain a gravity field solution which has a spatial resolution of 400 km with monthly basis. The resolution on seasonal and interannual mass changes is limited to $\approx$ 20 mm of equivalent water height while the secular trends can be monitored with a precision of about 0.5 mm of equivalent water height per year [32, 33, 34]. Figure 1.1 shows which phenomena are currently monitored with the actual satellite and ground-based gravimetry and what could be measured by improving the actual state of art. For space gravimetry, the limitation on the accuracy of the gravity field solution derives mainly from the microwave link noise, the performance of the accelerometer and accuracy of the models used for evaluating short time scale mass variations (i.e. atmospheric models) [35].

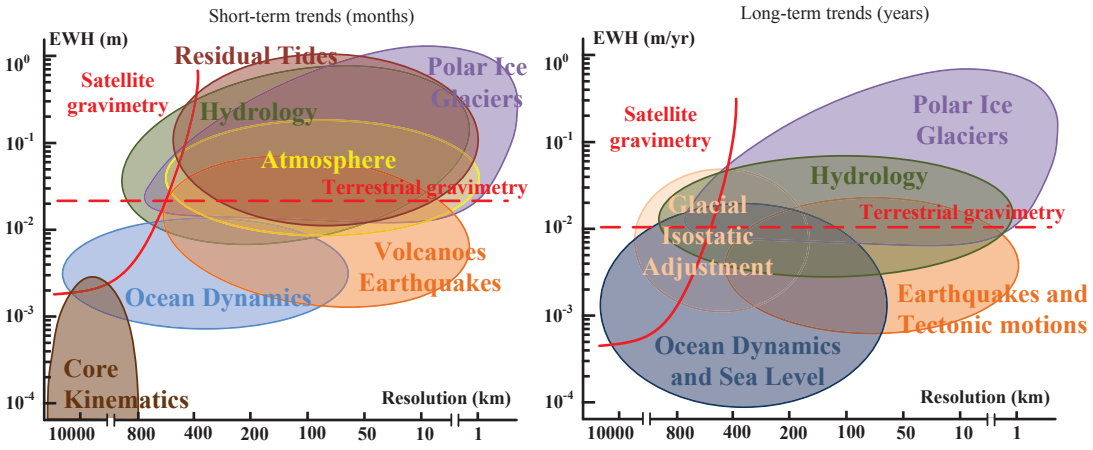

Figure 1.1: This image depicts the spatial scales and amplitudes (in terms of equivalent water height - EWH in the figure) of the gravitational signal which are relevant for the study of climate and mass redistribution. The image on the left depicts the short-term trends while the image on the right the long term trends. The limit of the terrestrial gravimetry is given by the accuracy of the FG5 gravity meter [36]. Image courtesy of the Institut für Erdmessung (IfE).

The replacement of the current microwave link with a laser link can overcome one of these limitations [37, 38]. For such a reason, the successor mission to GRACE, namely GRACE

Follow-On, is going to mount, together with the primary microwave instrument, the LRI as a technology demonstrator [39, 40]. Most of the technology of the LRI is an outgrowth of the technology of the LISA mission, although its performance are severely reduced especially because of the disturbances present in the Low Earth Orbit (LEO) environment in which the instrument is operated. The LRI is expected to improve the range measurement by a factor of 20 (from 2 µm to about 50 nm) up to 0.1 Hz with a performance decay at lower frequencies given by the Noise Shape Function (NSF)

$$NSF\,(f) = \sqrt{1 + \left(\frac{f}{2\mathrm{mHz}}\right)^{-2}} \times \sqrt{1 + \left(\frac{f}{10\mathrm{mHz}}\right)^{-2}} \tag{1.1}$$

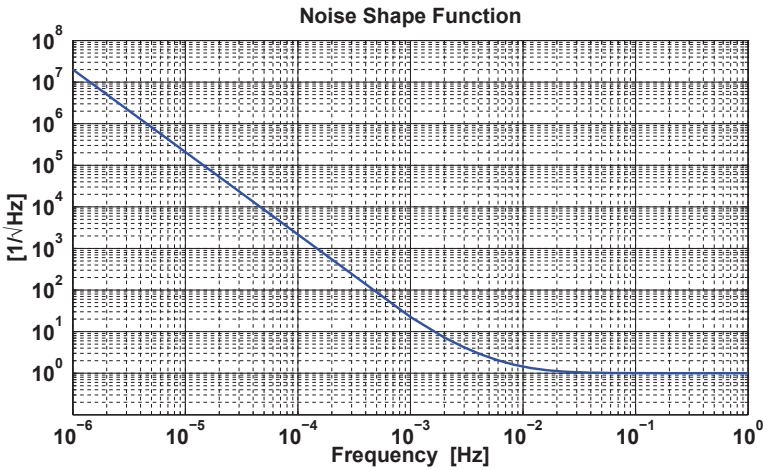

Figure 1.2: This image shows the trend of the NSF of Eq. 1.1 in a bandwidth that spans from 1 µHz to 1 Hz.

The measurement principle of the LRI is different from the one of the microwave instrument; the laser carrier phase is not measured separately in each satellite but the laser on-board one satellite is locked to a reference cavity while the second laser is phase-locked to the laser light received. Unlike for the GRACE mission, it is thus possible to identify a master satellite (the one with the cavity stabilized laser) and a slave satellite. Since both satellites mount a cavity for symmetry reasons, it is possible to exchange their operating mode during the mission.

Because the platform of GRACE Follow-On mission is a rebuild of the GRACE platform [41], the optical layout of the laser interferometer is constrained by the free space available within the satellite bus. As the measurement line of sight (ideal line connecting the fiducial points of the two accelerometers) is occupied by the microwave instrument, the optical design includes a beam routing device (the Triple Mirror Assembly (TMA)) [39, 40] which still allows to estimate the temporal displacement between the fiducial points of the accelerometers minimizing measurement artifacts (especially attitude related ones).

Although the GRACE Follow-On mission is yet to be launched (currently the launch is scheduled for 2017), the scientific community and (inter)governmental organisations (i.e. ESA with the next generation gravity mission studies) are already planning a next generation low-low satellite-to-satellite tracking mission which embeds a laser instrument as the primary metrology device. The following chapters discuss alternative solutions which aim to improve some of the aspects of laser instruments employed for geodesy missions. Since there is a direct link between the laser technology development for geodesy missions and the one for space-borne gravitational waves observatories, some of the arguments treated in this work are applicable in both of these fields. Hence, where possible, solutions for the eLISA mission are also presented.

1.1 Thesis structure and specific contributions

Together with this introductory chapter, this thesis has six additional chapters and three appendices. The chapters can be read in sequence or according to the hierarchy depicted in Fig. 1.3.

Chapter 2 describes the basic measurement principle of a laser interferometer and presents three possible configurations for the layout of the instrument. Also in this chapter, the operating principle of a phasemeter is described together with a novel design of its frequency acquisition unit. Always in this chapter, the principal noise sources which deteriorate the measurement performance of the instrument are identified. At the end of this chapter, the expected measurement accuracy of the three layouts presented beforehand is calculated using design parameters which are compatible with a future geodesy mission.

Chapter 3 describes how the principal constituting components of the interferometer have been modelled and how these operate together in order to establish a measurement link between the satellites. This models are embedded in a simulator which is used to perform, as far as possible, realistic studies of some of the critical aspects of the laser link between the satellites (in particular, laser link acquisition and reduction of measurement noise). For some components, a stand-alone (detailed) simulator is coded in parallel with the main laser link simulator because of computational constraints (the main simulator can only include a simplified model). The detailed models allow to study the behaviour of a particular sub-system when exposed to different external stimuli in order to find their operating optima.

Chapter 4 discusses in detail one of the most critical phases of the mission such as the initial signal acquisition. This chapter is conceived not to provide the solution to a specific acquisition problem but to a most generic one. Indeed, the building blocks of the acquisition algorithm are provided as functions of specific parameters of the acquisition problem (i.e. signal detection time, maximum initial pointing offset etc.). This chapter also contains the guidelines for designing an acquisition algorithm accordingly with the boundary constraints of the mission analyzed and new solutions not considered in the existing literature regarding this topic (in particular, the use of random processes). The final part of this chapter reports the outcome of the signal acquisition simulations performed with the laser link simulator introduced in the third chapter of this thesis.

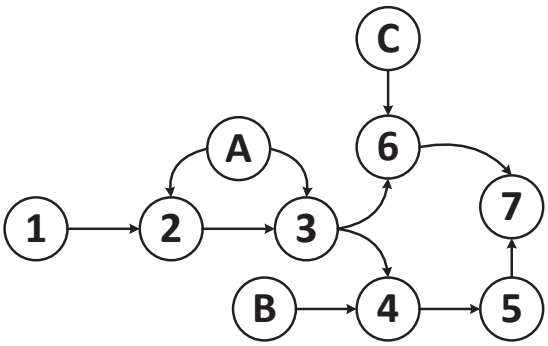

Figure 1.3: Structure of the chapters of this thesis.

Chapter 5 describes the experimental tests performed for verifying the correct implementation of the phasemeter, the design robustness of its frequency acquisition unit and the pointing performance of the steering mirror.

Chapter 6 presents of a calibration solution capable of mitigating, during data post-processing, the attitude induced measurement noise caused by the non-ideality of the laser interferometer. The first part of this chapter presents an algorithm capable of recovering the coefficients that couple the attitude signal with the measurement signal using both the incoherent and the co-

herent calibration technique. In the second part of this chapter, the calibration algorithm is employed using both simulated data of the GRACE Follow-On mission and real flight data of the GRACE mission. The improvement to the ranging accuracy and the limits of applicability of this calibration algorithm are also discussed here.

The last chapter of this thesis summarizes the main results of this work while the three appendices are intended to improve the readability of the chapters by providing full mathematical formulations or further descriptions of design choices.

Nomenclature and definitions

For this thesis, the following nomenclature is adopted; bold capital letters (i.e. $\mathbf{R}$ or $\mathbf{C}$) are used to identify matrices while bold letters and bold symbols (i.e. $\mathbf{u}$ and $\boldsymbol{\rho}$), if not otherwise specified, are used to identify vectors. The symbol ϑ, unless specified, identifies a generic angular scalar while the symbols Y, P and R are used to identify the Tait-Bryan angles (Yaw, Pitch and Roll respectively). Any parameter which has the subscript m identifies a quantity relative to the master satellite while any parameter with the subscript s is used to identify a quantity relative to the slave satellite.

The trend of measurements, time series or noise sources in the frequency domain are evaluated using the Amplitude Spectral Density (ASD). The ASD is the square root of the power spectral density of the analyzed data set and is calculated using the overlapped segmented averaging of modified periodograms method [42]. The ASD plots which are depicted in the following chapters are obtained using a minimum 4-term Blackman-Harris window whose sidelobes adjacent to the main peak have an attenuation of 92 dB [43] while the window overlap is set to 50%.

Chapter 2

Interferometers for Future Gravity Missions

With a low-low satellite-to-satellite tracking mission, the Earth's gravity filed is mapped measuring changes in the distance connecting the two centers of mass of the satellites along their orbit. In order to achieve this metrology objective, the instrument requires a specific optical layout since its measurement has to be equivalent to the displacement of the center of masses of the two satellites. The high ranging accuracy is instead guaranteed by a highly stable high opto-mechanical design and by the usage of low-noise optronics.

In this chapter, three different layouts of the instrument are analyzed together with two fundamental optronic components; the photodiode and the phasemeter. Herein, particular attention is given to the phasemeter since its capability of detecting a heterodyne signal when buried into noise and the accuracy of the phase measurement are strongly dependant on the implementation solution adopted.

This chapter is organized as follows: in paragraph 2.1 three possible layouts of a laser ranging interferometer are described together with their measurement principle. The photodiode and the phasemeter are discussed in paragraphs 2.2 and 2.3 respectively. In paragraph 2.4, the principle noise sources which degrade the overall measurement performance of each of the three layouts are investigated and compared to the GRACE Follow-On requirement.

2.1 The interferometer

The interferometers which are here analyzed as possible candidates for a future geodesy mission are based on the *Mach-Zehnder interferometer*. Because of the limited power available on board a satellite it would not be possible to use a single laser to cover an intra satellite distance of hundreds of kilometers. For such a reason, the instrument is conceived to operate according to a transponder configuration. Of the satellite pair, one is going to lock its laser to a reference cavity and acts as a frequency reference while the other satellite is going to phase-lock its laser to the frequency of the received light.

The optical axis of the system is the one which connects the reference test masses of the accelerometers. Since these are not directly accessible, the layout of the interferometer requires an expedient which allows to reference the instrument's measurement to these points without introducing measurement artifacts. Hereafter, three possible solutions are presented.

2.1.1 The on-axis layout

In order to minimize the mechanism which couples the attitude jitter of the satellite into an apparent longitudinal measurement (effect known in literature as Tilt-to-Piston Coupling

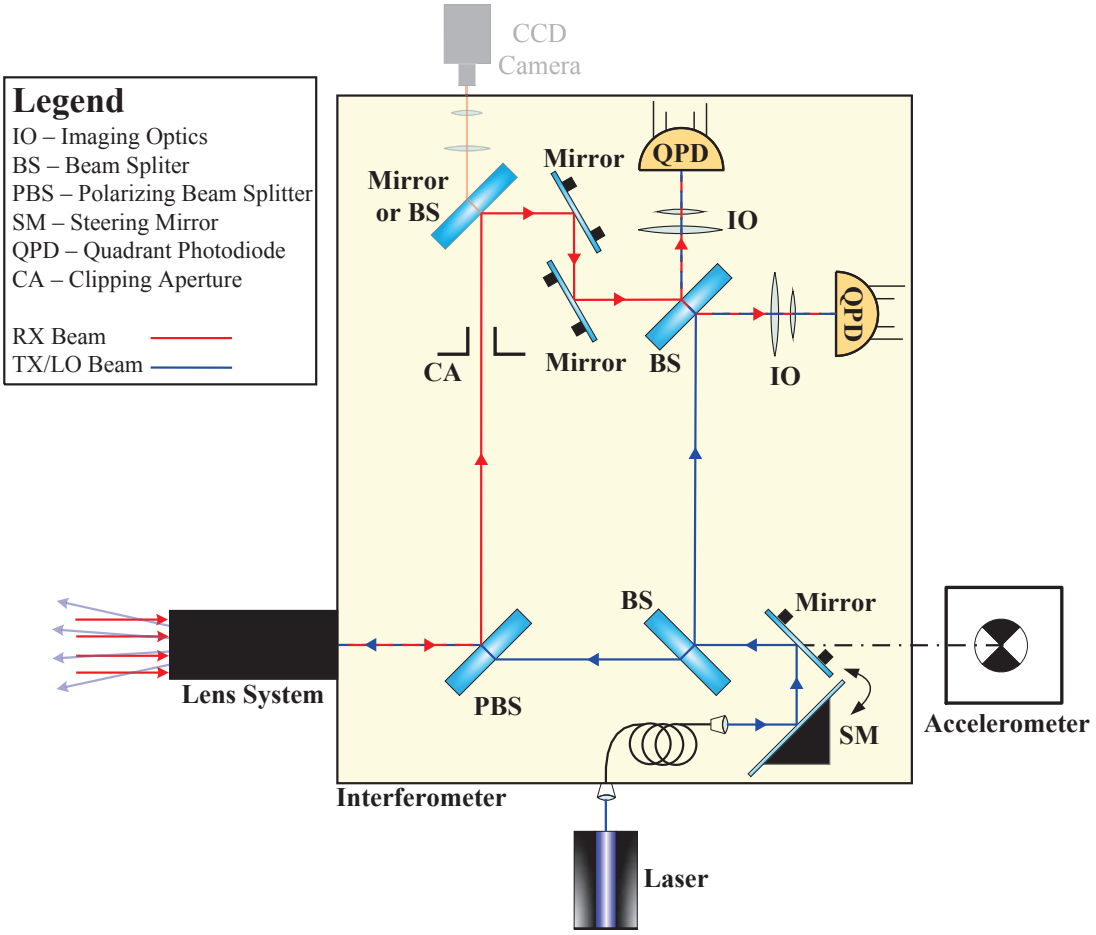

Figure 2.1: This picture shows a bi-dimensional sketch of the layout of the interferometer. In reality the mirrors need to be properly configured in the three dimensional space (i.e. the three mirrors after the clipping aperture have to form a corner cube) in order to align the incoming and outgoing beam, the LO beam and RX beam at the photodiodes and to correctly match the beam paths. The image shows also the modification that needs to be applied in order to include an acquisition sensor on the receive path. This representation is intended to show the operating principle of this layout and the beam routing and the arrangement of the optical components of a real on-axis system might differ from the one represented.

(TPC) noise), a lens system is introduced in front of the optical bench of the interferometer (a schematic layout of this design is depicted in Fig. 2.1).

The goal of the lens system is to image the RX light illuminating the aperture of the instrument onto the clipping aperture of the optical bench. Since the measurement has to be performed with respect to the accelerometer, the external pupil of the lens system has to be coincident with the reference point of the accelerometer. The Transmitted (TX) beam has to rotate with respect to accelerometer reference point, therefore the internal pupil of the lens system has to be placed on the steering mirror and the pathlength from the aperture of the instrument to the steering mirror has to be identical to the pathlength from the aperture of the instrument to the clipping aperture of the optical bench. For this design, the clipping aperture represents the aperture stop of the instrument and the lens system can act as a 1:1 imaging system (magnification is not required).

The imaging optics reduces the size of the RX beam so that the photodiode detects all of the light and does not clip it. In order to make this part of the interferometer insensitive to TPC noise, the optics has to image the clipping aperture and the Steering Mirror (SM) on

the photodiode. Since the imaging optics and the lens system represent a multiple stage relay system, the real pupil of the lens system has to be coincident with the entrance pupil of the imaging optics. Hence the entrance pupil of the imaging optics coincides with the clipping aperture of the optical bench and with the steering mirror. The exit pupil of the imaging optics is instead coincident with the photodiode. The Quadrant-PhotoDiode (QPD)s have to be concentric with the clipping aperture although their diameter has to be a bit smaller than the diameter of the clipping aperture in order to avoid clipping overlap (which introduces TPC noise). A representation of the pupil matching for this layout is given in Fig. 2.2.

The number of mirrors and their arrangement after the clipping aperture is designed for matching the pathlength of the RX beam and the pathlength of the LO beam. The contrast at the photodiode, although not strictly necessary, can be maximized by routing the RX beam such that its direction, at the photodiodes, is antiparallel with respect to the direction of the LO beam.

By placing a mirror with a 45° angle between the lens system and the polarizing beam splitter it is possible to mount the whole interferometer orthogonal with respect to the line of sigh of the instrument (the lens system would also be tilted of 90° with respect to the sketch of Fig. 2.1). This would allow to build compact interferometer-accelerometer assembly.

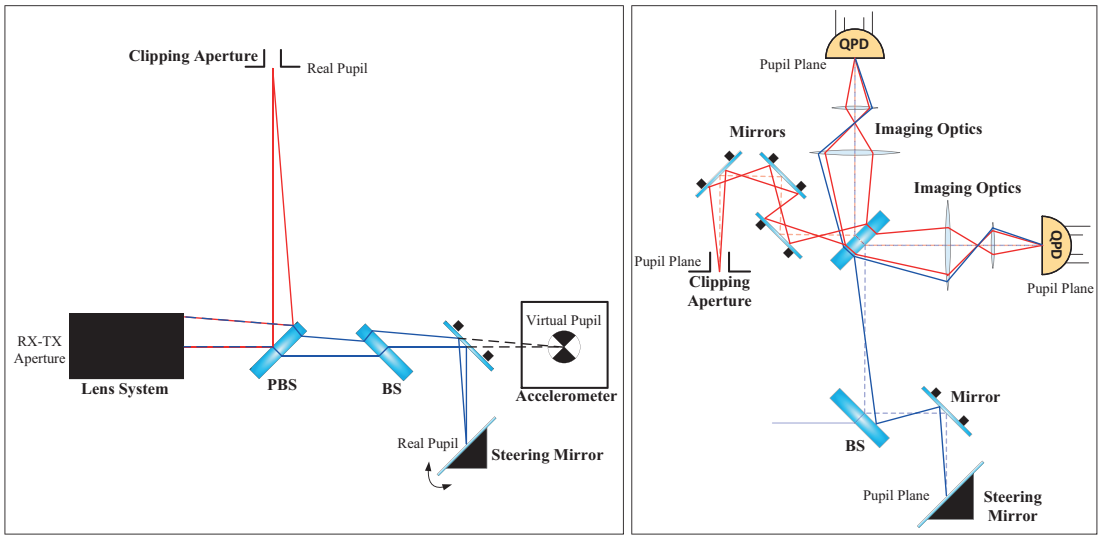

Figure 2.2: The left panel depicts the arrangement of the real and virtual pupil planes of the lens system while the right panel depicts the arrangement of the pupil planes of the imaging optics. For this particular application, the image planes and pupil planes of the lens system and of the imaging optics are coincident.

Measurement principle

The electrical fields of the two interfering beams can be written as

$$\begin{aligned} E_{\mathrm{m}}(t) &= A_{\mathrm{m}} e^{\mathrm{i}\,[\omega_{\mathrm{m}} t - k d_{\mathrm{m}} - \psi_{\mathrm{m}}]} \\ E_{\mathrm{s}}(t) &= A_{\mathrm{s}} e^{\mathrm{i}\,[\omega_{\mathrm{s}} t - k d_{\mathrm{s}} - \psi_{\mathrm{s}}]} \end{aligned} \tag{2.1}$$

where $\omega_i = 2\pi f_i$ and is f_i the laser frequency. ψ_i and d_i (with $i = \mathrm{m}, \mathrm{s}$)[1] are respectively the phase fluctuations of the laser and the distance that the beams have travelled before interfering while k is the wavenumber. The frequency ω_{m} can be rewritten as $\omega_{\mathrm{s}} + \Delta\omega$ where the term $\Delta\omega$ represents the frequency difference. This value is positive if the frequency of the field E_{m}

[1] the subscript i should not be confused with the term i of Eq. 2.1 which represents the imaginary unit.

is bigger than the frequency of the field E_s otherwise it is negative. The electrical field $E(t)$ of the interference beam can be written as the sum of the two fields defined beforehand while the photocurrent at the photodiode, proportional to $|E(t)|^2$, is equal to

$$|E(t)|^2 = |E_\mathrm{m}(t)|^2 + |E_\mathrm{s}(t)|^2 + 2|E_\mathrm{m}(t)| \cdot |E_\mathrm{s}(t)| \cos\{\arg[E_\mathrm{m}^*(t)\, E_\mathrm{s}(t)]\} \tag{2.2}$$

Considering $\omega_\mathrm{m} > \omega_\mathrm{s}$ and neglecting the amplitude coefficients and the wavelength difference between the laser beams, the last term of Eq. 2.2 can be approximated to

$$\cos[\Delta\omega t - \underbrace{(\psi_\mathrm{m} + kd_\mathrm{m} - \psi_\mathrm{s} - kd_\mathrm{s})}_{\Psi}] \tag{2.3}$$

where Ψ represents the measurement of the phasemeter. Dividing Ψ by the wavenumber k yields the phasemeter measurement in length units. The term ψ_i/k (with $i = \mathrm{m}, \mathrm{s}$) represents the pathlength error caused by the phase fluctuations.

With the active transponder scheme, the offset phase-lock is applied to the slave satellite and the main measurement signal, Ψ_m, is effectively the sum of Ψ_m and Ψ_s. Indeed the phase information of Ψ_s is transmitted back to the master satellite via the phase-lock of the free running laser. According to the schematic representation of the optical link given in Fig. 2.3, the phasemeters' measurements in length units are

$$\begin{aligned} \Psi_\mathrm{m} &= (e + g + p_\mathrm{m}) - (a + p_\mathrm{s} + b + D + g) \\ \Psi_\mathrm{s} &= (a + c + p_\mathrm{s}) - (e + p_\mathrm{m} + f + D + c) \\ &\downarrow \\ \Psi_\mathrm{m} + \Psi_\mathrm{s} &= -b - 2D - f \approx 2\Lambda \end{aligned} \tag{2.4}$$

In reality, since the light travel time is finite, the laser phase noises (p_m and p_s) do not cancel out. The finite light travel time also introduces measurement noise because of changes in the distance between the laser source and the beamsplitter. This last effect is nevertheless negligible if compared to the laser phase noise [40]. This optical layout requires an accurate alignment of the components of the optical bench otherwise the range measurement can be severely affected by noise (especially TPC noise).

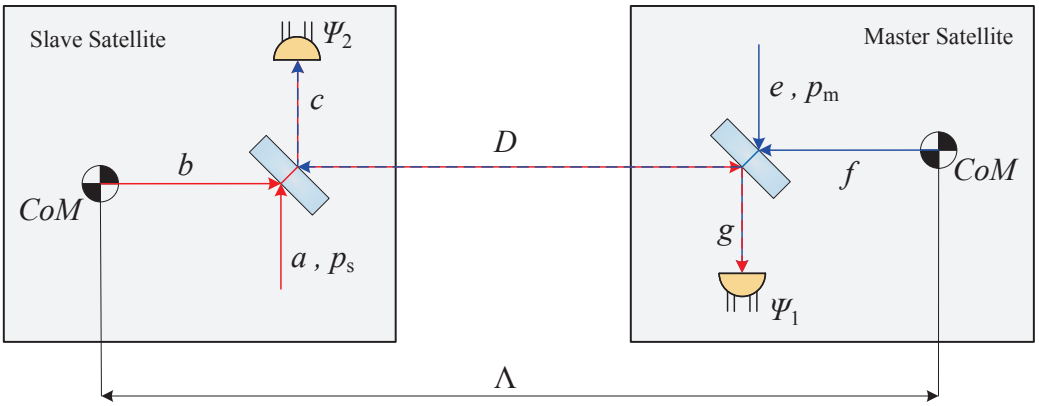

Figure 2.3: Representation of the optical pathlength measured with an on-axis interferometer. The measurement is referenced to the fiducial point of the accelerometer thanks to the lens system.

2.1.2 Racetrack layout - TMA Configuration

The instrument is designed according to a racetrack layout similar to the one adopted for the LRI of the GRACE Follow-On mission [39, 40, 44, 45]. Although this is an off-axis system,

the TPC noise is severely reduced thanks to the usage of a TMA [46, 47]. The mirrors of the TMA are configured as faces of a Corner Cube Retroreflector (CCR) but since the movement of the laser beam on the mirrors is limited to a few µrad, the whole structure of the CCR is not necessary. Because the TMA is indeed a cut out of a corner cube, this inherits all of its properties. Moreover, its vertex is not a physical point and can be aligned to the fiducial point of the accelerometer without any mechanical interference. Compared to the LRI, this design uses one of the mirrors of the corner cube as the beam splitter of the optical bench. This modification allows to remove the compensation plate [40] since the interference between the TX beam and LO beam occurs at the front face of the beam splitter (which has a R-T ratio of 5 : 95 or similar).

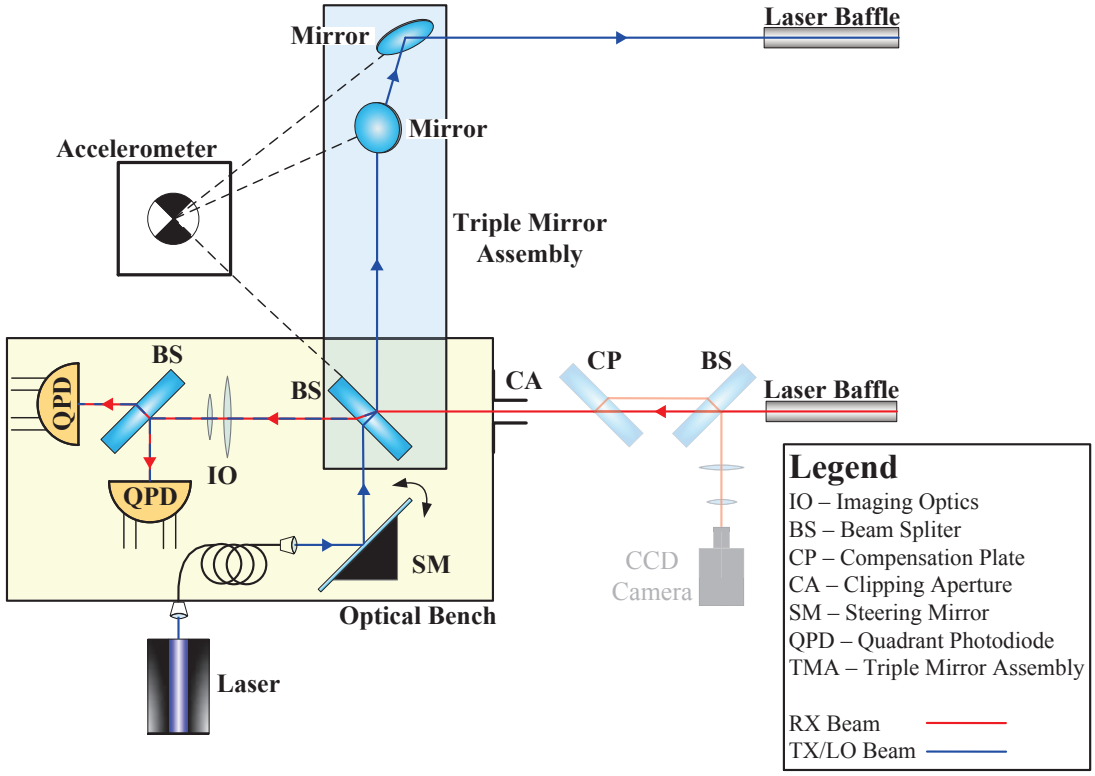

Figure 2.4: The picture shows a sketch of the layout of the interferometer. In the picture, the two main assemblies are highlighted (the TMA and optical bench) although, unlike the LRI, these will most probably constitute a unique structure. The RX path also includes the optics necessary to eventually include an acquisition sensor. Although this is just a schematic representation of the operating principle of this interferometer, a real layout is not going to significantly differ from the one here depicted.

The imaging optics is designed such that rotations of the steering mirror do not introduce TPC noise at the photodiodes. Therefore the real pupils of this lens system are located at the clipping aperture, at the steering mirror and at the photodiodes. The operating principle of the imaging optics is therefore identical to the one of the on-axis layout (see the right panel of Fig 2.2).

Measurement principle

The measurement principle of the interferometer is identical to the one described in paragraph 2.1.1. Labelling the beam paths with the same nomenclature adopted in Fig. 2.5, the

interferometric measurement is representative of the inter-satellite distance

$$\begin{gathered}\Psi_{\mathrm{m}} = (e + f + p_{\mathrm{m}}) - (a + p_{\mathrm{s}} + c + D + f) \\ \Psi_{\mathrm{s}} = (a + b + p_{\mathrm{s}}) - (e + p_{\mathrm{m}} + g + H + b) \\ \downarrow \\ \Psi_{\mathrm{m}} + \Psi_{\mathrm{s}} = (c + D + g + H) = 2\Lambda\end{gathered} \tag{2.5}$$

Also in this case, the effects of the finite light travel time have not been included in the final estimation of the pathlength measurement. Since the beam splitter of the optical bench is coincident with one of the mirrors of the TMA, the stability of the optical bench and its alignment with respect to the other two mirrors of the TMA cannot be relaxed (unlike for the LRI [40]) as these actively modify the position of the vertex of the TMA. For such a reason, TMA and optical bench should be manufactured as a single structure although further analysis would be necessary in order to evaluate the complexity of such a design and if other unconsidered mechanism degrade the measurement performance of the instrument.

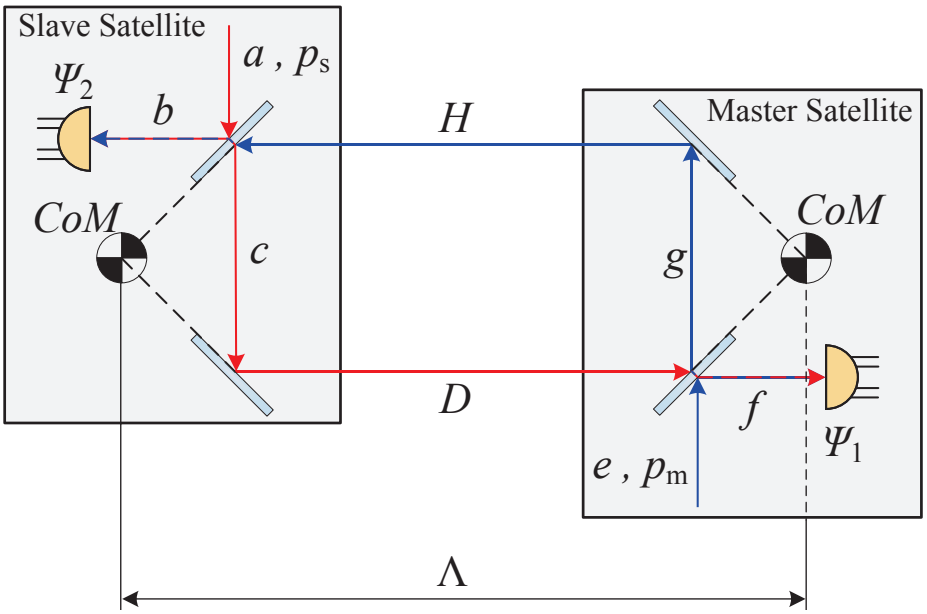

Figure 2.5: Representation of the optical pathlength for the racetrack configuration.

2.1.3 Racetrack layout - Compact Corner Cube

The size of the GRACE Follow-On like interferometer depends on the dimension of the accelerometer. Indeed, the minimum length of the TMA has to (at least) equal the distance from the fiducial point of the accelerometer to its external housing. A viable solution for reducing the dimensions of the interferometer is to allow an offset between the vertex of the TMA and the fiducial point of the accelerometer along the Line of Sight (LoS) of the instrument. In this case, the TMA structure can be replaced by a classical corner cube with compact dimensions [48]. This alternative configuration is depicted in Fig. 2.6.

With this layout, a static angular offset of the satellite pointing shifts sideways the LoS of the interferometer with respect to the LoS of the measurement (see Fig. 2.7). This offset increases severely the displacement noise of the instrument since the TPC phenomena is enhanced. The magnitude of the TPC noise is proportional to the magnitude of the static pointing offset, to the magnitude of the distance between the vertex of the corner cube and the fiducial point of the accelerometer and from the magnitude of the residual pointing jitter of the satellite.

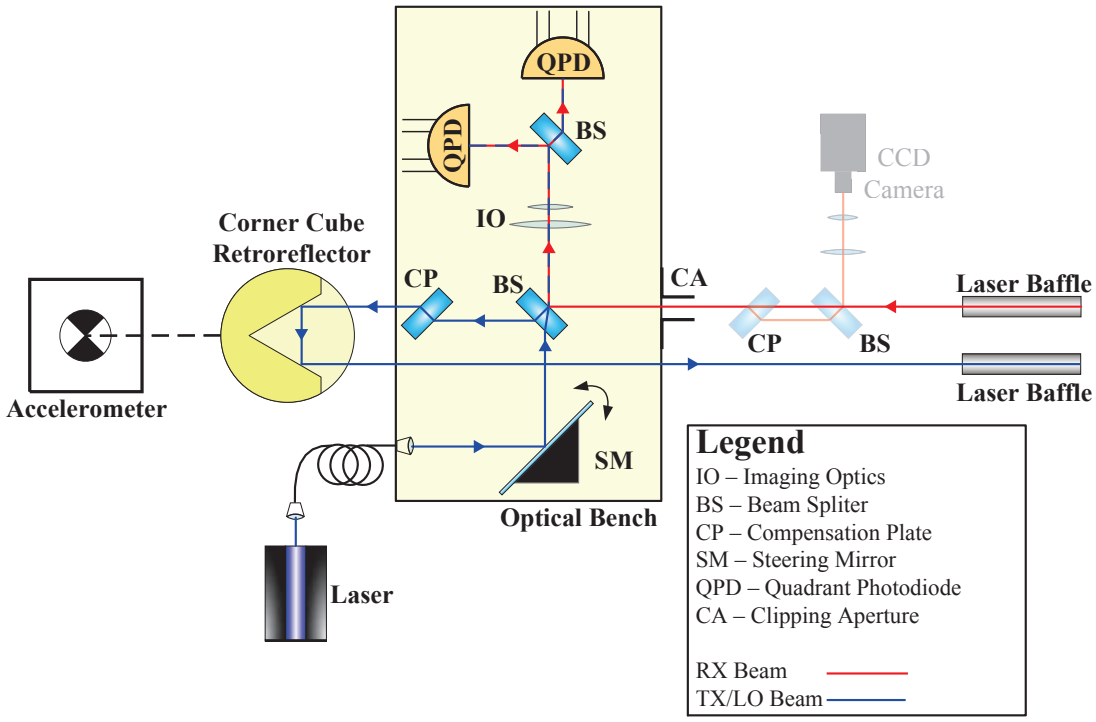

Figure 2.6: This layout of this instrument is identical to the LRI of GRACE Follow-On. The TMA in here replaced by a corner cube whose vertex has a pre-defined offset along the line of sight of the instrument with respect to the fiducial point of the accelerometer.

Considering only Yaw rotations

$$\begin{aligned} \Delta x &= \bar{o}\cos\left(\mathrm{Y}_0\right) \\ \Delta y &= \bar{o}\sin\left(\mathrm{Y}_0\right) \\ &\downarrow \\ \delta p\left(t\right) &= -\Delta x \mathrm{Y}^2\left(t\right) + 2\Delta y \mathrm{Y}\left(t\right) \end{aligned} \tag{2.6}$$

where Y_0 is the static pointing offset in Yaw, $\mathrm{Y}\left(t\right)$ the Yaw residual jitter and $\bar{o}$ the static offset between the vertex of the corner cube and the fiducial point of the accelerometer. Similarly, a static offset in Pitch returns a TPC noise equal to $\delta p\left(t\right) = -\Delta x \mathrm{P}^2\left(t\right) + 2\Delta y \mathrm{P}\left(t\right)$ where Δx and Δy are now calculated substituting Y_0 with P_0. Assuming a vertex offset of 200 mm, a static pointing offset of 1 mrad and a residual in band jitter of $\pm 100\,\mu\mathrm{rad}/\sqrt{\mathrm{Hz}}$, the resulting TPC noise is equal to $\pm 40\,\mathrm{nm}/\sqrt{\mathrm{Hz}}$. The magnitude of this error is thus unacceptable if the single link ranging noise of the instrument has to be between $10 - 50\,\mathrm{nm}/\sqrt{\mathrm{Hz}}$ or lower.

The measurement principle of this design is similar to the one of the GRACE mission. Indeed, the phase center of the K-Band Ranging (KBR) instrument is not coincident with the fiducial point of the accelerometer but has a static offset. The range measurement is corrected on-ground through the knowledge of the KBR-accelerometer distance and using the measurement of the Star Tracker (STR) for evaluating the attitude of the satellite. A similar approach can be used here to mitigate the TPC noise. Indeed both the static pointing offset of the satellite and the residual jitter (Pitch and Yaw) can be measured through Differential Wavefront Sensing (DWS) with a much higher precision compared to the one provided by STRs. The distance between the vertex of the corner cube and the fiducial point of the accelerometer can be, instead, either measured on ground or in-orbit through a calibration maneuver similar to the phase-center calibration maneuver of the KBR [49].

The measurement principle of this layout is conceptually identical to the one of Fig. 2.5,

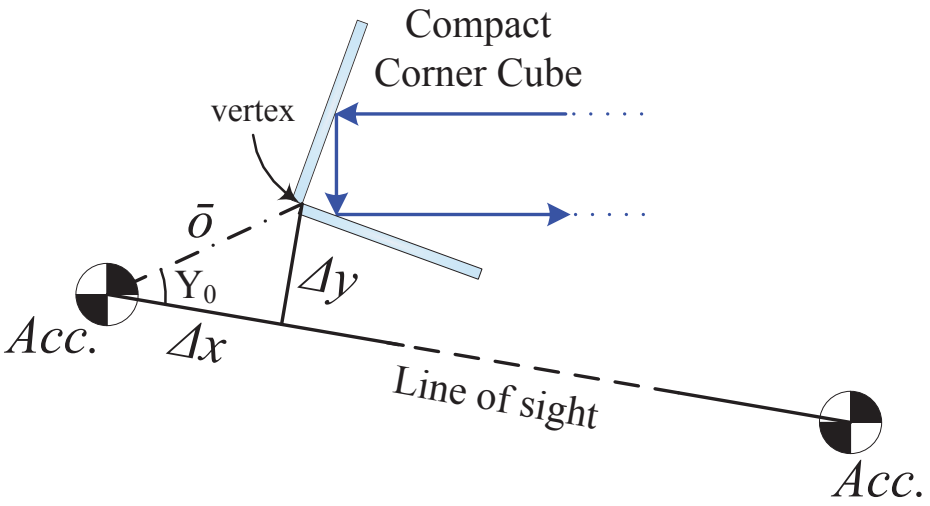

Figure 2.7: Position of the vertex of the corner cube with respect to the line of sight of the measurement. This picture depicts a static offset in Yaw.

although the instrument does not measure the distance $2L$ but $2L - 2\bar{o}$. Since the position of the vertex of the corner cube is independent from the location of the optical bench, the dimensional stability of the optical bench is not critical for fulfilling the noise requirement (as for the LRI) since pathlength errors on the RX side are compensated by an equal change on the TX side.

2.2 QPDs and Differential Wavefront Sensing

The QPD is a key component of the interferometer since it allows to recover angular and range information by manipulating the photocurrent output of each quadrant. The photocurrent of a single quadrant of the QPD is proportional to the time averaged power of the electrical field of the LO beam superimposed to the electrical field of the RX beam. In general, the time varying part of the photocurrent of a single quadrant can be written as

$$I_i(t) = 2\,\rho_{\mathrm{QPD}}\,h(f_{\mathrm{het}})\,\sqrt{P_{\mathrm{LO},i}P_{\mathrm{RX},i}\eta_{\mathrm{het}}}\cos(2\pi f_{\mathrm{het}}t + \phi_i) \quad \text{where} \quad i = \mathrm{A},\,\mathrm{B},\,\mathrm{C},\,\mathrm{D} \tag{2.7}$$

where ρ_{QPD} is the responsivity of the photodiode while $h(f_{\mathrm{het}})$ is its frequency dependency. The other terms, $P_{\mathrm{LO},i}$, $P_{\mathrm{RX},i}$, η_{het} and ϕ_i are respectively the power of the LO beam, the power of the RX beam, the heterodyne efficiency and the photocurrent's phase of the i^{th} quadrant. Figure 2.8 shows, as example, the offset between the two interfering beams and the resulting output current of each quadrant of the photodiode. The horizontal and vertical misalignments between the RX beam and the LO beam cause a phase difference in the output currents of each quadrant (see the right panel of Fig. 2.8). Properly combining these phases, it is possible to derive the horizontal and vertical DWS signal [50, 51]

$$\begin{aligned} \mathrm{DWS}_{\mathrm{hor}} &= (\phi_{\mathrm{A}} + \phi_{\mathrm{C}}) - (\phi_{\mathrm{B}} + \phi_{\mathrm{D}}) \\ \mathrm{DWS}_{\mathrm{ver}} &= (\phi_{\mathrm{A}} + \phi_{\mathrm{B}}) - (\phi_{\mathrm{C}} + \phi_{\mathrm{D}}) \end{aligned} \tag{2.8}$$

where ϕ_i is the phase of i^{th} quadrant. If the vertical and horizontal tilt angles (α and β) are sufficiently small, the photodiode operates in its linear range and the DWS signal is directly proportional to the offset between the interfering beams

$$\begin{aligned} \mathrm{DWS}_{\mathrm{hor}} &\approx C_{\mathrm{DWS}} \cdot \alpha \\ \mathrm{DWS}_{\mathrm{ver}} &\approx C_{\mathrm{DWS}} \cdot \beta \end{aligned} \tag{2.9}$$

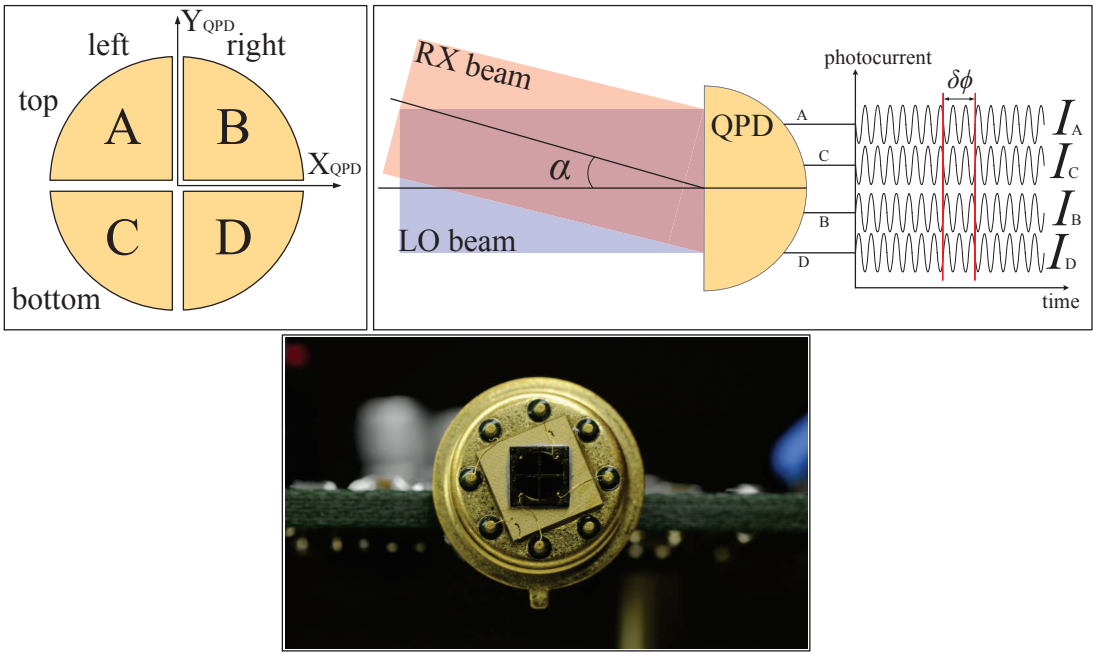

Figure 2.8: The left panel shows a sketch of the front view of a QPD. The right panel shows how an offset between the two interfering beams affects the photocurrent output of the four quadrants. The lower panel depicts the front view of a real QPD used in for laboratory experiments.

where C_{DWS} is the coupling factor between tilt angle and phase offset [52]. As demonstrated for its positioning (see Eq. 2.4 and 2.5) also the alignment of the QPD is not critical for the measurement accuracy of the interferometer since this error is common mode for the RX beam and the LO beam.

The phase of the interference signal (ϕ_i) also contains the information on the distance travelled by the laser beam before the interference. In order to extract this information, the photocurrent is fed to a transimpedance amplifier before being demodulated.

2.3 The phasemeter

The outcome of the transimpedance amplifier is a voltage signal (hereafter referred as interference signal) whose phase and frequency are the phase and the frequency of the heterodyne signal. The phase of the interference signal, containing the range measurement information, is extracted using a Digital Phase-Locked Loop (DPLL) because this digital circuit is capable of tracking the phase of a signal even if its frequency changes over time. The circuit used to lock, track and, extract the phase information of the interference signal is also known in literature as *phasemeter*. Up to date, phasemeters for space-borne laser interferometers have been principally studied for the for the LISA mission [53, 54, 55, 56, 57, 58, 59, 60]. Indeed, the phasemeter used for the LRI of GRACE Follow-On is an adaptation of the LISA phasemeter.

The studies on the LISA phasemeter showed how a mixing-phase detector DPLL is the most suitable choice with respect to other DPLL detectors because it is the most accurate in measuring the phase of the signal to which it is locked to. According to the selected bandwidth of this DPLL, the chances of locking the interference signal and the speed with which it is locked strongly depend on the difference between the frequency of the interference signal and the frequency of the Numerically Controlled Oscillator (NCO) [61, 62]. The overwhelming factor driving the bandwidth of the DPLL is the cut-off frequency of the Low-Pass Filter (LPF) after the mixing-phase detector. Indeed, this has to be small enough to reject broadband noise but

also large enough for reducing the locking time. A good compromise can be found using cut-off frequencies which vary from 10 kHz to 300 kHz although a locking time in the millisecond range can be achieved only if the maximum frequency offset between the interference signal and the NCO is about 20 kHz or smaller.

Due to launch vibrations and temperature changes between space and ground it is not possible to exactly establish the operating frequency (and therefore the heterodyne frequency) of the lasers on-board the orbiting satellites (the initial frequency offset can reach up to 200 MHz [63, 64]). Under these circumstances, a phasemeter would not be able to lock to the interference signal especially if this is also hidden by noise. The phasemeter therefore requires a frequency estimation unit in order to correctly tune the frequency of its NCO and lock to the interference signal.

Up to date, this initial frequency estimation problem has been tackled using Discrete Fast Fourier Transform (DFFT) algorithms [63, 65]. The DFFT algorithm itself is not directly capable of adjusting the frequency of the NCO but requires a separate frequency identification algorithm which can be rather complex. Moreover, DFFT algorithms extensively use computational resources and cannot be implemented as simple digital circuits. A phasemeter which uses this type of frequency estimation is labelled hereafter as DFFT based phasemeter and is not analyzed in detail since discussed in literature.

Here, a different approach for the frequency estimation is presented. The frequency of the heterodyne signal is estimated combining a phase-frequency detector DPLL [61] and a Kalman filter. The phase-frequency detector offers a virtually unlimited pull-in range and prevents false locks (the DPLL does not synchronize in e.g. with a harmonic of the input signal) allowing the DPLL to work under more difficult operating conditions than a mixing phase detector. Nevertheless, it cannot be used to replace the mixing phase detector DPLL because it is highly affected by cycle slips in presence of noise (with an SNR below 5 dB a phase-frequency detector hardly reaches lock).

Since high SNRs are not always achievable for space applications, a de-noising system based on elements of the discrete wavelet transform theory [66] is included in the architecture of the phasemeter (this is similar to the de-noising technique adopted for acquiring Global Positioning System (GPS) signals [67, 68, 69]). The combination of the phase-frequency detector DPLL, the Kalman filter and the de-noising system define the *frequency estimation unit* which allows estimation of the frequency of the interference signal with an accuracy comparable to the lock range of the mixing-phase detector DPLL. This is than used for phase-locking the slave laser and is labelled hereafter as *main DPLL*.

With the offset phase-locked transponder configuration the frequency of the heterodyne signal represents the absolute value of the frequency difference between the two interfering beams. Indeed, the same positive or negative offset between the frequency of the phase-locked laser and to the (reference) frequency of the cavity stabilized laser result in the same heterodyne signal. In order to control the frequency of the phase-locked laser and keep it within the bandwidth of the phasemeter, it is necessary to know the sign of the offset. If this is not correctly identified immediately after acquiring the signal, any attempt of the laser control system to phase-lock the two lasers will fail in 50% of the cases. For such a reason, together with the frequency acquisition unit, the phasemeter requires an *offset-lock control unit* which is capable of identifying in which sideband the phasemeter detected the signal.

The architecture of the phasemeter is depicted as a block diagram in Fig. 2.9. It can be divided into three major subsystems, the frequency estimation unit, the main DPLL and the offset-lock control unit. The frequency estimation unit in turn combines a de-noising system, a phase-frequency detector DPLL and a Kalman filter and is designed with the aim of minimizing the use of computational resources. Since the de-noising system uses the Wavelet Packet Decomposition (WPD) to increase the SNR of the signal, this phasemeter is labelled as *WPD based phasemeter*.

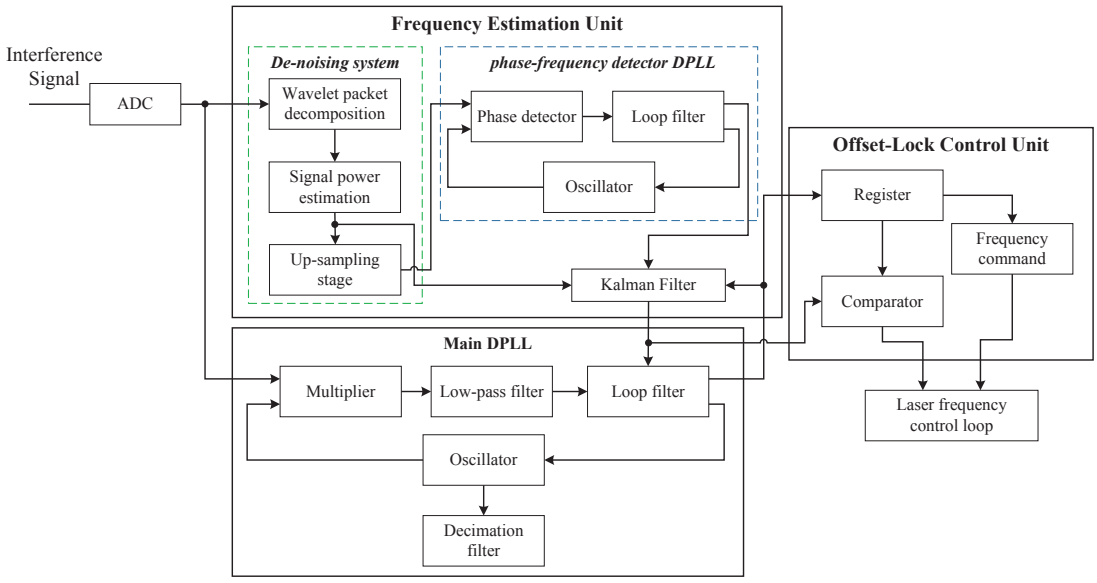

Figure 2.9: Block diagram of the signal acquisition system of the phasemeter. The main DPLL is integrated with the frequency estimation unit and the offset-lock control unit.

2.3.1 The operating principle of the WPD based phasemeter

The de-noising unit

The measurement signal, once digitized, is processed via the WPD tree. The WPD tree divides the electronics bandwidth into several equal sub-bands, thus increasing the SNR in each sub-band. The left panel of Fig. 2.10 depicts the classical implementation of a wavelet packet decomposition tree. The right panel shows the optimized wavelet packet decomposition tree used in the de-noising system. After that the signal has been filtered, it is multiplexed using a binary counter. The multiplexer alternates the input signal of the filters in the n^{th} stage with the outputs of the stage n - 1, thus simulating the downsampling process. This expedient allows the total number of filters required to be reduced. In particular,

$$\underbrace{F = \sum_{i=1}^{n} 2^i}_{\text{classic WPD}} \quad \rightarrow \quad \underbrace{F = 2n}_{\text{optimized WPD}} \tag{2.10}$$

where F is the total number of filters and n the number of stages. The wavelet packet decomposition tree depicted in Fig. 2.10 also differs from the classical one as it neglects the down-sampling process of the last stage. This increases the speed of the overall signal processing, but also implies that the sub-bands of the last stage are not sorted in frequency according to an ascending order.

The de-noising capability of the wavelet packet decomposition is proportional to the number of stages implemented. These have to be chosen for compatibility with the SNR required to operate the following subsystems.

The last stage of the wavelet packet decomposition tree is connected to a signal power estimation unit which is used to detect the sub-band with the highest power. The output signal of the sub-band with the highest power is routed to the up-sampling unit using a multiplexer commanded by the sub-band index signal. For some applications it may be necessary to void the output of the lowest frequency sub-bands as the noise power hides the measurement signal. For this reason, the signal power estimation unit includes a look up table (labelled as LUT in Fig. 2.11) which can exclude some sub-bands from being processed, if required.

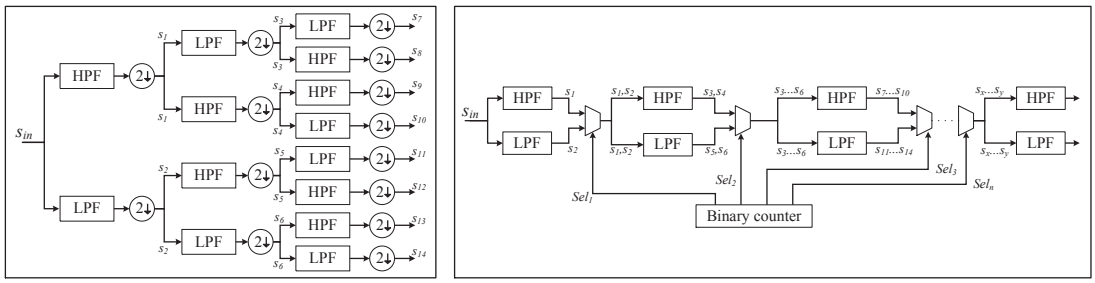

Figure 2.10: Block diagram of wavelet packet decomposition tree. The left panel shows a classical implementation of three stages while the right one depicts an optimized implementation of n stages.

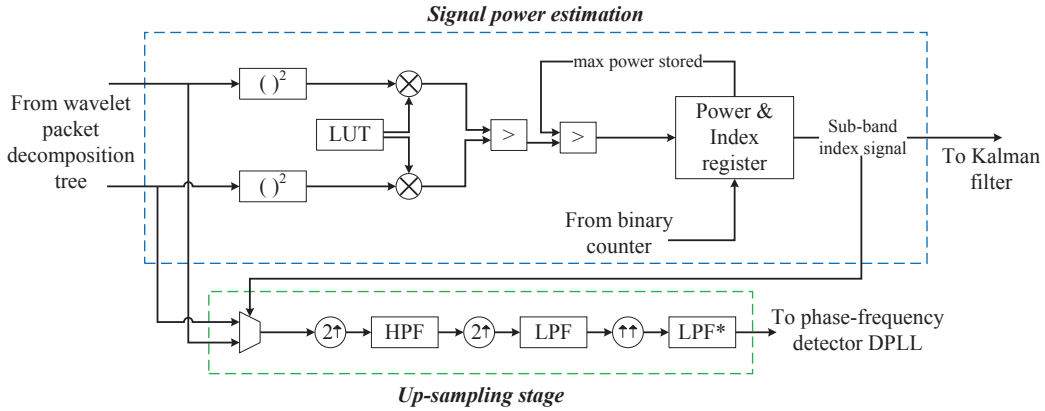

Figure 2.11: This figure shows a simplified block diagram of the power estimation unit and the up-sampling stage. The first two up-sampling blocks of the up-sampling stage are used to double the frequency of the input signal while the last up-sampling block is used to raise to frequency of the input signal to the sampling frequency.

After the signal power estimation stage, the operating frequency of the phasemeter is reduced by a factor $1/[2(n-1)]$ (where n is the number of stages of the wavelet packer decomposition tree) with respect to the clock frequency of the phasemeter. The phase-frequency detector would also have to operate with a signal that could vary within the bandwidth of the phasemeter. This would increase the time required by the phase-frequency detector DPLL to lock the signal as the parameters of its loop filter can be optimized only for a smaller frequency range ($\approx 2\,\mathrm{MHz}$). In order to overcome these restrictions, an up-sampling stage is implemented within the de-noising system.

The up-sampling is performed using the zero padding technique. This technique introduces repetitions of the up-sampled signal within the frequency spectrum at frequencies higher than the Nyquist frequency. By properly sequencing high-pass filters, low-pass filters and up-sampling blocks (see Fig. 2.11) this imaging effect can be used to map the output of any sub-band of the wavelet packet decomposition tree in a fixed frequency range. This allows optimization of the tuning parameters of the phase-frequency detector for a specific frequency interval.

The phase-frequency detector DPLL and the Kalman filter

The phase-frequency detector DPLL, whose block diagram is depicted in Fig. 2.12, is used to estimate the frequency of the interference signal. The oscillator of the phase frequency detector DPLL is a register while the loop filter is a Proportional-Integral (PI) controller. The frequency used to initialize the main DPLL is derived from the integrator block of the loop filter as it

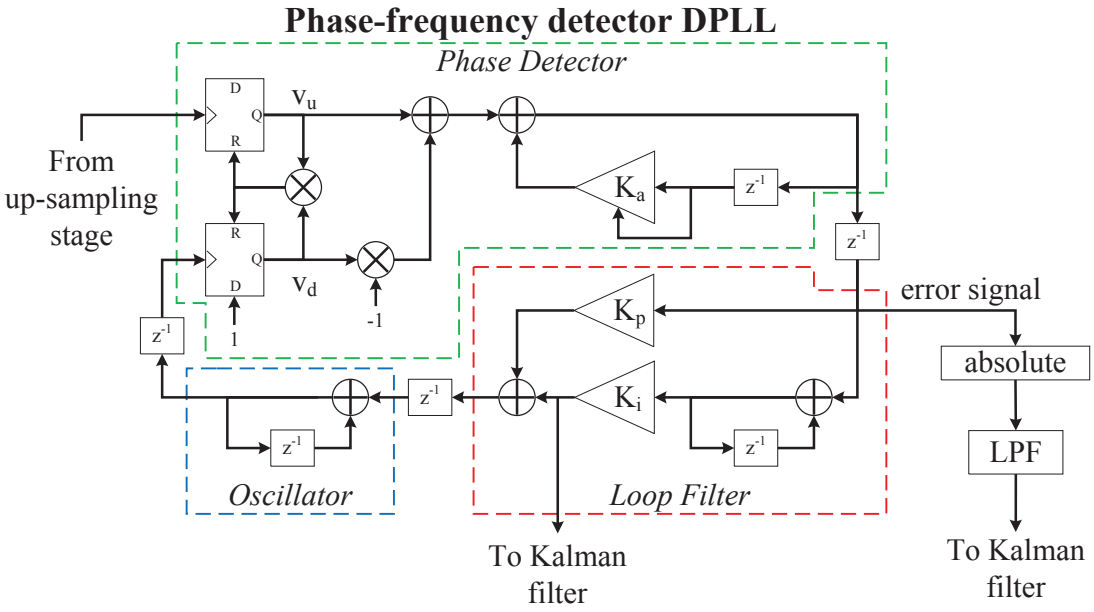

Figure 2.12: This picture depicts a detailed block diagram of the phase-frequency detector DPLL implemented.

returns a more accurate estimate of the frequency of the interference signal when compared to the frequency value returned by oscillator (the oscillator in this DPLL is used to track the phase of the interference signal).

As mentioned beforehand, the sub-bands of the wavelet packet decomposition tree are not ordered in frequency according to an ascending order. Moreover, with the up-sampling unit, the interference signal is confined in a fixed region of the frequency spectrum. Therefore, the frequency estimated by the integrator block of the loop filter cannot be directly used to initialize the main DPLL. The correct frequency value is recovered using the two least significant bits of the digital sub-band index which is stored in the signal power estimation unit. This leads to four different cases:

$$\begin{aligned}
\text{LSBs} = 00 &\rightarrow f_i = (i_{sb} + 4) \cdot \Delta f_{sb} - f_{osc} \\
\text{LSBs} = 01 &\rightarrow f_i = (i_{sb} + 3) \cdot \Delta f_{sb} - f_{osc} \\
\text{LSBs} = 10 &\rightarrow f_i = (i_{sb} - 2) \cdot \Delta f_{sb} + f_{osc} \\
\text{LSBs} = 11 &\rightarrow f_i = (i_{sb} - 3) \cdot \Delta f_{sb} + f_{osc}
\end{aligned}$$

where i_{sb} is the sub-band index expressed in decimal units, Δf_{sb} is the frequency width of the sub-bands and f_{osc} is the frequency value derived from the integrator block (loop filter) of the phase-frequency detector DPLL.

Due to residual noise in the measurement bandwidth and processing chain, the frequency value f_i is estimated with an uncertainty of 100 kHz. For this reason, f_i is smoothed by means of a scalar Kalman filter before it is used to initialize the main DPLL.

Since the system dynamics are unknown in the millisecond timescale, the derivative of the frequency is chosen to be null ($\dot{f} = 0$) while the uncertainty of the system model is set to unit ($q_k = 1$). This yields,

$$\begin{aligned}
f^-_{(k+1)} &= f^+_k \\
p^-_{(k+1)} &= p^+_k + 1
\end{aligned} \tag{2.11}$$

The covariance of the observation is calculated based on the lock indication of the phase-

frequency detector DPLL and is expressed as

$$r_k = 2^{11} lock^4 \tag{2.12}$$

The lock indication (*lock* in Eq. 2.12) signal is the absolute value of the error signal which has been low-pass filtered. A small value of the lock indication signal represents an accurate value of the estimated frequency. The power of 4 is derived from experimental testing and is aimed to reduce the weight of high values of the lock indication signal. The lock indication signal of Eq. 2.12 is also multiplied by a factor 2^{11} in order to reduce the cutoff frequency of the low-pass characteristic of the Kalman filter.

Considering r_k larger than p_k^- the Kalman gain is expressed as

$$k_k = \frac{p_k^-}{p_k^- + r_k} \approx \frac{p_k^-}{r_k} = 2^{\left(\log_2 p_k^- - \log_2 r_k\right)} \tag{2.13}$$

In order to avoid a large register size and the division in the Kalman gain calculation, the binary logarithm of r_k and p_k is used in Eq. 2.13. The frequency of the interference signal is

$$f_k^+ = f_k^- - k_k \left(f_k^- - f_i\right) \tag{2.14}$$

while the updated covariance of the state is

$$p_k^+ = (1 - k_k)\, p_k^- \tag{2.15}$$

The covariance of Eq. 2.15 is used to control the re-initialization of the main DPLL. When this parameter is below a prefixed threshold, f_k^+ is compared with the operating frequency of the main DPLL. If the difference between these two frequencies is above 1 MHz, the main DPLL is re-initialized. The re-initialization occurs re-setting the integrator part of the main DPLL's loop filter with f_k^+. Once the main DPLL is locked, a new initialization can occur only if it loses lock.

The main DPLL

The main DPLL uses a mixing-phase detector and is depicted in Fig. 2.13. A PI controller is

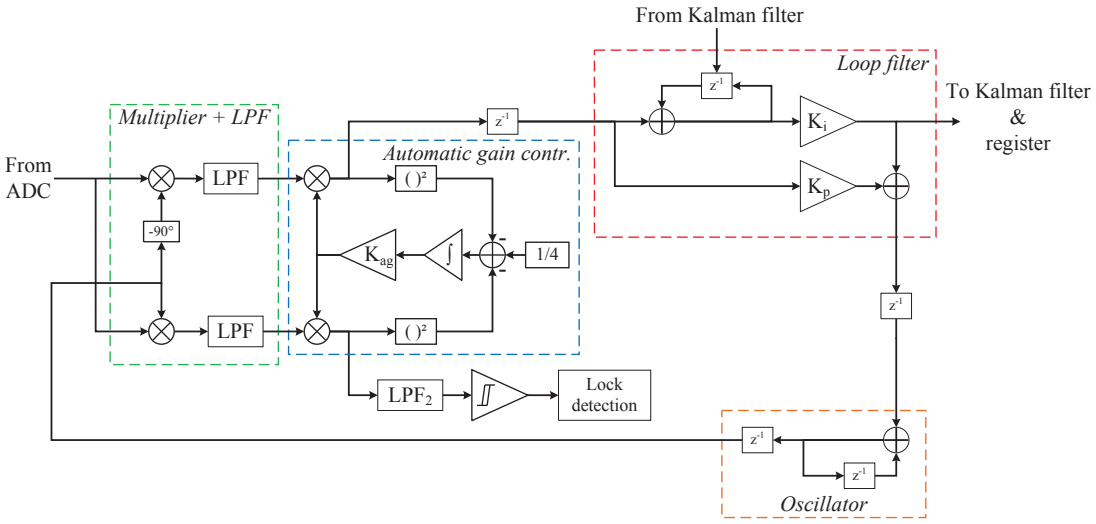

Figure 2.13: The figure depicts a detailed block diagram of the design of the main DPLL. Together with the mixing phase detector, the main DPLL integrates an automatic gain controller and a lock control unit.

also used here as loop filter and has to be tuned in order to guarantee optimal performance in terms of phase measurements and locking time. A loop bandwidth of about 10 kHz would increase the phase measurement accuracy while a loop bandwidth grater than 50 kHz would reduce the time required by the main DPLL to lock. For this reason, the main DPLL is designed to operate in two different modes; acquisition mode (loop bandwidth $>$ 50 kHz) and measurement mode (loop bandwidth $\leq$ 10 kHz). When the main DPLL is locked it is operated in measurement mode, otherwise the acquisition mode is used. The mode switch is controlled by monitoring the lock signal and is operated by changing the parameters of the PI controller and the LPFs.

In order to evaluate if the DPLL is locked to the interference signal, the in-phase component of the mixing phase-detector is processed with an LPF (labelled as LPF_2 in Fig. 2.13). In case the main DPLL is locked, the outcome of this LPF is a signal whose amplitude is half of the amplitude of the interference signal. A Schmitt trigger, placed after the LPF, allows evaluation of the operating state (locked or unlocked) of the main DPLL. In order to define the threshold of the Schmitt trigger, the main DPLL includes an automatic gain controller [70] which controls the amplitude of the interference signal to be unit irrespective of its real magnitude. This also allows optimal tuning of the parameters of the loop-filter and LPF of the mixing phase detector.

The last stage of the phasemeter is dedicated to the data decimation for signal processing. Since the frequency components of the signal of interest are below 1 Hz, extensive downsampling can be performed using a cascade integrator-comb filter [71].

The offset-lock control unit

Once the main DPLL is locked, the lock signal triggers the offset-lock control unit which immediately stores the current frequency value of the interference signal in a register. Afterwards the piezo-electric driver increases the laser frequency by 1 MHz using a step command. Since the bandwidth of the main DPLL is at maximum a few hundreds of kHz, immediately after the 1 MHz step command, the main DPLL loses lock. In this transient phase, the phasemeter uses the frequency value provided by the Kalman filter in order to compare the new frequency of the interference signal with the one stored in the register of the offset-lock control unit until the main DPLL re-locks. If the step command increases the frequency of the interference signal, the frequency of the controlled laser is higher than the reference frequency of the cavity stabilized laser otherwise it is lower. In this latter case, the bit controlling the sign of the error signal of the laser frequency control loop is inverted. Since the time scale of this whole procedure is of a few microseconds, the frequency of the free-running laser can be considered constant. Once the bit sign of the error signal of the frequency control loop has been correctly identified, the offset-lock control unit is bypassed and the output of the loop-filter is used to control the frequency of the free-running laser.

In order to prevent that the step command brings the interference signal out of the bandwidth of the phasemeter the upper and lower sub-bands of the WPD tree have to be masked. This is done using the look-up table of the signal power estimation sub-system (LUT in Fig. 2.11).

Alternatively to the step command, the laser frequency could be linearly increased in order to keep the main DPLL always locked. In this case though, since the slope of the ramp is limited by the bandwidth of the main DPLL, the laser frequency noise can compromise the correct estimation of the sideband in which the interference signal has been locked. Moreover, the duration of the sideband detection operation increases from a few microseconds to a few seconds. For these reasons, this alternative solution has not been further investigated.

Phase-lock modes

Once the sideband is correctly estimated, the phasemeter phase-locks the free-running laser to the heterodyne signal. The locking mode of the free-running laser can be implemented either keeping the frequency of the heterodyne signal on the phasemeter constant for the slave satellite or allowing that this varies with the Doppler.

If the frequency of the heterodyne signal is kept constant, the free-running laser is controlled such that this frequency is always in the middle of the bandwidth of the slave satellite's phasemeter. Yields that the frequency modulation applied to the phase locked laser is

$$\begin{gathered} f_{het}^{\mathrm{s}}(t) = [f_{\mathrm{m}} - f_{\mathrm{s}}(t)] + f_{\mathrm{D}}(t) + n_f(t) = \frac{f_{bw}}{2} + \hat{n}_f(t) \\ \downarrow \\ f_{\mathrm{s}}(t) = f_{\mathrm{m}} + f_{\mathrm{D}}(t) - \frac{f_{bw}}{2} + \tilde{n}_f(t) \end{gathered} \tag{2.16}$$

where f_{m} and f_{s} are the frequency of the cavity stabilized laser and of the free-running laser, $f_{\mathrm{D}}(t)$ is the frequency variation caused by the Doppler, f_{bw} is the frequency bandwidth of the phasemeter and the terms $n_f(t)$ are frequency noise (these are different because of the noise contributions which enter in specific points of the processing chain). The heterodyne frequency measured by the phasemeter of the master satellite is thus

$$f_{het}^{\mathrm{m}}(t) = [f_{\mathrm{m}} - f_{\mathrm{s}}(t)] - f_{\mathrm{D}}(t) + \check{n}_f(t) = -2f_{\mathrm{D}}(t) + \frac{f_{bw}}{2} + \acute{n}_f(t) \tag{2.17}$$

Hence, on the slave satellite the heterodyne frequency is constant while on the master satellite the beat frequency oscillates in the center of the phasemeter's bandwidth with a maximum amplitude equal to twice the frequency shift of the Doppler.

The second scheme implies that also the slave satellite reads out a time varying frequency (including the Doppler contribution). In order to do so, the frequency shift caused by the Doppler has to be estimated and subtracted from the modulation signal used to control the frequency of the phase-locked laser. Yields,

$$\begin{gathered} f_{het}^{\mathrm{s}}(t) = [f_{\mathrm{m}} - f_{\mathrm{s}}(t)] + f_{\mathrm{D}}(t) + n_f(t) = \frac{f_{bw}}{2} + \bar{f}_{\mathrm{D}}(t) + \hat{n}_f(t) \\ \downarrow \\ f_{\mathrm{s}}(t) = f_{\mathrm{m}} + f_{\mathrm{D}}(t) - \frac{f_{bw}}{2} - \bar{f}_{\mathrm{D}}(t) + +\hat{n}_f(t) \end{gathered} \tag{2.18}$$

where $\bar{f}_{\mathrm{D}}(t)$ is the estimated Doppler frequency while the other terms have been defined beforehand. The heterodyne frequency measured by the phasemeter of the master satellite is thus

$$f_{het}^{\mathrm{m}}(t) = [f_{\mathrm{m}} - f_{\mathrm{s}}(t)] - f_{\mathrm{D}}(t) + \check{n}_f(t) = -f_{\mathrm{D}}(t) + \frac{f_{bw}}{2} + \acute{n}_f(t) \tag{2.19}$$

In this case, the readout of both phasemeters vary with the Doppler frequency and are centered in the middle of the bandwidth of the phasemeter. Although the frequency noises in Eq. 2.16, Eq. 2.17, Eq. 2.18 and Eq. 2.19 are labelled in the same manner, the ones of Eq. 2.18 and Eq. 2.19 include the Doppler estimation error.

Having the frequency of the heterodyne signal that oscillates with twice the Doppler amplitude requires phasemeter whose bandwidth can cope with such signal amplitudes. Removing the Doppler modulation from the frequency of the phase-locked laser requires its correct estimation on-board and thus additional computational effort.

2.4 Top-level noise budget

The principal noise sources that influence the performance of the instrument are here investigated. These are distinguished in noise sources which are independent from the optical layout and in noise sources which are related to the layout of the instrument. Unless specified, all the noise sources discussed hereafter are expressed in $\mathrm{nm}/\sqrt{\mathrm{Hz}}$.

In the continuation of this chapter, the system variables contributing to the top-level noise budget (such as satellites separation, laser power etc.) are identified according to the nomenclature of Tab.2.1, Tab.2.2 and Tab.2.3.

Platform stability and orbit parameters			
Λ	Satellites separation	θ_{LOS}	Pointing offset
$\vartheta_{\mathrm{jitt}}$	Attitude jitter	$S\,(T)$	Thermal stability
ΔT	Temperature variation per orbit	ΔT_{ABS}	Offset from mean operating temp.

Table 2.1

The satellites separation Λ corresponds to the Center of Mass (CoM) to CoM separation or, equivalently, to the separation between the two fiducial points of the accelerometers. In order to have a noise budget which is robust within the specified limits of Λ, the value considered is always the one which would generate the largest noise in the budget. θ_{LOS} correspond to the offset between the actual line of sight and the nominal line of sight of the instrument per degree of freedom. The term ΔT_{ABS} represents the offset of the operating temperature of the instrument (in-orbit) from its aligment/integration temperature. Indeed the system has to be able to minimize the alignment variations when the temperature changes.

Parameters of the optical instrument			
P_{L}	Laser Power	λ	Laser wavelength
δ_f	Frequency stability	RIN	Relative intensity noise
δ_{DWS}	DWS noise floor	M^2	Beam quality factor
η_{opt}	Optical efficiency	WFE	Wavefront error
η_{het}	Heterodyne efficiency	f_{het}	Heterodyne frequency
$\Delta\vartheta_{\mathrm{SM}}$	SM pointing offset	α_{SM}	SM residual jitter
$\Delta T_{\mathrm{SM/K}}$	SM thermal drift per Kelvin	$\Delta\beta_{\mathrm{SM}}$	Alignment accuracy between SM and optical bench frame
R_{QPD}	QPD radius	A_{slit}	Slit area of the QPD
η_{eff}	Efficiency of the detector	η_{qe}	Quantum efficiency
M_1	Magnification of the imaging optics	R	Defining aperture radius
I_{amp}	Input current noise density of the amplifier	ω_0	Gaussian radius of the TX beam in the optical bench

Table 2.2

P_{L} corresponds to the power of the frequency-stabilised laser available at the output of the fibre connector. The wavefront error should be distinguished in received and transmitted. The wavefront error on the TX path consist of a contribution coming from the fibre launcher and of a contribution coming from the rest of the optical surfaces encountered by the beam before leaving the satellite. On the RX path this error corresponds to the differential wavefront amplitude between RX beam and LO beam at the QPD. This last value also includes the effect

of the transmission through the optics of the instrument.

Instrument alignment			
Description		**Parameter**	
		lateral	longitudinal
Absolute offset of:	QPD	ℓ_{QPD}	x_{QPD}
	steering mirror*	ℓ_{SM}	x_{SM}
	RX aperture†	ℓ_{RX}	x_{RX}
	TX aperture	ℓ_{TX}	x_{TX}
	Instrument phase center	$\ell_{\text{Fp-Acc}}$	$x_{\text{Fp-Acc}}$
	RX and LO beam	$\ell_{\text{RX-LO}}$	-
		knowledge	variation
Angular alignment of:	OB Rf and satellite Rf	$\theta_{\text{OB-SC}}$	$\Delta\theta_{\text{OB-SC/K}}$
	LoS and OB Rf	$\theta_{\text{LOS-OB}}$	$\Delta\theta_{\text{LOS-OB/K}}$

* For an on-axis system, this value also corresponds to the absolute lateral and longitudinal offset of the clipping aperture with respect to the real pupil of the lens system. Yields that $\ell_{\mathrm{RX}} = \ell_{\text{CA-LS}}$ and $x_{\mathrm{RX}} = x_{\text{CA-LS}}$.

† For an on-axis system, this value also corresponds to the absolute lateral and longitudinal offset of the steering mirror with respect to the real pupil of the lens system. Yields that $\ell_{\mathrm{SM}} = \ell_{\text{SM-LS}}$ and $x_{\mathrm{SM}} = x_{\text{SM-LS}}$.

Table 2.3: In this table, OB and Rf are the acronyms of optical bench and reference frame respectively.

The alignments described in Tab.2.3 are representative of the optical instruments described in the previous paragraphs. It is worth mentioning that, with a detailed optical design, there might be additional alignment contributions which have to be taken into account especially for the calculation of the TPC noise. The terms $\ell_{\text{Fp-Acc}}$ and $x_{\text{Fp-Acc}}$ are the Root of Sum of Squares (RSS) of the knowledge of the position of the phase center and the absolute alignment accuracy between this point and the fiducial point of the accelerometer.

2.4.1 Pointing budget

The pointing budget is important for understanding both the level of in-band residual jitter which results into TPC noise and for estimating the amount of power detected by the instrument. The error in the beam pointing with respect to the line of sight is calculated differently according to the layout adopted. Indeed, for the on-axis layout and for the racetrack layout, this quantity is calculated as

$$\begin{aligned} \theta_{\mathrm{err}} &= \sqrt{\Delta\vartheta_{\mathrm{SM}}^2 + \theta_{\mathrm{LS}}^2} + \theta_{\mathrm{PA}} && \text{On-axis layout} \\ \theta_{\mathrm{err}} &= \sqrt{\theta_{\mathrm{RT}}^2 + \Delta\vartheta_{\mathrm{SM}}^2 + \left[\Delta\theta_{\mathrm{RT/K}}\left(\Delta T_{\mathrm{ABS}} + \Delta T\right)\right]^2} + \theta_{\mathrm{PA}} && \text{Racetrack layout} \end{aligned} \tag{2.20}$$

where the term θ_{LS} represents the pointing error introduced by the lens system (although this is most likely negligible since the RX and TX beam counter propagate) while the terms θ_{RT} and $\Delta\theta_{\mathrm{RT/K}}$ represent the input-output beam parallelism of the corner cube (either TMA like or compact) and the variation of this quantity per Kelvin respectively. The term θ_{PA} is the point-ahead angle error (see Appendix A.1).

In order to reduce, during data post-processing, the TPC noise level of the "compact corner cube interferometer", it is necessary to calculate the relative knowledge of the real line of sight

with respect to the line of sight of the instrument

$$\theta_{\text{LoS-rel}} = \sqrt{\Delta\vartheta_{\text{SM}}^2 + \Delta\beta_{\text{SM}}^2 + \left[\Delta T_{\text{SM/K}}\left(\Delta T_{\text{ABS}} + \Delta T\right)\right]^2 + \theta_{\text{LOS-OB}}^2} \tag{2.21}$$

It is also necessary to estimate accurately the jitter of each satellite along the TPC sensitive axis. This can be done by means of the DWS signal and is equal to

$$\Delta\vartheta_{\text{jitt}} = \sqrt{\delta_{\text{DWS}}^2 + \vartheta_{\text{jitt}}^2} \tag{2.22}$$

The knowledge of the satellite jitter along the third axis can be also estimated replacing the DWS noise floor with the STR noise floor. Since Roll rotations introduce TPC via the co-alignment error of the incoming-outgoing beams (which is a 2$^{\text{nd}}$ order effect [72]). The knowledge of the Roll jitter is, at first order, not necessary since this noise mechanism can be neglected.

2.4.2 Link power budget

This power budget is used to estimate how much power is received by the QPDs of the interferometer. Since the pointing accuracy is dependant on the layout of the instrument, the power received by the QPDs depends on the layout adopted (on-axis or racetrack). Nevertheless, since the equations used to calculate the link power budget are parametric, these can be used for either the on-axis layout or racetrack layout by changing the layout dependant parameters accordingly with Tab.2.4.

Parameters	**Instrument layout**	
	On-axis	*Racetrack*
TX aperture radius	$R_{\text{TX}} = R \cdot M_{\text{LS}}$	$R_{\text{TX}} = R$
RX aperture radius	$R_{\text{RX}} = R \cdot M_{\text{LS}}$	$R_{\text{RX}} = R$
Beam radius in inertial space	$\bar{\omega}_0 = \omega_0 \cdot M_{\text{LS}}$	$\bar{\omega}_0 = \omega_0$
Beam pointing offset in inertial space	$\theta_{\text{err-IS}} = \theta_{\text{err}} \cdot M_{\text{LS}}$	$\theta_{\text{err-IS}} = \theta_{\text{err}}$

Table 2.4: The parameter M_{LS} corresponds to the magnification introduced by the lens system. The maximum pointing offset of the laser beam with respect to the line of sight is calculated according to Eq. 2.20. In this table, the TX and RX apertures of the racetrack layout are the same and coincident with the radius of the defining aperture. This condition is not a mandatory requirement since these two apertures can have different sizes.

Without loss of generality, the beam transmitted by each satellite can be approximated to a Gaussian beam ($1/e^2$). The divergence of a truncated Gaussian beam in the far field can be approximated as

$$\vartheta_{\text{DIV}} = \frac{\lambda M^2}{4\bar{\omega}_0}\sqrt{\frac{\exp\left[1\right]}{1-\exp\left[-\frac{R_{\text{TX}}}{\bar{\omega}_0}\right]} - 1} \tag{2.23}$$

while the power of the field at the receiving aperture of the twin satellite is calculated as

$$P_{\text{RX}} = P_{\text{L}}\eta_{\text{TX}}\frac{2R_{\text{RX}}^2}{\left(\vartheta_{\text{DIV}}\Lambda\right)^2}\exp\left[-2\frac{\theta_{\text{err-IS}}^2}{\vartheta_{\text{DIV}}^2}\right] \tag{2.24}$$

where η_{TX} is the efficiency of the optics on the TX side. η_{TX} is calculated as the product of the reflectivity or transmissivity coefficients of the optical components with which the beam interacts on its TX path. These coefficients are all expressed as factors smaller than one except for the transmissivity of the TX aperture which is calculated as $\eta_{R_{\text{TX}}} = \left[1 - \exp\left(-2R^2/\omega_0^2\right)\right]$.

The radius of the RX beam and of the LO beam at the photodiode can be calculated respectively as $\omega_{\mathrm{RX}}^{\mathrm{QPD}} = R/M_1$ and $\omega_{\mathrm{LO}}^{\mathrm{QPD}} = \omega_0/M_1$. The power delivered by the RX beam and by the LO beam at each quadrant of the photodiode is

$$\begin{aligned} P_{\text{RX-quad}} &= P_{\mathrm{RX}}\eta_{\mathrm{RX}}\left(\frac{R_{\mathrm{QPD}}}{\omega_{\mathrm{RX}}^{\mathrm{QPD}}}\right)^2\frac{\eta_{\mathrm{ap}}}{4} \\ P_{\text{LO-quad}} &= P_{\mathrm{L}}\eta_{\mathrm{LO}}\left\{1-\exp\left[-2\left(\frac{R_{\mathrm{QPD}}}{\omega_{\mathrm{RX}}^{\mathrm{QPD}}}\right)^2\right]\right\}\frac{\eta_{\mathrm{ap}}}{4} \end{aligned} \tag{2.25}$$

where the terms η_{RX} and η_{LO} represent the product of the efficiencies of the optical components encountered by the RX beam and by the LO beam respectively. η_{ap} is an efficiency that takes into account the reduced area of the photodiode because of the slit aperture. This parameter can be calculated as $\left(\pi R_{\mathrm{QPD}}^2 - A_{\mathrm{slit}}\right) / \left(\pi R_{\mathrm{QPD}}^2\right)$.

2.4.3 Laser noise

One of the biggest contributions to the noise of the system is given by the *laser frequency noise*. Indeed, with an interferometer which has an unequal arm length, fluctuations in the laser frequency couple into the length measurement. This noise contribution relates to the satellite separation as

$$\delta x_f = \frac{\delta f}{c}\lambda\Lambda \tag{2.26}$$

where c is the speed of light. This noise is independent from the layout of the interferometer and from the laser power.

Another noise contribution is coming from the instability in the power level of the laser. The *relative intensity noise* is also independent from the laser power and, at the heterodyne frequency, is equal to

$$\delta x_{\mathrm{RIN}} = \frac{\lambda}{2\pi}\sqrt{\frac{\left(\mathrm{RIN}\,P_{\mathrm{tot}}\right)^2}{2\eta_{\mathrm{het}}\eta_{\mathrm{opt}}P_{\text{LO-quad}}P_{\text{RX-quad}}}} \tag{2.27}$$

where $P_{\mathrm{tot}} = P_{\text{LO-quad}} + P_{\text{RX-quad}}$ (see Appendix A.2). Contrary to the case of the laser frequency noise, this term depends on the layout adopted through the terms $P_{\text{LO-quad}}$ and $P_{\text{RX-quad}}$.

2.4.4 Measurement noise

The measurement noise is introduced by the hardware used to detect the signal and by the analog and digital signal processing chain. In the case of a heterodyne signal generated by two beams with different power levels (for this application the power of the LO is much higher than the power of the RX beam), the *shot noise* is equal to

$$\delta x_{\mathrm{Sh}} = \frac{\lambda}{2\pi\sqrt{N_q}}\sqrt{\mathrm{e}\frac{P_{\mathrm{tot}}}{\eta_{\mathrm{resp}}\eta_{\mathrm{het}}\eta_{\mathrm{opt}}P_{\text{LO-quad}}P_{\text{RX-quad}}}} \tag{2.28}$$

where e is the electron charge and N_q is the number of quadrants used to reconstruct the measurement signal. η_{resp} is the responsivity of the photosensitive component and is related to the quantum efficiency through the laser wavelength

$$\eta_{\mathrm{resp}} = \frac{\lambda\mathrm{e}}{hc}\eta_{\mathrm{qe}} \tag{2.29}$$

where h is the Plank constant and c the speed of light.

Another contribution to the phase noise is coming from the analog chain which is used to convert the photocurrent into a voltage signal. This is quantified as

$$\delta x_{\mathrm{Ac}} = \frac{\lambda}{2\pi\sqrt{N_q}} \sqrt{\frac{I_{\mathrm{amp}}^2}{2\eta_{\mathrm{resp}}^2 \eta_{\mathrm{het}} \eta_{\mathrm{opt}} P_{\text{LO-quad}} P_{\text{RX-quad}}}} \tag{2.30}$$

Once the photocurrent signal is converted to a voltage signal this is digitalized in order to be processed by the phasemeter. The digitalization process is responsible of introducing a quantization error (or *quantization noise*) which, according to studies on the LISA phasemeter [57], is equal to

$$\delta x_{\mathrm{QN}} = \frac{V_{\max}}{V} \frac{2^{-N_b}}{\pi\sqrt{6 f_s}} \tag{2.31}$$

(expressed as cycles/$\sqrt{\mathrm{Hz}}$) where N_b is the number of bits used to digitalize the analog signal, f_s is the sampling frequency while V and $V_{\max}$ represent the actual and the maximum amplitude of the analog signal respectively. Another noise source introduced by the signal digitalization is caused by the jitter of the Analog-to-Digital Converter (ADC). Indeed, the uncertainty in the sampling time of the analog signal introduces a phase error which is equal to $\phi_{\mathrm{ADC}} = \tilde{t}_s / f_{\mathrm{het}}$ where $\tilde{t}_s$ is the sampling time error. This error though can be significantly mitigated by means of a pilot tone (see paragraph 5.2).

The timing reference on board each satellite is generated using a Ultra-Stable Oscillator (USO). Therefore, any frequency fluctuation of the USO couples into the measurement as a phase error via the ADC clock. This noise term can be quantified as

$$\delta x_{\mathrm{USO}} = \frac{\lambda}{2\pi} \left(\frac{f_{\mathrm{het}}}{f_0} \right)^2 \mathcal{L}(f) \tag{2.32}$$

where $\mathcal{L}(f)$ is the single sideband power spectral density of the phase noise of the USO [73].

2.4.5 Thermal induced noise

Temperature changes and temperature fluctuations are also responsible of measurement errors. In particular, the thermal noise can be distinguished in low-frequency thermal noise and in-band thermal noise. The low-frequency thermal noise is responsible for the misalignment of the optical components while the in-band thermal noise is responsible of the dimensional changes of the interferometer. The exact magnitude of the thermal noise to the overall top-level noise budget can only be evaluated once an optical design is completed. Hence the following inputs to this budget are intended to give an overview of how temperature variations enter the noise budget and what is the magnitude of their contribution.

The dimensional changes of the interferometer (in-band thermal noise) enter into the noise budget through the non-common mode propagation of the laser beams. Defining as ΔL_{opt} the total non-common mode glass transmission and as ΔL_{OB} the length of the non-common optical path of the laser beam within the optical bench, the in-band noise contribution to the overall thermal noise is equal to

$$\begin{aligned} \delta x_{\mathrm{opt}} &= \Delta L_{\mathrm{opt}} \cdot \mathrm{a}_{\mathrm{opt}} \cdot S(T) \\ \delta x_{\mathrm{OB}} &= \Delta L_{\mathrm{OB}} \cdot \mathrm{a}_{\mathrm{OB}} \cdot S(T) \end{aligned} \tag{2.33}$$

where the terms $\mathrm{a}_{\mathrm{opt}}$ and a_{OB} are the coefficients of thermal expansion of the optical components and of the optical bench respectively.

For an on-axis system any separation between the fiducial points of the optical bench and the fiducial point of the accelerometer couples into noise since these define the baseline for the optical measurement. Labelling as $\Delta L_{\text{Acc-OB}}$ the distance between these fiducial points, the

noise contribution introduced by the baseline change is equal to

$$\delta x_{\text{Acc-OB}} = \Delta L_{\text{Acc-OB}} \cdot \mathrm{a}_{\text{OB}} \cdot S\left(T\right) \tag{2.34}$$

For a racetrack configuration, the baseline for the optical measurement is defined by the vertex (or point of minimal coupling - see next paragraph) of the corner cube - either compact or TMA like - and the fiducial point of the accelerometer). For this layout, changes in the dimensions of the corner cube also introduce measurement noise. Labeling as L_{CC} the length of the corner cube and as a_{CC} its coefficient of thermal expansion, the measurement noise introduced by the dimensional variation of the corner cube can be calculated similarly to Eq. 2.33 and Eq. 2.34 ($\delta x_{\text{CC}} = L_{\text{CC}} \cdot \mathrm{a}_{\text{CC}} \cdot S\left(T\right)$).

Since thermal effects cannot be considered fully uncorrelated, the overall thermal noise is calculated as the linear sum of the single noise contributions

$$\delta x_{\text{therm}} = \delta x_{\text{opt}} + \delta x_{\text{OB}} + \underbrace{\overbrace{\delta x_{\text{Acc-OB}}}^{\text{on-axis}} \; \underbrace{\delta x_{\text{Acc-CC}} + \delta x_{\text{CC}}}_{\text{racetrack}}} + \delta x_{\text{Lf}} \tag{2.35}$$

where δx_{Lf} is the low-frequency thermal noise which can be only quantified either experimentally or through numerical simulations.

2.4.6 Tilt-to-piston coupling noise

The design of the optical instrument (independently from the layout) is conceived to minimize the TPC noise. Nevertheless, due to manufacturing and alignment limitations, the optical elements employed to minimize the TPC noise (i.e. corner cube, lens system, imaging optics) will themselves impart some residual TPC noise. Moreover, TPC noise introduced by the wavefront error cannot be suppressed by optical elements and needs to be taken into account as additional noise source. Some of the contributions to the TPC noise have been identified in performance studies for the eLISA mission [74] and are here adapted to the layouts presented in the previous paragraph. Hereafter, the TPC contributions are distinguished in those which couple from the TX beam to the far field and in those which couple form the RX beam to the QPD.

For the TX path, the contributions to the TPC noise come from

- *Misalignment of the TX defining aperture from the TX beam*: The steering mirror rotates the beam in order to compensate for the satellite jitter, but is also affected by its own jitter. Therefore, this noise term is influenced by both jitters.

- *Wavefront error in the far-field*: Because of the wavefront error, the transmitted beam is not a perfect spherical wavefront. Any movement of the laser beam with respect to the aperture of the trailing/following satellite will translate into TPC noise. Since the steering mirrors compensate for the jitters of the satellites, this noise mechanism only couples with jitter of the steering mirror.

- *Change of the optical path with field angle*: With non-perfect optics, changes in the optical path with the field angle also introduce a measurement error. For an on axis-system a mismatch between TX and RX beam given by the jitter of the steering mirror generates TPC noise (the change of optical path is non-common mode as the beams counter-propagate). For a racetrack layout instead, this noise mechanism couples with the jitter of the satellite (the steering mirror rotates the beam to compensate this jitter) and with the jitter of the steering mirror itself.

- *Lateral misalignment of the instrument's fiducial point from the accelerometer's fiducial point*: The lever arm between the fiducial point of the interferometer and the fiducial point of the accelerometer generates TPC noise proportionally to the magnitude of the offset. The fiducial point of the interferometer depends on the layout adopted. For an on-axis system the fiducial point of the measurement corresponds to the virtual pupil of the lens system while for the racetrack configuration this corresponds to the vertex (or to the point of minimal coupling) of the corner cube. This noise mechanism couples with the pointing jitter of the satellite.
- *Longitudinal misalignment of the optics reference from the accelerometer fiducial point*: This misalignment contributes to the TPC noise because the line of sight of the measurement is not fixed but jitters causing this longitudinal offset to generate noise as if it was a lateral offset (same effect as the one depicted in Fig. 2.7). Also this noise mechanism couples with the pointing jitter of the satellite.

The previous sources of TPC noise are either independent or common to the layouts presented. Additionally, the on-axis layout contributes to the TPC noise with

- *Misalignment of the steering mirror from the pupil of the lens system*: Since the TX beam is not rotating with respect to the reference point of the accelerometer, this translates into TPC noise. This noise mechanism couples with the jitter of the satellite and with the jitter of the steering mirror.

while the racetrack layout contributes with

- *Misalignment of the beam splitter and compensation plate*: The optical path difference introduced by the passage of the laser beam through the beam splitter at different incident angles is eliminated by the compensation place only if this is perfectly tilted of 90° with respect to the beam splitter. This alignment uncertainty couples with the measurement via the jitter of the satellite and the jitter of the steering mirror. This noise term is present for the layout with the small corner cube or if the TMA is separated from the optical bench as for the LRI.
- *Imperfect corner cube retroreflector*: When the corner cube is rotated about its vertex, the optical path is insensitive to the rotation only if the mirrors of the corner cube a mutually orthogonal. When this condition is not satisfied, rotations of this assembly linearly couple into a displacement error. This noise mechanism couples with the jitter of the satellite.

For the RX path, the contributions to the TPC noise come from

- *Misalignment of the RX defining aperture from the object plane of the imaging optics*: This noise source couples with the jitter of the satellite.
- *Misalignment of the QPD with respect to the imaging optics*: This noise source couples with the jitter of the steering mirror since the satellite jitter is common mode for LO and RX beam.
- *Misalignment of the steering mirror with respect to the imaging optics*: This noise source couples with the jitter of the satellite and the jitter of the steering mirror.
- *Change of the optical path with field angle through the imaging optics*: Since the propagation of the RX beam and LO beam is common mode this noise mechanism couples with the jitter of the steering mirror.
- *Non-common mode wavefront error at the QPD*: Also on the RX path the wavefront error introduces TPC noise although this only couples with the difference in pointing between LO and RX beam, which is given by the jitter of the steering mirror.

- *Offset of LO beam and RX beam*: Since the interference signal is generated overlapping a flat-top beam with a Gaussian beam, a misalignment of these two beams introduces phase noise because of the asymmetry of the phase profile of the interference beam. This noise couples with the jitter of the steering mirror.

Additionally, the on-axis layout contributes with

- *Misalignment of the clipping aperture from the real pupil of the lens system*: As the RX beam would not rotate with respect to the accelerometer reference point, this introduces TPC noise whose magnitude depends on the jitter of the satellite.

The TPC noise generated by a generic source is typically expressed as TPC factor (in units of length over units of rotation) times the magnitude of the rotation that couples with the source of noise. For example, if C_{WFE} is the TPC factor of the wavefront error in the far field and α_{SM} is the jitter of the steering mirror, the displacement noise δx_{WFE} is equal to $C_{\mathrm{WFE}} \cdot \alpha_{\mathrm{SM}}$. Sometimes the coupling factor is calculated as linearly dependent on the magnitude of the component misalignment which introduces TPC noise (i.e. µm/µrad per mm). Labelling $C_{\ell-\mathrm{QPD}}$ the coupling factor of the lateral misalignment of the QPD with respect to the imaging optics, the TPC noise introduced by this source is equal to $\delta x_{\ell-\mathrm{QPD}} = C_{\ell-\mathrm{QPD}} \cdot \ell_{\,\mathrm{QPD}} \cdot \alpha_{\mathrm{SM}}$.

The TPC factors are often calculated using numerical simulations (as done for the eLISA noise budget) since their empirical determination is difficult and not always possible.

TPC correction for the layout with a compact corner cube

The TPC noise introduced by the static longitudinal offset of the vertex of the corner cube (see Eq. 2.6) can be corrected on ground using the knowledge of the line of sight with respect to the nominal line of sight and using the knowledge of the satellite jitter measured with the DWS. Considering only the linear coupling term of Eq. 2.6 and replacing the angle Y_0 with the generic angle ϑ_0 (indeed the static offset is in both Pitch and Yaw), according to the Gaussian error propagation, the residual TPC error after the correction (single-axis) is equal to

$$\begin{aligned}\delta x_{\text{TPC-corr}} = \Big[&(x_{\mathrm{CCR}}\vartheta_0\vartheta_{\mathrm{jitt}})^2 + (\bar{o}\theta_{\text{LoS-rel}}\vartheta_{\mathrm{jitt}})^2 + (x_{\mathrm{CCR}}\theta_{\text{LoS-rel}}\vartheta_{\mathrm{jitt}})^2 + (\bar{o}\vartheta_0\Delta\vartheta_{\mathrm{jitt}})^2 + \\ &+ (x_{\mathrm{CCR}}\vartheta_0\Delta\vartheta_{\mathrm{jitt}})^2 + (\bar{o}\theta_{\text{LoS-rel}}\Delta\vartheta_{\mathrm{jitt}})^2 + (x_{\mathrm{CCR}}\theta_{\text{LoS-rel}}\Delta\vartheta_{\mathrm{jitt}})^2\Big]^{0.5}\end{aligned} \tag{2.36}$$

where the terms $\theta_{\text{LoS-rel}}$ and $\Delta\vartheta_{\mathrm{jitt}}$ are defined in Eq. 2.21 and Eq. 2.22 respectively. x_{CCR} is the longitudinal alignment error for the compact corner cube. Without loss of generality, this value is equal to $x_{\text{Fp-Acc}}$.

The point of minimal coupling

The TPC noise is generated by different sources, each of which artificially "increases" or "decreases" the distance travelled by the light. A possible strategy for mitigating this noise mechanism is to mutually compensate the different effects that generate TPC noise during the manufacturing and alignment of the instrument. An example of this compensation concept is given analyzing the optical properties of the TMA.

Two of the main noise contributions of the TMA to the TPC noise come from the misalignment of its vertex from the fiducial point of the accelerometer and from the non-ideal alignment (normal vectors not mutually orthogonal) of its mirrors (see appendix A.3). The sensitivity of the TPC noise to rotation given by the misalignment of the vertex of the TMA with respect to

the fiducial point of the accelerometer is equal to (see appendix A.4)

$$\mathbf{s_v}\left(\mathrm{P},\mathrm{Y},\mathbf{v}\right)=\begin{bmatrix}\dfrac{\partial\Delta\mathrm{L}}{\partial\mathrm{R}}\\ \dfrac{\partial\Delta\mathrm{L}}{\partial\mathrm{P}}\\ \dfrac{\partial\Delta\mathrm{L}}{\partial\mathrm{Y}}\end{bmatrix}=2\underbrace{\begin{bmatrix}0 & \mathrm{P} & \mathrm{Y}\\ -\mathrm{P} & \mathrm{R} & -1\\ -\mathrm{Y} & 1 & \mathrm{R}\end{bmatrix}}_{[\mathrm{m}/(\mathrm{m\,rad})]}\cdot\begin{bmatrix}\mathrm{v_x}\\ \mathrm{v_y}\\ \mathrm{v_z}\end{bmatrix} \tag{2.37}$$

where v_i with $[\,i=\mathrm{x}\,,\,\mathrm{y}\,,\,\mathrm{z}\,]$ are the coordinates of the vertex of the TMA with respect to the body frame of the satellite (centered in the rotation point of the assembly - see appendix A.5).

The pathlength sensitivity with respect to a rotation around the vertex of the TMA introduced by the non-ideality of the alignment of its mirrors is derived through numerical simulations and is equal to

$$\mathbf{s}_{\mathrm{TMA}}\left(\mathbf{S},\boldsymbol{\varepsilon},\mathrm{l},\mathrm{h}\right)=\begin{bmatrix}\dfrac{\partial\Delta\mathrm{L}}{\partial\mathrm{P}}\\ \dfrac{\partial\Delta\mathrm{L}}{\partial\mathrm{Y}}\end{bmatrix}=\begin{bmatrix}\mathrm{l} & 0\\ 0 & \mathrm{h}\end{bmatrix}\cdot\underbrace{\mathbf{S}}_{[\mathrm{m}/(\mathrm{m\,rad^2})]}\cdot\begin{bmatrix}\varepsilon_{\mathrm{x}}^{\mathrm{M1}} & \varepsilon_{\mathrm{y}}^{\mathrm{M1}} & \varepsilon_{\mathrm{x}}^{\mathrm{M2}} & \varepsilon_{\mathrm{y}}^{\mathrm{M2}} & \varepsilon_{\mathrm{x}}^{\mathrm{M3}} & \varepsilon_{\mathrm{y}}^{\mathrm{M3}}\end{bmatrix}^{\mathrm{T}} \tag{2.38}$$

where the terms l and h represent the length and the hight of the TMA while the terms ε_i^{Mj} with $[\,i=\mathrm{x}\,,\,\mathrm{y}\,]$ and $[\,j=1\,,\,2\,,\,3\,]$ are the alignment errors of the mirror expressed in the reference frame of the mirror (see appendix A.5). The matrix $\mathbf{S}$ depends on the arrangement of the mirrors of the TMA. For an assembly whose mirrors are aligned according to Tab. 2.5, this matrix is equal to

$$\mathbf{S}=\begin{bmatrix}0 & 0.7071 & 0.8657 & 0 & -0.2889 & 0.8169\\ 0 & 0.7144 & -0.8629 & 0 & 0.2939 & -0.8165\end{bmatrix} \tag{2.39}$$

Position and orientation of the TMA mirrors								
Mirror 1			Mirror 2			Mirror 3		
x	y	z	x	y	z	x	y	z
24,00	-300,00	-300,00	24,00	266,06	-300,00	-24,00	300,00	-333,94
$\mathrm{n_x}$	$\mathrm{n_y}$	$\mathrm{n_z}$	$\mathrm{n_x}$	$\mathrm{n_y}$	$\mathrm{n_z}$	$\mathrm{n_x}$	$\mathrm{n_y}$	$\mathrm{n_z}$
0	$-1/\sqrt{2}$	$1/\sqrt{2}$	$1/\sqrt{2}$	0,5	0,5	$-1/\sqrt{2}$	0,5	0,5

Table 2.5: This table reports a possible TMA assembly [46, 75]. The coordinates x , y , z represent the position of the central point of the mirror and are expressed in millimeters. The position and the orientation of the mirror are evaluated with respect of to the body frame of the satellite (see appendix A.5).

The sensitivity of this mirror assembly with respect to rotation is thus given by the sum of these two contributions.

$$\mathbf{s}_{\mathrm{tot}}=\mathbf{s_v}\left(\mathrm{P},\mathrm{Y},\mathbf{v}\right)+\mathbf{s}_{\mathrm{TMA}}\left(\mathbf{S},\boldsymbol{\varepsilon},\mathrm{l},\mathrm{h}\right) \tag{2.40}$$

In order to minimize the measurement error introduced by the non-ideality of the TMA, its vertex should not be coincident with the rotation point of the assembly but should have an appropriate offset. The magnitude of this offset in the three-dimensional space defines a point known as *point of minimal coupling* [76]. It is thus the point of minimal coupling that has to be aligned to the fiducial point of the accelerometer in order to minimize the TPC noise of the TMA. The coordinates of the point of minimal coupling can be found substituting Eq. 2.37 and Eq.2.38 in Eq. 2.40 and matching the term on the left side of the equal to zero. Neglecting

the linear terms of Eq. 2.37 yields

$$\mathbf{s_v}\left(\mathbf{v}\right) = -\mathbf{s}_{\mathrm{TMA}}\left(\mathbf{S}, \boldsymbol{\varepsilon}, \mathrm{l}, \mathrm{h}\right) \longrightarrow \begin{cases} \mathrm{p_x} = \mathrm{v_x} \\ \mathrm{p_y} = \mathrm{v_y} - \dfrac{\mathrm{h}}{2}\mathbf{S}_2 \cdot \boldsymbol{\varepsilon} \\ \mathrm{p_z} = \mathrm{v_z} + \dfrac{\mathrm{l}}{2}\mathbf{S}_1 \cdot \boldsymbol{\varepsilon} \end{cases} \tag{2.41}$$

where $\mathbf{S}_1$ and $\mathbf{S}_2$ are the first and second row of the matrix $\mathbf{S}$ (Eq. 2.39).

Mirror misalignments [mrad]					
Mirror 1		Mirror 2		Mirror 3	
ε_x	ε_y	ε_x	ε_y	ε_x	ε_y
10	10	10	1	0	0
Vertex [µm]		Point of minimal coupling [µm]			
$\mathbf{v} = \begin{bmatrix} 64.84 \\ -335.62 \\ 221.64 \end{bmatrix}$		$\mathbf{p} = \begin{bmatrix} 64.84 \\ -58.76 \\ -189.12 \end{bmatrix}$			

Table 2.6: This table reports the misalignments used to calculate the point of minimal coupling of the TMA assembly. The misalignments are expressed in the frame of the mirror. $\mathbf{v}$ and $\mathbf{p}$ are the coordinates of the vertex of the TMA and of the point of minimal coupling.

Equation 2.41 shows that, if the TMA is ideal, the point of minimal coupling corresponds to the vertex of the TMA otherwise this has an offset with respect to this point which is dependant on the alignment accuracy of the mirrors of the assembly. In Fig. 2.14 the pathlength sensitivity of a non-ideal TMA (see Tab. 2.6) with respect to Yaw and Pitch rotations is evaluated through numerical simulations. As the plots show, if the assembly is rotated with respect to the point of minimal coupling, the sensitivity of the instrument is always minimized.

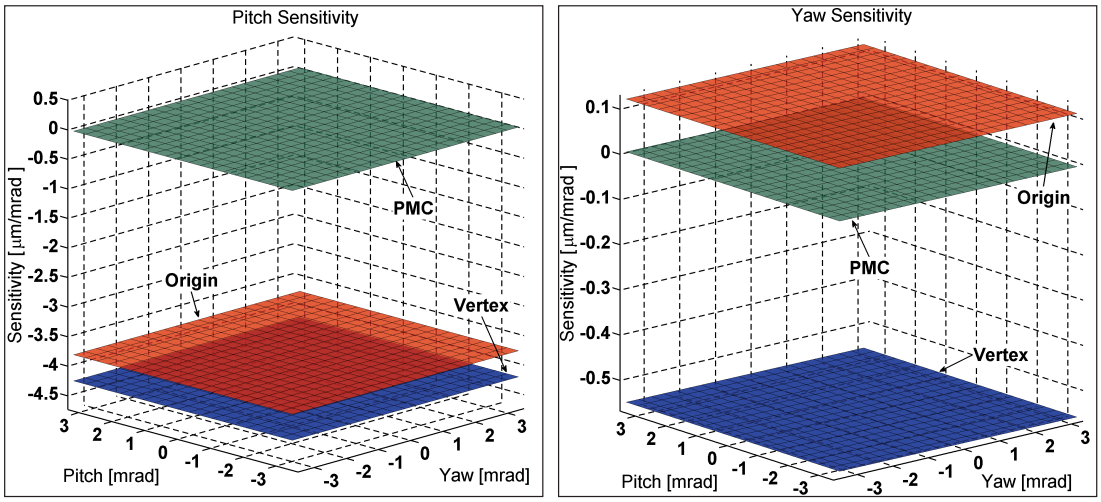

Figure 2.14: The left panel shows the pathlength sensitivity with respect to the angle of Pitch when the TMA assembly is rotated about the origin of the body frame, about its vertex and about the point of minimal coupling (PMC) in both Pitch and Yaw. The right panel of this figure shows the sensitivity of the instrument with respect to the Yaw angle. Also in this case the sensitivity is evaluated rotating the assembly about the origin of the body frame, about its vertex and about the point of minimal coupling (PMC) in both Pitch and Yaw. This plot is generated using alignment errors of the mirrors of the TMA of the order of milliradians in order to clearly distinguish the sensitivity curves.

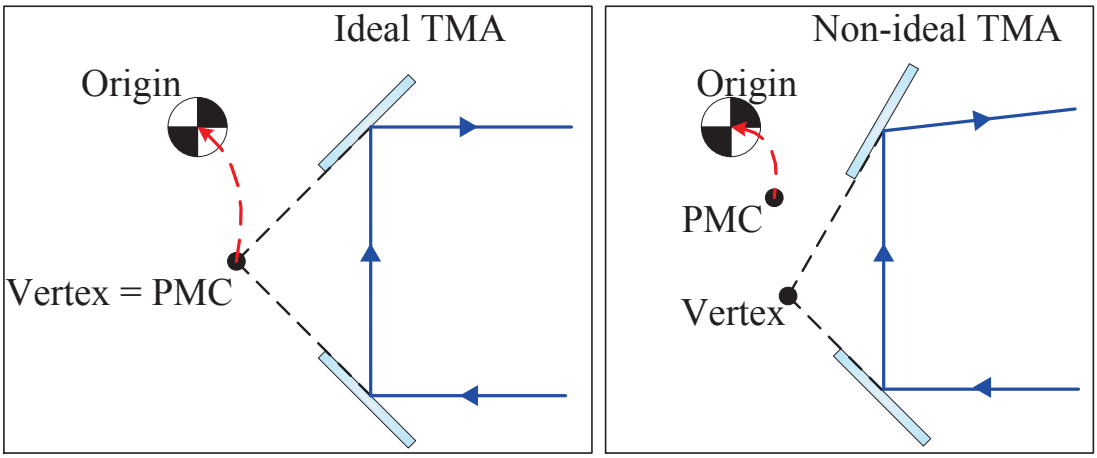

Figure 2.15: When the TMA is ideal (left panel), the point of minimal coupling (PMC) is coincident with the vertex of the TMA. Thus, in order to mitigate the TPC noise, this point has to be aligned to the fiducial point of the accelerometer (coincident with the origin of the body frame). With a non-ideal TMA (right panel), point of minimal coupling and TMA vertex are not coincident. In this case it is necessary to align the point of minimal coupling to the fiducial point of the accelerometer in order to mitigate the TPC noise.

The device, used here for mitigating the TPC noise of the TMA, can be extended to the entire instrument. Indeed if the system is well characterized, the TPC noise on the RX path could be compensated by the TPC noise of the TX path. Alternatively the overall TPC noise could be mitigated by a known misalignment of the phase center of the instrument with respect to the fiducial point of the accelerometer.

2.4.7 Other noise sources

Displacement noise is introduced by straylight and ghost beams which reach the photodetectors ($\delta x_{\mathrm{St/Gh}}$). In order to quantify the magnitude of this noise, a detailed model of the system is required together with realistic simulations of light propagation within the instrument.

The ion density in the intra-spacecraft medium also introduces a displacement error in the measurement. This error can be calculated as

$$\delta x_{\mathrm{ion}} = \frac{\lambda\Lambda}{(2\pi c)^2}\sqrt{\frac{\mathrm{e}^2\rho_{\mathrm{e}}}{\epsilon_0 \mathrm{m_e}}} \tag{2.42}$$

where ϵ_0 is the vacuum permittivity, $\mathrm{m_e}$ the electron mass and ρ_{e} the ion density in the intra-spacecraft link. For a LEO, the maximum ion density is concentrated at the equator and is equal to 10^6 electrons per cubic centimeter. This contribution is non-negligible for electromagnetic signals whose frequency is below 1 THz (indeed the KBR instrument of GRACE uses the K-band and the Ka-band in order to correct for ionospheric effects) while it is negligible for a laser instrument.

With a racetrack layout, the laser round trip measurement forms a closed area. Hence, any rotation about the normal of the plane that encloses the round trip measurement produces a phase shift proportional to the magnitude of the rotation (Saganc effect). In standard orbits there is no nominal rotational component around this plane, therefore this noise can be neglected. However in pendulum orbits [77, 78, 79], there will be a non-negligible Sagnac component (δx_{Sgn}) concentrated at the orbital frequency.

2.4.8 Measurement performance

Independently from the layout adopted, the measurement of the phasemeter corresponds to twice the displacement of the accelerometers (see Eq. 2.4 and Eq. 2.5). Assuming a Gaussian error propagation model, halving the error accrued on a round trip will then correspond to the measurement error accrued over the distance Λ. Since both sides of the system are identical, it is possible to consider as the performance of the pathlength measurement the error budget of a single link.

The error budget of a single link can be calculated as the RSS of the noise terms defined in the previous paragraphs. In particular

$$\delta x_{\text{link}} = \sqrt{\delta x^2_{\text{therm}} + \delta x^2_{\text{Las}} + \delta x^2_{\text{R-out}} + \delta x^2_{\text{oth}} + \delta x^2_{\text{TPC}}} \tag{2.43}$$

where δx_{therm} is the contribution of the thermal noise defined in Eq. 2.35 while the contribution of laser noise (δx_{Las}), read-out noise ($\delta x_{\text{R-out}}$), other noise sources (δx_{oth}) and TPC noise (δx_{TPC}) are defined as

$$\begin{aligned}
\delta x_{\text{Las}} &= \sqrt{\delta x_f^2 + \delta x^2_{\text{RIN}}} \\
\delta x_{\text{R-out}} &= \sqrt{\delta x^2_{\text{Sh}} + \delta x^2_{\text{Ac}} + \delta x^2_{\text{QN}} + \delta x^2_{\text{USO}}} \\
\delta x_{\text{oth}} &= \sqrt{\delta x^2_{\text{St}} + \delta x^2_{\text{Gh}} + \delta x^2_{\text{Sgn}}} \\
\delta x_{\text{TPC}} &= \sqrt{2 \sum \delta x^2_{\text{TPC-i}}}
\end{aligned} \tag{2.44}$$

where $\delta x_{\text{TPC-i}}$ is the generic TPC noise source. The TPC noise is multiplied by a $\sqrt{2}$ factor sine its contribution comes from two degrees of freedom (Pitch and Yaw).

Evaluating the measurement performance through the top-level noise budget: example application

The accuracy of the gravity field estimation from the GRACE Follow-On mission depends not only on the noise level of the instrument, but also on other elements such as, in example, the orbit determination precision, accelerometer performance and the accuracy of the models used for removing aliasing artifacts. Since the LRI should not be limiting the overall performance of the gravity recovery process, $50\,\text{nm}/\sqrt{\text{Hz}} \times \text{NSF}\,(f)$ (where the NSF has been defined in Eq. 1.1) have been proposed as instrument requirement for the single link ranging noise [80]. Within this requirement, the sub-allocation for the noise sources is

Noise budget	
Laser Frequency Noise →	$30\,\text{nm}/\sqrt{\text{Hz}} \times \text{NSF}\,(f)$
TPC Noise →	$30\,\text{nm}/\sqrt{\text{Hz}} \times \text{NSF}\,(f)$
Other Noise Sources →	$25\,\text{nm}/\sqrt{\text{Hz}} \times \text{NSF}\,(f)$
RSS →	$50\,\text{nm}/\sqrt{\text{Hz}} \times \text{NSF}\,(f)$

In order to perform a top-level estimate of the noise performance of the layouts described and compare the results to the noise allocations for the LRI, the parameters used to describe the equations of the noise budget are replaced with values which are representative of LEO gravity mission. In particular, the orbit and platform parameters are derived from the GRACE mission, the GOCE mission, and from simulations studies of the GRACE Follow-On mission. The parameters defining the optical system (especially the alignment requirement and the coupling factors of the TPC noise) are all derived from simulations and heritage of the eLISA interferometer. The generic inputs for the calculation of the top-level noise budget are listed

	Parameter	Value	Units	Description
common parameters	Λ	220	km	
	θ_{LOS}	1.4	mrad	G-FO simulations
	$\vartheta_{\mathrm{jitt}}$	0.1	mrad/$\sqrt{\mathrm{Hz}}$	G-FO simulations
	$S\,(T)$	4	mK/$\sqrt{\mathrm{Hz}}$	GOCE real orbit
	ΔT	0.5	K	G-FO simulations
	ΔT_{ABS}	10	K	G-FO simulations
	P_{L}	50	mW	
	λ	1064	nm	
	δf	30	Hz/$\sqrt{\mathrm{Hz}}$	
	RIN	10^{-6}	1/$\sqrt{\mathrm{Hz}}$	at 10 MHz
	δ_{DWS}	20	nrad/$\sqrt{\mathrm{Hz}}$	
	M^2	1.1	-	
	η_{opt}	0.5	-	at end of life
	η_{het}	0.7	-	
	$\Delta\vartheta_{\mathrm{SM}}$	10	µrad	
	α_{SM}	10	µrad/$\sqrt{\mathrm{Hz}}$	
	$\Delta T_{\mathrm{SM/K}}$	2	µrad/K	
	$\Delta\beta_{\mathrm{SM}}$	50	µrad	
	R_{QPD}	0.5	mm	
	A_{slit}	0.04	mm^2	
	η_{eff}	0.65	A/W	InGaAs QPD
	η_{qe}	0.757	-	
	M_1	4	-	
	R	4	mm	
	I_{amp}	4	pA/$\sqrt{\mathrm{Hz}}$	
	ω_0	2.5	mm	
	$\Delta L_{\mathrm{Acc\text{-}OB}}$	250	mm	see Eq.2.34
	$\theta_{\mathrm{LOS\text{-}OB}}$	50	µrad	
	$\mathrm{a}_{\mathrm{Tit}}$	8.6×10^{-6}	m/(m K)	CTE of Titanium
	$\mathrm{a}_{\mathrm{CFRP}}$	2×10^{-6}	m/(m K)	CTE of CFRP
	a_{GC}	2×10^{-8}	m/(m K)	CTE of Glass Ceramic
	$\mathrm{a}_{\mathrm{BK7}}$	7×10^{-6}	m/(m K)	CTE of BK7
Layout	**Parameter**	**Value**	**Units**	**Description**
On-axis	$\Delta L_{\mathrm{opt\text{-}OA}}$	60	mm	see Eq.2.33
	$\Delta L_{\mathrm{OB\text{-}OA}}$	200	mm	see Eq.2.33
	M_{LS}	1	-	
racetrack	$\Delta L_{\mathrm{opt\text{-}RT}}$	17	mm	see Eq.2.33
	$\Delta L_{\mathrm{OB\text{-}RT}}$	5	mm	see Eq.2.33
	L_{CC}	70 - 400*	mm	corner cube length
	θ_{RT}	10 - 80*	µrad	see Eq.2.20
	$\Delta\theta_{\mathrm{RT/K}}$	0.1 - 1*	µrad/K	see Eq.2.20

* The value on the left corresponds to a layout with a small corner cube while the value on the right corresponds to a TMA layout.

Table 2.7: Parameters used in the top-level noise budget. G-FO and CTE are the acronyms of GRACE Follow-On and coefficient of thermal expansion respectively.

in Tab.2.7 while the inputs necessary for the calculation of the TPC noise are listed in Tab.2.8 (the labelling of the equation parameters is given either in Tab.2.1, Tab.2.2 or Tab.2.3).

The contribution of the TPC noise to the overall displacement noise is calculated as the RSS of its single sources. In particular

$$\delta x_{\mathrm{TPC}} = \sqrt{2\left[\left(\sum_i \delta x^{\mathrm{comm}}_{\mathrm{TPC}-i}\right)^2 + \left(\sum_i \delta x^{\mathrm{On\text{-}axis}}_{\mathrm{TPC}-i}\right)^2\right]} \qquad \text{On-axis}$$

$$\delta x_{\mathrm{TPC}} = \sqrt{2\left(\sum_i \delta x^{\mathrm{comm}}_{\mathrm{TPC}-i}\right)^2} \qquad \text{TMA} \tag{2.45}$$

$$\delta x_{\mathrm{TPC}} = \sqrt{2\left[\left(\sum_i \delta x^{\mathrm{comm}}_{\mathrm{TPC}-i}\right)^2 + \delta x^2_{\mathrm{TPC\text{-}corr}}\right]} \qquad \text{Small CCR}$$

where $\delta x^{\mathrm{comm}}_{\mathrm{TPC}-i}$ is the i^{th} TPC noise source common to all the layouts, $\delta x^{\mathrm{On\text{-}axis}}_{\mathrm{TPC}-i}$ is the i^{th} TPC noise source for the on-axis layout and the term $\delta x_{\mathrm{TPC\text{-}corr}}$ has been calculated in Eq. 2.36. When calculating the TPC of the racetrack layout with the TMA, the values $\ell_{\mathrm{Fp\text{-}Acc}}$ and $x_{\mathrm{Fp\text{-}Acc}}$ are considered relative to the point of minimal coupling of the TMA with respect to the accelerometer (hence the non-ideality of the TMA cancels out). When calculating the TPC noise of the layout with the small corner cube, the contribution given by the misalignment of the compensation plate with respect to the beam splitter is also not included since it is negligible.

Table 2.9 lists the magnitude of the noise sources which have been considered as entries for the top-level noise budget. The laser frequency noise, the TPC noise and the thermal noise (when implementing an optical bench of titanium) are the major sources of displacement noise and they all contribute roughly with the same magnitude. By replacing the material of the optical bench with glass ceramic it is possible to reduce the thermal noise by a factor of 3.

In Tab. 2.10, the single contributions are gathered in three sub-allocations and compared to the noise allocations of the LRI. Both the sub-allocations and the overall measurement performance are below the LRI requirement (independently from the constituting material of the optical bench) hence the alignments and the environmental parameters used for this noise budget would be consistent with the requirement of GRACE Follow-On.

The results of Tab. 2.10 also show that the displacement noise of the instrument is almost independent form the layout adopted. Although many of the design parameters used come from the heritage of other missions, these are consistent with the scenario of a future gravity mission. Hence, the layout with a small CCR could be used if the ranging requirement of the instrument is similar to the one of GRACE Follow-On. Indeed, due to its compact dimensions and its design and manufacturing simplicity, the instrument costs would be significantly contained.

For some studies of a future geodesy mission [81], the noise requirement of the interferometer is in the range of $25\,\mathrm{nm}/\sqrt{\mathrm{Hz}} \times \mathrm{NSF}\,(f)$ or less. In this case, with the environmental parameters adopted, the instrument would not be capable of fulfilling the noise requirement (independently from the layout adopted or from the material of the optical bench). In order to cope with this requirement, all the major noise sources which have been identified need refinement.

The thermal noise can be reduced minimizing the non-common mode optical walks and glass transitions, by using materials with small CTE for all the assemblies (i.e. also for the TMA) and eventually by improving the thermal stability of the satellite platform.

The calculation of the TPC noise as the RSS of the single sources can result in an overestimate of this contribution. Indeed, as done for the TMA, also for a more generic interferometer

RX beam	**Misalignments Contribution**			**Coupling Factor** [m/(m rad)]	
	Parameter	**Value**	**Units**	**Magnitude**	**Couples via***
On-axis	$\ell_{\text{CA-LS}}$	20	µm	0.84	ϑ_{jitt}
	$x_{\text{CA-LS}}$	1	mm	2×10^{-4}	
common sources	ℓ_{QPD}	20	µm	1.7	α_{SM}
	ℓ_{RX}	20	µm	0.84	ϑ_{jitt}
	ℓ_{SM}	20	µm	0.84	Total jitter
	$\ell_{\text{RX-LO}}$	20	µm	0.15	α_{SM}
	x_{QPD}	1	mm	4×10^{-4}	α_{SM}
	x_{RX}	1	mm	2×10^{-4}	ϑ_{jitt}
	x_{SM}	1	mm	2×10^{-4}	Total jitter
	Other Effects			**Coupling Factor** [m/rad]	
				Magnitude	**Couples via**
	non-common mode WFE at the QPD**			15×10^{-6}	α_{SM}
	OPD in the IO with field angle			25×10^{-6}	
TX beam	**Misalignments Contribution**			**Coupling Factor** [m/(m rad)]	
	Parameter	**Value**	**Units**	**Magnitude**	**Couples via***
On-axis	$\ell_{\text{SM-LS}}$	20	µm	0.84	Total jitter
	$x_{\text{SM-LS}}$	1	mm	2×10^{-4}	
common sources	ℓ_{TX}	20	µm	0.5	Total jitter
	$\ell_{\text{Fp-Acc}}$	100	µm	1	ϑ_{jitt}
	$x_{\text{Fp-Acc}}$	2 - 200†	mm	$\approx \theta_{\text{LOS}} \cdot x_{\text{Fp-Acc}}$	ϑ_{jitt}
	Other Effects			**Coupling Factor** [m/rad]	
				Magnitude	**Couples via**
	WFE in the far field**			46×10^{-6}	α_{SM}
	OPD in the optics with field angle			25×10^{-6}	††

* The total jitter is evaluated as the RSS of ϑ_{jitt} and α_{SM}.

† For the layout with a compact corner cube this value corresponds to $\bar{o}$ (Fig. 2.6) and is equal to 200 mm.

** Calculated using $\lambda/20$ RMS as wavefront error.

†† This mechanism couples with the total jitter for the racetrack layout and with the jitter of steering mirror for the on-axis layout.

Table 2.8: This table lists the effects which introduce TPC noise and their corresponding coupling factors. WFE, OPD and IO are the acronyms of wavefront error, optical path difference and imaging optics respectively.

it is possible to compensate different sources of TPC noise during the alignment of the single components and during the alignment of the whole instrument with the accelerometer. The identification of all the relevant TPC noise sources and how to accurately compensate them is a valid solution for improving the noise performance of the instrument and would require further investigation. Moreover, the TPC noise can be further mitigated in post-processing by means of a calibration algorithm (see chapter 6).

Finally, for reducing the laser frequency noise, studies on high stability lasers are currently ongoing [82].

Noise contributions (Units: nm/$\sqrt{\text{Hz}}$)						
Laser frequency noise (δx_f)	23.42					
Link noise	**Instrument layout**					
	On-axis		**TMA**		**small CCR**	
δx_{RIN}	0.851		1.04		0.854	
δx_{Sh}	0.02		0.024		0.02	
δx_{Ac}	0.011		0.014		0.011	
δx_{QN}	0.01		0.01		0.01	
δx_{USO}	1		1		1	
δx_{St}*	2		2		2	
δx_{Gh}*	3		2		2	
Thermal noise†	GC	Ti	GC-CFRP	Ti-CFRP	GC-GC	Ti-GC
δx_{opt}‡	1.68	1.68	0.48	0.48	0.48	0.48
δx_{OB}	16×10^{-3}	6.88	4×10^{-4}	1.72	4×10^{-4}	1.72
δx_{CC}	-	-	3.2	3.2	6×10^{-3}	6×10^{-3}
$\delta x_{\text{Acc-OB}}$	20×10^{-3}	8.6	-	-	-	-
$\delta x_{\text{Acc-CC}}$	-	-	20×10^{-3}	8.6	20×10^{-3}	8.6
δx_{Lf}*	3	5	3	5	3	5
δx_{therm}	6.08	22.5	6.70	19	3.5	15.8
TPC noise						
common sources	14.64		14.64		14.64	
specific sources	3.37		-		2.11	
δx_{TPC}	15.023		14.64		14.79	

* The values assigned to these variables are generic noise allocations.
† The thermal noise budget is evaluated for an optical bench made of titanium (Ti) or glass ceramic (GC). The TMA and the small corner cube are always considered made of CFRP and glass ceramic respectively.
‡ BK7 optics considered.

Table 2.9

Top-level noise budget (Units: nm/$\sqrt{\text{Hz}}$)				
	Sub-allocations			**Total RSS**
	Laser frequency noise	**TPC noise**	**Other noise sources**	
Requirement	*30*	*30*	*25*	***50***
On-axis (Ti)	23.42	15.023	22.5	**35.78**
On-axis (GC)			6.08	**28.48**
TMA (Ti-CFRP)		14.64	19.25	**33.67**
TMA (GC-CFRP)			7.4	**28.59**
small CCR (Ti-GC)		14.79	16.11	**32.04**
small CCR (GC-GC)			4.7	**28.09**

Table 2.10: Top-level noise budget of the instrument. The contribution of the "other noise sources" is given by the RSS of the "Link noise" terms and δx_{therm} of Tab. 2.9.

Chapter 3

Design and Implementation of a Laser Link Simulator

One of the tasks of this work is to develop a robust algorithm aimed to optimize the first attempt of establishing an optical link (see chapter 4) and a calibration algorithm which minimizes the attitude related TPC noise (see chapter 6). In order to verify the validity of these algorithms it is necessary to understand how the link evolves along the orbital trajectory of the satellites, how attitude couples with the range measurement and how the limited pointing performances of the satellite complicate the first attempt to acquire the signal. Although feasible, experimental studies performed on ground are expensive and often limited by the surrounding environment as this differs from the realistic orbit scenario [83]. For such a reason, the acquisition and calibration algorithms are tested throughout this thesis by means of numerical simulations using a model of the laser instrument which reproduces as far as possible the behaviour of the real one.

The development of a realistic laser simulator is not a simple task since the beam propagation has to be calculated integrating the equations of its electrical field. Nevertheless, for the scope of studying the signal acquisition and on the TPC noise calibration, a complex solution of the field equations of the laser beam is not necessary and its propagation through the optical link can be evaluated, without loss of generality, using the ray tracing technique [84]. With this simplification the optics of the instrument can be modelled using geometrical surfaces. For sub-systems such as steering mirror and phasemeter, more realistic and detailed models are developed since these serve as supports for further laboratory tests (see chapter 5). The laser link simulator is developed in the MATLAB-Simulink environment.

This chapter gives an overview of the laser link simulator together with its sub-systems and is organized as follows; paragraph 3.1 describes the attitude and orbit time series used for performing the simulations and how these can be connected to the laser link simulator. Paragraphs 3.2, 3.3, 3.4, 3.5, 3.6 and 3.7 describe the noise models and the parametric equations used for each sub-system while paragraph 3.8 gives an overview of the structure of the simulator.

3.1 GNC time series

The evolution of the attitude of the satellite and of its orbit positioning are not calculated with the simulator but are provided as external inputs. Therefore, the simulator can use either time series coming from simulation studies or the real attitude and orbit telemetry (or date products) of an orbiting satellite. The simulations presented in the following chapters use the real Guidance Navigation and Control (GNC) data products (Level-1B) of GRACE [85] (used specifically for calibration simulations) and the GNC time series coming from Attitude and Orbit Control System (AOCS) simulation studies for the GRACE Follow-On mission (used for both initial acquisition and calibration simulations).

Since the GRACE Follow-On GNC simulations have to be as far as possible compliant with the real space environment, attitude and orbit data are calculated using the models of Earth rotation (including Greenwich apparent sidereal time), precession and nutation, Earth gravitational acceleration, sun and moon gravitational acceleration, magnetic field and atmospheric drag. The gravity field is calculated using the JGM-3 [86] gravity model with degree and order 10. The magnetic field and the atmospheric density are calculated respectively using the IGRF-11 [87] magnetic field model (with degree and order 13) and the MSISE-86 density model [88] (considering a moderate solar activity with an average flux of 140). The Albedo and infrared loads from the Earth are computed by integration over a map with randomly distributed Albedo factors and infrared emissions. The attitude and the position of the satellite along the orbit are "virtually" measured using dedicated models of the coarse Earth and sun sensor, of the magnetometer, of the inertial measurement unit, of the STRs and of the GPS receiver. The satellite actuation is carried out using a model of the magnetic torquers and of the propulsion system of GRACE Follow-On. The propulsion system consists of twelve small cold gas thrusters (10 mN) which provide force-free attitude control when the capability of the magnetic torquers is exceeded and two orbit control thrusters (50 mN) which are used for along-track maneuvers.

3.2 Noise model of star trackers and DWS signal

Although the attitude data, the orbit data and their respective measurements are provided externally to the simulator, a valid noise model of the STR is necessary for performing acquisition and calibration simulations. The noise model of the DWS is used to perform calibration simulations, acquisition simulations and simulations using detailed models of the phasemeter and of the SM.

The measurement of the STRs is affected by three main noise sources; namely temporal noise, high spatial frequency noise and low spatial frequency noise. Temporal noise can be modelled as white Gaussian noise and is not correlated to the other two noises [89] while high spatial frequency noise and low spatial frequency noise are both considered as red noises [90] with different correlation times.

The correlation time of the high spatial frequency noise along the i^{th} axis of the STR frame (see appendix A.5) is calculated as

$$T_i^{\text{HSFN}} = \frac{\varphi_{\text{HSFN}}}{|\omega_i|} \quad \text{with} \quad i = x\,,\, y\,,\, z \tag{3.1}$$

where φ_{HSFN} is the angular width which is relevant for the correlation of this noise (i.e. the angular width of the window used for computing the centroid of the star) while ω_i is the angular rate of the STR along the i^{th} axis of the STR frame. Similarly, the correlation time of the low spatial frequency noise along the i^{th} axis of the STR frame is calculated as

$$T_i^{\text{LSFN}} = \frac{\varphi_{\text{STR}}}{\sqrt{N}\,|\omega_i|} \quad \text{with} \quad i = x\,,\, y\,,\, z \tag{3.2}$$

where φ_{STR} is the field of view of the STR, N is the number of stars used to compute the attitude of the satellite while ω_i is once more the angular rate of the STR.

The temporal noise is modelled as white Gaussian noise and along the i^{th} axis of the STR frame. This is equal to $\mathbf{n}_i^{\text{TN}}(k) = \sigma \mathbf{w}_i(k)$ where σ is the standard deviation of the noise. Both the high and low spatial frequency noise are modelled as first order Gauss-Markov noises whose equations of the discrete time state space system are equal to (note that in the following equation small bold letters denote random variables and not vectors)

$$\begin{aligned} \mathbf{x}_i^j(k+1) &= \mathbf{A}_i^j \mathbf{x}_i^j(k) + \mathbf{B}_i^j \mathbf{u}_i(k) \\ \mathbf{n}_i^j(k+1) &= \mathbf{C}_i^j \mathbf{x}_i^j(k) + \mathbf{D}_i^j \mathbf{u}_i(k) \end{aligned} \quad \text{with} \quad i = x\,,\, y\,,\, z \quad \text{and} \quad j = \text{HSFN}\,,\, \text{LSFN} \tag{3.3}$$

and the four matrices of the state space system are equal to

$$\mathbf{A}_i^j = e^{-\Delta t/T_i^j} \quad ; \quad \mathbf{B}_i^j = \sigma\sqrt{1-e^{-2\Delta t/T_i^j}} \quad ; \quad \mathbf{C}_i^j = 1 \quad ; \quad \mathbf{D}_i^j = 0 \tag{3.4}$$

where Δt is the sampling time of the STR (or of the model), T_i^j is the correlation noise of the j^{th} source along the i^{th} axis of the STR frame while σ is the standard deviation of the noise. The random variables $\mathbf{u}_i$ and $\mathbf{w}_i$ are distributed according to a standard normal distribution [91]. The total STR noise is given by the sum of the three different sources along each axis.

The DWS noise is modelled using a noise shape filter whose transfer function is coincident with the NSF of the GRACE Follow-On mission. The floor of the DWS noise is calculated as the RSS sum of RIN noise (Eq. 2.27), shot noise (Eq. 2.28), analog chain noise (Eq. 2.30), quantization noise (Eq. 2.31), stray light noise and ghost beams noise

$$n_{\text{DWS}} = \frac{1}{m_{\text{DWS}}}\sqrt{\frac{N_{\text{DWS}}}{N}\left(\delta x_{\text{RIN}}^2 + \delta x_{\text{Sh}}^2 + \delta x_{\text{Ac}}^2 + \delta x_{\text{QN}}^2 + \delta x_{\text{St}}^2 + \delta x_{\text{Gh}}^2\right)} \tag{3.5}$$

where N_{DWS} is the number of QPD quadrants used to construct the DWS signal while N is the total number of quadrants used for pathlength metrology and m_{DWS} is the slope of the DWS measurement.

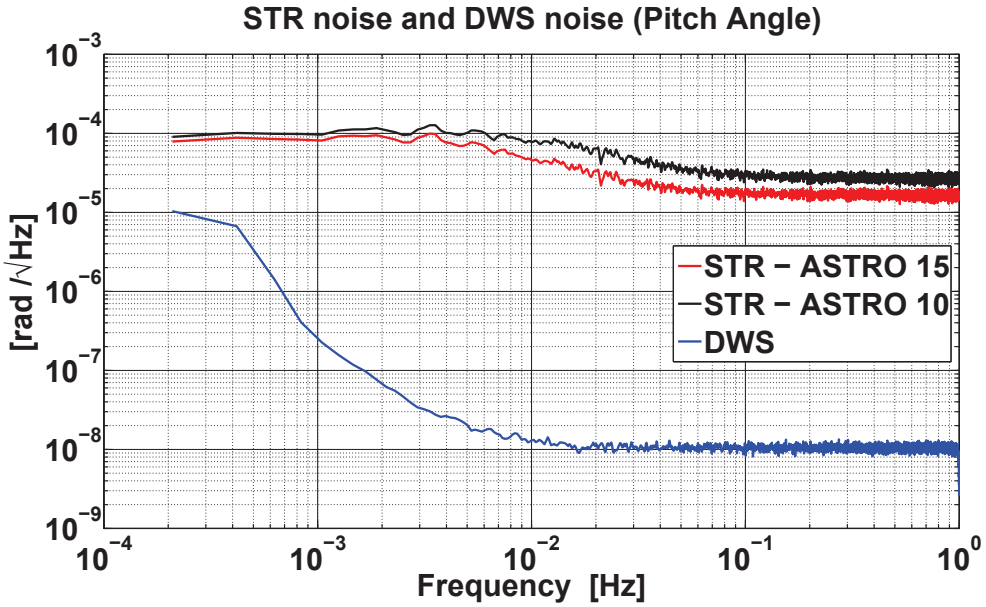

Figure 3.1: Comparison between the noise performance of the two STRs of Tab. 3.1 and the noise performance of the DWS measurement. The STR noise does not include low frequency thermal effects as the DWS noise. For such a reason, the ASD of the STR noise is flat for frequencies below 10^{-2} Hz.

Figure 3.1 depicts the ASD of the STR noise and the DWS noise. The parameters used to calculate the STR noise come from two commercial STRs [92, 93] and are listed in Tab. 3.1 while the noise floor of the DWS measurement is set to $10\,\text{nm}/\sqrt{\text{Hz}}$.

3.3 Readout model of the QPD

Since the laser link simulator adopts the ray tracing technique for evaluating the beam path throughout the instrument, the behaviour of a real QPD can be significantly simplified since this component has to provide only the offset between the RX beam and the LO beam. This

Parameter	ASTRO 10	ASTRO 15	Units
Line of sight accuracy - cross axis	3	1	arcsec
Line of sight accuracy - bore-sight axis	15	10	arcsec
Number of pixels	1024	1024	-
Effective field of view	13.5	13.25	rad
STR angular rate	1	0.5	rad/s

Table 3.1: Parameters used to calculate the STR noise.

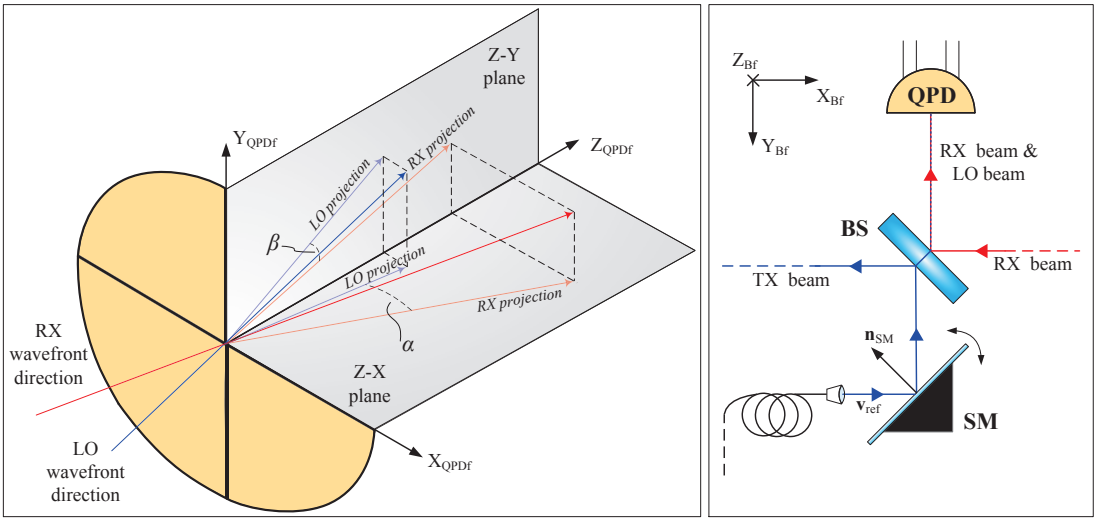

Figure 3.2: The left panel shows the geometrical equivalent of the operating principle of the photodiode while the right panel depicts a possible arrangement for an interferometric measurement.

offset is afterwards converted into DWS measurement in order to control the pointing of the TX beam using the SM.

The left panel of Fig. 3.2 shows the DWS measurement from a geometrical prospective. Indeed, the horizontal DWS in nothing more than the angle between the RX beam and LO beam projected on the Z-X plane of the QPD frame (see appendix A.5) while the vertical DWS is the same measurement with respect to the Z-Y plane of the QPD frame. Thus, labelling as $\mathbf{v}_{\mathrm{RX}}$ the direction of propagation of the RX beam in the QPD frame and as $\mathbf{v}_{\mathrm{LO}}$ the direction of propagation of the LO beam in the QPD frame, according to Eq. 2.9, the DWS measurements are

$$\begin{aligned} \mathrm{DWS}_{\mathrm{hor}} &= C_{\mathrm{DWS}} \cdot \left[\sin^{-1}\left(\frac{\mathrm{v}^{y}_{\mathrm{RX}}}{||\mathbf{v}_{\mathrm{RX}}||} \right) - \sin^{-1}\left(\frac{\mathrm{v}^{y}_{\mathrm{LO}}}{||\mathbf{v}_{\mathrm{LO}}||} \right) \right] + n_{\mathrm{DWS}} \\ \mathrm{DWS}_{\mathrm{ver}} &= C_{\mathrm{DWS}} \cdot \left[\tan^{-1}\left(\frac{\mathrm{v}^{x}_{\mathrm{RX}}}{\mathrm{v}^{z}_{\mathrm{RX}}} \right) - \tan^{-1}\left(\frac{\mathrm{v}^{x}_{\mathrm{LO}}}{\mathrm{v}^{z}_{\mathrm{LO}}} \right) \right] + n_{\mathrm{DWS}} \end{aligned} \tag{3.6}$$

where v^{j}_{i} (with $i = \mathrm{RX}, \mathrm{LO}$ and $j = x, y, z$) is the component of the vector $\mathbf{v}_i$ along the j^{th} axis of the QPD frame while n_{DWS} is the DWS noise (see Eq. 3.5).

3.3.1 Commanding the steering mirror with the DWS signal

In order to calculate the tip-tilt angles of the SM which align the LO beam to the RX beam, it is first necessary to estimate the orientation of the RX wavefront at the QPD. According to the arrangement of the instrument depicted in Fig. 3.2, the direction of the LO beam in the

QPD frame is

$$\mathbf{v}^*_{\mathrm{LO}} = \mathbf{R}_{\text{QPDf-Bf}} \left\{ \mathbf{v}_{\mathrm{ref}} + 2 \left[\mathbf{n}_{\mathrm{SM}} \cdot (-\mathbf{v}_{\mathrm{ref}}) \right] \mathbf{n}_{\mathrm{SM}} \right\} \tag{3.7}$$

where $\mathbf{R}_{\text{QPDf-Bf}}$ is the rotation matrix from body frame to QPD frame, $\mathbf{n}_{\mathrm{SM}}$ is the normal of the steering mirror at the instant t expressed in body frame while $\mathbf{v}_{\mathrm{ref}}$ is the direction of the laser beam before hitting the steering mirror (which is, in this case, coincident with the direction of the unit vector of the X-axis of the body frame - see Fig. 3.2). Combining $\mathbf{v}^*_{\mathrm{LO}}$ with the DWS measurement (Eq. 3.6), it is possible to derive the incoming direction of the RX wavefront at the QPD

$$\begin{aligned} \alpha^* &= \frac{\mathrm{DWS}_{\mathrm{ver}}}{C_{\mathrm{DWS}}} + \sin^{-1}\left(\frac{\mathrm{v}^{*y}_{\mathrm{LO}}}{||\mathbf{v}^*_{\mathrm{LO}}||} \right) \\ \beta^* &= \frac{\mathrm{DWS}_{\mathrm{hor}}}{C_{\mathrm{DWS}}} + \tan^{-1}\left(\frac{\mathrm{v}^{*x}_{\mathrm{LO}}}{\mathrm{v}^{*z}_{\mathrm{LO}}} \right) \end{aligned} \quad \Rightarrow \quad \mathbf{v}^*_{\mathrm{RX}} = \begin{bmatrix} \cos(\alpha^*) \sin(\beta^*) \\ \sin(\alpha^*) \\ \cos(\alpha^*) \cos(\beta^*) \end{bmatrix} \tag{3.8}$$

where α^* and β^* are the (estimated) angles of the RX beam in the Z-X plane and the Z-Y plane of the QPD frame.

At the instant $t + \Delta t$ (where $\Delta t = 1/f_s$ with f_s the sampling frequency of the computer of the steering mirror electronics), the direction $\mathbf{v}^*_{\mathrm{LO}}(t + \Delta t) = \mathbf{v}^*_{\mathrm{RX}}(t)$. Yields that the normal of the SM expressed in body frame at the instant $t + \Delta t$ is

$$\mathbf{R}^{-1}_{\text{QPDf-Bf}} \mathbf{v}^*_{\mathrm{RX}} = \mathbf{v}_{\mathrm{ref}} + 2 \left[\mathbf{n}_{\mathrm{SM}} \cdot (-\mathbf{v}_{\mathrm{ref}}) \right] \mathbf{n}_{\mathrm{SM}} \quad \Rightarrow \quad \mathbf{n}^*_{\mathrm{SM}} = \begin{bmatrix} \frac{1}{\sqrt{2}} \sqrt{\mathrm{v}'^{x}_{\mathrm{RX}} + 1} \\ \frac{1}{\sqrt{2}} \frac{\mathrm{v}'^{y}_{\mathrm{RX}}}{\sqrt{\mathrm{v}'^{x}_{\mathrm{RX}} + 1}} \\ \frac{1}{\sqrt{2}} \frac{\mathrm{v}'^{z}_{\mathrm{RX}}}{\sqrt{\mathrm{v}'^{x}_{\mathrm{RX}} + 1}} \end{bmatrix} \tag{3.9}$$

where $\mathbf{v}'_{\mathrm{RX}} = \mathbf{R}^{-1}_{\text{QPDf-Bf}} \mathbf{v}^*_{\mathrm{RX}}$ is the calculated direction of the RX beam expressed in body frame and the terms $\mathrm{v}'^{i}_{\mathrm{RX}}$ (with $i = x, y, z$) are the components of the vector $\mathbf{v}'_{\mathrm{RX}}$ along the axes of the body frame. The closed-form solution given by Eq. 3.9 is valid only if the direction $\mathbf{v}_{\mathrm{ref}}$ is parallel to X-axis of the body frame (if $\mathbf{v}_{\mathrm{ref}}$ is parallel to another axis of the body frame, the closed-form solution is similar). If this condition is not true, it is necessary to define a new reference frame (namely a laser frame) such that $\mathbf{v}_{\mathrm{ref}}$ is parallel to one of the axis of this frame otherwise $\mathbf{n}^*_{\mathrm{SM}}$ cannot be determined using a closed-form solution (similar to Eq. 3.9) but through a numeric minimization algorithm. The normal of the steering mirror $\mathbf{n}^*_{\mathrm{SM}}$ should be thus calculated in this "laser frame" and then converted to the mirror frame through an appropriate rotation matrix.

The tip-tilt angles of the steering mirror are finally calculated as

$$\mathbf{n}_{\mathrm{SM}}(t + \Delta t) = \mathbf{R}_{\text{Mf-Bf}} \mathbf{n}^*_{\mathrm{SM}} \quad \Rightarrow \quad \begin{aligned} \theta(t + \Delta t) &= \sin^{-1}\left(\frac{\mathrm{n}^{y}_{\mathrm{SM}}}{||\mathbf{n}_{\mathrm{SM}}||} \right) \\ \phi(t + \Delta t) &= \tan^{-1}\left(\frac{\mathrm{n}^{x}_{\mathrm{SM}}}{\mathrm{n}^{z}_{\mathrm{SM}}} \right) \end{aligned} \tag{3.10}$$

where $\mathbf{R}_{\text{Mf-Bf}}$ is the rotation matrix from body frame to mirror frame.

The relation between vector components and angles used in the previous equations (i.e. in Eq. 3.8 or Eq. 3.10) is valid only if the reference frames have the same orientation as the one described in appendix A.5. If one or more frames are oriented differently, then the components of the vectors are arranged differently and the relation between vector components and angles (i.e. of Eq. 3.10) is different.

3.3.2 Beam pointing control using on-board measurements

When both phasemeters are locked, the DWS signal is used to keep the two laser beams aligned. When the system has not yet acquired the signal, if the laser beams have to firmly point towards a fixed direction, the SM drive electronics has to use the on-board attitude and GPS measurements.

Through the onboard attitude control system it is possible to evaluate the deviations of the satellite pointing from the nominal one using the angles of corrected Roll (R_c), corrected Pitch (P_c), corrected Yaw (Y_c) (these are given as the sum of the Tait-Bryan angles and the point ahead angle θ_{pa} - see appendix A.1) and the difference between the position vector of the measured orbit and the nominal orbit ($\Delta\mathbf{o}$). Labeling as $\mathbf{p}_{\text{d}}$ the originating point of the laser beam in the intra-satellite medium (this can be i.e. coincident with the centroid of the laser baffle) it is possible to calculate which should be the new tip-tilt angles of the SM such that the deviations of the real satellite orbit and satellite attitude from the nominal ones do not influence the pointing direction of the laser beam. The expected direction of the TX beam, expressed in body frame, can be calculated as

$$\mathbf{p}_{\text{d}}^{*} = \Delta\mathbf{o} - \mathbf{R}_{\vartheta}\mathbf{p}_{\text{d}} \quad \Rightarrow \quad \hat{\mathbf{d}}_{\text{L}} = \mathbf{R}_{R_c P_c Y_c}\left(-\frac{\mathbf{p}_{\text{ref}} - \mathbf{p}_{\text{d}}^{*}}{||\mathbf{p}_{\text{ref}} - \mathbf{p}_{\text{d}}^{*}||}\right) \tag{3.11}$$

where $\mathbf{p}_{\text{d}}^{*}$ is the new position of the originating point of the laser beam, $\mathbf{p}_{\text{ref}}$ is the reference point on the surface of the twin satellite towards where the TX beam should be pointed while the matrix $\mathbf{R}_{\vartheta}$ is given by the product $\mathbf{R}_{R_c}\mathbf{R}_{P_c}\mathbf{R}_{Y_c}$. The matrices $\mathbf{R}_{R_c}$, $\mathbf{R}_{P_c}$, $\mathbf{R}_{Y_c}$ are the rotation matrices around the X, the Y and the Z-axis of the body frame while the magnitudes of the rotations are given by the angles R_c, P_c and Y_c. Backward propagating the vector $\hat{\mathbf{p}}_{\text{d}}$ through the optics of the interferometer it is possible to calculate the direction of the laser beam at the SM ($\hat{\mathbf{p}}_{\text{d}}^{\text{sm}}$). Substituting $\mathbf{v}_{\text{RX}}^{*}$ with $\hat{\mathbf{p}}_{\text{d}}^{\text{sm}}$ in Eq. 3.9 it is possible to calculate the normal of the steering mirror which allows to firmly point the TX beam towards its target. Through Eq. 3.10 it is then possible to recover the tip-tilt angles of the SM.

Since the attitude and the orbit measurement are affected by high frequency noise ($\geq 1\,\text{Hz}$), the pointing of the beam would not be extremely stable because STR noise and GPS noise would couple as induced jitter of the SM. For such a reason, the attitude and orbit data which are used to reconstruct the normal of the SM are pre-filtered using an LPF which removes the out of measurement band noise.

3.4 The steering mirror model

The SM is an electro-mechanical system with a gimballed mirror that can be rotated around two of its axis. The actuation of the gimballed mirror is accomplished using voice coil motors which enable the mechanism to rapidly change its inclination. The deflection of the mirror is measured by a position sensor system which converts into a voltage signal the angular position of the mirror. This allows to operate the mirror in a closed-loop.

In order to properly design the close-control loop of the SM a state-space model of this component has been derived. Treating the mirror as a rigid two-body object (see appendix A.7), its general equation of motion can be written as

$$\underbrace{\begin{bmatrix} \mathbf{M}_j & 0 \\ 0 & \mathbf{M}_k \end{bmatrix}\begin{Bmatrix} \dot{\boldsymbol{\nu}}_j \\ \dot{\boldsymbol{\nu}}_k \end{Bmatrix} = \begin{Bmatrix} \mathbf{g}_j \\ \mathbf{g}_k \end{Bmatrix}}_{\text{Newton-Euler equations}} + \underbrace{\begin{bmatrix} \mathbf{H}_j^{\text{T}} \\ \mathbf{H}_k^{\text{T}} \end{bmatrix}\begin{Bmatrix} \boldsymbol{\lambda}_j \\ \boldsymbol{\lambda}_k \end{Bmatrix}}_{\text{Motion constrain}} \tag{3.12}$$

where the subscript j is refereed to the first body and subscript k to the second. From the general equation of motion it is possible to derive the state space equation of the steering

mirror by applying a coordinate transformation. In particular, the mirror can be treated as two bodies which are connected through a revolute joint [94]. Thus, applying the joint coordinate transformation $\boldsymbol{\nu} = \mathbf{R}\dot{\boldsymbol{\vartheta}}$ in Eq.3.12 yields

$$\ddot{\boldsymbol{\vartheta}} = \left(\mathbf{R}^{\mathrm{T}}\mathbf{M}\mathbf{R}\right)^{-1}\mathbf{R}^{\mathrm{T}}\left(\mathbf{g} - \mathbf{M}\dot{\mathbf{R}}\dot{\boldsymbol{\vartheta}}\right) \tag{3.13}$$

The transformation matrices $\mathbf{R}$, $\dot{\mathbf{R}}$ and the force vector $\mathbf{g}$ are equal to

$$\mathbf{R} = \begin{bmatrix} \mathbf{0} & \mathbf{0} \\ \mathbf{u}_1 & \mathbf{0} \\ \mathbf{0} & \mathbf{0} \\ \mathbf{u}_1 & \mathbf{u}_2 \end{bmatrix} \quad , \quad \dot{\mathbf{R}} = \begin{bmatrix} \mathbf{0} & \mathbf{0} \\ \tilde{\boldsymbol{\omega}}_1\mathbf{u}_1 & \mathbf{0} \\ \mathbf{0} & \mathbf{0} \\ \tilde{\boldsymbol{\omega}}_1\mathbf{u}_1 & \tilde{\boldsymbol{\omega}}_2\mathbf{u}_2 \end{bmatrix} \quad , \quad \mathbf{g} = \begin{bmatrix} \mathbf{0} \\ \boldsymbol{\tau}_j + \mathbf{S}_j\boldsymbol{\omega}_1 - \tilde{\boldsymbol{\omega}}_1\mathbf{J}_j\boldsymbol{\omega}_1 - \mathbf{K}_j\boldsymbol{\Theta}_j \\ \mathbf{0} \\ \boldsymbol{\tau}_k + \mathbf{S}_k\boldsymbol{\omega}_2 - \tilde{\boldsymbol{\omega}}_2\mathbf{J}_k\boldsymbol{\omega}_2 - \mathbf{K}_k\boldsymbol{\Theta}_k \end{bmatrix} \tag{3.14}$$

where the vectors $\mathbf{u}_1 = [1\,,\,0\,,\,0]^{\mathrm{T}}$, $\mathbf{u}_2 = [0\,,\,1\,,\,0]^{\mathrm{T}}$ are directed like of the X and Y-axis of the mirror mount. The vector $\boldsymbol{\omega}_1 = \left[\dot{\theta}\,,\,0\,,\,0\right]^{\mathrm{T}}$, the vector $\boldsymbol{\omega}_2 = \left[0\,,\,\dot{\phi}\,,\,0\right]^{\mathrm{T}}$ while the matrix $\tilde{\boldsymbol{\omega}}_i$ is the skew matrix of the vector $\boldsymbol{\omega}_i$ (with $i = 1\,,\,2$). The matrices $\mathbf{T}_i$, $\mathbf{S}_i$, $\mathbf{K}_i$ and $\mathbf{J}_i$ (with $i = j\,,\,k$) are the torque matrix, the damping factor matrix, the spring constant matrix and the rotational inertia matrix of the two bodies which are used to model the mirror. These matrices are all diagonal matrices.

Solving Eq. 3.13 and introducing the state space vector $\mathbf{x} = \left[\theta\ \phi\ \dot{\theta}\ \dot{\phi}\right]^{\mathrm{T}}$ it is possible to derive the state space equations of the steering mirror

$$\begin{gathered} \dot{\mathbf{x}} = \mathbf{A}\mathbf{x} + \mathbf{B}\boldsymbol{\tau} \\ \mathbf{y} = \mathbf{C}\mathbf{x} + \mathbf{D}\boldsymbol{\tau} \\ \downarrow \\ \dot{\mathbf{x}} = \begin{bmatrix} 0 & 0 & 1 & 0 \\ 0 & 0 & 0 & 1 \\ -\dfrac{K_x}{J_x} & 0 & -\dfrac{S_x}{J_x} & 0 \\ 0 & -\dfrac{K_y}{J_y} & 0 & -\dfrac{S_y}{J_y} \end{bmatrix} \begin{bmatrix} \theta \\ \phi \\ \dot{\theta} \\ \dot{\phi} \end{bmatrix} + \begin{bmatrix} 0 & 0 \\ 0 & 0 \\ -\dfrac{1}{J_x} & 0 \\ 0 & -\dfrac{1}{J_y} \end{bmatrix} \begin{bmatrix} \tau_x \\ \tau_y \end{bmatrix} \\ \mathbf{y} = \begin{bmatrix} 1 & 0 & 0 & 0 \\ 0 & 1 & 0 & 0 \end{bmatrix} \begin{bmatrix} \theta \\ \phi \\ \dot{\theta} \\ \dot{\phi} \end{bmatrix} + \mathbf{0}_{2\times 2}\,\boldsymbol{\tau} \end{gathered} \tag{3.15}$$

where $\mathbf{0}_{2\times 2}$ is the 2×2 null matrix while the vector $\boldsymbol{\tau}$ is the vector of the torques applied to the mirror by the voice coil motors.

In order to generate a desired tilt of the SM, it is necessary to provide an input current to the coils of the motors equivalent to the torque which needs to be applied. Moreover, both the motors and the sensors can be adjusted with an angular offset (with respect to the axes of rotation of the mirror) within the SM housing in order to have a compact component. For such a reason, the matrices $\mathbf{B}$ and $\mathbf{C}$ of Eq. 3.15 have to be modified accordingly. Assuming that θ_{mot} is the angle between the motors frame and the SM frame and that θ_{sen} is the angle between the sensor frame and the SM frame (see appendix A.5)

$$\begin{bmatrix} \tau_x \\ \tau_y \end{bmatrix} = \underbrace{\mathrm{K}_I \begin{bmatrix} \dfrac{\cos\left(\theta_{\mathrm{mot}}\right)}{J_x} & \dfrac{\sin\left(\theta_{\mathrm{mot}}\right)}{J_x} \\ -\dfrac{\sin\left(\theta_{\mathrm{mot}}\right)}{J_y} & \dfrac{\cos\left(\theta_{\mathrm{mot}}\right)}{J_y} \end{bmatrix}}_{\mathbf{B}_{\mathrm{mot}}} \begin{bmatrix} I_{Mx} \\ I_{My} \end{bmatrix} \tag{3.16}$$

$$\begin{bmatrix} \theta \\ \phi \end{bmatrix} = \underbrace{\mathrm{K_V} \begin{bmatrix} \cos(\theta_{\mathrm{sen}}) & \sin(\theta_{\mathrm{sen}}) \\ -\sin(\theta_{\mathrm{sen}}) & \cos(\theta_{\mathrm{sen}}) \end{bmatrix}}_{\mathbf{C}_{\mathrm{sen}}} \begin{bmatrix} \mathrm{V}_{Sx} \\ \mathrm{V}_{Sy} \end{bmatrix} \tag{3.17}$$

where K_I and $\mathrm{K_V}$ are conversion factors whose units are [N m/A] and [rad/V] respectively. The term I_{Mi} (with $i = x\,,\, y$) is the current injected in the motors which lie along the i-axis of the motors frame while the term V_{Si} (with $i = x\,,\, y$) is the voltage readout of the position sensor which lies along the i^{th} axis of the sensors frame. Substituting Eq. 3.16 and Eq. 3.17 in Eq. 3.15, the matrices $\mathbf{B}$ and $\mathbf{C}$ become

$$\mathbf{B} = \begin{bmatrix} 0 & 0 \\ 0 & 0 \\ \mathbf{B}_{\mathrm{mot}} \end{bmatrix} \quad ; \quad \mathbf{C} = \begin{bmatrix} \mathbf{C}_{\mathrm{sen}}^{-1} & 0 & 0 \\ & 0 & 0 \end{bmatrix} \tag{3.18}$$

and the vector τ is replaced by the vector $\mathbf{i}_M = [\, I_{Mx}\,,\, I_{My}\,]^{\mathrm{T}}$.

The open-loop transfer function of the steering mirror evaluated through the state space model presented beforehand is compared with the measured open-loop transfer function of the steering mirror (flight model) which is embedded in the optical bench of the LRI of GRACE Follow-On (see Fig. 3.3). Unfortunately, since the design of this steering mirror is an intellectual property of Airbus, it is not possible to report in this thesis the parameters which are used to initialize the state space model.

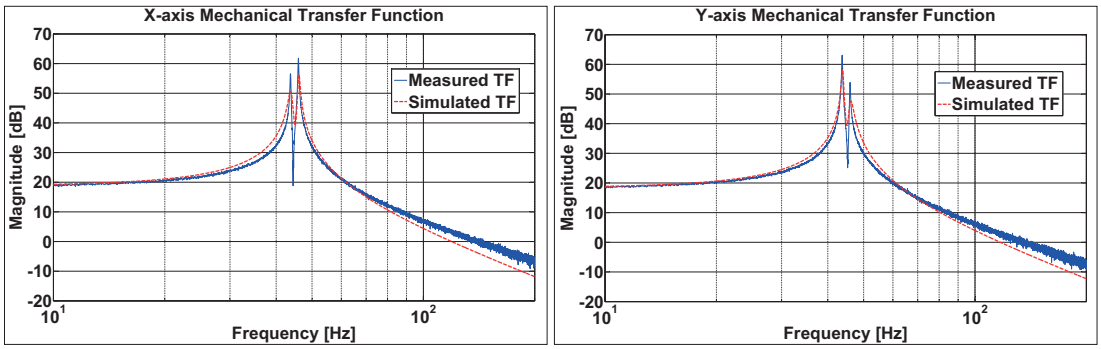

Figure 3.3: The left panel depicts the mechanical transfer function (TF) of the SM along the X-axis while the right panel depicts the mechanical transfer function along the Y-axis. These plots compare the transfer function provided by the state space model of the SM (dashed line) with the measured transfer function of the flight model of the SM of GRACE Follow-On (solid line).

In general the relation between the optical angles and the mechanical angles for both the rotation axes of the mirror is $\vartheta_{\mathrm{opt}} = 2\vartheta_{\mathrm{mech}}$. If the SM is mounted with a static inclination with respect to the direction of the beam impinging on its surface, then the conversion between mechanical and optical angles may not be identical for both axes. Indeed if the mirror is mounted with an angle of 45° with respect to the incoming-outgoing direction of the laser beam (like in Fig. 2.1, Fig. 2.4 and Fig. 2.6) the relation between optical and mechanical angles is $\vartheta_{\mathrm{opt}} = 2\vartheta_{\mathrm{mech}}$ for one axis and $\vartheta_{\mathrm{opt}} = \sqrt{2}\vartheta_{\mathrm{mech}}$ for the other axis.

3.4.1 Closed-loop performance and optimization

The closed-loop pointing performance of the SM are strongly dependant on the layout of the controller. Since the SM has to be capable of tracking a setpoint which can vary (rapidly) in time, a digital Proportional-Integral-Derivative (PID) controller is used. Indeed, the process output has to be coincident with the setpoint at steady state and the controller has to provide

predictive and anticipatory action. The simplest way to tune the controller is to use the Ziegler-Nicholos method [95] although the little process information that is used would lead the closed-loop system to lack in robustness [96]. The gains of the PID controller of the SM are here tuned using a modification of the modified Ziegler-Nicholos formula [97] which aims to optimize the control effects of the proportional, integral and derivative gain on the Nyquist plot

$$\begin{aligned} \mathrm{K_p} &= \gamma \mathrm{K_u} r_\mathrm{b} \cos(\psi) \\ \mathrm{K_i} &= \frac{\mathrm{K_u}}{T_\mathrm{u}} r_\mathrm{b} \pi \gamma \beta \frac{\cos^2(\psi)}{1+\sin(\psi)} \\ \mathrm{K_d} &= \mathrm{K_u} T_\mathrm{u} \frac{r_\mathrm{b}}{\pi} \gamma \alpha [1+\sin(\psi)] \end{aligned} \tag{3.19}$$

where $\mathrm{K_p}$, $\mathrm{K_i}$ and $\mathrm{K_d}$ are the proportional, integral and derivative gain respectively. The parameters r_b, ψ and α are the tuning parameters of the modified Ziegler-Nicholos formula while γ and β are two additional scaling factors introduced for improving the tunability of the gains of the controller. $\mathrm{K_u}$ and T_u are the critical value of the proportional gain (also known as ultimate gain) and the resulting oscillation period of the system (these provide the point of the Nyquist curve where the phase lag is π). The transfer function of the PID controller is therefore

$$\mathrm{K_{PID}} = \frac{\mathrm{K_d} s^2 + \mathrm{K_p} s + \mathrm{K_i}}{s} \tag{3.20}$$

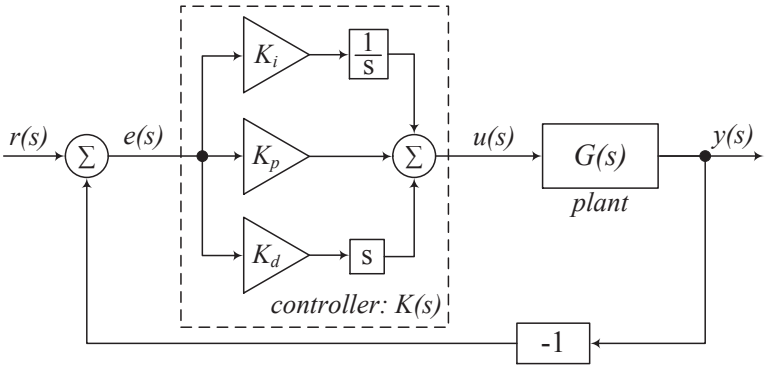

Figure 3.4: Closed-loop system with a PID controller which uses error feedback.

The gains of the controller determine not only its robustness, but also how this reacts to a setpoint command and how much time the system needs to reach steady state. In order to maximize the pointing performance of the SM, an optimization tool is used to derive the gains of the controller. This optimization tool combines a Genetic Algorithm [98] with a Particle Swarm Optimization [99]. In principle, the particle swarm optimization would be capable of finding an optimal solution within the predefined interval. Nevertheless, when the search interval is several orders of magnitude wide, there is a high likelihood that the swarm is attracted by a local optimum close to the right extreme of the boundary. The genetic algorithm is generally used when the parameters that have to be optimized can assume predefined values within the search interval (i.e. binary values). Although there is also a chance that the solution returned by the genetic algorithm is at a local minima, this risk can be mitigated by increasing the rate of mutation of the individuals.

These two algorithms have been here combined such that the genetic algorithm reduces the search space of the solution and the particle swarm optimizations finds the optima within this interval. Figure 3.5 depicts the flow diagram of the optimization algorithm while a more detailed description of the sub-routines is given in appendix A.8. The algorithm is terminated when the maximum number of iterations is reached or when the convergence criteria is fulfilled.

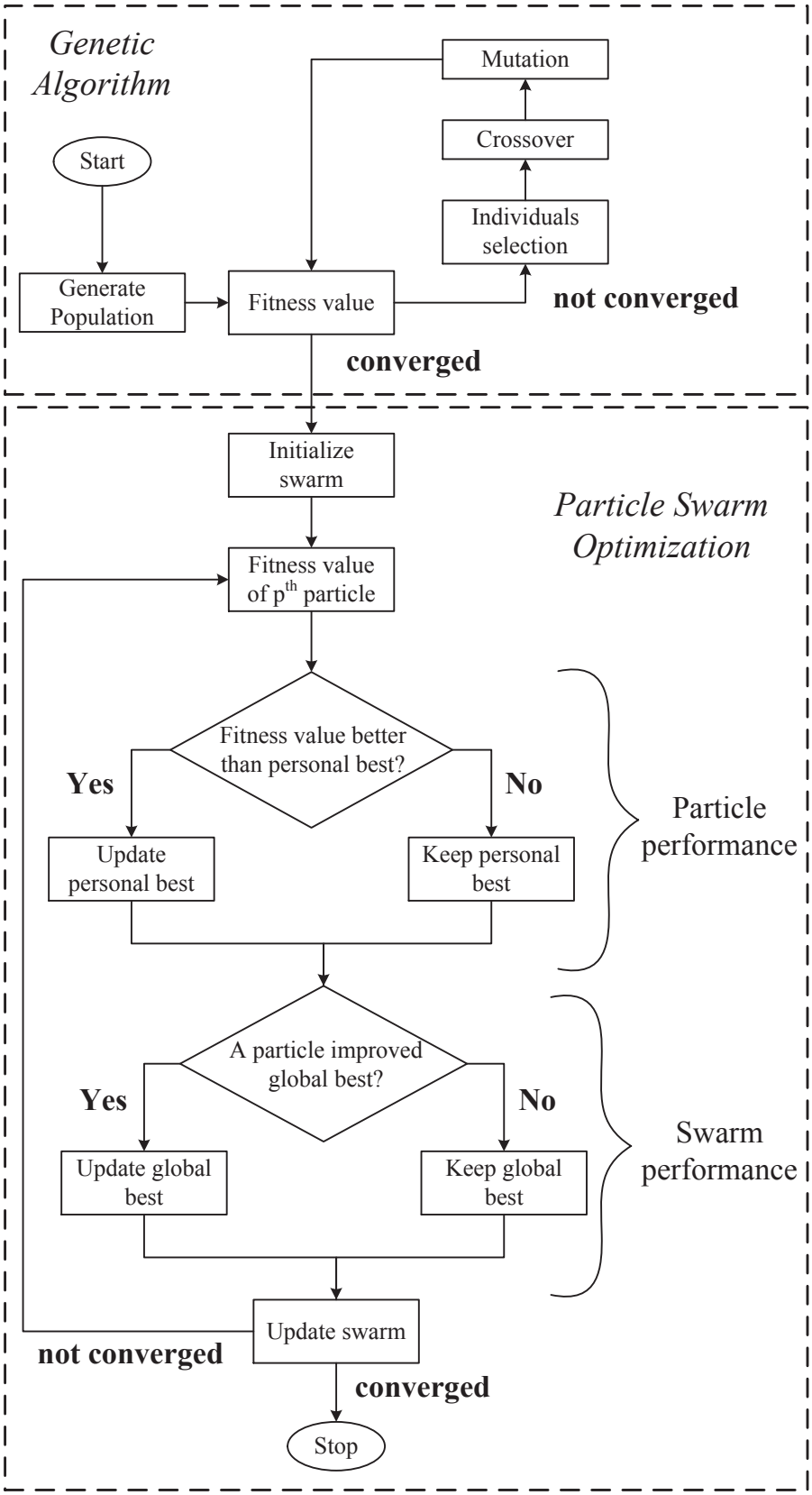

Figure 3.5: The flow diagram of the optimization algorithm used to estimate the optimal parameters of the controller is here depicted.

The optimal solution is the one that satisfies the robustness constrains listed in Tab. 3.2 and has the best fitness function. The fitness function is calculated trying to minimize the difference of the system response from a step command

$$\mathrm{F_f}\left(\mathbf{x}\right) = a_1 \left(t_{\mathrm{set}}\right)^2 + a_2 \left(\bar{\Delta}_{\mathrm{resp}}\right)^2 \tag{3.21}$$

where t_{set} is the settling time, $\bar{\Delta}_{\mathrm{resp}}$ is the mean error between an ideal step input and the response of the mirror before it reaches steady state, $\mathbf{x}$ is the vector containing the parameters which need to be optimized (it corresponds to an individual of the population - genetic algorithm - or a particle of the swarm) while the coefficients a_1 and a_2 are weighting factors. A small settling time is important for a system that has to rapidly react to time varying setpoint while the term $\bar{\Delta}_{\mathrm{resp}}$ is used to minimize the error at steady state.

Description	**Robustness constraints**
Delay margin	$\Delta\tau \geq T_{\mathrm{samp}}$
Gain margin	$\mathrm{G_{marg}} \geq 6\,\mathrm{dB}$
Phase margin	$\Delta\phi_{\mathrm{marg}} \geq 30°$
Close-loop bandwidth	$\mathrm{CL_{bw}} \leq 1.1\,\mathrm{kHz}$
	Other constraints
Maximum Overshoot	$\lvert \mathrm{O}_s^{\mathrm{max}} \rvert \leq 20\%$
Maximum Undershoot	$\lvert \mathrm{U}_s^{\mathrm{max}} \rvert \leq 20\%$

Table 3.2: Robustness constraints used to design the controllers of the SM.

The optimization routine is tested for an hypothetical SM whose state space parameters are listed in Tab. 3.3. The transfer function of the SM (plant of the model) is multiplied with a transfer function of a time delay in order to include the non-instantaneous response of the mirror to a setpoint command. The controller parameters and the performance of the system to a step command are listed in Tab. 3.4. The bandwidth of the controller is constrained to 1.1 kHz in line with the hardware limitations the steering mirror of GRACE Follow-On and with the close-loop sampling rate of the SM bench used to test the controller (limited to 18 kHz - see also paragraph 5.4.1). The bode diagram of the closed-loop transfer function is depicted in Fig. 3.6. The plot shows that the SM is capable of tracking a setpoint with a maximum frequency of 100 Hz before the performance decay of about 20 dB per decade (similar to the behaviour of a classical first-order lag element).

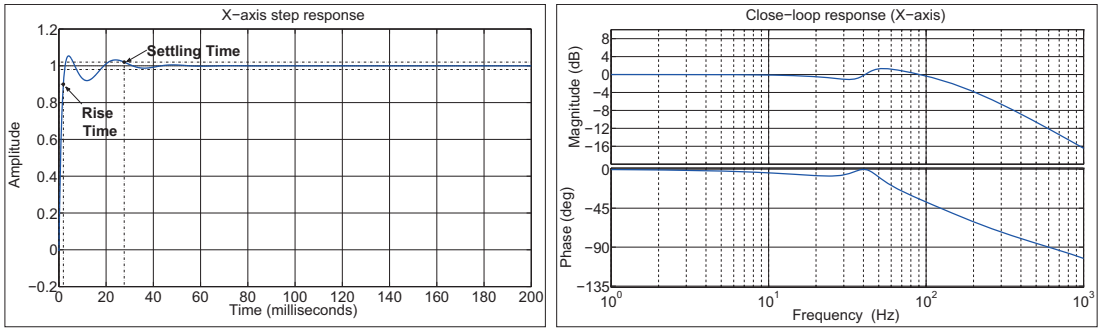

Figure 3.6: The left panel shows the step response of the SM along the X-axis while the right panel shows the frequency response of the closed-loop system along the same axis. Since the close-loop response has a low pass filter behaviour, low frequency commands can be tacked without error and the system suppresses well high frequency noise. Since the parameters of the SM along the Y-axis are similar, this pictures are representative of the mirror response along both of its rotating axes.

Parameter	Value	Units
J_x	3.962	$\mathrm{kg \cdot m^2}$
J_y	3.618	$\mathrm{kg \cdot m^2}$
S_i*	1×10^{-5}	-
K_i*	0.262	$\mathrm{N \cdot m/rad}$
θ_{sens}	0	rad
θ_{mot}	0	rad
K_I	1	$\mathrm{N \cdot m/A}$
$\mathrm{K_V}$	1	V/rad
T_d†	100	µs

* With $i = x\,,\, y$.

† The transfer function of the time delay is modeled using a second order Padé approximation [100].

Table 3.3: State space parameters of an hypothetical SM used to derive the gains of the controller.

Parameter		X-axis		Y-axis	
		Value	Units	Value	Units
Controller gains	$\mathrm{K_p}$	1.038	-	0.946	-
	$\mathrm{K_i}$	223.7	-	208.1	-
	$\mathrm{K_d}$	0.003	-	0.0026	-
Robustness margins	$\Delta\tau$	1.48	ms	1.48	ms
	$\mathrm{G_{marg}}$	30.02	dB	30.11	dB
	$\Delta\phi_{\mathrm{marg}}$	77.3	°	78.4	°
	$\mathrm{CL_{bw}}$	1.1	kHz	1.1	kHz
Response to step command	$\lvert \mathrm{O}_s \rvert$	6.31	%	5.37	%
	$\lvert \mathrm{U}_s \rvert$	8.45	%	8.05	%
	t_{rise}	1.75	ms	1.73	ms
	t_{set}	15.56	ms	15.09	ms

Table 3.4: The robustness margins are calculated solving the characteristic equation $1+G\,(s)\,K\,(s) = 0$. The term t_{rise} is the rise time while t_{set} is the settling time. O_s and U_s are the maximum overshoot and undershoot given by the step response of the controlled system (see Fig. 3.6). Since the genetic algorithm reduces the search space of the swarm, there is no significant difference between the three different boundary conditions used for the particle swarm optimization routine (see appendix A.8).

Because of the limited controller bandwidth, it is not possible to further improve the response of the SM to a step command without compromising its stability. If the setpoint has a small amplitude and varies rapidly in time, the controlled SM is not going to accurately track it and the output is going to be distorted version of the command signal. This can severely limit the type of inputs which can be feeded to the SM especially if this is used to scan a bi-dimensional area (typical problem of initial signal acquisition - see paragraph 4.3.1 and paragraph 5.4).

The setpoint distortion can be suppressed by including a feedforward controller in the closed loop system. With the configuration depicted in Fig. 3.7, the reference feedforward controller is used to track the setpoint while the feedback (PID) controller is used to suppress the noise which deviates the actual pointing of the mirror from the commanded one. Although the feedforward compensation allows the elimination of disturbances, it is much more sensitive to

process variations than the feedback controller. Therefore if the feedforward controller is used to optimize the response to command signals, these have to be known beforehand.

According to the layout of the control loop depicted in Fig. 3.7, the transfer function from setpoint to output is equal to

$$\begin{aligned}\frac{y(s)}{r(s)} =& \frac{G(s)\left[K(s)P(s)+FF(s)\right]}{1+K(s)G(s)} \\ =& P(s)+\frac{G(s)FF(s)-P(s)}{1+K(s)G(s)}\end{aligned} \tag{3.22}$$

The perfect feedforward compensation is thus obtained by choosing

$$FF(s) = \frac{P(s)}{G(s)} \tag{3.23}$$

In order to have a stable control loop, $P(s)$ cannot be chosen arbitrary but the order of this transfer function has to be either smaller or equivalent to the order of the transfer function of the plant [101]. Since the characteristic equation of Eq. 3.22 does not include the term $FF(s)$, a stable feedforward controller cannot introduce instability although it can lead to poor performance if not properly designed.

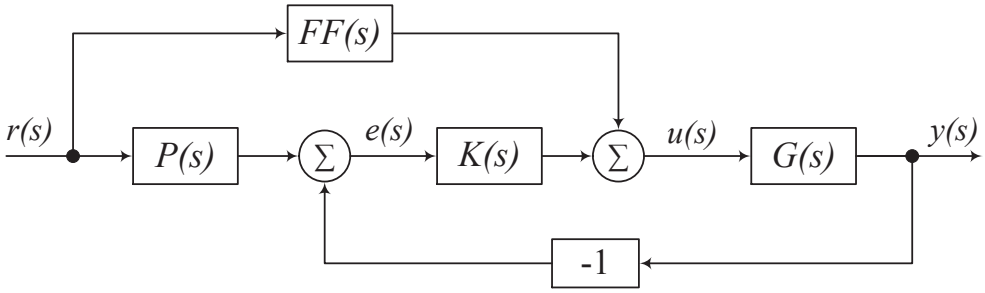

Figure 3.7: This figure depicts the layout of the closed-loop control system when the reference feedforward controller is included.

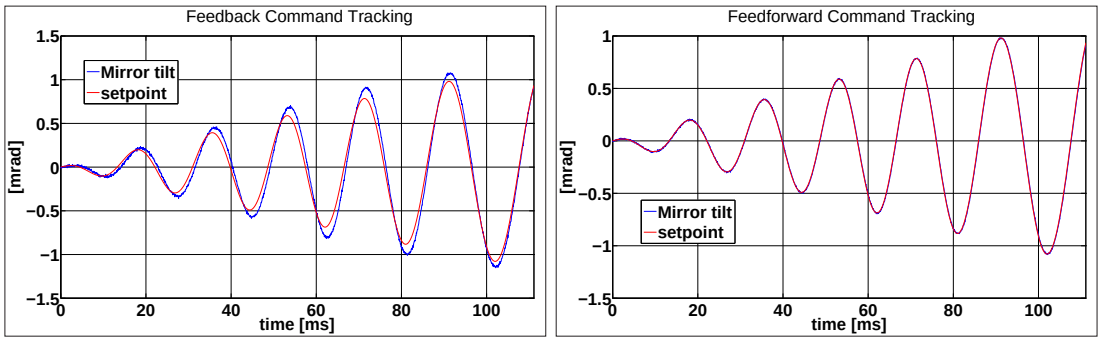

Figure 3.8: This picture depicts the pointing time trend of the SM when this is tracking a rapidly changing setpoint with a feedback controller (left panel) or with a feedforward controller (right panel).

The feedforward controller is designed optimizing $P(s)$ which is here modelled as a series of two first order lag elements ($P(s) = \mathrm{PT1}_1(s) \times \mathrm{PT1}_2(s)$). Since the transfer function of a first order lag element is

$$\mathrm{PT1}_i(s) = \frac{C_i s}{s + f_c^i} \qquad \text{with} \quad i = 1, 2 \tag{3.24}$$

the parameters which have to be optimized are the constant C_i and the cutoff frequency f_c^i for both PT1 elements. The optimization process is carried out once more using the genetic algorithm - particle swarm optimization routine and the fitness function is calculated as the square of the mean difference between setpoint and the effective tilt of the mirror.

Figure 3.8 depicts the time trend of the tilt angle of the steering mirror (in this particular case, the tilt around the X-axis of the mirror frame) when it tries to track a setpoint which rapidly varies in time using only a feedback controller (left panel) and when using the feedforward controller (right panel). As this picture shows, the process noise is not influencing the pointing performance since the feedback controller takes care of it (see appendix A.9).

3.4.2 Model of the position sensors measurement

For the purpose of this work, the modelling of the sensors is necessary for implementing the feedback control of the mirror pointing. Since the position sensors can vary form SM to SM (indeed some may use inductive sensors while others capacitive sensors) the sensor readout is not modelled as a transfer function but through a geometrical model. The sensor noise can be added later using a noise shape filter.

When the mirror is in its rest position, the normal of the surface of the mirror is $\mathbf{n}_0$ while a generic point on the mirror surface is $\mathbf{p}_0$ (both defined in mirror frame - see Fig. 3.9). When the mirror is rotated of θ about the X-axis of the mirror frame and of ϕ about the Y-axis of the mirror frame the new normal of the mirror and the new position of $\mathbf{p}_0$ are calculates as

$$\begin{aligned} \mathbf{n}_{\text{rot}} &= \mathbf{R}_\phi \mathbf{R}_\theta \mathbf{n}_0 \\ \mathbf{p}_{\text{rot}} &= \mathbf{r}_\text{p} + \mathbf{R}_\phi \left\{ [\mathbf{r}_\text{p} + \mathbf{R}_\theta (\mathbf{p}_0 - \mathbf{r}_\text{p})] - \mathbf{r}_\text{p} \right\} \end{aligned} \tag{3.25}$$

since the mirror is considered as a two body assembly. The matrices $\mathbf{R}_\phi$ and $\mathbf{R}_\theta$ are the rotation matrices around the Y-axis and around the X-axis of the SM frame respectively while $\mathbf{r}_\text{p}$ is the point around which the two bodies of the assembly rotate (it is here considered to be the same for both bodies of the mirror although this condition may not be always true). Introducing the rotation matrix from mirror frame to sensor frame $\mathbf{R}_{\text{SF-MF}}$, the rotated normal and the rotated point of the mirror surface can be evaluated in the sensor frame ($\mathbf{n}_{\text{rot}}^{\text{sf}} = \mathbf{R}_{\text{SF-MF}} \mathbf{n}_{\text{rot}}$ and $\mathbf{p}_{\text{rot}}^{\text{sf}} = \mathbf{R}_{\text{SF-MF}} \mathbf{p}_{\text{rot}}$ since the origin of the two frames is coincident - see appendix A.5).

The sensor measures the distance between the sensitive surface of the sensor and the surface of the mirror. Geometrically, for the i^{th} sensor, the variation of the sensor readout can be calculated as

$$\Delta \text{q}^i = \left|\left| \left[\mathbf{s}_i + \mathbf{n}_s^i \frac{-\left(\mathbf{n}_{\text{rot}}^{\text{sf}} \cdot \mathbf{s}_i\right) + \left(\mathbf{n}_{\text{rot}}^{\text{sf}} \cdot \mathbf{p}_{\text{rot}}^{\text{sf}}\right)}{\mathbf{n}_{\text{rot}}^{\text{sf}} \cdot \mathbf{n}_s^i} \right] - \mathbf{q}_0^i \right|\right| \tag{3.26}$$

where $\mathbf{s}_i$ and $\mathbf{n}_s^i$ are the reference position and normal of the i^{th} sensor while $\mathbf{q}_0^i$ is the sensor measurement when the mirror is at rest (namely 0). The output of the sensor is, in general, a voltage signal which is equivalent to the distance variation Δq^i (or to the absolute distance). Since the distance variation is proportional to the tilt of the mirror this can be properly converted to a voltage signal through an appropriate conversion factor. Assuming a linear relation between angular tilt and sensor readout, the voltage output of the i^{th} sensor is equal to

$$\text{V}^i = \underbrace{\frac{2\Delta \text{q}\left(\vartheta_{\max}\right)}{\text{V}_{\max}^+ + \text{V}_{\max}^-} K_{V-\Delta \text{q}}}_{m_i} \Delta \text{q}^i + n_i \tag{3.27}$$

where $\Delta \text{q}\left(\vartheta_{\max}\right)$ is the maximum displacement variation measured by the sensor, $\text{V}_{\max}^+$ ad $\text{V}_{\max}^-$ are the maximum voltages outputs when the mirror is completely tilted (positive and negative tilts can return different output voltages if the sensor is biased), $K_{V-\Delta \text{q}}$ is the factor

which converts the displacement into voltage and n_i is the sensor noise which is added to the measurement using a noise shape filter.

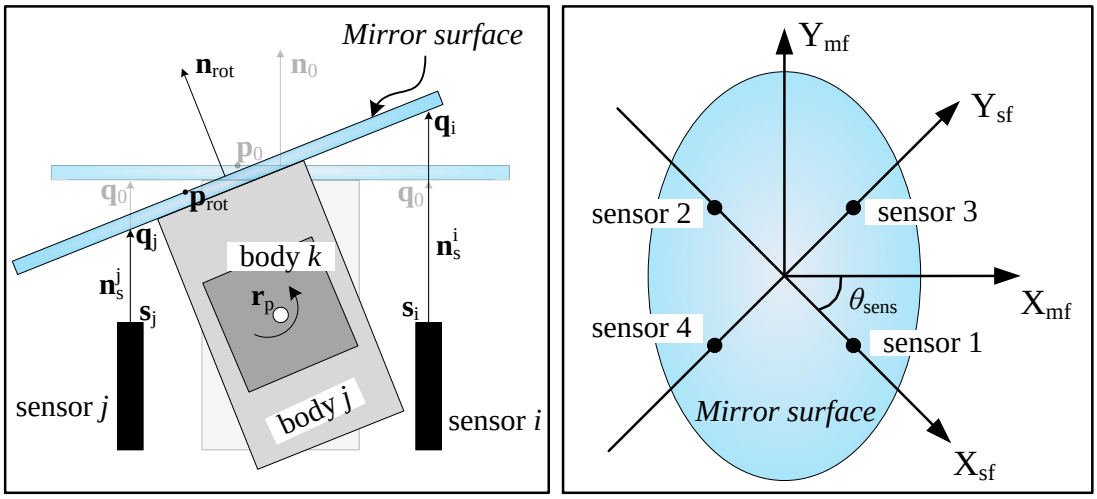

Figure 3.9: This picture shows the position of the sensors with respect to the mirror surface (right panel) and their geometrical measurement when the mirror is tilted (left panel).

3.4.3 Model of the readout of the position sensors electronics

The voltage outputs of the sensors are converted into the tip-tilt angles of the mirror using the sensors electronics. Also here, the tip-tilt angles are re-derived from the voltage measurement using a geometrical model which is equivalent to the conversion performed by the look-up tables of the sensors electronics.

The voltage output of the sensors is converted back into a displacement of the mirror applying the inverse relation $\Delta \mathrm{q}^i = \mathrm{V}^i/m_i$ with $i = 1\,,\,\ldots\,,\,4$ (because of the sensor noise and calibration error, even though the labelling is the same, $\Delta \mathrm{q}^i$ and m_i are not identical to the ones of Eq. 3.27). In order to derive the right sign of the rotation angles it is necessary to compare the sensors measurement. Labeling θ and ϕ the rotation angles around X-axis and Y-axis and considering as positive clockwise rotations, according to the sensor position shown in Fig. 3.9

- $\Delta \mathrm{q}^1$ is the biggest displacement $\longrightarrow \theta > 0$ and $\phi > 0$
- $\Delta \mathrm{q}^2$ is the biggest displacement $\longrightarrow \theta < 0$ and $\phi < 0$
- $\Delta \mathrm{q}^3$ is the biggest displacement $\longrightarrow \theta > 0$ and $\phi < 0$
- $\Delta \mathrm{q}^4$ is the biggest displacement $\longrightarrow \theta < 0$ and $\phi > 0$

Since the rotation of the mirror (ideally) changes the distance between the mirror and the sensor only along the z component of the sensor frame, the point $\mathbf{q}^i$ has components $\mathbf{q}^i = \left[s_i^x\,,\,s_i^y\,,\,\Delta \mathrm{q}^i\right]^{\mathrm{T}}$. Labeling as $\hat{\mathbf{v}}_{4-1}$ the unit vector pointing from $\mathbf{q}^4$ to $\mathbf{q}^1$ and as $\hat{\mathbf{x}}_{\mathrm{mf}}^{\mathrm{sf}}$ the unit vector of the X-axis of the mirror frame expressed in the sensor frame

$$\begin{aligned} \hat{\mathbf{v}}_{4-1} = \frac{\mathbf{q}^1 - \mathbf{q}^4}{||\mathbf{q}^1 - \mathbf{q}^4||} \quad ; \quad \hat{\mathbf{x}}_{\mathrm{mf}}^{\mathrm{sf}} = \mathbf{R}_{\text{SF-MF}}\hat{\mathbf{x}}_{\mathrm{mf}} \\ \downarrow \\ \phi = \sin^{-1}\left(\left|\left|\hat{\mathbf{v}}_{4-1} \times \hat{\mathbf{x}}_{\mathrm{mf}}^{\mathrm{sf}}\right|\right|\right) \end{aligned} \tag{3.28}$$

where $\mathbf{R}_{\text{SF-MF}}$ is the rotation matrix from mirror frame to sensor frame. The sign of ϕ is chosen according to the criteria described beforehand.

In order to derive the magnitude of the rotation around the X-axis of the mirror frame it is first necessary to evaluate the rotated normal of the mirror ($\mathbf{n}_{\text{rot}}$). Using three of the four sensor measurements (i.e. the measurement of sensor 1, sensor 2 and sensor 4) it is possible to calculate the equation of the plane containing the mirror surface and thus the rotated normal of the mirror

$$\begin{gathered} \mathbf{q}_{4-1} = \mathbf{q}^1 - \mathbf{q}^4 \quad ; \quad \mathbf{q}_{4-2} = \mathbf{q}^2 - \mathbf{q}^4 \\ \downarrow \\ \mathbf{n}_{\text{rot}} = \frac{\mathbf{q}_{4-1} \times \mathbf{q}_{4-2}}{\left|\left|\mathbf{q}_{4-1} \times \mathbf{q}_{4-2}\right|\right|} \end{gathered} \tag{3.29}$$

Knowing ϕ, it is possible to calculate the normal of the mirror surface ($\mathbf{n}_\theta$) given by a rotation θ around the X-axis. Same thing can be done for a generic point $\mathbf{p}_\theta$ which lies on the surface of the mirror. Hence,

$$\begin{aligned} \mathbf{n}_\theta &= \mathbf{R}_{\text{SF-MF}} \mathbf{R}_y\left(-\phi\right) \mathbf{R}_{\text{SF-MF}}^{-1} \mathbf{n}_{\text{rot}} \\ \mathbf{p}_\theta &= \mathbf{R}_{\text{SF-MF}} \left[\mathbf{r}_{\text{p}} + \mathbf{R}_y\left(-\phi\right) \left(\mathbf{R}_{\text{SF-MF}}^{-1} \mathbf{q}^i - \mathbf{r}_{\text{p}}\right)\right] \end{aligned} \tag{3.30}$$

where both $\mathbf{n}_\theta$ and $\mathbf{p}_\theta$ are expressed in the sensor frame. In this case, the point $\mathbf{p}_\theta$ can be calculated using the measurement vector $\mathbf{q}^i$ of any of the four sensors. If the mirror would rotate only around the X-axis, the measurement returned by sensor 2 and sensor 4 expressed as a vector would be

$$\mathbf{q}_*^i = \mathbf{s}_i + \mathbf{n}_s^i \frac{-\left(\mathbf{n}_\theta \cdot \mathbf{s}_i\right) + \left(\mathbf{n}_\theta \cdot \mathbf{p}_\theta\right)}{\mathbf{n}_\theta \cdot \mathbf{n}_s^i} \quad \text{with } i = 2\,,\,4 \tag{3.31}$$

Labeling as $\hat{\mathbf{v}}_{2-4}$ the unit vector pointing from $\mathbf{q}_*^4$ to $\mathbf{q}_*^2$ and as $\hat{\mathbf{y}}_{\text{mf}}^{\text{sf}}$ the unit vector of the Y-axis of the mirror frame expressed in the sensor frame

$$\begin{gathered} \hat{\mathbf{v}}_{2-4} = \frac{\mathbf{q}_*^4 - \mathbf{q}_*^2}{||\mathbf{q}_*^4 - \mathbf{q}_*^2||} \quad ; \quad \hat{\mathbf{y}}_{\text{mf}}^{\text{sf}} = \mathbf{R}_{\text{SF-MF}} \hat{\mathbf{y}}_{\text{mf}} \\ \downarrow \\ \theta = \sin^{-1}\left(\left|\left|\hat{\mathbf{v}}_{2-4} \times \hat{\mathbf{y}}_{\text{mf}}^{\text{sf}}\right|\right|\right) \end{gathered} \tag{3.32}$$

and the sign of θ is once more derived using the measurement of the four sensors. Although throughout this paragraph most of the parameters have been labelled identically with the parameters of Fig. 3.9 for clearness, these are not identical. Taking as examples Eq. 3.30 and Eq. 3.31, the terms $\mathbf{r}_{\text{p}}$ and $\mathbf{n}_s^i$ are not the real rotation point or the real position of the i^{th} sensor but their knowledge. Hence, this model allows to include both measurement noise and conversion errors in the final estimate of the tip-tilt angles of the mirror.

3.5 Noise model of the lasers

Both the free-running laser and the cavity stabilized laser are included in the simulator through their noise models. Indeed, for simulating the frequency drift of the laser neither a detailed model of this component (i.e. that simulates the stimulated emission) nor a detailed simulation which includes cavity lock and stabilization is necessary. The noise model of the free-running laser is derived from a zero-pole fitting of early measurements of the Tesat laser [80] while the noise model of the stabilized laser is derived form the zero-pole fitting of the frequency stability requirement of LISA [102]. Figure 3.10 shows the ASD of these two noise models in comparison with their expected behaviour.

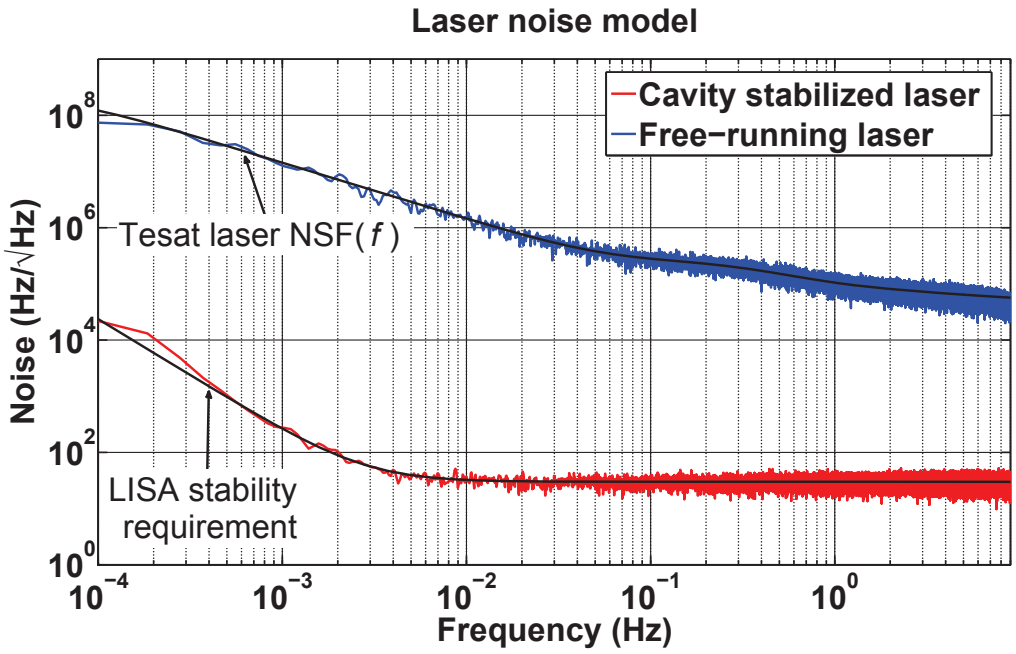

Figure 3.10: This picture depicts the ASD of the free-running laser noise and the cavity stabilized noise used for performing simulations.

3.6 Model of the optics

The optics of the interferometer is modelled using planar surfaces which have reflective and refractive properties according if these are mirrors or beam splitters. Since the beam is reduced to its principal ray, the imaging optics can be neglected. The new direction of a beam (modelled as a structure which has an originating point and a direction) impinging on a surface is calculated using Snell's laws

$$\underline{\text{Reflection}} \qquad \mathbf{v}_{\text{refl}} = \mathbf{v}_0 - 2\,(\mathbf{n}_{\text{m}} \cdot \mathbf{v}_0)\,\mathbf{n}_{\text{m}} \tag{3.33}$$

$$\underline{\text{Refraction}} \qquad \mathbf{v}_{\text{refr}} = \frac{r_1}{r_2}\mathbf{v}_0 + \left\{ \mp\frac{r_1}{r_2}\,(\mathbf{n}_{\text{m}} \cdot \mathbf{v}_0) \mp \sqrt{1 - \left(\frac{r_1}{r_2}\right)^2 \left[1 - (-\mathbf{n}_{\text{m}} \cdot \mathbf{v}_0)^2\right]} \right\} \tag{3.34}$$

where r_1 and r_2 are the refraction indices of the medium before and after the beam encounters the refracting surface. The vectors $\mathbf{n}_{\text{m}}$ and $\mathbf{v}_0$ represent the normal of the surface of the mirror/beam splitter and the direction of the beam before being reflected/refracted. The correct sign of the term within angular brackets of Eq. 3.34 depends on the sign of $(-\mathbf{n}_{\text{m}} \cdot \mathbf{v}_0)$; if this is positive the sign is negative otherwise it is positive. The point where the laser beam hits the optical surface and the distance travelled by the beam while propagating between two optical components are calculated as

$$\begin{aligned} \mathbf{p} &= \mathbf{p}_0 - \frac{((\mathbf{n}_{\text{m}} \cdot \mathbf{p}_0)) + (-\mathbf{n}_{\text{m}} \cdot \mathbf{p}_{\text{m}})}{\mathbf{n}_{\text{m}} \cdot \mathbf{v}_0}\mathbf{v}_0 \\ L &= ||\mathbf{p} - \mathbf{p}_0|| \end{aligned} \tag{3.35}$$

where $\mathbf{p}_0$ is the originating point of the beam on the surface previously encountered, $\mathbf{p}_{\text{m}}$ is a point on the surface on which the beam impinges and L is the pathlength between $\mathbf{p}_0$ and $\mathbf{p}$.

The other parameters have been defined beforehand. After interacting with an optical surface, the power of the beam is multiplied by a factor η (with $\eta \leq 1$) which is equivalent to the optical efficiency of the component. This allows to estimate the power of the beams at the photodiode.

3.7 Model of the phasemeter

A stand-alone model of the phasemeter is used for calculating the filter coefficients of the WPD and the tuning parameters of the DPLLs. This significantly simplifies the effort required in testing this sub-system with a Field Programmable Gate Array (FPGA) (see chapter 5). Indeed, the computer model of the phasemeter allows to visualize errors and/or artifacts caused i.e. by the filtering process. These errors would be more complex to identify once the phasemeter is implemented in the FPGA.

Nevertheless, due to the operating frequency of this sub-system (the sampling frequency is 50 MHz) the model of the phasemeter requires minutes to perform a µs of measurement. Thus, for testing the acquisition and calibration algorithms, the complexity and the slowness of this complete model would not allow to exploit a (simulated) day/week of measurement in a reasonable amount of time. For such a reason, the complete model of the phasemeter is omitted in the laser link simulator and is replaced by a function which sums the pathlength accrued by the beams when propagating through the two instruments and in the intra-satellite medium.

3.8 The laser link simulator

The laser link simulator is developed within the MATLAB-Simulink environment according to a three level nested system. Indeed, its hierarchical structure includes a main view, a system view and a sub-system view.

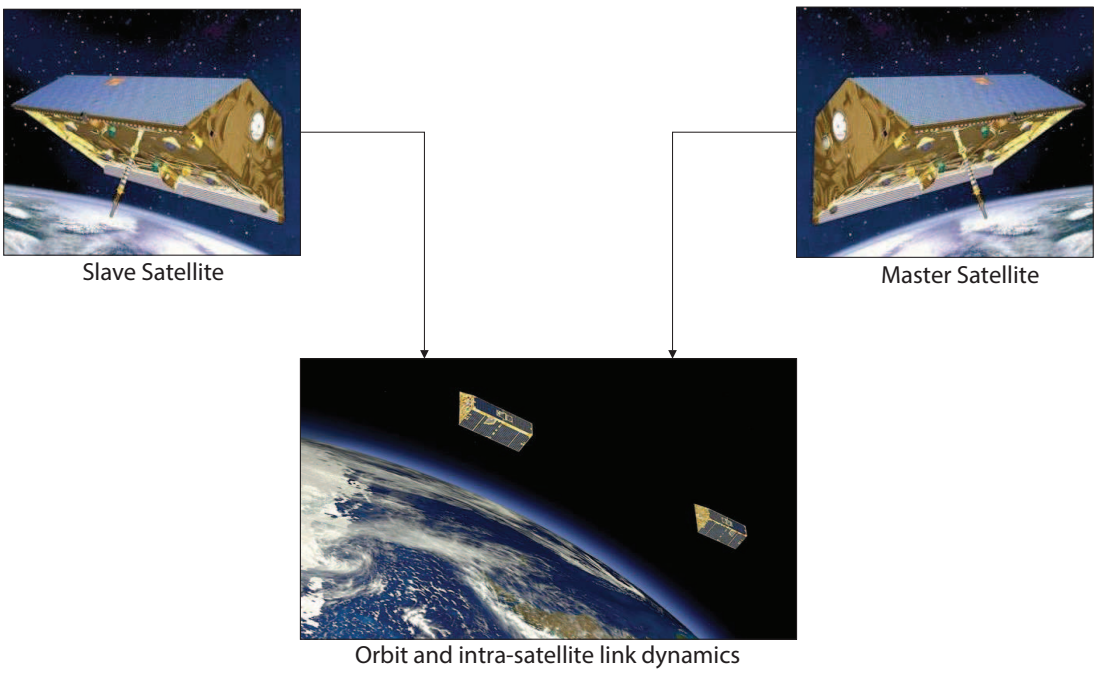

Figure 3.11: Main view of the laser link simulator. The images of the two satellites are courtesy of NASA/JPL-Caltech.

The main view contains three principal blocks (see Fig. 3.11); two identify the satellite of the constellation while the third block is used to simulate the orbit dynamics and the intra-satellite laser link.

The system view identifies the constituting elements of the interferometer and which information these exchange. The system view depicted in Fig. 3.12 is representative of the optical layout of Fig. 2.4. Nevertheless, the constituting blocks can be moved and additional blocks can be added to reproduce a different optical layout.

The sub-system view contains the model of a sub-system of the optical layout. For example, Fig. 3.13 shows the sub-system view of the steering mirror. The sub-system view is divided in the physics models (green blocks in Fig. 3.13) and control blocks (red blocks in Fig. 3.13). The physics blocks are used to reproduce the physical behaviour of the system while the control block are the ones tunable by the user. Taking as example the position sensor system of the steering mirror, the sensors represent physical components with defined properties while the sensors electronics represents the control block because it can be tuned in order to provide the correct sensor readout. Below the constituting blocks of the sub-system view it is possible to find the code that defines their properties and/or functions.

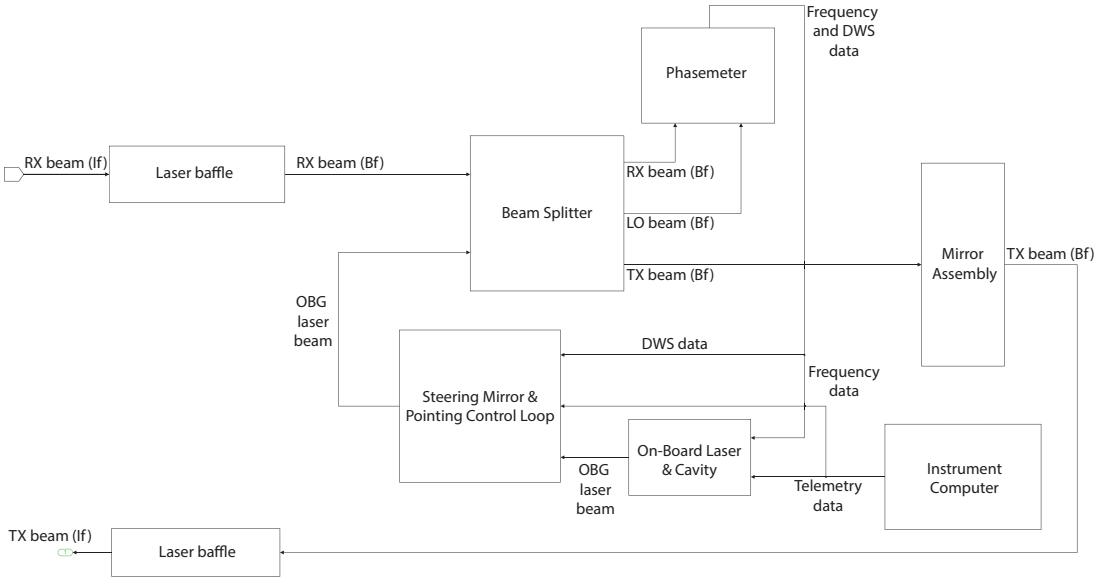

Figure 3.12: This picture shows the constituting blocks of the laser instrument of the slave satellite and how the numerical quantities are routed between the sub-systems. The difference with the system view of the master satellite is given by the on-board laser and cavity block. For the slave satellite, this sub-system implements the noise model of the Tesat laser and the laser frequency control unit. For the master satellite, only the noise model of the cavity stabilized laser is included within this sub-system.

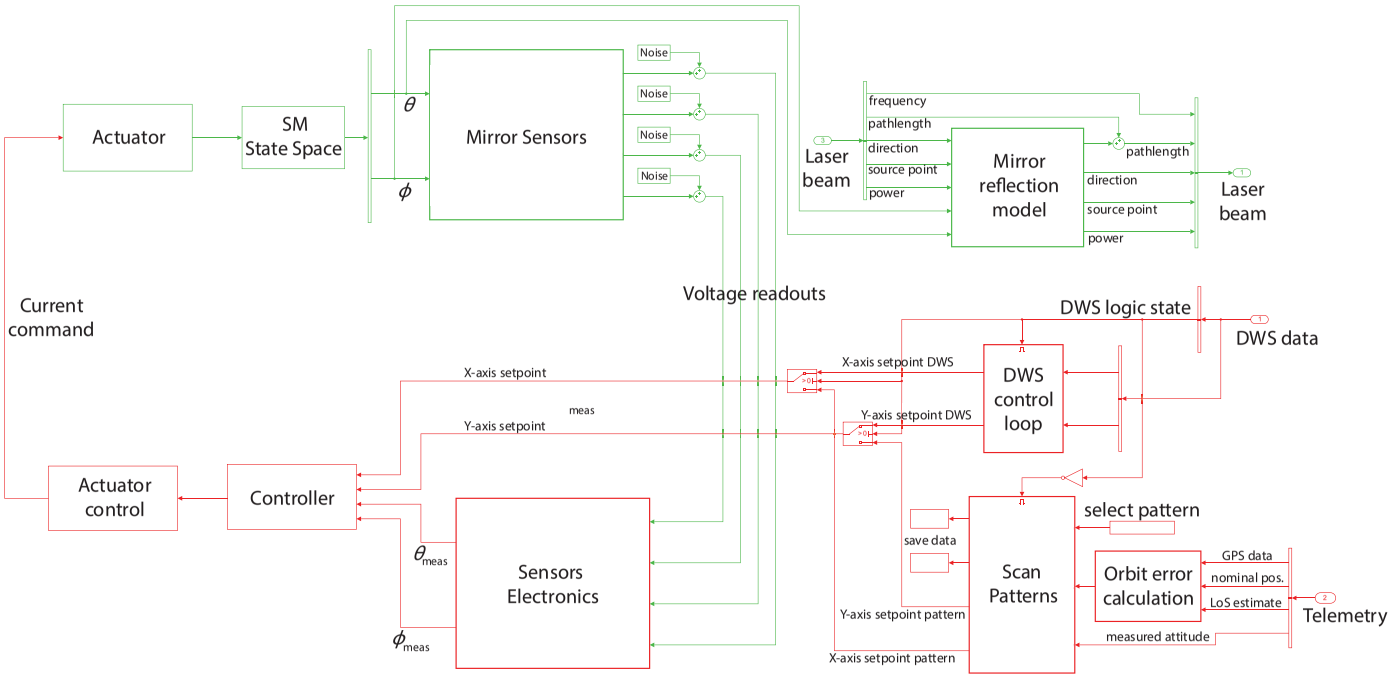

Figure 3.13: This figure depicts the sub-system block diagram of the simulator of the SM. Together with the mirror dynamics model and the position control system, this sub-system includes the blocks relative to the pointing control of the SM. Indeed, the SM can be operated in acquisition mode (the pointing of the mirror is controlled according to a specific pattern) or tracking mode (when the phasemeter is locked the DWS signal is used to control the beam pointing). The actuator control is used to limit the current which is injected in the voice coil motors of the mirror.

Chapter 4

Signal Acquisition within a Multidimensional Uncertainty Domain

Before the laser interferometer can be employed for ranging metrology, it is necessary that the link between the two satellites is established. When using a transponder configuration without acquisition sensors or beam expanders, the two laser beams have to be aligned to the line of sight of the instrument with µrad precision in order to have a sufficient contrast at the photodiodes. Moreover, the maximum frequency offset between the two laser beams has to be within the bandwidth of the electronics of the photoreceiver. A first attempt to establish an optical link is most likely bound to fail because the pointing of the satellites and the operating frequency of the lasers can be estimated with an accuracy which is not compatible with the capabilities of the instrument.

For such a reasons, before entering science mode, the instrument requires an intermediate in-orbit commissioning phase known as *initial signal acquisition* phase. The objective of this phase is to correctly aligning the two laser beams to the line of sight and ensure that the frequency offset between them is brought below the Nyquist frequency of the photoreceiver. Since the initial acquisition phase has to combine corrections of the beam pointing and frequency tunings it can be, in turn, split into *spatial acquisition* and *frequency acquisition* (which, in general, are not independent from each other).

This chapter is organized as follows: paragraph 4.1 discusses the problem of the initial acquisition. The spatial acquisition, the frequency acquisition and how these can be linked are discussed in paragraphs 4.2, 4.3, 4.4 and 4.5. Paragraph 4.5 also presents a time optimized approach for designing an acquisition algorithm while paragraph 4.6 is dedicated to acquisition simulations. The last paragraph discusses how an acquisition sensor can simplify the initial acquisition process.

4.1 The dimension of the uncertainty domain

For stable science operations, the alignment error of the laser beams with respect to the line of sight of the instrument has to be below a certain threshold [40, 63]. On the first attempt to establish the optical link, the line of sight of the instrument has to be estimated by using the attitude measurement of the star trackers and through on-board orbit prediction. The uncertainty between the estimated line of sight and the real line of sight usually exceeds the absolute pointing error requirement of about one order of magnitude. The bi-dimensional area centered in the intersection point between the vector of the estimated line of sight and the plane containing the incoming aperture of the facing satellite is also known as the *uncertainty cone*. The width of the uncertainty cone depends on the expected alignment knowledge between the

star trackers and the line of sight of the laser instrument, the alignment of the instrument components, the onboard absolute attitude knowledge error and the navigation error.

The problem of acquiring a laser signal can be supported by using dedicated beacon beams with high power and high divergence together with dedicated acquisition sensors which widen the field of view of the instrument [103, 104, 105, 106, 107, 108, 109]. Another possible solution would be the real-time exchange of GPS data which could improve the pointing knowledge [81]. Although these solutions significantly simplify the signal acquisition process they all require additional hardware and processing capabilities on-board the spacecrafts. Beaconless acquisition for a satellite-to-satellite optical communication link has also been studied and demonstrated as a feasible solution even though the acquisition time is not as good as in the previous cases [110].

When no additional hardware is used to simplify the acquisition of the laser signal, a well defined repointing sequence of the laser beams is employed in order to remove the initial pointing bias. The repointing sequence can be executed by either rotating the entire satellite [111], by implementing an optical element capable of steering the outgoing laser beam of each instrument in Azimuth and Elevation (in general a steering mirror [112]) or using a combination of both solutions. For a LEO satellite mission, the first solution would require a considerable amount of thrust pulses. Moreover, the time required to carry out the repointing maneuver is not sufficient to neglect the pointing drifts introduced by the orbit disturbances. For such a reason, the second solution is the method of choice.

The photoreceivers described in paragraph 2.3 have a bandwidth with a lower limit of $2-5\,\mathrm{MHz}$ and an upper limit of $16-22\,\mathrm{MHz}$. Due to the change of environmental conditions and after undergoing the vibrations of the launch, the initial operating frequencies of the cavity stabilized laser and the free-running laser have an offset which can vary from 200 MHz up to 1 GHz (values derived from laboratory experience on laser characterization). The scope of the frequency acquisition is to reduce this offset below the bandwidth of the photoreceiver in order to phase-lock the free-running laser to the cavity stabilized one. This goal is achieved by changing the frequency of the free running laser according to a well-defined sequence.

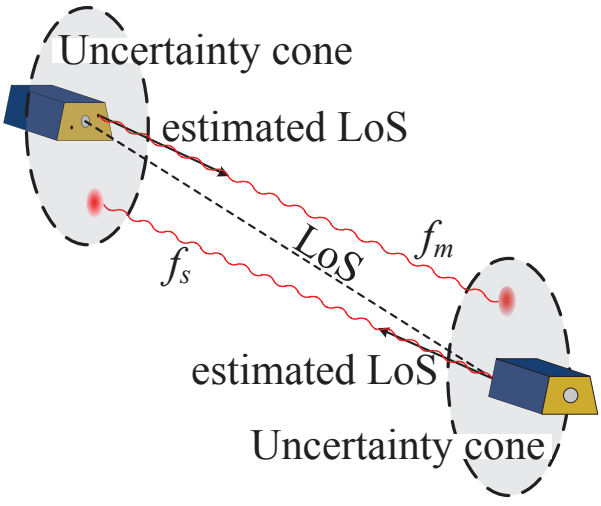

Figure 4.1: Representation of the initial acquisition problem for a constellation of two satellites. The satellites will acquire the signal only if the two beams are aligned to the line of sight (LoS) while the frequency offset between the laser beams ($f_m - f_s$) is compatible with the bandwidth of the photoreceiver.

Hence, the pointing offsets of each satellite defines a search space with four degrees of freedom (only the Pitch and Yaw offsets are relevant) while the frequency offset between the lasers adds an additional degree of freedom to the acquisition problem (see Fig. 4.1). In

order to successfully acquire the laser signal, all five degrees of freedom have to be resolved contemporary. Hereafter, different strategies for acquiring the optical link in a five degrees of freedom search space are discussed. The usage of additional hardware does not invalidate the presented strategies but simply reduces the degrees of freedom and the complexity of the acquisition logic (see paragraph 4.7).

4.1.1 Signal acquisition strategy

The strategy for acquiring the laser signal can be implemented according to two different approaches named respectively *split acquisition* and *direct acquisition*. The split acquisition is a semi-autonomous acquisition strategy. Indeed, once the signal acquisition phase is triggered, the five degrees of freedom of the uncertainty domain are fully covered and each satellite stores the tip-tilt angles of the steering mirror and the operating frequency of the laser whenever the interferometer detects the signal. This data are then sent to ground for post-processing. At the next passage of the satellite pair over the commanding ground station, the initial acquisition phase is again triggered but over a reduced uncertainty domain. If the signal is detected, the instrument tries to phase lock the free-running laser and switch to science operations. The split acquisition is therefore characterized by two modes. The first is conceived for estimating the line of sight and the heterodyne frequency while the second one for acquiring the signal. These two modes are labelled as *target detection* and *link attainment*. In some literature these two modes are referenced as initial acquisition and re-acquisition or as line of sight calibration and acquisition [63]. In this thesis this labelling is avoided in order to distinguish the process of establishment the laser link for the first time from the process of establishing the laser link if this is lost during science operations and to separate the study of the initial link acquisition from the study on data calibration discussed in chapter 6.

The direct acquisition is intended to be fully autonomous. Hence the instrument tries to switch to science operations whenever it detects the signal. This is equivalent in using the link attainment mode over the full width of the multidimensional uncertainty domain.

As it will be shown in paragraph 4.4, the difference between split acquisition and direct acquisition is in the duration of the five dimensional uncertainty scan. Neither the spatial acquisition logic nor the frequency acquisition logic are affected by these strategies.

4.2 Frequency acquisition

The offset between the frequencies of the two lasers can be reduced by just changing the frequency of the free running laser on board the slave satellite since the heterodyne beat frequency is independent from the absolute frequency of each laser.

The operating frequency of the free running laser can be modified according to a linear ramp or performing discrete frequency steps. The obvious difference between these two methods is that in the first case the frequency of the laser constantly sweeps through the uncertainty range while in the latter case the frequency is kept at a quasi-constant value for a prefixed time (the laser is free running and its frequency drift cannot be suppressed). The acquisition unit of the phasemeter (either based on the WPD or on the DFFT algorithm) subdivides its bandwidth into sub-bands (the width of the sub-bands depends on the number of stages of the WPD tree or on the number of bins of the DFFT). If the heterodyne frequency crosses two sub-bands (or moves between adjacent bins) while the phasemeter is acquiring the signal, the time it needs to lock it increases significantly (in case of a DFFT phasemeter the signal might not be even detected because of the significant reduction of the SNR). For such a reason, it is preferable to perform the frequency acquisition using discrete steps[1].

[1] Also with discrete steps it is also not possible to fully exclude the possibility of crossing a sub-band while the signal is being acquired mainly because of the frequency drift of the free-running laser. Nevertheless in the time scales of the signal acquisition, this frequency drift is negligible and the frequency of the free-running laser

In order to cover the frequency uncertainty without gaps, the maxim width of each step has to be equal to the bandwidth of the phasemeter. The number of steps required to cover the frequency uncertainty is equal to

$$N_f = \frac{2\,|\mathrm{F}_{unc}|}{K_f \Delta f_{bw}} \tag{4.1}$$

where Δf_{bw} is the bandwidth of the phasemeter, F_{unc} is the width of the frequency uncertainty and K_f $(0 < K_f < 1)$ is a factor used to scale the width between two consecutive steps of the frequency scan in order to take into account the frequency drift of the free-running laser. The magnitude of this value is calculated from the expected laser frequency drift over the time interval in which the frequency has to be kept constant. Yields,

$$K_f = \frac{\Delta f}{\Delta f + \delta f\,(t_f)} \tag{4.2}$$

where $\delta f\,(t_f)$ is the expected drift in the time interval $[\,0\,,\,t_f\,]$.

If the frequency uncertainty is scanned according to a linear ramp, the maximum slope of the ramp has to be equal to

$$m_f = \frac{K_f \Delta f_{bw}}{t_f} \tag{4.3}$$

where t_f is the amount of time in which the laser frequency is expected to sweep a frequency interval as wide as the bandwidth of the phasemeter. The magnitude of the scaling factor K_f can be calculated as in Eq. 4.2. The frequency scan using a linear ramp can be seen as a sequence of steps connected to each other by a line. Therefore, the number of equivalent frequency steps can be calculated as in Eq. 4.1.

Since the satellites move along eccentric orbits, the frequency of the laser signal is affected by a Doppler shift. When the time scale of the frequency acquisition process is one order of magnitude smaller than the orbital period, the frequency shift induced by the Doppler can be neglected. Otherwise it has to be taken into account in order to guarantee a full coverage of the frequency uncertainty region. The frequency variation caused by the Doppler can be modeled as

$$f_D(t) = \frac{\Delta V_{max}}{\lambda} \sin\left(\sqrt{\frac{\mu}{a^3}}\,t + \varphi_0\right) \tag{4.4}$$

where λ is the wavelength of the laser beam, μ is the gravitational parameter of the planet, a is the semi-major axis of the orbit of the satellites, ΔV_{max} is the maximum speed difference experienced by the satellites along the orbit and φ_0 is the initial phase of the Doppler frequency. φ_0 depends on the orbital position of the satellites when the frequency acquisition process is triggered. Taking into account Eq. 4.4, the frequency of the free-running laser, when performing the frequency acquisition, is

$$\begin{aligned} f_{las}(t) &= f^i_{las} + \delta f(t) + f_{tune}(t) \\ &= f^i_{las} + \delta f(t) + f_j(t) - f_D(t) + \epsilon(t) \end{aligned} \qquad \text{where} \quad j = \text{ramp}\,,\,\text{step} \tag{4.5}$$

where f^i_{las} is the frequency of the free-running laser when the signal acquisition process is triggered while $f_j(t)$ is the frequency variation at the instant t given by the frequency scan algorithm adopted and $\epsilon(t)$ the frequency tuning error.

4.3 Spatial acquisition

The alignment requirement of the two laser beams defines a sensitive surface around the axis of symmetry of each laser beam which is labelled as *scanning cone*. If the line of sight falls

can be considered constant.

within the scanning cones of the beams and these are aligned with an offset smaller or equal to the radius of the scanning cone, the signal can be acquired. By repointing the laser beam with the steering mirror, the scanning cones are also moved in the spatial uncertainty domain.

The repointing patterns discussed herein are distinguished in *continuous patterns* and *random patterns*. With the continuous patterns, the scanning cone is repointed following a curve while the random pattern repoints the scanning cone following a sequence of points each of which has a likelihood of occurring defined by a probability density function. The timing relation between the patterns used to repoint the two laser beams defines the acquisition *guidance scheme*.

4.3.1 Continuous patterns

With a continuous pattern, both satellites scan the uncertainty area following a well defined curve. The curves have to guarantee that each satellite covers two degrees of freedom without leaving gaps. Since there is no information exchange between the satellites, the instruments have no chance of knowing if the laser beams are aligned when the frequency requirement is not fulfilled. For such a reason, the curves have to be repeatable since, in all probability, the spatial domain needs to be scanned more than once before the signal is effectively acquired. The maximum distance between two consecutive points of the curve cannot be bigger than twice the maximum offset allowable between the laser beams otherwise area gaps are introduced in the four-dimensional search strategy.

The curves can be implemented on-board as a continuous time functions or as a sequence of points. In the first case, the laser beams moves along the profile of the curve[2] while in the latter case the laser beam jumps between two consecutive points of the curve. Because the step between two consecutive points can be, at maximum, twice the radius of the scanning cone, the overshoot/undershoot of the steering mirror between consecutive steps is here neglected. Nevertheless, in the presence of a beam widener this hypothesis might not be valid.

The laser beam can be in principle repointed compatibly with the maximum repointing performance of the steering mirror. This would guarantee that any curve is executed in the minimum amount of time. The scan patterns though have to guarantee not only that at some point in time the two beams are overlapped but that this condition is also predictable. For such a reason, the ratio between the periods of the two curves cannot be chosen arbitrarily.

If the pointing coordinates of the curves are expressed in polar coordinates and the origin of the coordinate system is chosen coincident with the center of one of the two uncertainty cones (in the following formulation the origin is coincident with the center of the uncertainty cone of the slave satellite), the guidance scheme has to fulfill the relation

$$\begin{cases} |\rho_s(t) - \rho_m^*(t)| \leq \delta \\ |\theta_s(t) - \theta_m^*(t)| \leq \gamma \end{cases} \tag{4.6}$$

where δ is the radius of the scanning cone and γ the corresponding angular constraint. ρ_j and θ_j (with $j = m\,,\, s$) are the pointing coordinates of the two curves expressed in polar coordinates. The pointing of the master satellite can be split in the constant contribution of the initial offset plus a time varying contribution related to the curve followed by the laser beam. In particular, $\rho_m^*(t) = \rho_i - \rho_m(t)$ and $\theta_m^*(t) = \theta_i - \theta_m(t)$. From the definition of the origin of the polar coordinate frame, $\rho_i = \rho_m^i + \rho_s^i$ and $\theta_i = \theta_m^i + \theta_s^i$. The initial pointing offsets belong to the intervals $\rho_i \,\epsilon\, [0\,,\, 2\rho_{unc}]$ while $\theta_i \,\epsilon\, [0\,,\, 2\pi]$. Substituting $\rho_m^*(t)$ and $\theta_m^*(t)$ in Eq. 4.6 yields

$$\begin{cases} |\rho_s(t) + \rho_m(t) - \rho_i| \leq \delta \\ |\theta_s(t) + \theta_m(t) - \theta_i| \leq \gamma \end{cases} \tag{4.7}$$

[2]In reality the curve moves following discrete steps whose steepness depends on the sampling frequency of the instrument's electronics.

Suppose the existence of a time t^* such that the first inequality of Eq.4.7 is satisfied. The angular component at t^* can be generally expressed as $\theta_j(t^*) = 2q_j^*\pi$ (with $q_j \epsilon [0\,,\,1]$ and $j = m\,,\,s$). The second inequality of Eq. 4.7 can be rewritten as

$$|2\pi q_s^* + 2\pi q_m^* - \theta_i| \leq \gamma \tag{4.8}$$

Introducing the factor $M = q_s^*/q_m^*$, yields

$$|2\pi q_m^*(1+M) - \theta_i| \leq \gamma \tag{4.9}$$

Equation 4.9 shows that the scaling factor M cannot be chosen arbitrarily but requires a prior knowledge of θ_i (in the most general case, $M = f(\rho_i, \theta_i)$). Therefore, the execution time of the guidance scheme cannot be minimized without the a priori knowledge of the initial pointing offsets. If M is irrational, the two curves form a non recursive pattern and cover all possible initial offsets. Although, the time required to cover the four degrees of freedom becomes infinite.

The initial conditions can be neglected from the spatial acquisition problem if the transition time between two consecutive points of one of the two curves is equal to the time required by the other curve to complete its bi-dimensional pattern. If, for example, the curve followed by the laser beam of the master satellite is set to be the slowest, in the interval $[t\,,\,t+t_{scan}]$ (where t_{scan} is the time required by the faster curve to cover the uncertainty area), the terms θ_m and ρ_m are constant. Since $\rho_i^{max} = 2\rho_{unc}$ and the curves are designed to cover the whole uncertainty cone ($\rho_m^{max} \geq \rho_{unc}$ and $\rho_s^{max} \geq \rho_{unc}$), in the complete four-dimensional scan there will be always at least one time interval t_1 where $\rho_m^*(t_1) \leq \rho_{unc}$. In order to cover the whole uncertainty domain without leaving gaps, in the time interval in which $\theta_s(t)$ swipes the angular range $[0\,,\,2\pi]$, the increase of the radial coordinate between two consecutive points of the curve is at maximum equal to 2δ. Since θ_m^* is, per definition, in the interval $[0\,,\,2\pi]$, for $t_2 \epsilon [t_1\,,\,t_1+t_{scan}]$ (since $\rho_m^*(t_1) \leq \rho_{unc}$), there is always at least one set of coordinates $\theta_s(t_2)$ and $\rho_s(t_2)$ which satisfy Eq.4.6. This reasoning can be expressed mathematically as

$$\begin{array}{c} \forall\, t \,\epsilon\, [0\,,\,t_{gs}]\;,\; \{\exists\, t_1 \,\epsilon\, [0\,,\,t_{gs}]\;:\; |\rho_i - \rho_m(t_1)| \leq \rho_{unc} \\ \Downarrow \\ \exists\, t_2 \epsilon\, [t_1\,,\,t_1+t_{scan}]\;:\; |\rho_s(t_2) - \rho_m(t_1)| \leq \delta \wedge \theta_s(t_2) - \theta_m(t_1) \leq \gamma\} \\ \Uparrow \\ \rho_m(t_1) - \rho_m(t_1+t_{scan}) = 0 \;\wedge\; \theta_m(t_1) - \theta_m(t_1+t_{scan}) = 0 \end{array} \tag{4.10}$$

where t_{gs} is the time required by the guidance scheme for covering the four degrees of freedom of the spatial domain. The time constraint introduced between two consecutive points of the slow scan pattern allows to divide the time interval $[0\,,\,t_{gs}]$ into N sub-intervals each of which lasts t_{scan}. Within each of these N intervals, the degrees of freedom of the spatial acquisition problem are only two since the pointing of one of the two laser beams is fixed. The geometry of the acquisition problem is also depicted in Fig. 4.2.

A second consequence of this simplification is that no extremely precise synchronization is required when triggering the spatial acquisition. In case of an initialization delay, the duration of the first scan reduces to $t_{scan} - t_d$ (where t_d is the time delay). With a certain degree of overlap between the uncertainty cones (as shown in the right panel of Fig. 4.2), if one solution is missed because of the delay (one laser beam moves just before the other one is approaching) the following solution is necessarily achieved because one of the two beams holds its pointing for t_{scan} and, in this time interval, the second beam covers the whole uncertainty cone. When the uncertainty cones are tangent, the existence of a solution depends on the initial conditions. Moreover, this reasoning is valid only for patterns which repeat themselves every t_{scan}. If this assumption is not true, then the existence of a solution in presence of a triggering delay cannot be guaranteed.

Independently from the curve used to cover the uncertainty area, since this is a discrete

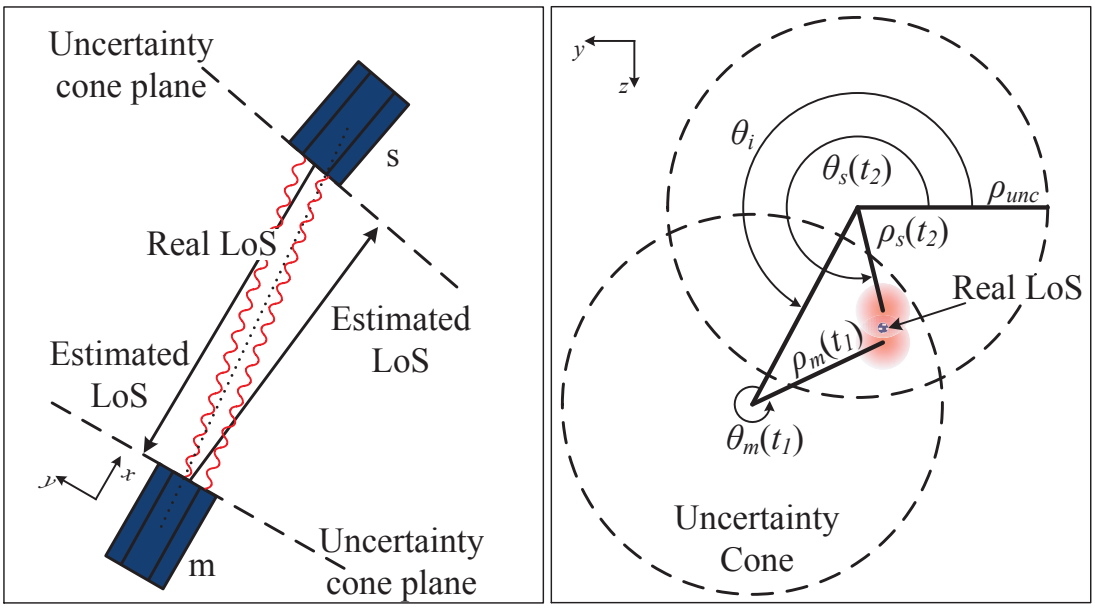

Figure 4.2: Representation of the spatial acquisition. During the time interval required by the faster curve to cover the uncertainty domain, the other laser beam "waits" wherever it is pointed. If the fast curve is properly designed (no gaps left within ρ_{unc}) and the other is pointing within the uncertainty cone of the twin satellite, there will be always at least one solution.

pattern, the distance between two points requires a certain degree of overlap between the cones of the laser beams. Moreover, in presence of pointing noise there is a high likelihood of introducing holes in the guidance scheme if no overlap between the scanning cones is foreseen. The left panel of Fig. 4.3 depicts the coverage of the uncertainty cone when using 2δ as distance between consecutive points while the right panel depicts the same coverage when consecutive and adjacent cones are superimposed by a factor K. Regardless of the resolution of the curve (which depends on the sampling frequency of the electronics of the instrument), the full coverage of the uncertainty cone is always guaranteed if the x coordinate of p_1 (Fig. 4.3) is smaller or equal to the x coordinate of p_2. By simple geometrical considerations, the coordinate $x_{p_1} = K\delta$ while the coordinate $x_{p_2} = \delta\sqrt{1-K^2}$. Since $x_{p_1} \leq x_{p_2}$ the superimposition factor is equal to $K \leq 1/\sqrt{2}$.

In order to guarantee that the signal is acquired, each point within the four-dimensional search space has to be covered for a certain amount of time. For the slowest pattern, this dwell time has to be equal to the time required by the faster pattern to cover the uncertainty area. For the faster patter, the dwell time depends on different factors (see paragraph 4.4). The shortest distance covered by the laser beam when following the example pattern of Fig. 4.3 is given by the chord $\overline{p_3 p_2}$ whose length is equal to $l = 2\delta\sqrt{1-K^2}$. Guaranteeing that the shortest distance of the patter is covered for the dwell time is one of the design parameters of all the curves studied.

If $2K\delta > \rho_{unc}$ the uncertainty cone can be scanned according to a circular curve whose radius is qual to $K\delta$ and whose angular velocity guarantees that the arc length $2K\delta$ is covered for the minimum dwell time

$$\omega = \frac{4\pi \sin^{-1}\left(\dfrac{K\delta}{\rho_{unc}}\right)}{t_{dwell}} \tag{4.11}$$

When $2K\delta < \rho_{unc}$ than the profile of the curve is not as simple as a circle. In this latter case, the cartesian coordinates of the curves which have been analyzed as possible candidates

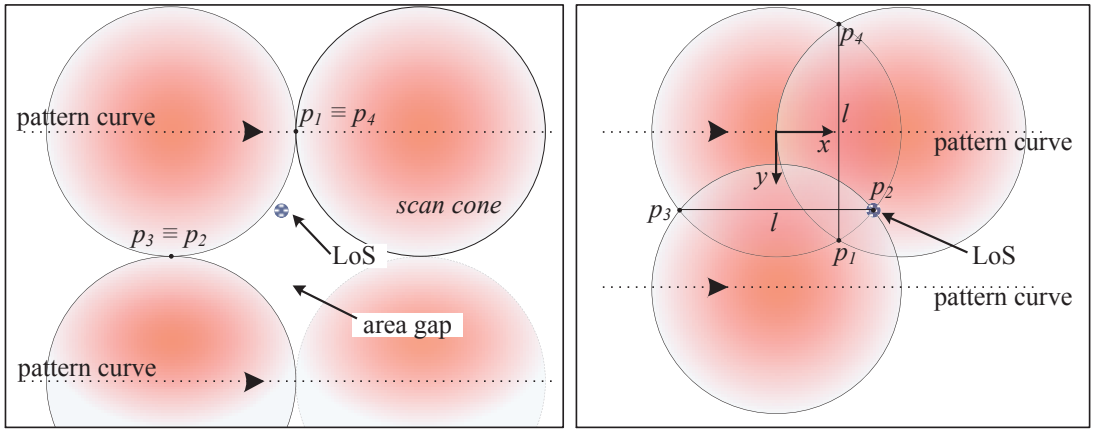

Figure 4.3: The panels show the area covered by the guidance scheme when the overlap factor is neglected (left) and when it is considered (right). Due to the pattern discretization, neglecting the overlap introduces holes in the area covered by the guidance scheme. The case depicted in the right panel is an extreme case. In reality, the gaps are not so emphasized since the curve is followed by the laser beam in a quasi-continuous motion. Because of the finite resolution of the curve though, unless the points which draw the pattern are pre-defined, it is not possible to exclude the presence of gaps if $1/\sqrt{2} < K \leq 1$.

for solving the spatial acquisition problem are all derivable from Eq. 4.12 by properly tuning of the equation parameters.

$$\begin{aligned} x(t) &= \mathcal{A}(t)\cos(\kappa\omega_1 t^n)\sin(\omega_1 t^n + \zeta) \\ y(t) &= \mathcal{B}(t)\cos(\kappa\omega_2 t^n)\sin(\omega_2 t^n + \varphi) \end{aligned} \tag{4.12}$$

where $\mathcal{A}(t) = a + c\,t^m$ and $\mathcal{B}(t) = b + d\,t^m$ (one should notice that also the circular pattern can be obtained from this equation). When implementing the guidance scheme it is not necessary that both satellites scan the uncertainty area following the same curve profile. Any combination of curves is possible as long as Eq. 4.10 is fulfilled. The patterns analyzed do not include raster curves [113, 114] since these cannot be implemented using a single set of equations. Together with the patterns described hereafter, also other curves (especially roulette curves [115]) have been considered as possible candidates for performing the spatial acquisition. Nevertheless, since these curves do not introduce any improvement to the acquisition process with respect to the ones discussed hereafter, these have not been included.

Lissajous pattern

In mathematics, a *Lissajous* curve [116] is the result of a system of parametric equations describing a complex harmonic motion. The equations of this curve can be derived substituting the terms of Tab. 4.1 in Eq. 4.12. This pattern is highly sensitive to the relative ratio of the angular velocities $\omega_r = \omega_a/\omega_b$. If ω_r is equal to a natural number, the pattern repeats itself after one round. If ω_r is a rational number, the pattern repeats itself after a finite number of rounds while if it is an irrational number, the pattern covers the whole delimiting space as the number of rounds increases.

The angular velocity ω_b is evaluated imposing that the distance of the two peaks of the curve close to the fast axis is equal to $2K\delta$ (see Fig. 4.4). Since the curve has to repeat itself after one round, the relative ratio of the angular velocities has to be a natural number which

Lissajous curve										
a	b	c	d	ω_1	ω_2	k	ζ	φ	n	m
ρ_{unc}	ρ_{unc}	0	0	ω_a	ω_b	0	0	0 or $\frac{\pi}{2}$	1	0
General equation in cartesian coordinates										
$x(t) = \rho_{unc} \sin(\omega_b t)$										
$y(t) = \rho_{unc} \sin(\omega_a t + \varphi)$										

Table 4.1: Coefficients used for tuning Eq. 4.12 in order to obtain the Lissajous curve.

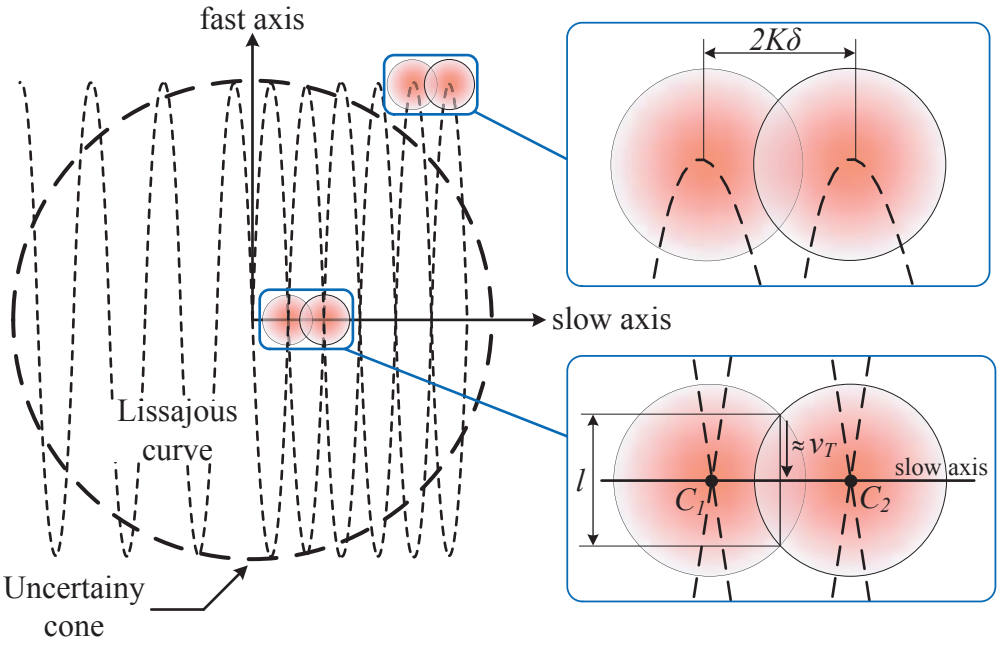

Figure 4.4: The picture shows the coverage of the uncertainty area using the Lissajous pattern. The fast axis identifies the coordinate which oscillates with the angular velocity ω_a. The orthogonal coordinate oscillates with angular velocity ω_b. The fast axis and the slow axis can be swapped without changing the properties of the curve.

satisfies the inequality (see appendix B.1)

$$\Theta = \cos\left(\frac{\pi}{\omega_r}\right) \sin\left(\frac{\pi}{2\omega_r}\right) \leq \frac{K\delta}{\rho_{unc}} \tag{4.13}$$

The trend of Θ as a function of ω_r is depicted in the left panel of Fig. 4.5. If ω_r is an even number, the pattern is shifted of $\pi/2$ after every quarter of its repetition period. In this case, the shape of the pattern is similar to the one displayed in Fig. 4.4 on the right hand side of the uncertainty cone. If the ratio between the angular velocities is an odd number, the track followed by the scanning cone during two consecutive quarters of the repetition period of the pattern is the same. In this case, the shape of the curve is equal to the one displayed in Fig. 4.4 on the left hand side of the uncertainty cone. The inequality of Eq. 4.13, in this case, can be satisfied if the term φ of Eq. 4.12 is equal to $\pi/2$.

The angular velocity ω_a has to be chosen such that each point of the uncertainty cone is covered for the expected dwell time. ω_a is calculated as the ratio between the distance of two consecutive scanning cones and the arc length of a complete oscillation of the fast

axis sinusoid. Labelling as $\vec{\mathbf{r}}(t) = [x(t)\, y(t)]^T$ the coordinate vector of the Lissajous curve, the corresponding arc length between two points of the curve can be calculated as $L = \int_a^b \sqrt{(\partial\vec{\mathbf{r}}(t)/\partial x)^2 + (\partial\vec{\mathbf{r}}(t)/\partial y)^2}$. By substituting the product $\omega_b t$ with the variable ξ, the angular velocity ω_a can be calculated as

$$\omega_a - \frac{4\pi K\delta}{\int_0^{\frac{2\pi}{\omega_r}} \sqrt{\rho_{unc}^2 \cos^2(\xi) + \frac{\rho_{unc}^2}{\sqrt{\omega_r}} \cos^2\left(\frac{\xi}{\omega_r}\right)} \mathrm{d}\xi} f_{dwell} = 0 \tag{4.14}$$

where $f_{dwell} = 1/t_{dwell}$ and t_{dwell} the expected dwell time. This equation has no closed form solution and has to be solved numerically. If $\omega_r > 20$ though, the arc length of a complete oscillation of the fast coordinate is about four times the radius of the uncertainty cone. In this case, simulation results have shown that Eq. 4.14 can be approximated to

$$\omega_a \approx \frac{\pi K\delta}{1.4\rho_{unc}} f_{dwell} \tag{4.15}$$

The maximum tangential velocity of the pattern is reached when the fast sinusoidal motion crosses the slow axis (see Fig. 4.4). Since the distance l has to be covered in t_{dwell}, the maximum tangential velocity (and consequently ω_a) has an upper limit. The separation between the cone centers in this region ($\overline{C_1C_2}$ in Fig. 4.4) is derived by simple geometric considerations and is equal to $\rho_{unc}\pi/\omega_r$. From the separation between two consecutive scanning cones, it is possible to calculate the distance l which is equal to $2\sqrt{\delta^2 - \rho_{unc}^2\pi^2/4\omega_r^2}$. Considering the tangential velocity in this region parallel to $\vec{l}$ (the validity of this assumption is realistic when $\omega_r \gg 1$), its magnitude cannot exceed $v_T^{max} = l/t_{dwell}$. If this constraint is not fulfilled, then the magnitude of ω_a has to be reduced.

The Lissajous curve can be drawn commanding the laser beam pointing with two numerically controlled oscillators whose frequency ratio is equal to ω_r. This is an advantage for the repointing mechanisms which are controlled with a constant frequency. The non-optimal coverage of the uncertainty area though, significantly increases the time required by this curve in covering a bi-dimensional uncertainty area (for each fast oscillation the beam is swiped through the entire width of the uncertainty cone). According to the right panel of Fig. 4.5, the maximum coverage of the uncertainty cone is achieved at its extremes while the region of minimum coverage is located in the center. Since in most of the acquisition problems, the initial error is expected to be normally distributed, this curve spends less time in the region where the line of sight is most likely located.

Rhodonea pattern

The *rhodonea* curve [117] is a hypocycloid whose parametric components have the same amplitude. For its flower-like shape, this curve is also commonly labelled in literature as rose or rosette. The equation of this curve expressed in cartesian coordinates is obtained after substituting the terms of Tab. 4.2 in Eq. 4.12.

The shape of the curve is determined by the parameter Υ. For $\Upsilon \in \mathbb{N}^+$, the shape will appear similar to a flower with Υ petals if Υ is odd or with 2Υ petals if Υ is even. If Υ is expressed as the ratio between an integer and a prime number, the curve is a less common form and some petals stretch overlapping other petals. If Υ is expressed as the ratio between an integer and a non prime number the curve will appear as a series of interlocking loops while if Υ is an irrational number the curve will have infinitely many petals and will cover the whole confining space. Since the pattern has to be predictable and recursive, the curves analyzed have $\Upsilon \in \mathbb{N}^+$.

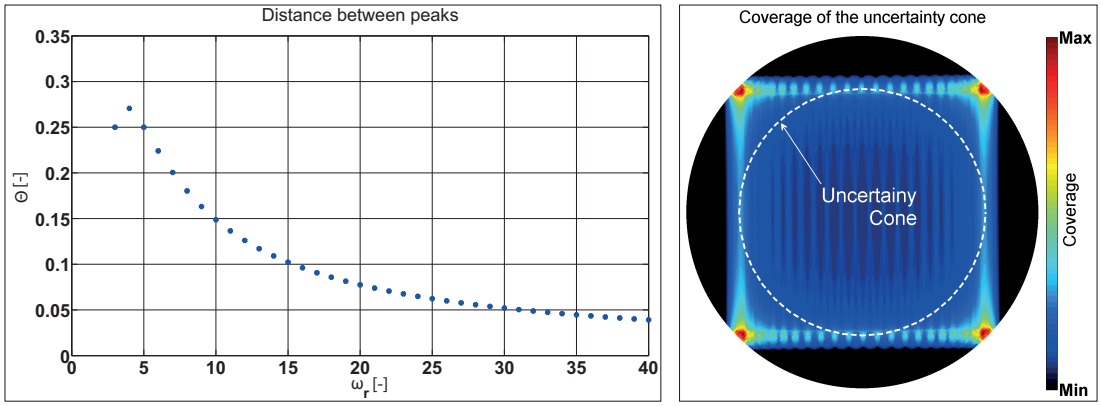

Figure 4.5: The left panel depicts the trend of Θ as a function of ω_r. The starting value of $\omega_r = 3$ since for lower values the uncertainty cone could be simply scanned using a circular motion. The right panel depicts for how much time each point of the uncertainty domain is covered by the scanning cone when it follows a Lissajous pattern ($\omega_r = 28$). The coverage shown here is not the dwell time of the scanning cone in one particular area of the uncertainty domain but it is the cumulative time of all the passages of the scanning cone over the same area during one scan.

Rhodonea curve										
a	b	c	d	ω_1	ω_2	k	ζ	φ	n	m
ρ_{unc}	ρ_{unc}	0	0	ω_{rho}	ω_{rho}	Υ	0	$\frac{\pi}{2}$	1	0
General equation in cartesian coordinates										
$x(t) = \rho_{unc} \cos(\Upsilon \omega_{rho} t) \sin(\omega_{rho} t)$										
$y(t) = \rho_{unc} \cos(\Upsilon \omega_{rho} t) \sin\left(\omega_{rho} t + \frac{\pi}{2}\right)$										

Table 4.2: Coefficients used for tuning Eq. 4.12 in order to obtain the rhodonea curve.

Using a flower like curve, the maximum separation between the scanning cones is achieved at the tip of the petals. In order to cover the full uncertainty cone, this distance ($\overline{C_1C_2}$ in the left panel of Fig. 4.6) has to satisfy the inequality (see appendix B.2)

$$\begin{aligned} \Theta &= \sqrt{1 - \cos\left(\frac{2\pi}{\Upsilon}\right)} \leq \frac{\sqrt{2} K \delta}{\rho_{unc}} \quad \text{if } \Upsilon \text{ is odd} \\ \Theta &= \sqrt{1 + \cos\left(\frac{\Upsilon + 1}{\Upsilon} \pi\right)} \leq \frac{\sqrt{2} K \delta}{\rho_{unc}} \quad \text{if } \Upsilon \text{ is even} \end{aligned} \tag{4.16}$$

The trend of Θ as a function of the shape parameter Υ is depicted in the lower panel of Fig. 4.6.

The repetition frequency of the pattern has to guarantee that each point of the uncertainty area is covered for the expected dwell time. Since the maximum distance between two consecutive pointing spots is $2K\delta$ and that the maximum tangential velocity is reached when the curve crosses the center of the uncertainty cone, from the analysis of the curve's equations in polar coordinates, yields

$$\omega_{rho} = \frac{2K\delta}{\Upsilon \rho_{unc}} f_{dwell} \tag{4.17}$$

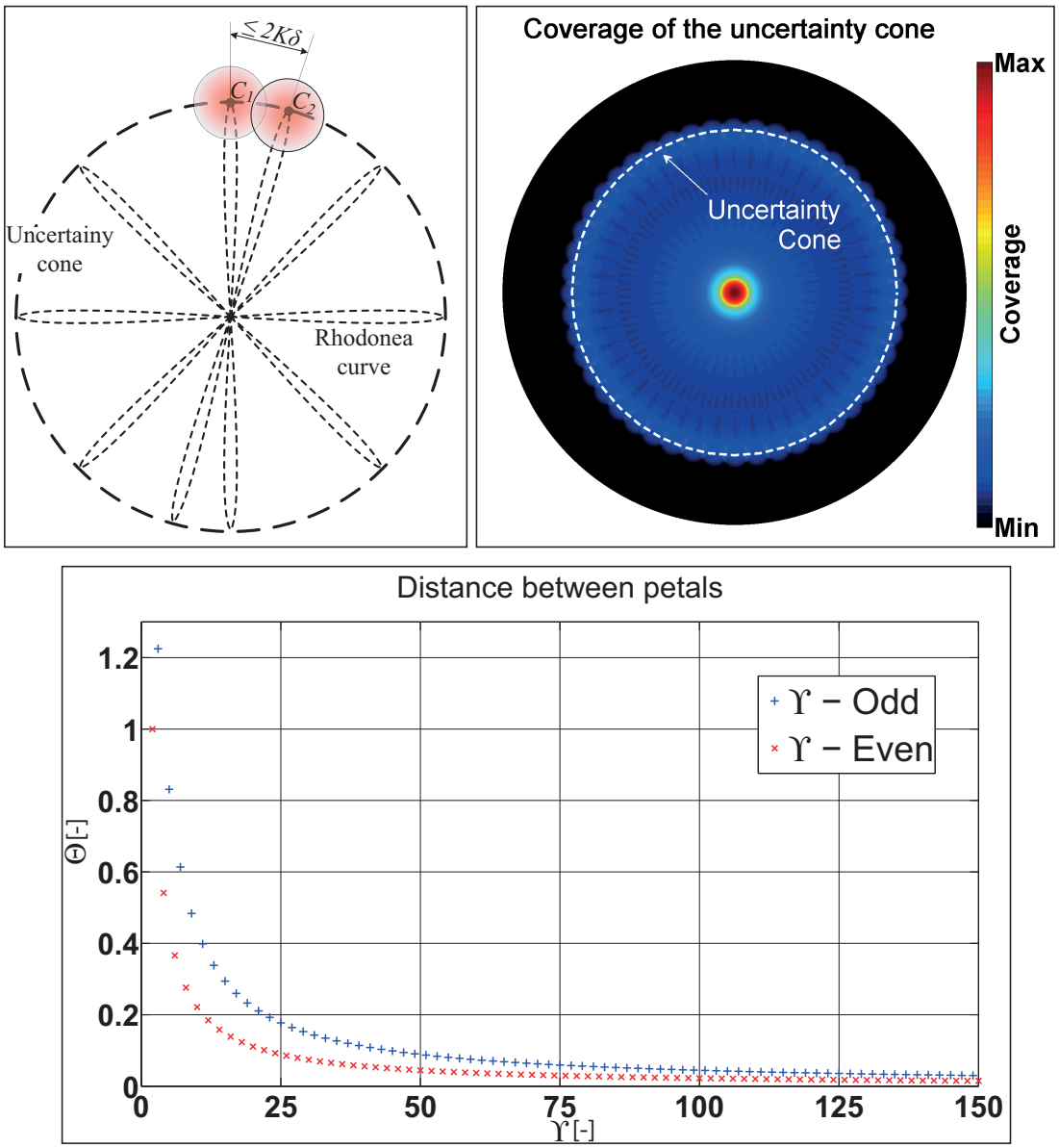

Figure 4.6: The left panel shows the trend of a rhodonea curve when covering the uncertainty area and the condition of maximum separation between the scanning cones. The right panel of this picture depicts the cumulative time distribution of the pointing within the uncertainty cone. The lower panel shows the separation between the petals as the parameter Υ increases. The plot considers odd and the even values of the shape parameter Υ.

As shown in the lower panel of Fig. 4.6, in order to satisfy the inequality of Eq. 4.16, the odd values of Υ are about twice the even values Υ. In the first case though, the pattern repeats itself after half period while in the latter case, every period. The total time required by the pattern to complete one round is therefore comparable for the two cases. In general, the minimum number of petals required to satisfy the inequality of Eq. 4.16 is smaller when Υ is odd.

Compared to the Lissajous pattern, the rhodonea curve is described by a more complex system of equations. The coverage of the uncertainty cone is nevertheless improved since the pattern has a high density coverage in the center of the uncertainty area and a quasi uniform

coverage in the rest of it (see the right panel of Fig. 4.6). Also in this case the beam swipes the whole width of the uncertainty cone when guided along the petals of the curve hence the total time required by this pattern in covering the uncertainty area is comparable to the one required by the Lissajous curve.

Spiral patterns

The spiral curve winds around a fixed center at a continuously increasing or decreasing distance from the starting point. The equation describing the spiral curve is not recursive. Since the distance from the center always increases (or decreases), it is necessary to stop the curve when the scanning cone reaches the boundary (or the center) of the uncertainty cone and repoint the laser beam towards the starting point of the guidance in order to repeat the pattern. In doing so, the repointing mechanism is subject to an abrupt stop which is immediately followed by repointing command whose amplitude is equal to ρ_{unc}. The discontinuity of the motion of the steering mirror (and its consequent mechanical stress) is avoided if this curve is not implemented with a single equation but the equation drawing the spiral switches form increasing (decreasing) radius to decreasing (increasing) radius once the boundary (center) of the uncertainty cone is reached (see paragraph 5.4.2). Since the transition between the two patterns should not introduce discontinuities in the motion of the repointing mechanism, it can take place only when the angular coordinate of the pattern is $\pi/2$ or $3\pi/2$ (or 0 and π according to the orientation of the pattern), or when its radial component is null. In these three points the two spirals trends are coincident and the motion of the steering mirror has a bumpless transition from increasing to decreasing radius spiral or viceversa.

In general, the parametric equation of a spiral can be expressed as

$$\rho_{sp} = p\,\theta_{sp}\,(t) \tag{4.18}$$

where ρ_{sp} and θ_{sp} are the radial and angular components of the curve in polar coordinates. The scanning cone following the spiral trend has to be always internally tangent to a circumference whose radius increases as $(2N_r + 1)\,K\delta$ where N_r are the number of complete windings of the spiral. After N_r rounds yields

$$\begin{cases} \rho_{sp} = \rho_{unc} - K\delta \\ \theta_{sp} = 2\pi N_r \\ \rho_{unc} = (2N_r + 1)\,K\delta \end{cases} \tag{4.19}$$

Combining Eq. 4.18 with Eq. 4.19, it is possible to find the parameter $p = K\delta/\pi$ which relates the increase of the radial component to the angular component. In order to map the entire uncertainty cone, the scanning cone has to follow the spiral pattern for $N_r + 1$ rounds.

The winding of the curve around its origin can be performed with a constant angular velocity ($\dot{\theta}_{sp} = \text{const}$) or with a constant tangential velocity ($\rho_{sp}\dot{\theta}_{sp} = \text{const}$). In the first case, the cartesian coordinates of the spiral are obtained after substituting the terms of Tab. 4.3 in Eq. 4.12. With a constant angular velocity spiral, the time coverage of the uncertainty cone decreases while the scanning cone moves towards its outer boundary. The angular velocity of the curve is chosen such that the expected dwell time is guaranteed for $v_T = v_T^{max}$ which is reached when $\omega_{sp} t_{tot} = 2\pi N_r$. From the terms listed in Tab. 4.3 yields

$$\begin{aligned} & v_T^{max} = 4\pi K\delta f_{sp}^2 t_{sp} \\ & N_r = \left\lfloor \frac{1}{2}\left(\frac{\rho_{unc}}{K\delta} - 1\right)\right\rfloor + \begin{array}{l} 0.25 \text{ if curve equations change at } \pi/2 \\ 0.75 \text{ if curve equations change at } 3\pi/2 \\ 1.25 \text{ if curve equations change at } \pi/2 \end{array} \\ & v_T^{max} t_{dwell} = 2K\delta \end{aligned} \tag{4.20}$$

Constant angular velocity spiral										
a	b	c	d	ω_1	ω_2	k	ζ	φ	n	m
0	0	$2K\delta f_{sp}$	$2K\delta f_{sp}$	$2\pi f_{sp}$	$2\pi f_{sp}$	0	0	$\frac{\pi}{2}$	1	1

General equation in cartesian coordinates	
Increasing radius	Decreasing radius
$x(t) = 2K\delta f_{sp} t \sin\left(2\pi f_{sp} t + \frac{\pi}{2}\right)$	$x(t) = 2K\delta f_{sp}\Delta t \sin\left(-2\pi f_{sp}\Delta t + \frac{\pi}{2}\right)$
$y(t) = 2K\delta f_{sp} t \sin(2\pi f_{sp} t)$	$y(t) = 2K\delta f_{sp}\Delta t \sin(-2\pi f_{sp}\Delta t)$

Table 4.3: Coefficients used for tuning Eq.4.12 in order to obtain the constant angular velocity spiral. The term $\Delta t = t_{sp} - t$ where t_{sp} is the time required by the spiral curve to cover the uncertainty cone.

where t_{sp} is the total time required by the spiral pattern to cover the uncertainty area. The number of rounds are increased of 0.25 if $\theta_{sp}(t_{sp}) \epsilon [0\,,\, \pi/2]$, of 0.75 if $\theta_{sp}(t_{sp}) \epsilon (\pi/2\,,\, 3\pi/2]$ and of 1.25 if $\theta_{sp}(t_{sp}) \epsilon (3\pi/2\,,\, 2\pi)$. Combining the parameters of Eq. 4.20, it is possible to derive the angular frequency of the spiral

$$f_{sp} = \frac{1}{2\pi (N_r + 1) t_{dwell}} \tag{4.21}$$

When the scanning cone follows a constant angular velocity spiral, the spatial coverage of the uncertainty cone is optimized since the highest coverage is located in its center where it is most likely to find the twin satellite (see the left panel of Fig. 4.7). Also in this case though, the curve is non time optimal since the scanning cone spends in every point within the uncertainty cone more time than the one actually needed.

When the tangential velocity of the spiral is kept constant, the whole uncertainty area is uniformly covered. Integrating equation $\rho_{sp}\dot{\theta}_{sp} = v_T = \text{const}$ with respect to time, yields

$$\theta_{sp} = \sqrt{\frac{2\pi v_T t}{K\delta}} \tag{4.22}$$

Combining Eq. 4.18, Eq. 4.19 and Eq. 4.22, it is possible to derive the coefficients of Eq. 4.12 (see Tab. 4.4).

The tangential velocity of the spiral is determined combining Eq. 4.19 with Eq. 4.22. Yields,

$$v_T = \frac{2\pi K\delta (N_r + 1)^2}{t_{sp}} \tag{4.23}$$

The number of rounds are also here evaluated as in Eq. 4.20. The total time required to cover the uncertainty cone is evaluated as the ratio between the area of the uncertainty cone and the area of the scanning cone times the dwell time. Since the number of rounds is increased in order to allow the bumpless transition of the motion, it is not possible to use the real radius of the uncertainty cone (ρ_{unc}) but the radius of the effective area covered with the N_r rounds (see Eq. 4.20)

$$\rho_{cov} = (2N_r + 1) K\delta \quad \longrightarrow \quad t_{sp} = \frac{\rho_{cov}^2}{(K\delta)^2} t_{dwell} \tag{4.24}$$

where ρ_{cov} is the radius of the area effectively covered by the pattern.

The time required by this curve in covering the spatial degrees of freedom of the acquisition problem is optimized with respect to the dwell time hence the repetition time of this pattern is always the lowest when compared to the repetition time of all the patterns considered so far. Towards the center of the uncertainty cone though, the angular velocity of the curve increases

Constant tangential velocity spiral					
a	b	c	d	ω_1	
0	0	$\sqrt{\frac{2K\delta v_T}{\pi}}$	$\sqrt{\frac{2K\delta v_T}{\pi}}$	$\sqrt{\frac{2\pi v_T}{K\delta}}$	
ω_2	k	ζ	φ	n	m
$\sqrt{\frac{2\pi v_T}{K\delta}}$	0	$\frac{\pi}{2}$	0	$\frac{1}{2}$	$\frac{1}{2}$

General equation in cartesian coordinates	
Increasing radius	Decreasing radius
$x(t) = \sqrt{\frac{2K\delta v_T}{\pi}} t \sin\left(\sqrt{\frac{2\pi v_T}{K\delta}} t + \frac{\pi}{2}\right)$	$x(t) = \sqrt{\frac{2K\delta v_T}{\pi}} t \sin\left(-\sqrt{\frac{2\pi v_T}{K\delta}} \Delta t + \frac{\pi}{2}\right)$
$y(t) = \sqrt{\frac{2K\delta v_T}{\pi}} t \sin\left(\sqrt{\frac{2\pi v_T}{K\delta}} t\right)$	$y(t) = \sqrt{\frac{2K\delta v_T}{\pi}} t \sin\left(-\sqrt{\frac{2\pi v_T}{K\delta}} \Delta t\right)$

Table 4.4: Coefficients used for tuning Eq.4.12 in order to obtain the constant angular velocity spiral. Also in this case, the term $\Delta t = t_{sp} - t$.

asymptotically and this spiral does not guarantee the wished coverage (see the right panel of Fig. 4.7). This singularity can be overcome by keeping the steering mirror in its idle position for t_{dwell} whenever the magnitude of ρ_{unc} is zero.

When the dwell time is too small, the trend of this spiral curve is severely distorted because the controller of the steering mirror is not capable of following the pattern profile especially when approaching the center of the curve (with a controller's bandwidth of 1 kHz the distortion occurs when the dwell time is lower than 2 ms - see paragraph 5.4.2). For this reason, even though the constant tangential velocity spiral is the pattern that minimizes the time required for covering the uncertainty area, it cannot be implemented if the dwell time is below a certain threshold.

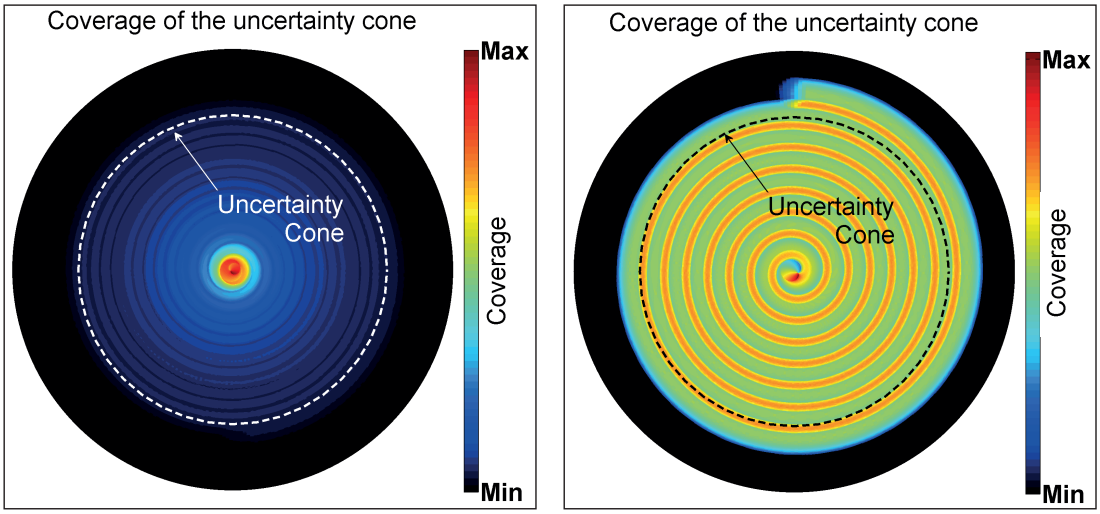

Figure 4.7: The cumulative dwell time of constant angular velocity spiral (left panel) and of a constant tangential velocity spiral (right panel) are here depicted.

As an alternative to the two spiral curves described, an hybrid spiral pattern which combines three different curve trends is also studied. This curve initially covers the uncertainty area with a constant tangential acceleration, followed by an in between phase in which the tangential acceleration is linearly reduced to zero. Afterwards, the uncertainty area is covered with a constant tangential velocity (see top panels of Fig. 4.8). The curve is designed using the angular acceleration of a constant angular velocity spiral and imposing that before starting the deceleration phase, the tangential velocity of the curve is half of the maximum one. Imposing that the maximum tangential velocity is the one of a constant tangential velocity spiral (Eq. 4.23), yields

$$\begin{gathered} \alpha_{sp}^{T_{max}} = 4\pi K \delta f_{sp}^2 \\ v_T\left(t_{ac}\right) = \frac{v_T^{max}}{2} \;\longrightarrow\; t_{ac} = \frac{\left(N_r+1\right)^2}{4 f_{sp}^2 t_{tot}} \end{gathered} \tag{4.25}$$

where $\alpha_{sp}^{T_{max}}$ and f_{sp} are respectively the tangential acceleration and the angular frequency of a constant angular velocity spiral, N_r is the number of rounds and t_{sp} is the time required to cover the uncertainty cone using a constant tangential velocity spiral. The frequency f_{sp} can be chosen either according to Eq. 4.21 or using the maximum repointing frequency of the steering mirror. One should notice that in the first case N_r is not the total number of rounds but the number of rounds performed in the time interval $[0\,,\,t_{ac}]$. The time t_{sp} can be instead calculated as in Eq. 4.24 because the total number of points drawing the curve is coincident with the one of a constant tangential velocity spiral.

During the decelerating phase, the tangential acceleration is expressed as $\alpha_{sp}^{T} = \alpha_{sp}^{T_{max}} - \beta t$. Since the tangential acceleration has to be null for $t = t^*$, the decelerating velocity β has to be equal to $\alpha_{sp}^{T_{max}}/t^*$. Combining Eq. 4.23 with Eq. 4.24 returns

$$t^* = \frac{\left(N_r+1\right)^2}{2 f_{sp}^2 t_{tot}} \;\;;\;\; \beta = \frac{8\pi K \delta f_{sp}^4 T_i}{\left(N_r+1\right)^2} \tag{4.26}$$

The constant tangential velocity spiral has very few dwell spots in the center of the uncertainty area because of the high angular velocity while the hybrid spiral has a better coverage of this region of the uncertainty cone. Nevertheless, since the total number of dwell spots in t_{sp} has to be the same for both curves, the points of the hybrid spiral become sparse when approaching t^*. Therefore it is necessary to increase the time t_{sp} by a factor $C > 1$. The magnitude of C depends on the dwell time and is derived empirically (see Tab. 4.5). Compared to the constant tangential velocity spiral, the total time required to cover the uncertainty area is now increased by the factor C but the distribution of dwell spots is significantly improved and the asymptotic behaviour of the angular velocity removed (see the lower panel of Fig. 4.8).

If the dwell time is too small, once more the trend of the curve is distorted because of the limited bandwidth of the feedback controller of the steering mirror. But, since the asymptotic behaviour of the angular velocity is removed, by replacing the feedback controller with a reference feedforward controller it is possible to remove the pattern distortion (see paragraph 3.4.1).

dwell time	0.35 ms	0.45 ms	0.5 ms	0.7 ms	1 ms	2 ms
C	1.35	1.29	1.17	1.14	1.12	1.11

Table 4.5: Factor used to increase the time t_{tot} when using the hybrid spiral. The coefficient C related to a dwell time bigger than 0.09 ms not listed in this table can be estimated using a quadratic interpolation curve.

Because the spiral profiles are generated using two different curves (increasing and decreasing radius), the full coverage of the uncertainty area introduced constraining the time relation

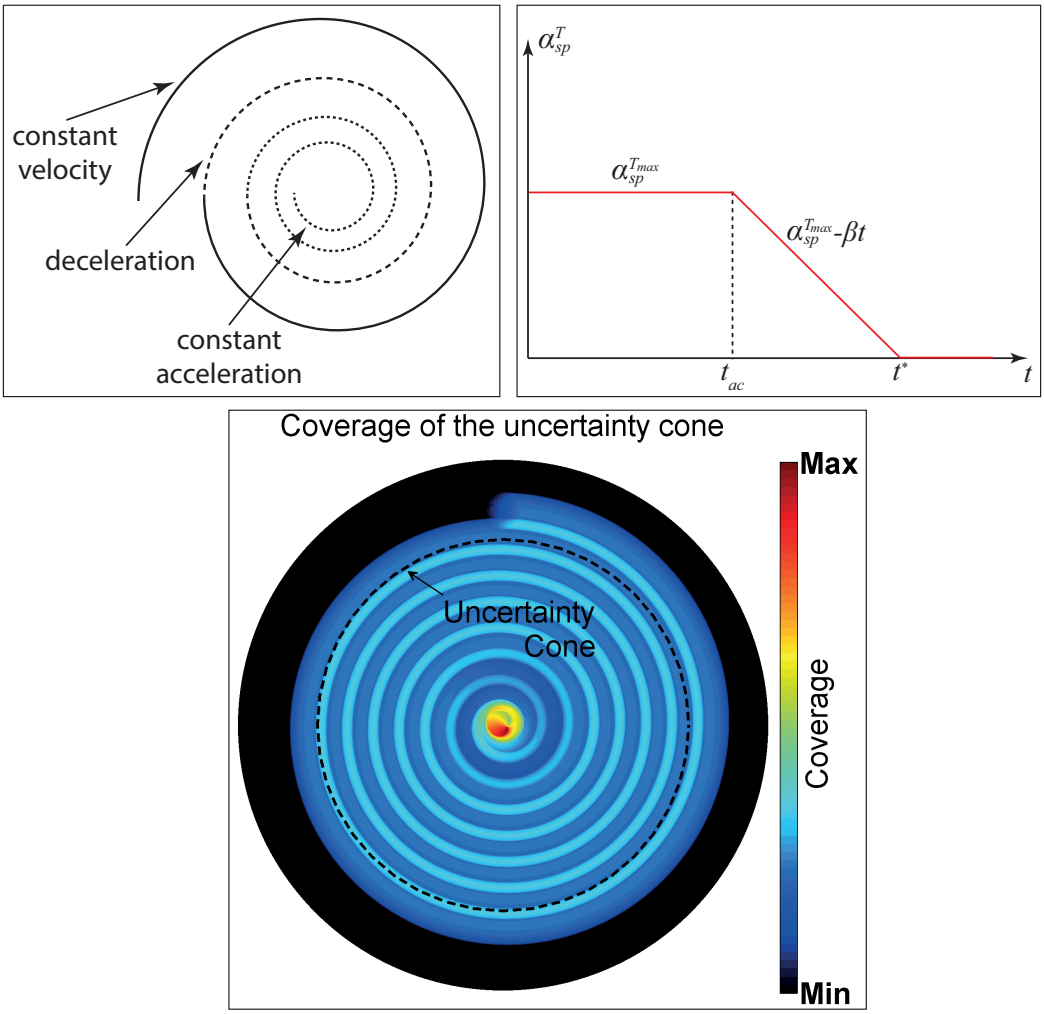

Figure 4.8: The upper left panel of this figure depicts the three different trends of the hybrid spiral while the upper right panel depicts the profile of the tangential acceleration over time. The lower panel shows the cumulative time of the pattern coverage within the uncertainty cone.

between the curves of the guidance scheme (Eq. 4.10) cannot be satisfied if the guidance scheme is not quasi-synchronized. Thanks to the trend of the spiral curve (most of the time is spent at the center of the uncertainty area) a synchronization offset below $2t_{dwell}$ would still guarantee an acceptable coverage of the uncertainty area while a bigger arbitrary time delay introduces non-negligible area gaps within the uncertainty domain.

This last problem can be solved by either considering the increasing-decreasing radius trend as a single curve (in this case though the execution time of the pattern is doubled) or by using an increasing/decreasing radius spiral which is re-connected to its origin by a link curve. In this latter case the link curve should not introduce a discontinuity in the first and second derivative of the trend of the pattern otherwise there is no bumpless transition between the two curves (the mirror oscillates[3] - see appendix B.3).

[3]Uncontrolled oscillations of the mirror increase the chance of a single sided detection. Indeed this uncontrolled motion could align one laser beam to the line of sight for a time not sufficient for both satellites to acquire the signal.

Comparison of the patterns

The difference between the various continuous patterns is mainly the time they require for covering the uncertainty cone. In Fig. 4.9, the execution time of the patterns described is evaluated as a function of the dwell time. The execution time of the constat tangential velocity spiral is evaluated only for $t_{dwell} > 2\,\text{ms}$ since for smaller values the curve exploits an unacceptable distortion with the available steering mirrors. The execution time of the other patterns is limited by the maximum repointing frequency of the steering mirror which is set to 100 Hz. The spiral patterns are much more sensitive to the limited bandwidth of a feedback

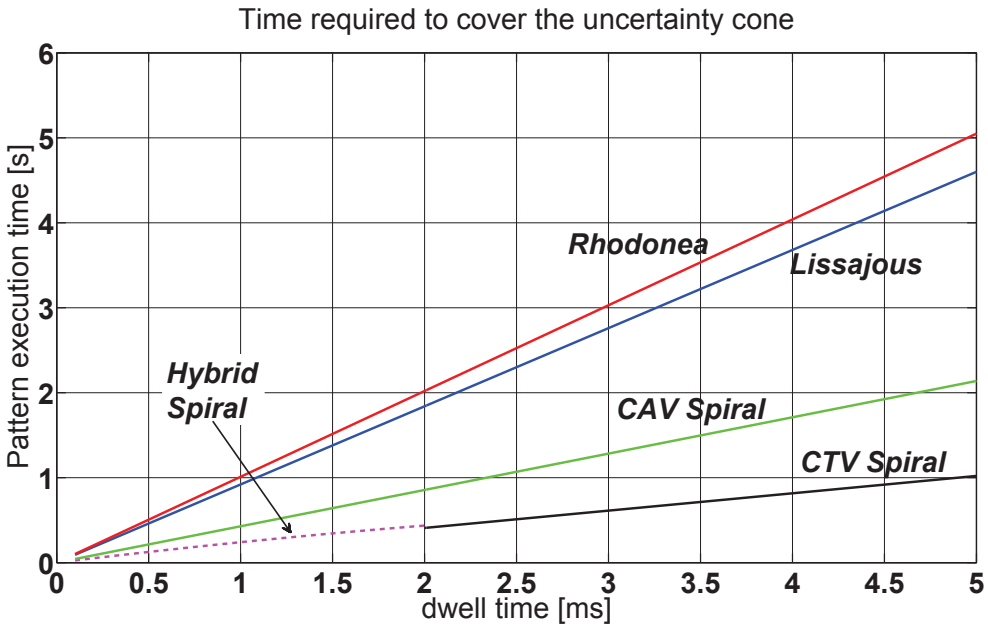

Figure 4.9: The time required to cover the uncertainty area using the patterns described as a function of the dwell time. The curves are determined using $\rho_{unc} = 1.4\,\text{mrad}$, $\delta = 140\,\mu\text{rad}$ and $K = 1/\sqrt{2}$. CAV and CTV are the acronyms of constant angular velocity and constant tangential velocity respectively. For $t_{dwell} < 1\,\text{ms}$, the CAV curve can be implemented only using a reference feedforward controller for commanding the pointing of the steering mirror.

controller when these are compared to the Lissajous and the rhodonea because even a small command error close to the center of the curve causes an unacceptable distortion. When the pattern is drawn with a high repetition frequency, this condition applies also to the Lissajous (or rhodonea) although in this case the error is less evident and can be neglected by increasing the overlap between two consecutive scanning cones (see paragraph 5.4.2).

4.3.2 Random patterns

With a random guidance scheme, the uncertainty cone is not covered according to continuous curves but following random pointing directions. The pointing directions can be generated according to a normally distributed Probability Density Function (PDF) or according to a uniform distributed PDF. The choice of the PDF depends on whether the line of sight is (most likely) located close to the center of the uncertainty cone or not. When using continuous curves, the spatial acquisition can be interfaced to the frequency acquisition problem via the repeatability of the pattern over time (see paragraph 4.5). When using a random pattern, these two problems are interfaced using the probability P of solving the four degrees of freedom of the spatial acquisition problem. In the continuation of this subparagraph, bold letters are used to denote random variables and not vectors.

Gaussian pattern

The pointing sequence of the laser beam of each satellite within the uncertainty cone is distributed in time according to a Gaussian PDF with null mean and unitary standard deviation ($\sigma = 1$).

$$f(i) = \frac{1}{\sqrt{2\pi}} e^{-\frac{i^2}{2}} \quad \text{with} \quad i = x\,,\, y \tag{4.27}$$

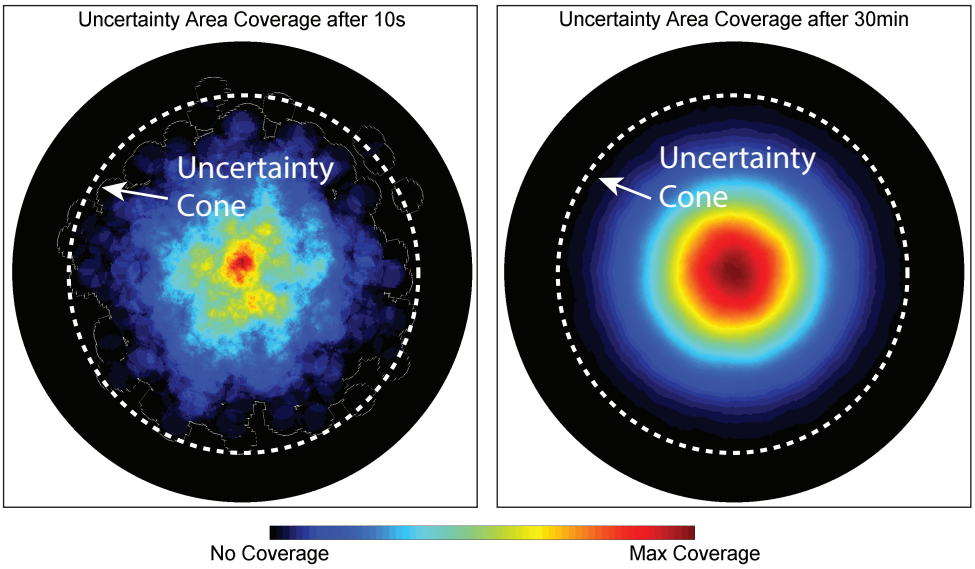

Figure 4.10: This picture depicts the coverage of the uncertainty cone as the execution time of the pattern increases (after 10 s in the left panel and after 30 min in the right panel).

Using this guidance scheme, the probability P of having the scanning cones overlapped to the line of sight is evaluated using the random variables theory (see appendix B.4) and is equal to

$$\mathrm{P}\{\mathbf{z} \leq \delta\,,\, \mathbf{v} \leq \delta, t\} = \left\{1 - \mathrm{Q}_1\left[\frac{\mu_z(t)}{\sigma_z}, \frac{\delta}{\sigma_z}\right]\right\}\left\{1 - \mathrm{Q}_1\left[\frac{\mu_v(t)}{\sigma_v}, \frac{\delta}{\sigma_v}\right]\right\} \tag{4.28}$$

which is a function of time and of the initial conditions. The term Q_1 is the Marcum Q-function of first order.

The left panel of Fig. 4.11 shows the overlap probability as a function of the initial pointing offsets (μ_z and μ_v) when the time dependant disturbances are set to zero. Larger initial pointing offsets result in a lower probability of overlapping the two laser beams. The right panel of Fig. 4.11 depicts the overlap probability as a function of time and as a function of the amplitude (ς) of the time dependant disturbances when the initial pointing offsets μ_z and μ_v are set to zero. The time dependant disturbances are modelled as sinusoidal oscillations of the estimated direction of the LoS. Combining the initial pointing offsets with the time dependant disturbances reduces the probability of detecting the signal since these linearly sum together. When the time dependant disturbances are different for the two satellites (i.e. thermal effects may affect the two satellites differently because one flies backwards with respect to the other) the peaks of maximum overlap probability are scaled in amplitude and shifted along the time axis. A similar trend over time is illustrated in the paper of *Arnon* and *Gill* which analyses the outage probability of an optical communication link [118]. A probabilistic approach to the study of signal acquisition is also performed by *Li et al* [119]. In their paper, the probability of acquiring the signal is coincident with the probability of finding the line of sight within the

uncertainty cone (which is equal to one when the radius of the generic scan pattern is equal to ρ_{unc}).

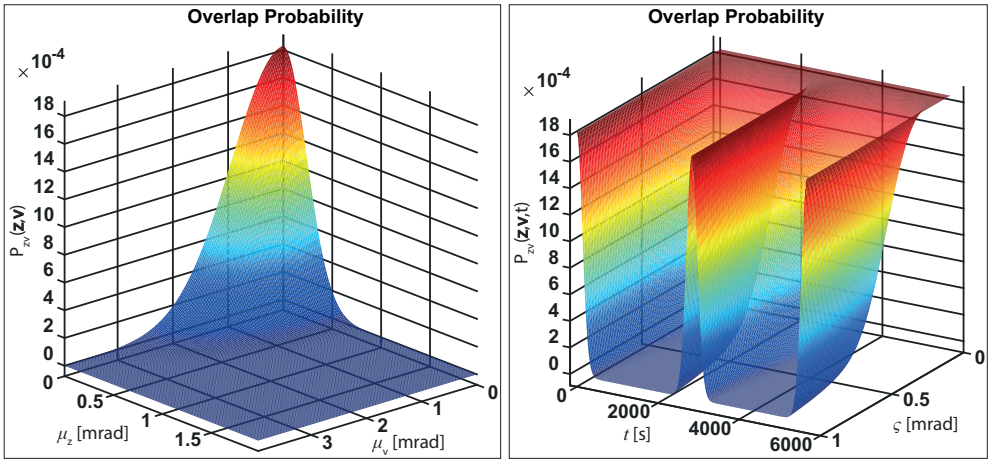

Figure 4.11: This figure shows the overlap probability as a function of the initial pointing offsets (left panel) and of the time dependant disturbances (right panel). The bigger the offset, the smaller the probability of acquiring the signal. Since the time dependent disturbances are modelled as sinusoids with orbital frequency, the probability of overlapping the laser beams has a periodicity of half of the orbital period.

Uniform pattern

The pointing coordinates of the two laser beams within the uncertainty cone are distributed according to a uniform PDF. Since the relation between the two independent coordinates x and y cannot be constrained (in order not to change the overall distribution of the guidance scheme) each satellite covers a square area rather than a circular one. Yields,

$$f(i) = \begin{cases} \dfrac{1}{2\rho_{unc}} & -\rho_{unc} \leq i \leq \rho_{unc} \\ 0 & \text{elsewhere} \end{cases} \quad \text{with} \quad i = x\,,\, y \tag{4.29}$$

According to this PDF, every point that is inside the uncertainty cone has the same probability of falling within the scanning cone. Therefore, by simple geometrical considerations, the probability of covering a particular region (event which is labelled as $\mathbf{z}$ or $\mathbf{r}$) with the laser beam of one of the two satellites is equal to

$$\mathrm{P}_i(\mathbf{z}) = \frac{\delta^2}{\rho_{unc}^2} \quad \text{with} \quad i = m\,,\, s \tag{4.30}$$

Since the pointing coordinates of the master and slave satellite are generated independently, the probability that the two satellites will point toward the line of sight is given by the product of the probabilities that both satellites contemporarily cover the same region of the uncertainty cone. Yields,

$$\mathrm{P}(\mathbf{z},\mathbf{r}) = \mathrm{P}_i(\mathbf{z})\,\mathrm{P}_i(\mathbf{r}) = \frac{\delta^4}{\rho_{unc}^4} \tag{4.31}$$

With a uniform distributed pointing, either the initial pointing offsets nor the time dependant disturbances affect the probability $\mathrm{P}(\mathbf{z},\mathbf{r})$ since this value is always constant within the square area whose side is equal to $2\rho_{unc}$. Outside this area, the chances of acquiring the signal are zero.

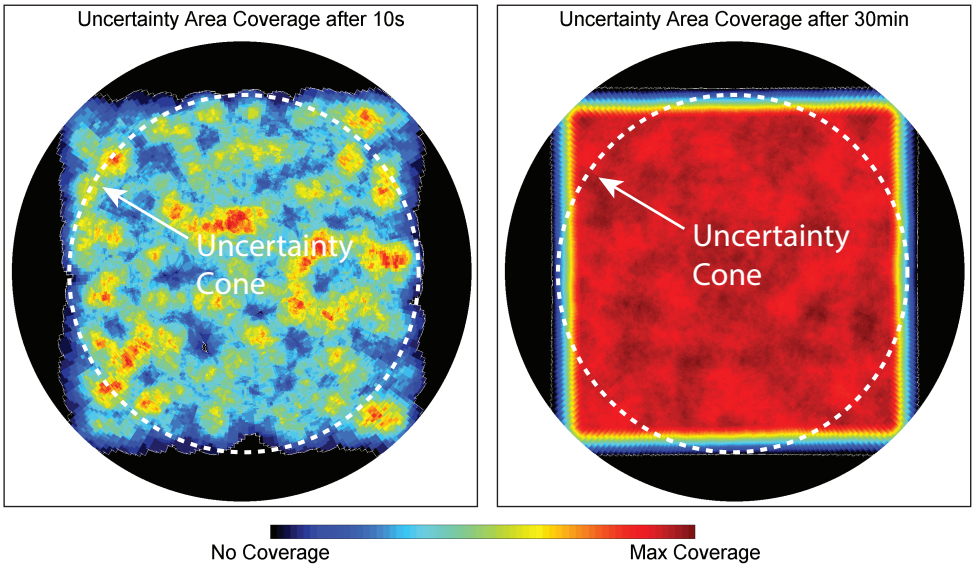

Figure 4.12: Coverage of the uncertainty cone using a uniform pattern as its execution time increases (after 10 s in the left panel and after 30 min in the right panel).

Time required to solve the spatial acquisition problem

Once the guidance algorithm is started, the two laser beams are randomly pointed within the uncertainty cone. The probability that after a certain time there is a solution to the spatial acquisition problem is equivalent to the sum of several independent and identical Bernoulli trials which have a small probability of occurrence [91] (when acquiring the signal, the time dependency of P can be neglected since t_{dwell} is much smaller than the orbital period). Labelling as $\mathcal{Q}$ the probability of not solving the spatial acquisition problem after the q^{th} trial ($\mathcal{Q} = 1 - \mathrm{P}$ with $\mathcal{Q} \gg \mathrm{P}$) and $\mathcal{N}$ the number of trials (number of repointing of the laser beam) required before solving the spatial acquisition problem, according to the Poisson theorem

$$\mathcal{N} \to \infty \qquad \mathcal{Q} \to 0 \qquad \text{such that} \qquad \mathcal{N}\mathrm{P} = \lambda = \text{const} \tag{4.32}$$

In general, the event (generically labelled here as χ) of having the two laser beams aligned to the line of sight will occur y times with a certain probability L. L can calculated as

$$L\left(\chi \geq y\right) = 1 - F_{\chi}(\chi) = 1 - \sum_{\hbar=0}^{y-1} L\left(\chi = \hbar\right) = 1 - e^{-\lambda} \sum_{\hbar=0}^{y-1} \frac{\lambda^{\hbar}}{\hbar!} \tag{4.33}$$

In order to acquire the signal, the two laser beams have to overlap at least once. Hence, choosing $\hbar = 1$, and substituting Eq. 4.32 in Eq. 4.33, yields

$$\mathcal{N} = -\frac{\ln\left(1 - L\right)}{\mathrm{P}} \tag{4.34}$$

which returns the required number of trials ($\mathcal{N}$) in order to obtain the probability L of having the two laser beams overlapped to the line of sight. The probability P is calculated according to Eq. 4.28 if the guidance scheme uses a Gaussian pattern, otherwise according to Eq. 4.31.

In order to avoid a precise synchronization in initializing the acquisition mode on board the satellites, it is necessary to chose different dwell times for the pattern of the master satellite and for the one of the slave satellite. When the ratio between the dwell times of the two satellites is set to 3/2, in the generic time interval t in which one satellite repoints its laser beam three times

the other one will repoint it only two times. This device implies that, in the time interval t, there is at least one sub-interval in which both satellite simultaneously maintain their pointing for t_{dwell}. Since $\mathcal{N}$ is a function of these two dwell times Eq. 4.34 can be rearranged such that

$$\mathcal{N} = \mathcal{N}^m + \mathcal{N}^s = \frac{t_{rand}}{t^m_{dwell}} + \frac{t_{rand}}{t^s_{dwell}} \longrightarrow t_{rand} = -\frac{t^m_{dwell} \times t^s_{dwell}}{t^m_{dwell} + t^s_{dwell}} \frac{\ln(1-L)}{\mathrm{P}} \tag{4.35}$$

which returns the execution time (t_{rand}) of the guidance scheme in order to solve the spatial acquisition problem with a probability equal to L. The terms t^m_{dwell} and t^s_{dwell} are the dwell times used for the master and the slave satellite when implementing the guidance scheme.

Optimal repointing maneuver

When using a random pattern, the mirror should jump from one pointing coordinate to another. Such operating conditions can compromise the operational life time of the steering mirror since this is repointed sending high current peaks to its motor coils rather than a low continuous current (the mirror has to be instantaneously accelerated). Indeed with a random pattern the maximum amplitude of the current injected to the motor coils can be up to three orders of magnitude higher than the one injected when the steering mirror is repointed according to a continuous pattern.

Additionally, the dwell time of each pointing coordinate is given by the sum of the acquisition time (see paragraph 4.4) and the time required by the steering mirror to repoint the laser beam to the next point of the guidance sequence. This latter time interval is referred hereafter as *repointing time*. The repointing time can be significantly high because it has to include the time required to extinguish the oscillatory motion of the mirror caused the step command (with a feedback controller this can take up to 20 ms).

These effects can be removed if the new pointing coordinate is obtained by rotating the mirror following a slew maneuver. In order to optimize the maneuver with respect to time, the accelerating phase and the decelerating phase are separated in time by a transition phase in which the mirror is moved with a constant angular velocity (coasting phase - see appendix B.5)

$$\begin{cases} t_{acc} = \dfrac{\omega}{\alpha} \\ t_{cost} = \dfrac{\Delta\rho}{\omega} \\ t_{dec} = t_{acc} + t_{cost} \end{cases} \longrightarrow \quad t_{rp} = t_{acc} + t_{cost} + t_{dec} \tag{4.36}$$

where the ω and α are respectively the angular velocity and angular acceleration of the mirror. The position of the steering mirror during the maneuver is given by

$$\begin{cases} \rho = \rho_i + \dfrac{1}{2}\alpha t^2_{acc} & \text{for} \quad t < t_{acc} \\ \rho = \rho_1 + \omega \dfrac{\Delta\rho}{|\Delta\rho|}(t - t_{cost}) & \text{for} \quad t_{acc} \le t < t_{cost} \\ \rho = \rho_f - \dfrac{1}{2}\alpha (t - t_{dec})^2 & \text{for} \quad t_{cost} \le t < t_{dec} \\ \rho = \rho_f & \text{for} \quad t_{dec} \le t \le t_{dwell} \end{cases} \tag{4.37}$$

By properly choosing the parameters ω and α it is possible to reduce the current injected in the motor coils and achieve power consumptions equivalent to the ones required by a continuous pattern. Nevertheless, α and ω cannot be chosen arbitrarily small but their minimum value has to guarantee that the distance δ is covered in less than the time required by the instrument to lock the signal. Indeed, this would significantly increase the likelihood of single sided detections. If ω and α are chosen such that $t_{cost} < t_{acc}$, then the mirror is accelerated for half of the time

of the maneuver and decelerated for the other half.

4.4 Analysis of the minimum dwell time

The smallest dwell time used to design the acquisition algorithm cannot be chosen arbitrary but depends on the type of pattern (continuous or random), on the acquisition strategy (split or direct) and on the type of phasemeter used to detect the heterodyne signal (WPD or DFFT based).

In a DFFT phasemeter it is possible to separate the DFFT algorithm, used to acquire the heterodyne signal, from the DPLL which is used to lock it and exploit the phase measurement (in some applications these devices have been embedded in two different processing units). In this case, the signal detection time (t_{det}) is the integration time of the DFFT and it is equal to the length of the DFFT divided by the sampling frequency of the data processing unit. The signal locking time (t_{lock}) depends on the accuracy with which the heterodyne signal is evaluated (hence, on the length of the DFFT). Therefore, it is possible to distinguish the detection time from the locking time.

The architecture of the WPD phasemeter (see paragraph 2.3) does not allow to separate the acquisition unit from the measurement unit and therefore the detection time is coincident with the time required by the main DPLL to lock the heterodyne signal ($t_{det} = t_{lock}$).

4.4.1 Split acquisition

The task of the target detection mode is to store the tip-tilt angles of the repointing mechanism and the laser frequency whenever the phasemeter locks the heterodyne signal (or detects a flash in the case of a DFFT phasemeter [63, 64]). Since the system does not have to perform other operations, the minimum dwell time of the fast spatial scan (the possibility of having a fast frequency scan is discarded - see paragraph 4.5) is $t^{min}_{dwell} = t_{det}$.

If random patterns are used to scan the uncertainty domain, the maximum repointing time (calculated according to Eq. 4.36 using $\Delta\rho = 2\rho_{unc}$) has to be summed to the acquisition time. Yields, $t^{min}_{dwell} = t^{max}_{rp} + t_{det}$.

The link attainment mode not only has to detect the presence of a heterodyne signal, but has to establish the optical link. Because it is not possible to exclude a single sided detection, the acquisition algorithm has to guarantee that when the instrument that has detected the signal points towards the direction of RX beam, this has not moved. Therefore the time required by one laser system to repoint its beam towards the light source has to be accounted. This time has to accommodate the command delay of the mirror, the transitory oscillation of the mirror caused by the step command of the new position and the time the twin satellite requires to lock the light signal and transit to DWS pointing control. The minimum time required to acquire the signal is $t^{min}_{acq} = 2t_{lock} + 2t_{DWS} + t^{DWS}_{rp}$. The terms t_{DWS} and t^{DWS}_{rp} are respectively the time required to switch to DWS pointing and the time required to firmly point towards the direction of the light source.

As in the case of the target detection mode, the minimum dwell time is different when using random patterns or continuous patterns. In the first case, $t^{min}_{dwell} = t^{max}_{rp} + t_{acq}$ while in the latter case $t^{min}_{dwell} = t_{acq}$.

4.4.2 Direct acquisition

The direct acquisition mode is nothing more than link attainment mode executed over a wider uncertainty domain. For such a reason, also in this case, the minimum dwell time can be calculated as $t^{min}_{dwell} = t^{max}_{rp} + t_{acq}$ or as $t^{min}_{dwell} = t_{acq}$ accordingly with the pattern used to cover the spatial uncertainty domain.

4.5 The acquisition algorithm

In order to acquire the signal it is necessary that the spatial scans and the frequency scan are performed according to a defined sequence. Here a distinction is made in the case of scanning the spatial uncertainty domain using a continuous or a random pattern. No distinction is instead made regarding the usage of a frequency sweep rather than frequency steps since these are equivalent from the point of view of the acquisition algorithm.

4.5.1 Case 1: continuous patterns

In this case, the simplest way to link the spatial scans to the frequency scan is to design the acquisition algorithm like a nested sequence of for cycles (see Fig. 4.13). This operating principle is identical to the one described in subparagraph 4.3.1 when the relation between the dwell time of two continuous patterns was analyzed (see Eq. 4.10). The position within the hierarchy of the two spatial scans and frequency scan is not important for fulfilling the coverage of the five degrees of freedom as long as the constraint on the dwell times is fulfilled.

The flow chart depicted in Fig. 4.13 allows to link the spatial scans to the frequency scan according to three different hierarchies

	Slow Scan		*Intermediate Scan*		*Fast Scan*
(1)	spatial scan	$\longrightarrow$	spatial scan	$\longrightarrow$	frequency scan
(2)	spatial scan	$\longrightarrow$	frequency scan	$\longrightarrow$	spatial scan
(3)	frequency scan	$\longrightarrow$	spatial scan	$\longrightarrow$	spatial scan

According to this sequence there is no difference in which satellite performs the fastest spatial scan. Therefore, without loss of generality, the slave spacecraft is here assigned to always perform the fastest spatial scan. From an algorithmic point of view, the difference between the three options is in the time they require to fully scan the five degrees of freedom.

Option 1

According to this option, the terms N_x and N_y in Fig. 4.13 are the total number of dwell spots, given by the pattern equations. Since there is no particular reason to chose two different patterns $N_x = N_y = N_{patt}$. The total time required to complete a scan of the five degrees of freedom is

$$T_1 = N_{patt}^2 T_f \tag{4.38}$$

where T_f is the time required by the frequency acquisition algorithm to scan the frequency uncertainty. When performing the frequency acquisition using discrete frequency steps the rate with which the frequency is changed is not as rapid as the repointing of the steering mirror. With an Nd:YAG Non-Planar Ring Oscillator (NPRO) laser the maximum frequency change rate is achieved with the piezo-electric tuner and is equal to 100 Mhz/s. If the bandwidth of the phasemeter is 15 MHz, the time it requires to lock the signal is 500 µsec (3σ value) and the width of the uncertainty area is 200 Mhz, the term $T_f = 7.5$ s (a non time optimal scan pattern - i.e. Lissajous or rhodonea - would cover an uncertainty cone of 3 mrad in less than one second if the scanning cone is 140 µrad wide).

With a linear ramp, the magnitude of T_f is strongly dependant of the phasemeter. Indeed, the steepness of the ramp is limited to about 100 MHz/s when using a DFFT based phasemeter with 4096 bins [63] or to 500 MHz/s when using the WPD based phasemeter with six stages (laboratory experience). A sweep rate of 500 MHz returns a T_f compatible with the time required to scan the uncertainty cone using a non time optimal scan pattern. For a LEO mission though, the external disturbances acting on the satellites do not allow a stable pointing

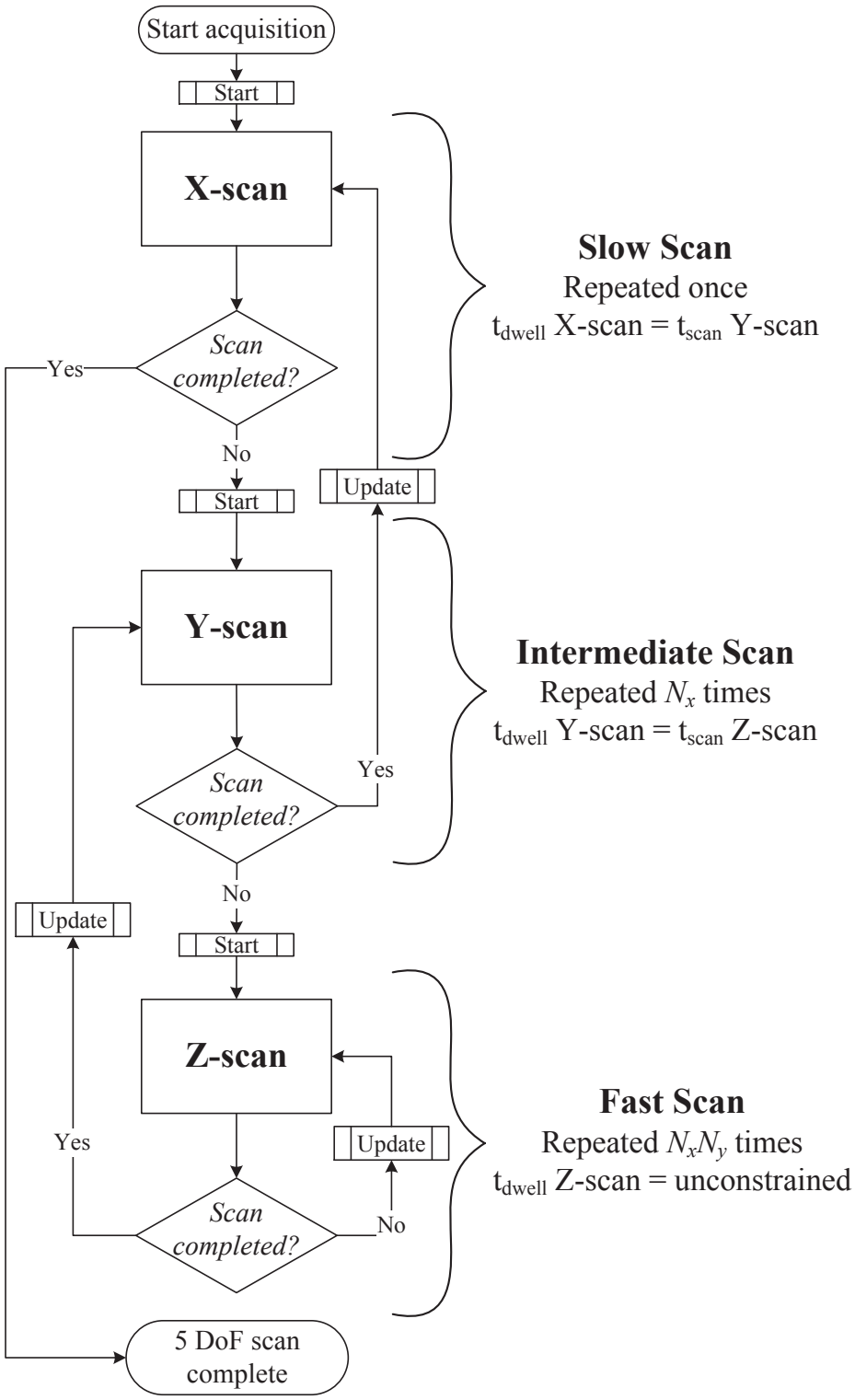

Figure 4.13: The hierarchy of the signal acquisition algorithm is here depicted. X, Y and Z can be replaced with "frequency" or "spatial" according to intended sequence of the acquisition algorithm. N_x and N_y are the total number of dwell spots of the X and Y scan respectively. The term t_{scan} represents the time required to cover the uncertainty according to the scanning law adopted. The dwell time of the Z-acquisition is unconstrained with respect to the dwell time of the Y-acquisition and of the X-acquisition but not arbitrary (see paragraph 4.4).

of the laser beam during the initial acquisition phase since the pointing control of the steering mirror can only use the STR data. To accommodate the pointing drift, the superimposition factor K used to design the guidance scheme has to be sufficiently small in order to exclude the possibility of introducing gaps during the spatial scan (with a consequent increase of N_{patt}).

Since the values used to evaluate the performance of this algorithm sequence are representative of a GRACE Follow-On like scenario, option 1 is most likely a not time-optimal solution and therefore discarded.

Option 2 and Option 3

According to these two options, the terms N_x and N_y in Fig. 4.13 are alternatively the number of dwell spots of the slowest spatial scan (which depend on the pattern) and the number of frequency steps given by Eq. 4.1. The five degrees of freedom are scanned in

$$\begin{aligned} T_2 &= N_{patt2} N_{f2} T_{patt} \\ T_3 &= N_{f3} N_{patt3} T_{patt} \end{aligned} \tag{4.39}$$

where T_{patt} is the time required to cover the uncertainty cone with the fast pattern. The two options are not equivalent since the longer the dwell time, the bigger the drift (either in pointing or in frequency) and the bigger the superimposition between two consecutive scans. Therefore $N_{patt2} > N_{patt3}$ and $N_{f2} < N_{f3}$.

The option which minimizes the acquisition time can be found through the analysis of the statistical distribution of the initial pointing offset and of the frequency offset. The frequency offset is expected to be uniformly distributed within its uncertainty domain since the frequency error is equiprobable. The radius of the uncertainty cone is the 3σ value of the sum of instrument alignment errors and computational uncertainties of the AOCS algorithms which can all be considered Gaussian distributed. Therefore the line of sight has a 95% probability of being within 2/3 of ρ_{unc}. If the spatial uncertainty is scanned using spiral patterns, in 95% of the acquisition problems, the maximum time required to detect the signal is

$$\begin{aligned} T_2 &= 0.67 N_{patt2} N_{f2} T_{patt} + 0.95 N_{f2} T_{patt} + 0.67 T_{patt} \\ T_3 &= 0.95 N_{f3} N_{patt3} T_{patt} + 0.67 N_{patt3} T_{patt} + 0.67 T_{patt} \end{aligned} \tag{4.40}$$

When performing the initial acquisition, the number of dwell spots in the spatial and frequency domain is grater than ten and the biggest contribution to T_2 and T_3 comes only from their first term. Introducing the scaling factors $K_{pr} = N_{patt2}/N_{patt3}$ and $K_{fr} = N_{f3}/N_{f2}$, the ratio T_2/T_3 can be approximated as

$$\frac{T_2}{T_3} \approx \frac{0.67 K_{pr}}{0.95 K_{fr}} \tag{4.41}$$

If $T_2 = T_3$, Eq. 4.41 returns $K_{pr}/K_{fr} \approx \sqrt{2}$. If $K_{pr}/K_{fr} > \sqrt{2}$ the drift of the satellite is dominant in the time scale of the acquisition algorithm and option 3 is expected to be faster than option 2 in 95% of the acquisition problems. If $K_{pr}/K_{fr} < \sqrt{2}$ holds the opposite condition.

If the pattern used to scan the uncertainty cone is not a spiral, it is not possible to consider only the 67% of N_{patt-i} (with $i = 1\,,\, 2$) since the beam is not progressively moved from the inner to the outer boundary of the uncertainty cone. Same condition applies when the line of sight has equiprobability of being in any point of the uncertainty cone. In these cases, the optimal sequence is the one which minimizes Eq. 4.39.

When using option 3 with a linear ramp, the frequency dwell time can be halved (or divided by a value i which is a multiple of 2) and the frequency scan performed twice (or i times). If the initial pointing offset is within half of the radius of the uncertainty cone, several spatial solutions are found and changing more often the frequency can reduce the overall time required

to acquire the laser signal. Nevertheless, synchronization errors between spatial scan and frequency scan can introduce gaps within the uncertainty region. This solution is, therefore, not recommendable although further research would be necessary.

The optimization described herein is only time driven. The introduction of system constraints (i.e. reliability of the laser system with respect to the steering mirror) could privilege a different option than the one suggested.

4.5.2 Case 2: random patterns

In this case, the frequency scan is linked to the spatial scan through Eq. 4.35. When N_f frequency scans are performed and each one lasts t_{rand} there is a probability L of acquiring the signal when the heterodyne beat frequency is within the bandwidth of the phasemeter. The magnitude of t_{rand} is strongly dependent on the probability P of having the two laser beams overlapped when performing a spatial acquisition trial (Eq. 4.28 or Eq. 4.31). For a uniform distributed pattern, P depends only on the width of uncertainty cone and scanning cone and therefore t_{rand} is fixed.

For a Gaussian pattern, P varies according to the magnitude of the initial pointing offset and with the time dependant pointing disturbances. Since these are not known beforehand, one choice is to select P accordingly with the worst expected conditions. This solution though is not time optimal and can be significantly improved by simple considerations on the nature of the pattern. Because t_{rand} (see Eq. 4.35) is the time required to accumulate $\mathcal{N}$ dwell spots within the uncertainty cone and each spot is uncorrelated with the previous ones, there is no difference if these $\mathcal{N}$ dwell spots are accumulated in a single time interval which lasts t_{rand} or in i non-consecutive time intervals each lasting t_{rand}/i. According to this reasoning it is possible to choose the frequency dwell time independently from t_{rand} since any value of P is accounted by repeating the frequency scan over time. Aside the relation between the dwell time of the master and slave satellite ($2t^m_{dwell} = 3t^s_{dwell}$ or vice versa) the spatial scans and the frequency scan are fully independent.

Extending this reasoning also for a uniform pattern, yields that the three domain scans do not require a rigid hierarchy and if $2t^m_{dwell} = 3t^s_{dwell}$ the acquisition algorithm is also robust to initialization delays. Figure 4.14 depicts the flow chart of the acquisition algorithm which uses two random pattern as guidance scheme.

4.5.3 General approach for defining the acquisition algorithm

Even if a guidance algorithm which uses the random patterns has an unconstrained hierarchy, the existence of a solution to the spatial acquisition problem is not certain but it is likely to occur. Instead, from a geometrical prospective, an acquisition algorithm that implements continuous pattern always finds at least one solution to the spatial acquisition problem when this is within the considered boundaries.

When using continuous patterns, if the dwell time is bigger than 2 ms, the constant tangential velocity spiral is the best choice since it optimizes the spatial scan in terms of run time and coverage of the uncertainty cone. If the dwell time is smaller and the ratio between the uncertainty cone and the scanning cone is below five, the pattern execution time is negligible and the Lissajous or the rhodonea are the most robust choice (especially in presence of synchronization errors). Since the execution time of these two curves is comparable, the choice depends on the likelihood of having the line of sight close to the center of the uncertainty cone or not. In case $\rho_{unc}/\delta > 5$, the most suitable pattern is the one that minimizes the execution time of the acquisition algorithm. This reasoning is summarised in the flow chart of Fig. 4.15. The constant angular velocity spiral is not taken into account since it is a non time optimal solution when compared to the other two spiral patterns herein analyzed.

The previous chart is conceived for designing an acquisition algorithm which minimizes its

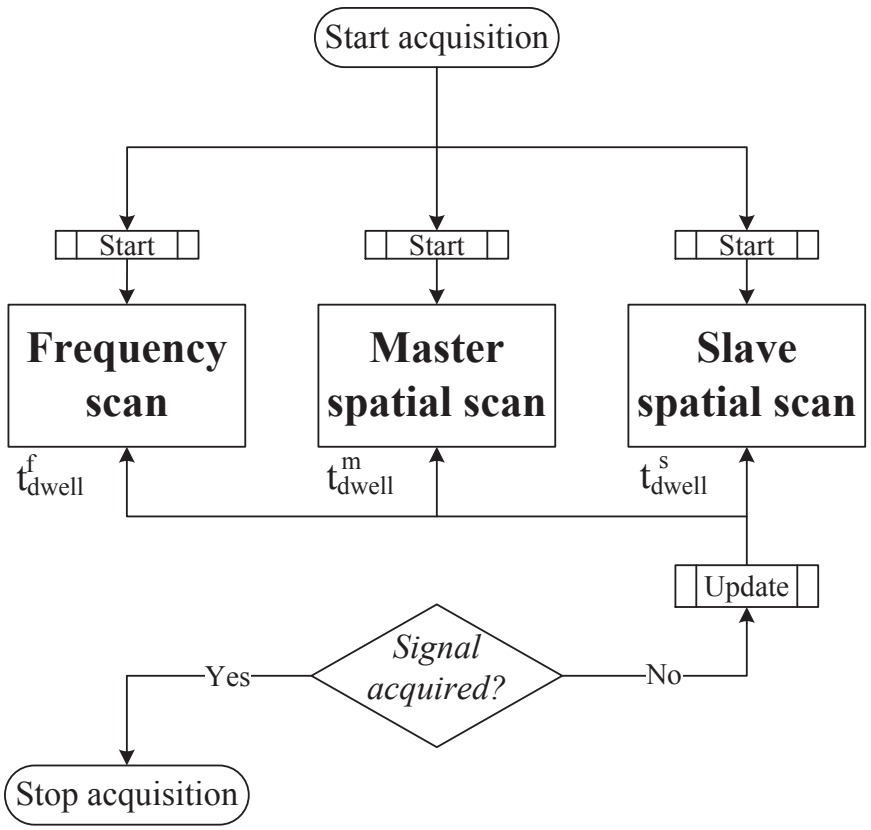

Figure 4.14: When using random patterns, the acquisition algorithm can be divided into three independent sub-algorithms.

execution time. This is, in general, the objective (minimizing this time allows to increase the measurement time) although the boundary conditions of each specific mission might introduce additional constraints on the usable patterns.

The trend used to scan the frequency domain is independent from any consideration on time optimization and is principally related to the laser system. If the laser is well characterized and it is possible to stably control its frequency, the usage of discrete steps is the best solution.

Example application: The acquisition algorithm of GRACE Follow-On

The acquisition algorithm of the LRI of GRACE Follow-On is used here as an example application of an algorithm designed applying the considerations made beforehand.

For the LRI the problem of acquiring the signal has five degrees of freedom and the acquisition strategy is implemented according to the split acquisition mode (decision principally driven by the computational complexity of the algorithm). The algorithm takes into account only continuous patterns as suitable scan laws while the frequency domain is scanned following a linear ramp.

Option 1 described in paragraph 4.5 would require a slope of the frequency ramp equal to 25 GHz/s. Since this value is not compatible with the SNR requirement of the phasemeter [63], this option is discarded. Although both option 2 and 3 are suitable for the hierarchy of the acquisition algorithm, the poor pointing stability of the satellites supports the use of option 2. Nevertheless, as suggested by *Mahrdth* [63] a deeper analysis would be necessary.

Using the design parameters of Tab. 4.6 and the decision chart depicted in Fig. 4.15, the acquisition problem has two possible solutions which depend on the beam pointing control (FF

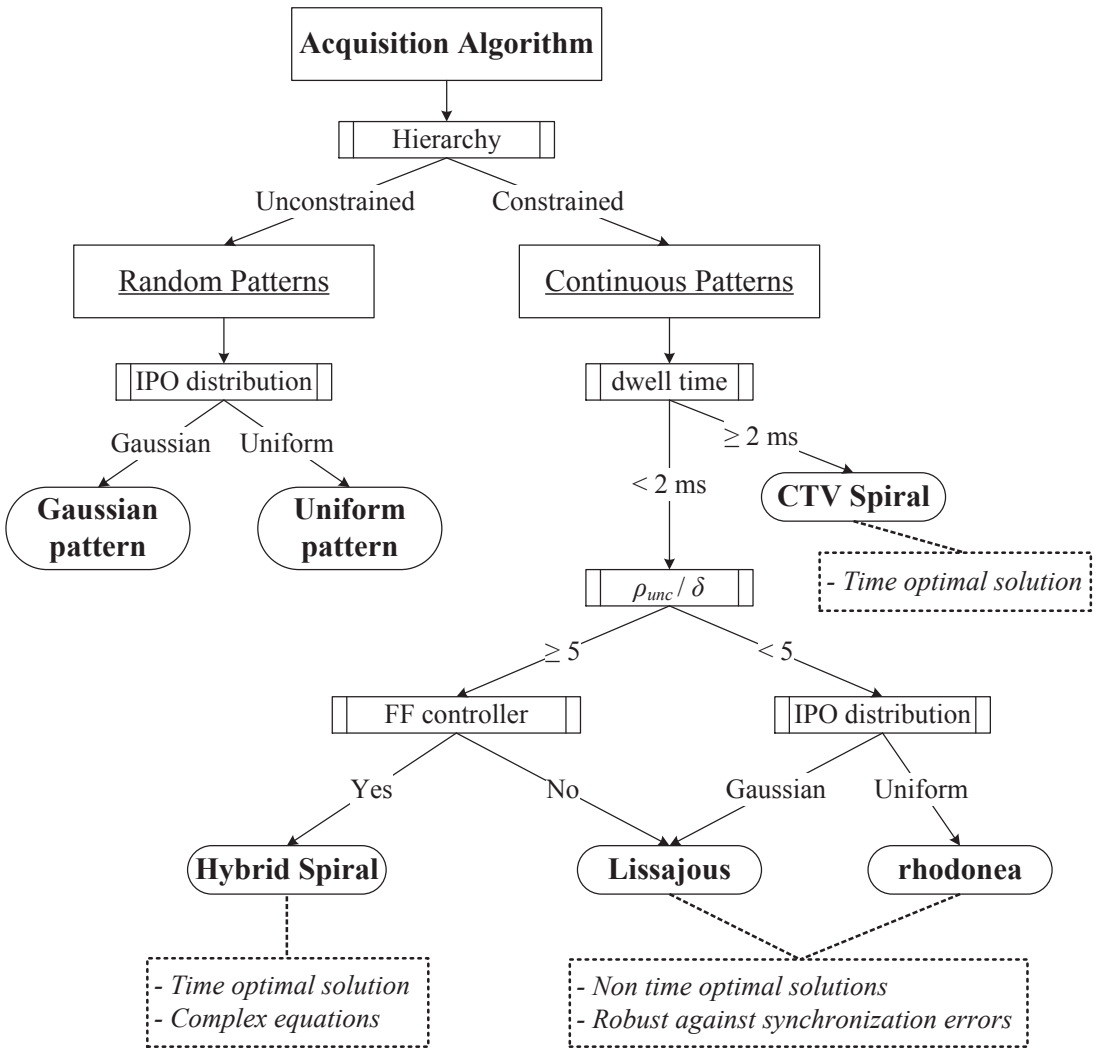

Figure 4.15: The flow diagram represent a possible decision chain behind the selection of a pattern for performing the spatial acquisition. IPO is the acronym of initial pointing offset while CTV is the acronym of constant tangential velocity.

controller or not)

	Fast Scan		*Intermediate Scan*		*Slow Scan*
(1)	Lissajous	$\longrightarrow$	CTV Spiral	$\longrightarrow$	Frequency ramp
(2)	Hybrid Spiral	$\longrightarrow$	CTV Spiral	$\longrightarrow$	Frequency ramp

As no FF control is foreseen for enhancing the beam pointing control of GRACE Follow-On, the first acquisition is indeed the one implemented for the LRI [63, 64].

The time required by the acquisition algorithm of the LRI to cover the five degrees of freedom, evaluated in Tab. 4.7, is compared with the execution time of two time optimal acquisition algorithms which implement the hybrid spiral as fast spatial scan. In particular, for the first time optimal algorithm (labelled as Optimal algo. 1 in Tab. 4.7) the dwell time is set to $t_\mathrm{d} = 0.35\,\mathrm{ms}$ while for the second optimal algorithm (labelled as Optimal algo. 2 in Tab. 4.7), the dwell time is set to $t_\mathrm{d} = 0.1\,\mathrm{ms}$.

Algorithm design parameters		
Description	**Value**	**Units**
Uncertainty cone - target detection	1.4	mrad
Uncertainty cone - link attainment	0.3	mrad
Frequency uncertainty	±500	MHz
Phasemeter's sampling frequency*	38	MHz
DFFT length*	4096	-
Phasemeter's detection time	0.1	ms

* The phasemeter is derived from LISA prototypes [40] and the signal acquisition is aided using a DFFT based algorithm. The optimal length of the DFFT is suggested by *Mahrdth* [63].

Table 4.6: Parameters used to design the acquisition algorithm for the GRACE Follow-On mission.

Parameter	**LRI algo.**	**Optimal algo. 1**		**Optimal algo. 2**	
t_{dwell}	0.1 ms	0.47 ms†	Δ [%]¶	0.166 ms†	Δ [%]¶
			+372%		+66%
$t_{\text{fast-scan}}$	0.56 s*	0.43 s	Δ [%]¶	0.153 s	Δ [%]¶
			−21.4%		−72.8%
$t_{\text{int-scan}}$‡	8 min 30 s	6 min 35 s		2 min 20 s	
$t_{\text{slow-scan}}$**	9 hours	6 hours 55 min		2 hours 28 min	

¶ Δ is the variation with respect to the same parameter of the Lissajous scan.

† The dwell time of the hybrid spirals has to be multiplied by the coefficient listed in Tab. 4.5. Choosing $t_{\text{d}} = 0.35\,\text{ms}$ for hybrid spiral 1 and $t_{\text{d}} = 0.1\,\text{ms}$ for the hybrid spiral 2, the coefficient are $C = 1.35$ and $C = 1.66$ respectively. Thus the effective dwell time is given by $t_{\text{dwell}} = C \cdot t_{\text{d}}$.

* Using a superimposition factor of $K = 1/\sqrt{2}$ [64], Eq. 4.14 returns that $f_a = \omega_a/2\pi = 212\,\text{Hz}$. Since this value exceeds the maximum repointing frequency of the steering mirror, f_a is limited to 100 Hz. Solving Eq. 4.13 yields that $\omega_r = 56$ and $1/f_b = \omega_r/f_a = 0.56\,\text{s}$.

‡ According to Fig. 4.13, the dwell time of the intermediate scan is equal to $t_{\text{fast-scan}}$ while the dwell time of the slow scan is equal to $t_{\text{int-scan}}$.

** Using a frequency superimposition of $K_f = 0.9$, each frequency step is 16 MHz wide. In order to cover an uncertainty of 1 GHz, the frequency scan has to perform 63 steps.

Table 4.7: In this table, the execution time of three different acquisition algorithms is calculated.

The improvement of the execution time of the fast scan ($t_{\text{fast-scan}}$) is representative of the effective reduction of the execution time of the acquisition algorithm since the intermediate (spatial) scan and the slow (frequency) scan are the same for all three algorithms.

This execution time calculated for the acquisition algorithm of the LRI is about 50% bigger than the one calculated by *Wuchenich et al* [64]. This discrepancy is given by the superimposition factor adopted. Indeed using $K = 0.95 \longrightarrow \omega_r = 36$ and the total execution time of the acquisition algorithm is approximately 6 hours (18 minutes faster than the 6 hours and 18 minutes calculated by *Wuchenich et al*).

For the target detection mode, since $\rho_{unc} > 2\delta$ it is not possible to cover the uncertainty area using a circular motion. The minimum dwell time is once more equal to 0.1 ms[4] while

[4]The link attainment mode of LRI is identical to the target detection mode only executed over a smaller uncertainty domain. Although, instead of sending the data to ground for post-processing, once the execution of the link attainment mode is completed, the instruments point towards the best "acquisition solution" and try to establish the optical link.

$\rho_{unc}/delta < 5$. Because the distribution of the initial pointing offset is now uniform, the Lissajous pattern is again the best pattern for performing the fast spatial scan. Choosing $\omega_r = 4$ yields $t_{gui} = 40\,\text{ms}$ allowing the slowest pattern to be a spiral. This guidance scheme is exactly the one intended for link attainment of the LRI.

Signal acquisition studies for eLISA

In the context of the eLISA mission, the signal acquisition has been investigated in the past years [111]. Although the acquisition process is simplified by the usage of an acquisition sensor (see paragraph 4.7) the considerations on how to select a pattern remain unchanged. For this mission, a steering mirror is not foreseen because not sufficiently stable for science operations while the mechanism used for field guiding can only move slowly along one degree of freedom. The best choice is therefore to repoint the laser beam by rotating the entire satellite.

From the boundary conditions of this acquisition problem, the acquisition algorithm has to solve only two spatial degrees of freedom. Since the hierarchy structure for a random pattern and a continuous pattern is, in this case, identical, a continuous pattern is preferable since the solution is not statistical. Because both the integration time of a Charge-Coupled Device (CCD) camera and the actuation of the satellite pointing through the thrusters is above 1 s, the constant tangential velocity spiral is the time optimal solution. And indeed repointing the satellite according to a spiral pattern is currently the baseline for performing the spatial scan for the eLISA mission.

4.6 Signal acquisition simulations

The simulator which is used to perform the acquisition simulations is identical to the one described in paragraph 3.8 except for the models of the steering mirror and of the phasementer which are simplified. Indeed, the sampling frequency of these components would not allow to simulate a process which can last hours in a reasonable amount of time. Nevertheless, the simulations has to include the millisecond time scale which is representative of the signal detection. For such a reason, the frequency of the simulator cannot be lower than 1 kHz.

Since the electronics which controls the steering mirror operates at 20 kHz it is not possible to include in the simulator the complete model of the steering mirror. In this case, the real tip-tilt angles of the mirror are coincident with the ones commanded. If the positioning sensors of the mirror are properly calibrated and the response of the mirror is well characterized, this error is below 1%. Under these circumstances, the coincidence between commanded angles and real mirror angles does not invalidate the simulations. The pointing error caused by the jitter of the steering mirror is also neglected since this is one order of magnitude smaller than the pointing jitter of the satellites ($0.1\,\text{mrad}/\sqrt{\text{Hz}}$ against $10\,\mu\text{rad}\sqrt{Hz}$).

With a simulation frequency of 1 kHz it is also not possible to use the model of the phasemeter since its sampling frequency is four orders of magnitude higher (50 MHz). Hence the phasemeter is replaced by a counter. If the acquisition problem is solved for a time $t > t_{acq}$, the phasemeter is considered locked and the steering mirror pointing is controlled by the DWS signal (in this case t_{DWS} is equal to one simulation step). If the acquisition conditions are not maintained for a sufficient time, the counter is reset to zero.

The simplified model of the phasemeter also includes a watch dog circuit for tacking into account single sided detections. If only one of the two satellites detects the signal, the phasemeter waits three simulation steps before the laser system returns back to "initial acquisition mode". If the algorithm uses continuous patterns, the new frequency of the free-running laser (if the single sided detection occurred on the slave satellite) and the new mirror position are the ones the instrument should have had at that point in time as if the no signal detection had occurred. This reduces the chances of a synchronization errors but leaves an uncovered gap in the uncertainty domain. If the algorithm uses random patterns, the "initial acquisition mode" is simply

restarted.

By limiting the simulation frequency it is also not possible to correctly represent the complete set of sates and transitions which define the finite state machine controlling the acquisition algorithm. The finite state machine which is used for these simulations is severely simplified with respect to the one of the real system and is depicted in Fig. 4.16.

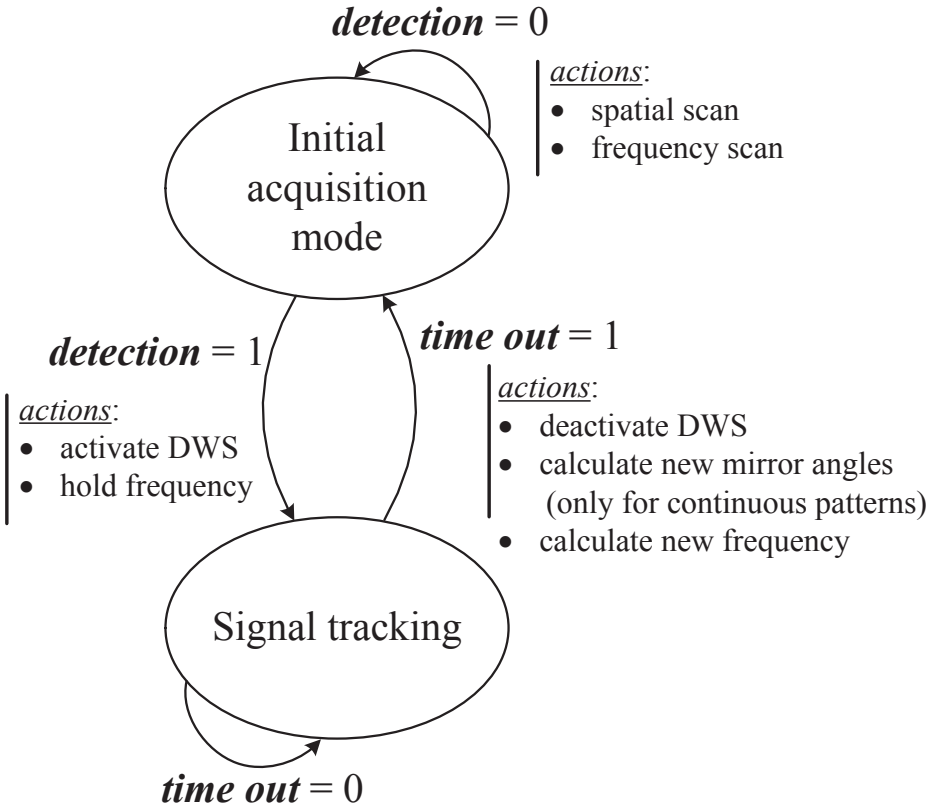

Figure 4.16: The state machine of the simulator is implemented by using only two states. Once the signal is detected it is tracked using the DWS signal and the watch dog circuit is activated. This machine is used for the slave satellite. For the master satellite, the actions on the laser frequency are omitted.

The initial pointing errors are introduced as a static offset of the time series of the satellites' attitude. Together with this offset, also a dynamic offset is added to the satellite pointing which is mainly representative of the thermal stability of the satellite platform along the orbit. The thermal deformation of the platform is modelled as a sinusoidal wave whose amplitude is equal to the expected stability and whose period is equal to the orbital one. This dynamic offset is taken into account as a deviation of the inertial frame body frame rotation matrix. In particular

$$\begin{gathered} \vartheta_{i,j,k} = \varsigma_{i,j,k} \sin\left(2\pi f_{orb} + \varphi_{i,j,k}\right) \\ \downarrow \\ \mathbf{R}_{\mathrm{JB}} = \mathbf{R}_{\mathrm{JB}}^{\mathrm{id}}\left(R, P, Y\right) \mathbf{R}_{i,j,k}\left(\vartheta_i, \vartheta_j, \vartheta_k\right) \end{gathered} \tag{4.42}$$

where $\mathbf{R}_{\mathrm{JB}}^{\mathrm{id}}$ is the ideal rotation matrix from body frame to Coordinate Reference System (CRS) J2000 while the matrix $\mathbf{R}_{i,j,k}$ is the deviation matrix. The angles $\vartheta_{i,j,k}$ represent the deviation between the real unit vector of the body frame and the one estimated on board. The parameter $\varphi_{i,j,k}$ allows to take into account asymmetric thermal effects acting on the platform and different thermal conditions between the two satellites since one files backwards with respect to the other.

4.6.1 Simulation parameters

The acquisition simulations described in this paragraph are performed for a LEO mission identical to GRACE Follow-On. Indeed, the time series of the satellites' position along the orbit and the time series of the attitudes are reproduced with the simulator used for the AOCS studies of this mission. For the GRACE Follow-On mission, the offset between the laser beams which still allows the instrument to acquire the optical signal is equal to 140 µrad [63]. Since the characteristics of the laser instrument for future geodesy missions are expected to be similar to the ones of the LRI [81], 140 µrad is herein used as the alignment requirement between the laser beams. The uncertainty cones and the frequency uncertainty are equal to 1.4 mrad and ±200 MHz respectively. Their magnitude is evaluated as the linear sum of the sub-allocations listed in Tab. 4.8. Other parameters which are relevant for the signal acquisition simulations are listed in Tab. 4.9.

Uncertainty cone		**Frequency uncertainty**	
Error	**Allocation**	**Error**	**Allocation**
Attitude knowledge	500 µrad	cavity temperature	50 MHz*
Reference direction error†	450 µrad	cavity drift	30 MHz
Alignment between STR and instrument LoS	450 µrad	1g unloading	20 MHz
		margin	100 MHz
Linear sum	1400 µrad	Linear sum	200 MHz

* The cavity is considered of glass ceramic and the offset from mean operating temperature is 10 K (see Eq. 4.43).
† Including navigation error.

Table 4.8: Sub-allocations of the pointing and frequency uncertainty. The final uncertainty is calculated as the linear sum in order to take into account the worst case conditions.

Simulation Parameters			
Variable	**Value**	**Units**	**Description**
Λ	210	km	Satellite separation
t_{det}	1	ms	Detection time
t_{DWS}	1	ms	DWS transition time
f_{bw}	20	MHz	Phasemeter bandwidth
$t_{rp}{}^{*}$	13	ms	repointing time
ω^{*}	0.8	rad/s	SM angular velocity
α^{*}	400	rad/s^2	SM angular accel.

* These parameters are relevant only for guidance schemes that make use of random patterns (see Eq. 4.36).

Table 4.9: Additional parameters used to initialize the simulator.

The frequency change of the cavity is calculated as

$$\delta f = \frac{c}{\lambda} \cdot \mathrm{a_{cav}} \cdot \Delta T_{ABS} \tag{4.43}$$

where c is the speed of light, λ the laser wavelength, $\mathrm{a_{cav}}$ the coefficient of thermal expansion of the cavity and ΔT_{ABS} is the offset of the effective temperature of the cavity from mean

operating temperature. By substituting ΔT_{ABS} with the temperature drift of the cavity it is possible to calculate the frequency error caused by the cavity drift.

The acquisition unit of the phasemeter is based on the WPD algorithm therefore $t_{det} = t_{lock}$. Experimental results have shown that the phasemeter is capable of locking the signal in 500 µs (see chapter 5) but for most of these simulations 1 ms is used as locking time. Since the transition to DWS mode occurs in one simulation step, t_{DWS} is also equal to 1 ms. For designing the frequency scan, the bandwidth of the phasemeter is set to 20 MHz.

Using the GRACE Follow-On orbit data, the point ahead angle given by the orbital motion of the satellites is 1.47 µrad (see appendix A.1) Since this value is negligible compared to the 140 µrad of the field of view, the point ahead angle correction is neglected. Thus, when performing the spatial scan, the beam pointing direction is calculated using only the STR and GPS data (see paragraph 3.3.2) and the high frequency noise is removed by means of exponential weighted moving average LPFs whit a cut-off frequency of 0.5 Hz (see appendix B.6).

4.6.2 The detection probability of the random patterns

In paragraph 4.3.2, the spatial acquisition problem of a random pattern is reduced to a series of independent Bernoulli random variables with low probability of occurrence. Here the simulator is used to analyze if this hypothesis is correct and if the probability of solving the spatial acquisition problem (Eq. 4.28 and Eq. 4.31) is also correctly formulated. For these simulations the frequency of the heterodyne signal is always compatible with the bandwidth of the phasemeter (the laser frequency noise is also neglected). In order to avoid that the STR affects these simulations, the beam pointing correction uses the real time series of the attitude and the satellites' position along the orbit.

The theoretical analysis is verified using a Gaussian pattern and a Gaussian distribution of the initial pointing offset. In order to have a sufficient number of solutions to the spatial acquisition problem, the maximal radial distance of the line of sight from the center of the two uncertainty cones is constrained to one fifth of the radius of the uncertainty cone (the time dependant disturbances are also neglected). The magnitudes of the initial pointing offsets are listed in Tab. 4.10. The signal detection time is set to 1 ms while the repointing time is set to 13 ms. Using the 2/3 relation between the dwell times, the slave satellite repoints its laser beam every 14 ms while the master satellite every 21 ms.

Pattern	*Master*		*Slave*		Δ [µrad]
	Pitch [µrad]	Yaw [µrad]	Pitch [µrad]	Yaw [µrad]	
Gaussian	-41	-46	-25	57	104
Uniform	-425	250	370	962	860

Table 4.10: Magnitude of the pointing biases used to perform the simulations. Δ is the distance between the centers of the uncertainty cones.

The distribution of the solutions as a function of the execution time of the guidance scheme is depicted in the left panel of Fig. 4.17. The execution time of the guidance scheme is reset to zero every time that the phasemeter locks the signal. The simulation result is compared to the theoretical one calculated using Eq. 4.28 and Eq. 4.35. Since the two curves are coincident, it is possible to conclude that the tentative of aligning the laser beams to the line of sight is nothing more than the sum of several and independent Bernoulli random variables whose collective sum tends to be Poisson.

The same simulation is performed with a uniform pattern and a uniform distributed initial pointing offset. Since the probability of aligning the laser beams to the line of sight is independent from the magnitude of the initial pointing offset, no restriction is applied to the

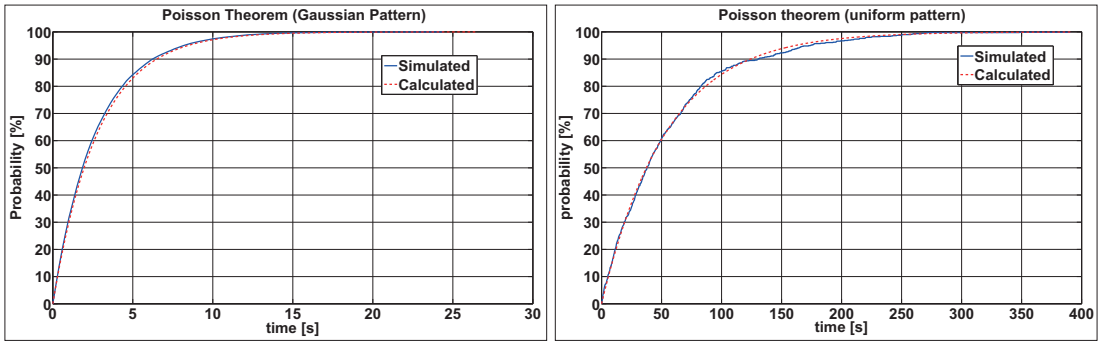

Figure 4.17: This figures shows for how much time the guidance scheme has to be executed before having a probability $\mathcal{P}$ of solving the spatial acquisition problem. The left panel depicts the case of a Gaussian pattern while the right panel the case of a uniform pattern. Both simulations are executed over a time span of 12 hours.

maximal radial distance of the line of sight from the center of the two uncertainty cones (see Tab. 4.10). The distribution of the number of solutions as a function of the execution time of the guidance scheme is depicted in the right panel of Fig. 4.17. Also in this case, Eq. 4.31 and Eq. 4.35 allow to correctly predict the time required to solve the spatial acquisition problem with a certain probability.

The coincidence between the empirical behavior and the predicted behavior is obtained also when changing the magnitudes of the initial pointing offsets, dwell times and acquisition time.

4.6.3 Comparison between patterns and strategies

The algorithms which have been tested using numerical simulations are four; two implement continuous patterns and the other two a random patterns. Because of the poor pointing stability of GRACE Follow-On, the algorithms which use continuous patterns are implemented according to option 3. The first algorithm (labelled as Algorithm 1) is designed according to the split acquisition strategy. The guidance scheme of the target detection mode is time optimized and therefore the fast pattern is a hybrid spiral. The dwell time used to design the pattern is 1 ms while $K = 0.7$. The slower pattern is instead a constant tangential velocity spiral and is designed using $t_{dwell} = 200$ ms (which is the execution time of the hybrid spiral) and $K = 0.7$. The frequency is scanned using a linear ramp and its slope is set to 225 kHz/s[5].

With the target detection mode it is possible to remove only the contribution of the instrument alignment from the estimate of the uncertainty cone's width. Considering a time interval of 48 hours between detecting the signal and triggering the link attainment mode, the pointing error of the satellite (and consequently the width of the uncertainty cone) is 300 µrad [120]. The dwell time of the fast scan is calculated using $t_{det} = 1$ ms, $t_{DWS} = 1$ ms and $t_{rp}^{DWS} = 2$ ms. This value is afterwards increased of 1.5 ms in order to use 0.15 s as dwell time of the slow spatial scan. According to the ASD of the Tesat laser, after 48 hours, the drift of the laser frequency is about 1 GHz. This value is used as the new initial frequency uncertainty. Since the spatial scan is now completed after 3 s, the frequency drift is only 1 MHz and the slope of the frequency ramp can be set to 6 MHz/s.

Algorithm 2 is identical to the link attainment mode except that it is executed over the whole width of the uncertainty cone. The slow spatial scan is designed reducing the superimposition factor from 0.7 to 0.65 in order to take into account the satellite drift (which is 10 µrad in

[5]The spatial uncertainty domain is scanned in 57.6 s. In this time interval, the frequency drift of the free-running laser is about 1 MHz. According to Eq.4.2 and Eq.4.3 the slope of the frequency ramp could be of 330 kHz/s. Since the split acquisition mode is, later on, compared to the direct acquisition mode the value of K_f is kept the same for both the frequency scans. Yields, $m_f = 225$ kHz/s.

Algorithm 1	*Target detection*¶			execution time
	hybrid spiral	CTV spiral	frequency ramp	$t_{gui} \approx 30\,\text{min}$
	$t_{dwell} = 1\,\text{ms}$	$t_{dwell} = 0.240\,\text{s}$	$m_f = 225\,\text{kHz/s}$	
	Link attainment¶			execution time
	CTV spiral*	CTV spiral*	frequency ramp†	$t_{gui} \approx 5.6\,\text{min}$
	$t_{dwell} = 7.5\,\text{ms}$	$t_{dwell} = 0.15\,\text{s}$	$m_f = 6\,\text{MHz/s}$	
Algorithm 2	*Direct acquisition*¶			execution time
	CTV spiral	CTV spiral	frequency steps	$t_{gui} \approx 3\,\text{h}\,50\,\text{min}$
	$t_{dwell} = 6\,\text{ms}$	$t_{dwell} = 1.632\,\text{s}$	$t_f = 443.9\,\text{s}$	
Algorithm 3	*Random guidance algorithm*			execution time
	Gaussian	Gaussian	frequency steps	$t_{gui} \approx 1\,\text{h}$‡
	$t_{dwell} = 14\,\text{ms}$	$t_{dwell} = 21\,\text{ms}$	$t_f = 22\,\text{s}$	
Algorithm 4	*Random guidance algorithm*			execution time
	uniform	uniform	frequency steps	$t_{gui} \approx 2\,\text{h}$‡
	$t_{dwell} = 14\,\text{ms}$	$t_{dwell} = 21\,\text{ms}$	$t_f = 22\,\text{s}$	

¶ The hierarchy corresponds to *option 3* discussed in paragraph 4.5.
* The width of the uncertainty cone is reduced to 300 µrad.
† The width of the frequency uncertainty remains ±1 GHz.
‡ Mean execution time derived from simulation results.

Table 4.11: The acquisition algorithms used for the Monte Carlo simulations. The acronym CTV stands for constant tangential velocity.

400 s). Because in the same time frame, the frequency drifts of 10 Mhz, $K_f \Delta f_{bw} = 13\,\text{MHz}$.

The other two algorithms (3 and 4) use random patterns to scan the uncertainty area. In particular, Algorithm 3 uses a Gaussian pattern while Algorithm 4 a uniform pattern. The dwell time of the two patters is identical to the one used in the previous subparagraph. The frequency dwell time of Algorithm 3 is calculated through Eq. 4.35 choosing $L = 97\%$ and calculating P not according to the worst case offset ($\mu_{\mathbf{z}} = \mu_{\mathbf{v}} = \rho_{unc}$) but using a much more optimistic value ($\mu_{\mathbf{z}} = \mu_{\mathbf{v}} = \rho_{unc}/7$)[6]. Yields, $t_f = 22\,\text{s}$. The frequency dwell time of Algorithm 4 is also set to 22 s.

The parameters of the four algorithms are resumed in Tab. 4.11. The other solutions suggested by Fig. 4.15 are not considered in this paragraph since these behave identically to Algorithm 1 or Algorithm 2 despite the fact that their total execution time is higher.

The performance of the acquisition algorithms are evaluated using Monte Carlo simulations consisting of at least 400 runs. For each run, the initial pointing offsets, the frequency offset and the initial biases of the deviation matrix ($\varphi_{i,j,k}$ in Eq. 4.42) are randomly generated. The distribution of the frequency offset and of the biases of the deviation matrix is uniform while the distribution of the initial pointing offset is either normal or uniform according to the pattern under analysis. The correlation between the noise sources of the simulator is minimized randomly generating, at each run, the seeds of the Pseudo-random number generators according to a uniform distribution. The performance of each algorithm are evaluated using 10 µrad, 100 µrad and 1 mrad as amplitude of the dynamic offsets ($\varsigma_{i,j,k}$ in Eq. 4.42). In order to compare the performance of the four algorithms, the runs of the Monte Carlo simulations are performed repeating the same sequence of initial conditions. Unless otherwise specified, each

[6] The algorithm is designed considering the real initial offset much smaller than the width of the uncertainty cone although a worst pointing condition is also accounted repeating the frequency scan more than once (see paragraph 4.5).

run lasts 12 hours.

Split acquisition mode Vs Direct acquisition mode

In this section, the performance of Algorithm 1 are compared to the performance of Algorithm 2. Both strategies are tested using three different (increasing) magnitudes of the time variable drifts in order to evaluate the minimum stability requirement of the platform. Since Algorithm 1 simulates the split acquisition strategy, in order to reproduce as far as possible the effective mission scenario, the simulation is executed as follows:

- The target detection mode is executed for the whole 5 dimensional search space. Whenever a solution is found by one of the two satellites, the tip-tilt angles of the steering mirror are stored in a register. If the slave satellite detects the signal, also the set point of the frequency control loop is stored.
- The solution to the 5 degrees of freedom problem is used as the zero of the link attainment mode. If more than one solution is found by the algorithm, the priority goes to the latest synchronous detection. If only single sided detections are present, the last solution is used in order to minimize noise contributions.
- The link attainment mode is executed using the same time series (AOCS and frequency noise) of the target detection mode despite the fact that the simulation in now started at $t_{\text{simul}} = 172800\,\text{s}$ instead of $t_{\text{simul}} = 0\,\text{s}$. The simulation stops whenever the link is attained.

The success rate of the target detection (SR_{td}) and link attainment (SR_{la}) is calculated as follows

$$\begin{aligned} SR_{\text{td}} &= S_{\text{detect}}/S \\ SR_{\text{la}} &= S_{\text{acq}}/S_{\text{detect}} \times SR_{\text{td}} \end{aligned} \tag{4.44}$$

where S_{detect} is the number of runs where at least one of the two satellites detected the signal, S_{acq} is the total number of runs where the signal is effectively acquired and S is the total number of runs performed in one Monte Carlo simulation. Hence according to this equation, the success rate of the link attainment is representative of the effective success rate of an acquisition algorithm which implements the split acquisition strategy.

Since the dwell time of the target detection mode corresponds to the time required by the phasemeter to lock the signal (see paragraph 4.4) the simulation step is reduced from 1 ms to 0.25 ms. In order to compare the strategies, the simulations of the direct acquisition strategy use also this simulation step.

In Fig. 4.18 the success rate of the two strategies is compared. In this figure, the number of successful acquisitions of the direct acquisition mode is evaluated when the algorithm is executed only once (1 run lasts 3 h 50 min - see Tab. 4.11) and when the algorithm is continuously executed for 12 hours. According to the results shown in Fig.4.18, if the magnitude of the time varying drifts is below 100 µrad, the probability of detecting the signal is identical to the probability of acquiring it (indeed both the target detection and the direct acquisition, after 3h and 50min, have about the same success rate). Nevertheless, the probability of acquiring the signal using of the split acquisition strategy is always lower to the one of the direct acquisition strategy (independently from its execution time). Hence with a latency of 48 hours, the effective pointing and frequency noise can behave differently than expected, thus the split acquisition strategy is not the best solution for acquiring the signal.

If the magnitude of the time variable drifts is equal or bigger than 1 mrad, the split acquisition mode is definitely not a viable acquisition strategy. Therefore, according to these results, the best way to acquire the signal is to execute the direct acquisition strategy more than once. Indeed, the success rate of this strategy over a time span of 12 hours is bigger than 95% even in presence of a low pointing stability.

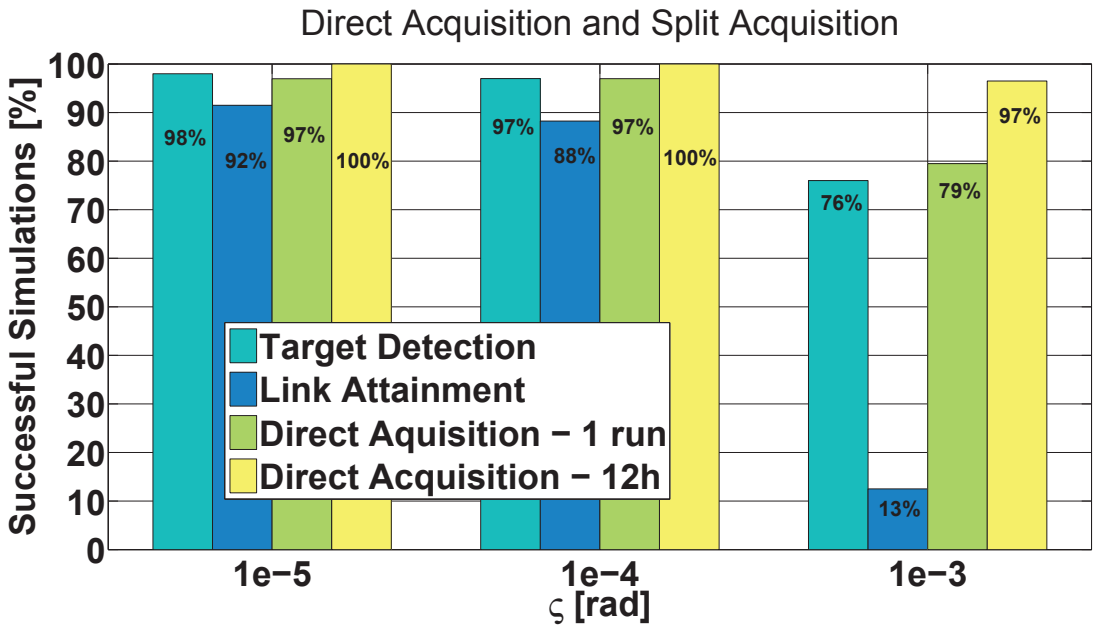

Figure 4.18: Comparison between the acquisition strategies. The success rate is evaluated over 400 simulations.

Signal acquisition using continuous patterns and random patterns

The direct acquisition strategy is here tested using random patterns and continuous patterns as guidance scheme. The comparison is made considering the initial pointing offset normally distributed (in this case, the random pattern is Gaussian) and uniform distributed (in this case, the random pattern is uniform). Once more, the simulations use different magnitudes of the time dependant disturbances.

The performance of the algorithms are evaluated as the probability of acquiring the signal to a given confidence level. This value is strongly dependant on the total number of failures (no acquisitions) observed during one Monte Carlo simulation. Given a maximum probability of failure ($\mathcal{P}_f^{max} = 1 - \mathcal{P}_{acq}$ where $\mathcal{P}_{acq}$ is the desired probability of acquiring the signal), the probability $\mathcal{P}_f$ with which the real number of failures is going to be smaller than the maximum one has a confidence level

$$C_L\left[\mathcal{P}_f \leq (1-\mathcal{P}_{acq})\right] = \frac{\int_0^{1-\mathcal{P}_{acq}} \mathcal{P}_f^{\,s_f} \left(1-\mathcal{P}_f\right)^{S-s_f} \mathrm{d}\mathcal{P}_f}{\int_0^1 \mathcal{P}_f^{\,s_f} \left(1-\mathcal{P}_f\right)^{N-s_f} \mathrm{d}\mathcal{P}_f} = I_{\mathcal{P}_f^{max}}\left(s_f+1, S-s_f+1\right) \tag{4.45}$$

where $I_{\mathcal{P}_f^{max}}$ is the incomplete beta function, S is the number of runs in one Monte Carlo simulation and s_f the number of failures occurred in these S runs. By fixing $C_L = 2\sigma$, the probability with which the algorithms are going to acquire the signal is calculated as $\mathcal{P} = 1 - \mathcal{P}_f$. Together with the acquisition probability, also the mean acquisition time (μ) and the standard deviation of the acquisition time (σ) are calculated.

Figure 4.19 depicts the acquisition success rate of the three algorithms which are tested over a time span of 12 hours. Since Algorithm 2 uses continuous patterns, its hierarchy is constrained and the slope of its success rate can be theoretically estimated assuming a success rate of 0 when the algorithm is triggered and a success rate of 1 when the algorithm is completed once. As Fig. 4.19 shows, when the magnitude of the dynamic offsets is negligible (below 100 µrad),

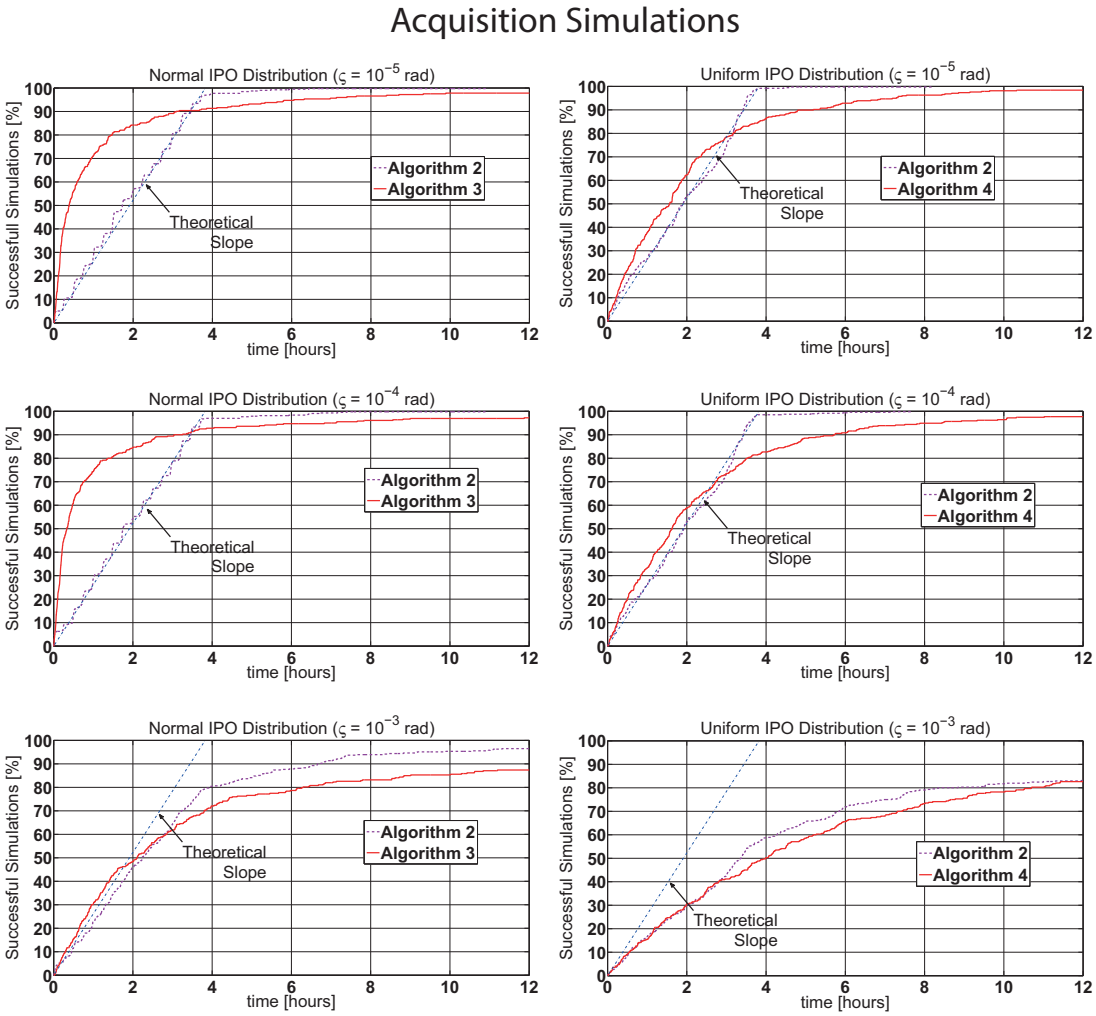

Figure 4.19: The success rates of algorithm 2 (dashed line), algorithm 3 and algorithm 4 (solid line) using different magnitudes of the dynamic offset are here depicted. The figures on the left side of this plot compare algorithm 2 to algorithm 3 since the distribution of the initial pointing offset (IPO) is Gaussian. The figures on the right side of this figure compare algorithm 2 to algorithm 4 since the initial pointing offset (IPO) is generated according to a uniform distribution.

the theoretical behaviour of the algorithm is coincident with the predicted one independently of the distribution of the initial pointing offset. Indeed, because the algorithm is executed according to a rigid structure, a solution can be found only at discrete time intervals. Each of these time intervals is wide as the dwell time of the slowest scan (this also explains the stepwise behaviour of the simulation curve). The fully predictable behaviour of Algorithm 2 is also confirmed by its performance (see Tab. 4.12). Indeed, when $\varsigma \leq 100\,\mu\text{rad}$, the sum of the mean time and its standard deviation are about equal to the execution time of the algorithm.

When the magnitude of the dynamic offsets is below 100 µrad, the acquisition success rate of Algorithm 3 rapidly increases before exhibiting a knee bend around 80% of successful acquisitions. After the knee bend, the slope of the acquisition rate decreases approaching a saturation trend. This behaviour is ascribable to the normal distribution of the initial pointing offsets that lead to a high number of simulations with initial pointing offsets close to the center of the spatial uncertainty (where the algorithm is optimized). Worse pointing condition do not compromise signal acquisition but deteriorate the guidance performances (indeed $\mathcal{P} = 96\%$

Normal IPO Distribution						
ς [mrad]	**Algorithm 2**			**Algorithm 3**		
	$\mathcal{P}$ [%] *	μ [hours]	σ [hours]	$\mathcal{P}$ [%] *	μ [hours]	σ [hours]
0.01	99.25	1.89	1.28	96	1.02	1.67
0.1	99.3	1.96	1.35	95.4	1.00	1.59
1	94.7	2.06	2.14	84	2.41	2.39
Uniform IPO Distribution						
ς [mrad]	**Algorithm 2**			**Algorithm 4**		
	$\mathcal{P}$ [%] *	μ [hours]	σ [hours]	$\mathcal{P}$ [%] *	μ [hours]	σ [hours]
0.01	99.2	1.93	1.20	97	1.98	1.96
0.1	99.2	1.97	1.23	96	2.19	2.11
1	79.9	3.27	2.47	79	3.76	3.00

* $C_L = 95\,\%$

Table 4.12: Comparison of the algorithm performance for two different conditions of the initial pointing offset (IPO). μ and σ are the mean acquisition time and the standard deviation of the acquisition time respectively.

after 12 hours).

For the same range of dynamic offsets, the trend of Algorithm 4 also shows an increase of the acquisition probability with time. Although in this case, the probability increases gradually and not rapidly since the solution is distributed over the whole uncertainty cone and not around a particular region. Since the uncertainty region is wider, a higher number of dwell spots is required before the probability of acquiring the signal is above the desired threshold (see Eq. 4.35).

When the magnitude of the dynamic offsets is equal to 1 mrad, the probability of acquiring the signal significantly drops independently from the algorithm. The success rate of Algorithm 2 is no longer coincident with its theoretical behaviour but assumes a trend which is similar to the one of a random pattern. A non-negligible amplitude of the dynamic offsets can bring the line of sight out of the uncertainty cone thus a solution may not be present in all instants of time. This is equivalent to having an uncertainty cone which changes its radius with time. When the distribution of the initial pointing offsets is normal, the Gaussian pattern is more sensible to this effect when compared to the continuous pattern ($\mathcal{P}$ of Algorithm 3 drops of almost 12% while for Algorithm 2 this quantity drops of only 5%) since the drift moves the line of sight away from the center of the uncertainty cone where the Gaussian pattern is optimized.

When the initial pointing offset is distributed according to a uniform PDF, it is more likely that the line of sight falls outside the uncertainty cone during the simulation since the number of solutions close to a border of the uncertainty cone are much higher than in the previous case. Hence, the drop of performance of the algorithms is more emphasized when compared to the case of normal distributed initial pointing offsets. Sice this affects both acquisition algorithms, their final performance is independent from the pattern implemented (the success rate after 12 hours is about the same for Algorithm 2 and Algorithm 4 - see Fig.4.19 and Tab. 4.12).

Performance of the random patters w.r.t the distribution of the initial pointing offset

The left panel of Fig. 4.20 shows the performance of Algorithm 3 and 4 when the initial pointing offset is normally distributed whereas the right panel of Fig. 4.20 shows the performance of the same algorithms when the initial pointing offset is uniformly distributed. These results are obtained using 10 µrad as the amplitude of the dynamic offsets.

Algorithm performance Vs IPO distribution						
IPO	**Algorithm 3**			**Algorithm 4**		
	$\mathcal{P}$ [%] *	μ [hours]	σ [hours]	$\mathcal{P}$ [%] *	μ [hours]	σ [hours]
Normal	96	1.02	1.66	97.2	1.89	1.74
Uniform	61.8	2.84	3.21	97	1.98	1.95

* $C_L = 95\,\%$

Table 4.13: Comparison of the algorithm performance for two different conditions of the initial pointing offset (IPO). μ and σ are the mean acquisition time and the standard deviation of the acquisition time respectively.

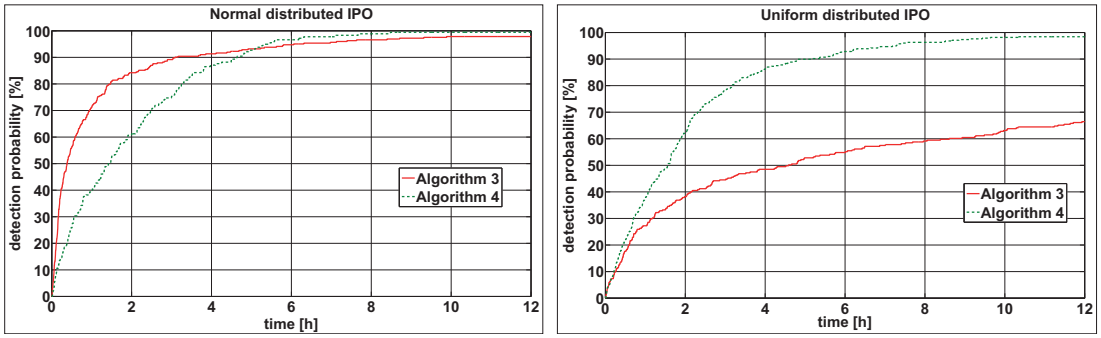

Figure 4.20: The left panel depicts the acquisition probability of algorithm 3 (solid line) and algorithm 4 (dashed line) when the distribution of the initial pointing offset is normal. In this case, both algorithms have an acquisition probability higher than 95% although algorithm 3 is faster. The right panel depicts the acquisition probability of the algorithms when the distribution of the initial pointing offset is uniform. In this case, the performance of algorithm 3 drop significantly since it is not optimized for these initial conditions. The curve of algorithm 4 is instead identical.

When the initial pointing offset is normally distributed the Gaussian pattern is capable of acquiring the signal in a small amount of time since it is optimized for this kind of initial conditions whilst, when the distribution of the initial pointing offset is uniform, the performance of this pattern drop drastically. In this latter case the algorithm is still capable of acquiring the signal, nevertheless the time it would require to reach a reasonable acquisition probability is strongly dependant on the distance between the centers of the uncertainty cones (in the extreme case of having $\mu_{\mathbf{z}}$ and $\mu_{\mathbf{v}}$ - Eq.4.28 - equal to ρ_{unc} the value of P is about 10^{-11} and $t_{rand} \approx 10^8$ s).

The uniform pattern has the same performance regardless of the distribution of the initial pointing offset because its probability of solving the spatial acquisition problem is constant. As confirmed by the simulations results of Tab. 4.13, the performance of this algorithm are the same for both a uniform and a Gaussian distribution of the initial pointing offset.

Hence, when the distribution of the initial pointing offset is unknown, it is better to use a uniform pattern since its performance are independent from the initial conditions.

4.7 Acquisition strategy using an acquisition sensor

The multidimensional scan of the acquisition algorithm can be reduced to a bi-dimensional spatial scan if the instruments mount a separate acquisition sensor (i.e. a CCD camera) with a broad field of view capable of detecting incoherent light signals.

In this case, the acquisition strategy would require that, once the acquisition algorithm is triggered, both acquisition sensors are turned on but only one of the two satellites (labelled

as the sender) performs the spatial scan while the other (labelled as the receiver) waits. Once the sender aligns the beam to the line of sight, the sensor of the receiver sees the laser beam independently from its frequency. Hence the instrument estimates the direction of the incoming light source and directs its laser beam towards it. When also the acquisition sensor of the sender detects light, the instrument can stop its spatial scan and point its laser beam in the direction of the incoming light. Now that both beams are aligned to the line of sight and the link is stable, the frequency scan is initiated in order to allow the phasemeter to lock the signal. The total degrees of freedom of the initial acquisition problem are reduce from five to two plus one, but despite this simplifications, the spatial scan and the frequency scan remain identical to the ones described previously.

In order to apply this strategy though, the alignment between the acquisition sensor and the line of sight of the instrument summed to the stability of the platform during the initial acquisition phase have to be better than the alignment requirement of the two laser beams. If this requirement is not met, the acquisition sensor can only reduce the width of the uncertainty cone. Hence the acquisition algorithm reduces to an autonomous split acquisition strategy.

For comparison, the duration of the initial acquisition is now estimated assuming the usage of a CCD camera as acquisition sensor. The integration frequency of a CCD camera is in general smaller or equal to 1 Hz and, considering also the time that the instrument needs to repoint the laser beam, the dwell time of the pattern is always $\geq 1\,\mathrm{s}$. A random pattern is unnecessary for this problem (the algorithm has no constrained hierarchy) therefore, according to Fig. 4.15, the time optimal pattern is a spiral. Using a dwell time of 2 s, $K = 0.5$, $\delta = 140\,\mu\mathrm{rad}$ and $\rho_{unc} = 3\,\mathrm{mrad}$, the spatial scan is completed in about one hour. Using a linear ramp with a slope of 50 MHz/s to scan a frequency uncertainty of ± 1 GHz, the frequency scan is completed after 40 s. Thus, such an algorithm would be six times faster than the acquisition algorithm of the LRI.

The usage of an acquisition sensor though, requires more complex data processing algorithms, tight alignment requirements between the sensor and the line of sight of the instrument and additional instrument costs. For a future mission like eLISA, the spatial scan is most likely going to be performed by rotating the entire satellite since the interferometer cannot embed a steering mirror. In this case, the usage of an acquisition sensor is mandatory for optimizing the initial acquisition.

The foreseen measurement accuracy of future geodesy missions instead does not prevent the usage of a steering mirror. Moreover, the width of the uncertainty cone could be in principle reduced, when compared to the width of the uncertainty cone of the LRI, modifying some of the design choices of the mission (i.e. refinement of AOCS algorithms, improved platform stability or usage of ion-thrusters). If the ratio ρ_{unc}/δ reduces, an acquisition algorithm which uses a random pattern could result in a valid alternative to acquiring the signal with the aid of an acquisition sensor. Indeed the complexity of the algorithm is comparable since, in both cases, spatial scans and frequency scans are independent. Nevertheless, without using an acquisition sensor, the general complexity and cost of the instrument would be much lower. Hence, additional studies in this direction would be strongly recommended for a successor mission of GRACE Follow-On.

Chapter 5

Experimental Evaluation of Sub-System Performance

This chapter describes the experimental tests that have been performed with the WPD phasemeter and with the SM in order to verify the measurement accuracy of the phasemeter, the logic of the frequency acquisition unit and the close-loop performance of the SM. It is organized as follows; paragraph 5.1 reports the tuning parameters of the phasemeter which allow to achieve the desired performance while in paragraph 5.2 are reported the results related to its measurement accuracy and the time it needs to lock to a sinusoidal input signal. Paragraph 5.3 describes the frequency acquisition experiment while paragraph 5.4 describes the tests performed with SM.

5.1 Implementation of the phasemeter in an FPGA

The phasemeter is coded in a Stratix III FPGA which is integrated in an Altera® DSP development board. It is tuned to operate in a frequency bandwidth from $1 - 25\,\mathrm{MHz}$ and with an SNR of $-11\,\mathrm{dB}$. This frequency range is chosen for compatibility with the Doppler induced frequency shifts of the beat frequency due to the orbit of the eLISA constellation [121] and with the noise performance of the photodiodes used in the eLISA interferometer [122, 123]. The operating SNR is derived from the carrier-to-noise density ratio calculated for the optical link of the GRACE Follow-On mission [40, 44, 124]. Both these parameters are used as an example application and can be chosen accordingly for a different mission scenario.

The filters of the wavelet packet decomposition tree are 13^{th} order elliptic halfband filters. They are implemented according to the minimum multiplier allpass filter structure [125] and have a maximum passband ripple of 0.5 dB. The passband edge is set at the normalized frequency $\Omega_0 = 0.25$ while the stopband starts at $\Omega_s = 0.25005$. The noise power reduction in the stopband is calculated as

$$\Delta P_n = 10 \cdot \log_{10}\left(5 + 10^{\,0.1\,\Omega_s^a}\right) \tag{5.1}$$

Using an attenuation $\Omega_s^a = 34$ dB in the stopband, Eq. 5.1 returns that the noise power is reduced by 3 dB in each stage. The phasemeter presented is designed to detect signals with an SNR of $-11\,\mathrm{dB}$. In order to operate the phase-frequency detector DPLL with an SNR grater than $5\,\mathrm{dB}$ the wavelet packet decomposition tree requires 6 stages.

For this specific application, the up-sampling stage is tuned such that the interference signal is always located in a frequency region equivalent to the third and forth sub-band of the wavelet packet decomposition tree, although this is not a strict requirement. The first two filters of the up-sampling unit are the same as the ones used in the wavelet packet decomposition tree. The last filter of the up-sampling unit (labelled as LPF* in Fig. 2.11) is a 5^{th} order elliptic low-pass filter with a cut-off frequency of 2.5 MHz and is used for anti-imaging.

The phase accumulator of the phase-frequency detector has to return a frequency value with an accuracy compatible with the pull-in range of the main DPLL. Using a clock frequency of 50 MHz and a phase accumulator with a register length (reg) of 16 bits, the uncertainty in the estimated frequency is

$$f_{unc} = \frac{f_c}{2^{reg}} \approx 763 \text{ Hz} \tag{5.2}$$

which is sufficiently accurate for the main DPLL to pull-in and lock to the interference signal. The parameters used to tune the loop filter of the phase-frequency detector DPLL have been derived empirically and are listed in Tab. 5.1.

K_a	K_p	K_i
$1 - 2^{-6}$	2^{-5}	2^{-14}

Table 5.1: Coefficients of the phase-frequency detector DPLL.

The coefficients used to tune the main DPLL are evaluated using its linear transfer function. The LPF used for the mixing phase detector is an infinite impulse response Butterworth filter of 3$^{\text{rd}}$ order and is implemented as a cascade of first order filters.

$$\begin{gathered} H_{a_i}(z) = \frac{a_i \cdot z}{z - (1 - a_i)} \text{ with } i = 1, 2, 3 \\ \downarrow \\ H_{\text{LPF}}(z) = H_{a_1}(z) H_{a_2}(z) H_{a_3}(z) \end{gathered} \tag{5.3}$$

with $z = e^{j2\pi f T_s}$ and T_s is the sampling time. The phase detector is expected to work in its linear range and can be modelled using the relation $K_{\text{MPD}} = A/2$ where the condition $A = 1$ is guaranteed by the automatic gain controller. The transfer function of the loop-filter is equal to

$$H_{\text{LF}}(z) = K_P + \frac{K_I T_s z}{z - 1} \tag{5.4}$$

The numerically controlled oscillator is modeled as in integrator and its transfer function is

$$H_{\text{NCO}}(z) = \frac{z}{z - 1} \tag{5.5}$$

In order to operate the main DPLL with a high clock frequency, pipelining is required. For this particular application, pipelining introduces a delay of five clock cycles

$$H_{\text{d}}(z) = z^{-5} \tag{5.6}$$

Combining Eq. 5.3, Eq. 5.4, Eq. 5.5 and Eq. 5.6 yields the open and close loop transfer functions of the main DPLL.

$$\begin{gathered} H_{\text{OL}}(z) = K_{\text{MPD}} H_{\text{LPF}}(z) H_{\text{LF}}(z) H_{\text{NCO}}(z) H_{\text{d}}(z) \\ H_{\text{CL}}(z) = \frac{H_{\text{OL}}(z)}{1 + H_{\text{OL}}(z)} \end{gathered} \tag{5.7}$$

Table 5.2 lists the coefficients of the LPF and the loop filter used to tune the main DPLL in acquisition and measurement mode respectively.

The computational resources required for implementing the frequency estimation stage are listed in Tab.5.3 together with the ones required for implementing a DFFT algorithm [126]. The size of the DFFT algorithm (4096) is chosen for compatibility with the frequency resolution required to initialize the main DPLL when the bandwidth of the phasemeter is 24 MHz. The

Close-Loop BW	f_c	a_1	a_2,a_3	K_p	$K_i \cdot T_s$
61 kHz	185 kHz	2^{-5}	2^{-4}	2^{-6}	2^{-15}
8 kHz	23 kHz	2^{-8}	2^{-7}	2^{-9}	2^{-21}

Table 5.2: LPF and loop filter coefficients of the main DPLL. These coefficients are valid for an input signal with unitary amplitude. BW is the acronym of bandwidth.

frequency estimation stage requires a high number of look-up tables and logic registers (mainly ascribable to the 12 filters used in the wavelet packet decomposition tree) but the use of memory (expressed in Bits) and multipliers (18 × 18 blocks) is significantly reduced. Unlike the frequency estimation stage, the DFFT itself is not capable of initializing the main DPLL but requires an additional subsystem or logic algorithm. The computational resources required by this additional subsystem (or logic algorithm) are not included in Tab.5.3.

Algorithm	LUTs	Logic Reg.	Memory	18x18 blocks
FES	37,072	23,290	8,388	2
4096 DFFT*	4,540	6,545	171,611	40
$\Delta\%$	$-87,75\%$	$-71,9\%$	$+1945,91\%$	$+1900\%$
4096 DFFT†	27,325	29,709	316,579	80
$\Delta\%$	$-27,46\%$	$+27,56\%$	$+3674,2\%$	$+3900\%$

* fixed point.
† floating point.

Table 5.3: Computational resources required to implement the Frequency Estimation Stage (FES) and a DFFT in the same FPGA.

5.2 The performance of the phasemeter

The phasemeter performance has been tested with a laboratory setup using signal generators. The phasemeter is operated using a sampling frequency of 50 MHz. The analog signals are digitized via a data conversion card which has two ADCs. A serial port is used to interface the DE3 board with a PC for data postprocessing (see Fig. 5.1).

A non-negligible noise source which directly influences the accuracy with which the phase is measured is the ADC aperture jitter [127, 128]. This jitter derives from the ADC uncertainty in sampling the analog signal in equidistant time intervals (the sampling interval is not Δt but $\Delta t + \epsilon(t)$). The consequent phase error

$$\begin{aligned} \phi_{if}(t) &= 2\pi f_{if}\left[t + \epsilon(t)\right] \\ &= 2\pi f_{if} t + \underbrace{2\pi f_{if}\epsilon(t)}_{\phi_j(t)} \end{aligned} \tag{5.8}$$

can be interpreted as phase noise. A possible mitigation strategy for this effect is to use a pilot tone which measures the aperture jitter with an additional phase stable signal at a different frequency. The pilot tone signal is applied to the ADC in parallel to the interference signal in order to have a common mode for both signals. As the aperture jitter also leads to a phase shift in the pilot tone (ϕ_j^p), this can be used to correct the phase of the interference signal

$$\phi_{if}^{corr}(t) = \phi_{if}(t) - \frac{f_{if}}{f_p}\phi_j^p \tag{5.9}$$

where the pilot tone frequency f_p is chosen to be slightly higher than the sampling frequency [57, 129]. For these performance tests, the pilot tone frequency is set to 50.3 MHz.

Since the measurement signal used to test the phasemeter is produced by a signal generator, it will be referred in the continuation of this paragraph as the input signal.

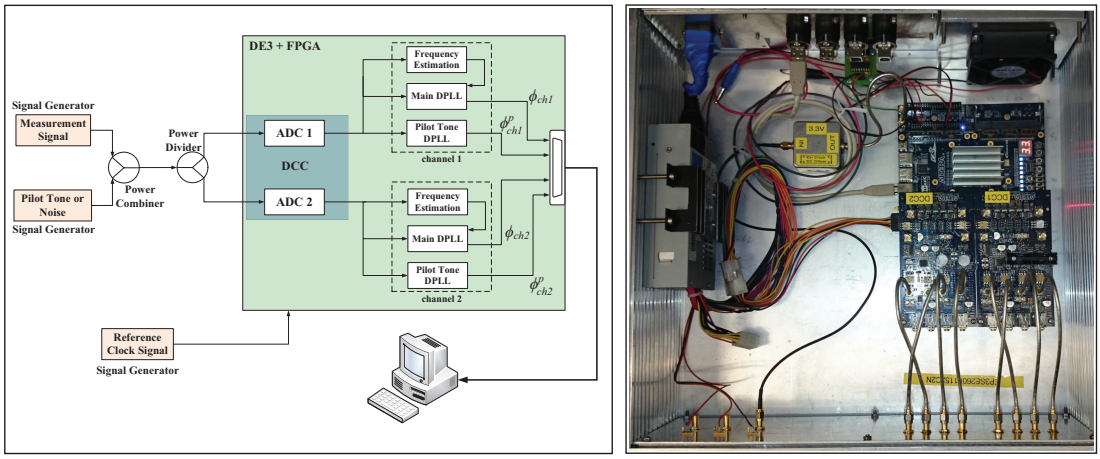

Figure 5.1: The left panel shows a schematic representation of the measurement setup while the right panel depicts the DE3 board with the integrated FPGA. Although two data conversion cards (DCCs) are connected to the board, only DCC1 is used for testing the phasemeter.

5.2.1 Time required to lock the input signal

An important feature of the phasemeter is the time it requires to lock the input signal. This time interval can become crucial especially for a operational phase of the mission such as the initial acquisition.

The locking time of the phasemeter is evaluated by switching the input signal between ADC1 and ADC2 every 20 ms and recording the time sample when the main DPLL achieves lock. This test is performed with the main DPLL set to acquisition mode and adding white Gaussian noise (in place of the pilot tone) to the input signal in order to simulate a low SNR environment.

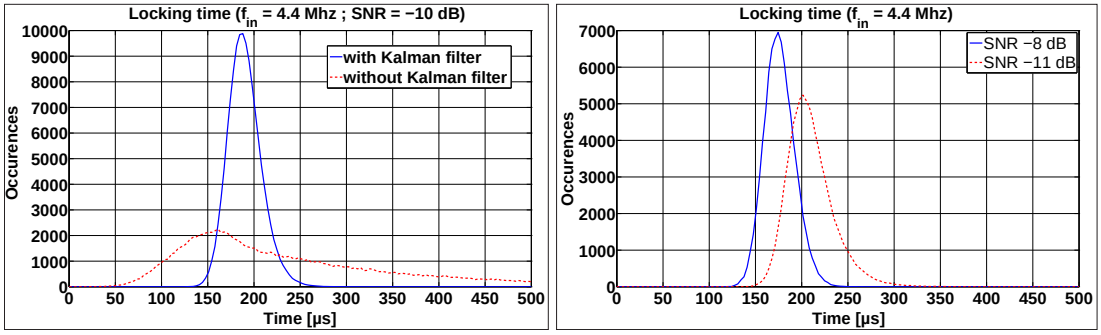

Figure 5.2: The left panel of this figure shows the trend of the time required by the phasemeter to lock the input signal. The solid line depicts the trend when the Kalman filter is implemented in the frequency estimation stage while the dashed line depicts the trend when the Kalman filter is omitted. During this test, 91689 locking attempts are performed. The right panel of this figure shows the trend of the time required by the phasemeter to lock the input signal when using −8 dB (solid line) and −11 dB (dashed line) as SNRs. During this test, 89842 locking attempts are performed.

The left panel of Fig. 5.2 depicts the acquisition time trend when the phasemeter is operated with and without the Kalman filter. After the Kalman filtering process, the estimated frequency

value of the input signal, derived from the phase-frequency detector DPLL, is further improved. The main DPLL is initialized with a frequency value which is within its lock range reducing the overall time required by the phasemeter to lock the input signal.

The right panel of Fig. 5.2 depicts the acquisition time trend using two different SNRs for the input signal. With a higher SNR, the frequency estimate is more accurate and the time the main DPLL needs to lock reduces. With a lower SNR the uncertainty of the system in detecting the correct input frequency slightly worsens (the dashed line in Fig. 5.2 has a wider spread of data on the time axis). Nevertheless, the mean time the main DPLL needs to lock is increased by only 34 µs. When using the Kalman filter the overall locking time is below 500 µs for all the test cases.

The test results are summarised in Tab.5.4. They are obtained using an input signal with a reference frequency of 4.4 MHz. Additional tests showed that these results are representative of the performance of the phasemeter across its operating frequency range.

f_{input}	KF	SNR	MLT	σ	LT $<$ 500 µs
4.4 MHz	No	-10 dB	258 µs	100 µs	92.52% of cases
4.4 MHz	Yes	-8 dB	176 µs	16 µs	100% of cases
4.4 MHz	Yes	-10 dB	190 µs	18 µs	100% of cases
4.4 MHz	Yes	-11 dB	210 µs	25 µs	100% of cases

Table 5.4: Locking performance of the phasemeter. KF, MLT and LT are the acronyms of Kalman filter, Mean Locking Time and Locking Time respectively while σ is the standard deviation of the locking time.

5.2.2 Phase measurement accuracy

The measurement accuracy of the phasemeter is compared with the canonical one used for the eLISA mission

$$\Delta\phi_{\mathrm{eLISA}} < 2\pi \times 10^{-6} \sqrt{\left[1 + \left(\frac{2.8 \times 10^{-3}}{f}\right)^4\right]} \tag{5.10}$$

which is expressed as rad/$\sqrt{\text{Hz}}$. eLISA is expected to measure gravitational waves in a frequency range that spans from 0.1 mHz to 1 Hz. In this band, the phasemeter has to fulfill the requirement without introducing measurement artifacts.

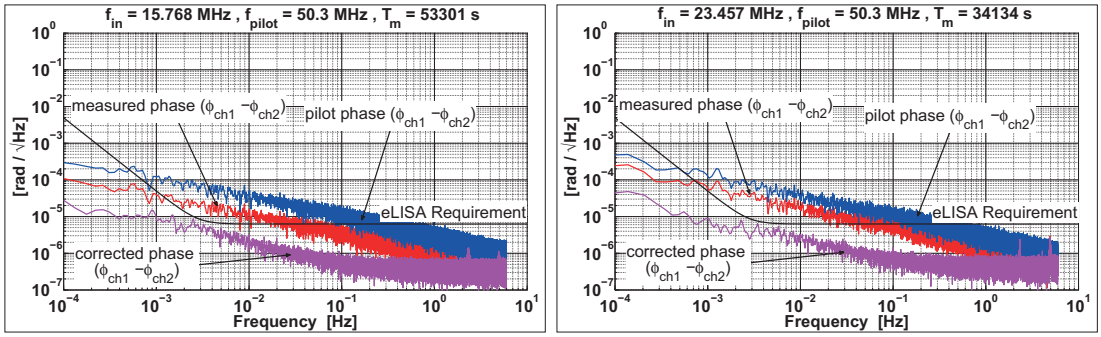

Figure 5.3: The left panel shows the phase measurement performance of the phasemeter using an input signal of 15 MHz. This measurement is performed over a time-span of 15 hours. The right panel shows the phase measurement performance of the phasemeter using an input signal of 23 MHz. This measurement is performed over a time-span of almost 10 hours.

The phase measurement accuracy is evaluated by calculating the difference between the phase of the input signal measured from the two ADC channels ($\Delta\phi = \phi_{\mathrm{ch1}} - \phi_{\mathrm{ch2}}$). The

results are presented as ASD of the measurement data set. Figure 5.3 depicts the measurement performance of the main DPLL using two different input frequencies (15 MHz and 23 MHz respectively). The plots show that, in order to fulfill the eLISA requirement, the pilot tone correction is mandatory. Both plots also depict two spikes on the corrected phase curve at ~ 2.5 Hz and ~ 5 Hz. These artifacts are introduced by the fan system used to cool-down the FPGA during overnight measurements. They do not compromise the measurement performance as they are below the requirements and not in the frequency range of interest.

5.3 Validation of the frequency acquisition logic

This paragraph summarises the results of a frequency acquisition experiment performed using the WPD phasemeter presented in chapter 2. The detailed descriptions of the electronics and of the parameters which have been selected to perform this experiment are available in the master thesis of Oliver Mandel.

This experiment aims to reproduce as far as possible the scenario of the initial frequency acquisition problem described in chapter 4. For such a reason the setup includes two solid state infrared Nd:YAG NPRO lasers (continuous wave) with a wavelength of 1064 nm [130, 131] one of which is locked to a reference cavity while the other is free running. Nevertheless, due to the reduced complexity of the acquisition problem (no spatial scans are necessary), the cavity stabilized laser functions as an external reference and the setup requires only one phasemeter and one laser control unit (both embedded in the same FPGA) which are used to control the free-running laser (this laser represents the slave satellite in the acquisition problem).

5.3.1 Cavity stabilized laser

In this experiment, the reference beam is obtained locking one of the two lasers to a high finesse optical cavity resonator [132, 133] using the Pound-Drever-Hall technique [134]. The environmental disturbances are suppressed by placing the cavity within a vacuum chamber. Such device allows to fulfill the phase stability requirement of the LISA mission [135]. Figure 5.4 depicts the cavity setup which is used to obtain the stabilized beam for the experiment.

5.3.2 The heterodyne setup

A schematic representation of the heterodyne setup is depicted in Fig. 5.5 while the real setup is depicted in Fig. 5.6. The elliptical polarization of the free-running laser is converted into a linear polarization using a tunable $\lambda/4$ wave plate and is further rotated using a $\lambda/2$ wave plate. The optical isolator avoids that the laser beam flows back to its source and also allows to adjusted the power of the laser beam that leaves the isolator by tuning the $\lambda/2$ wave plate embedded in the isolator. The power of the beam that leaves the isolator is set to 0.5 mW.

The power of the cavity stabilized laser is also adjusted through a tunable $\lambda/2$ wave plate to 0.5 mW before this is interfered with the free-running laser at the 50 : 50 beam splitter. The mirrors between the $\lambda/2$ wave plate and the beam splitter are inserted for aligning purposes.

Before reaching the measurement photodetector the superimposed beam passes through two neutral density filters (ND 2.0 and a ND 1.25 filter in Fig. 5.5) in order to attenuate the power of the superimposed beam from $\approx 224\,\mu$W to ≈ 126 nW. The photodetector is a New Focus Model 1811 with a bandwidth that goes from DC to 125 MHz. The readout of the photodetector is processed by its internal transimpedance amplifier and afterwards amplified by two channels of a SRS SR445A amplifier (the total voltage gain of 25). Because of the low optical power of the superimposed beam and because of the noise introduced by the two amplification stages, the input signal at the ADC board of the phasemeter has an SNR which is comparable with the expected SNR of GRACE Follow-On. Since the bandwidth of the photodetector is higher than the sampling frequency of the ADC (50 MHz), an anti-aliasing LPF is used before the ADC

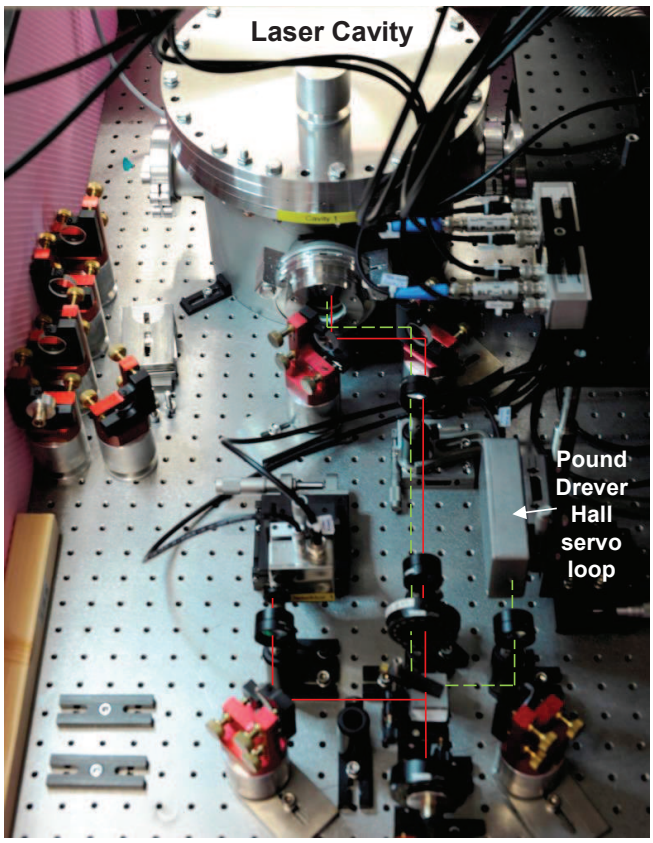

Figure 5.4: This picture shows the optical setup used to generate the cavity stabilized beam. The solid line indicates the beam routing towards the cavity while the dashed line indicates the beam routing from the cavity to the Pound-Drever-Hall servo loop.

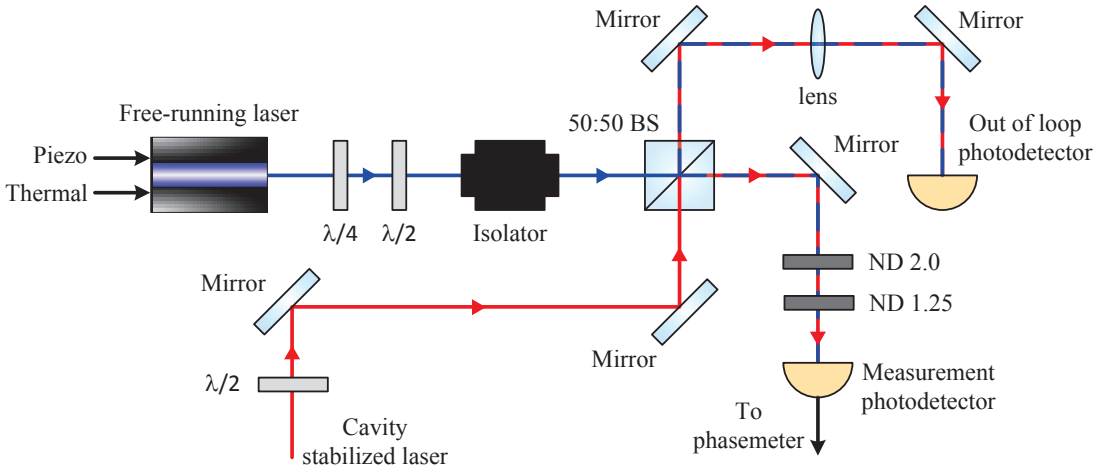

Figure 5.5: This picture depicts the layout of the optical setup used to test the frequency acquisition.

in order to avoid that the phasemeter locks to an aliased frequency. (i.e. a beat frequency of 40 MHz is aliased to 10 MHz). The filter has a Chebyshev filter response [125] with a passband ripple of 0.43 dB and a cut-off frequency 17.7 MHz.

The superimposed beam is also routed to a second photodetector for out-of-loop measurements. This photodetecotr is an EOT ET-3500 with a bandwidth of 12.5 GHz. The high bandwidth of this photodiode allows to track the frequency of the beat signal even when the

free-running laser is performing its frequency scan. A lens is introduced in this light path in order to correctly image the superimposed beam of the active area of the photodiode (about 32 µm wide).

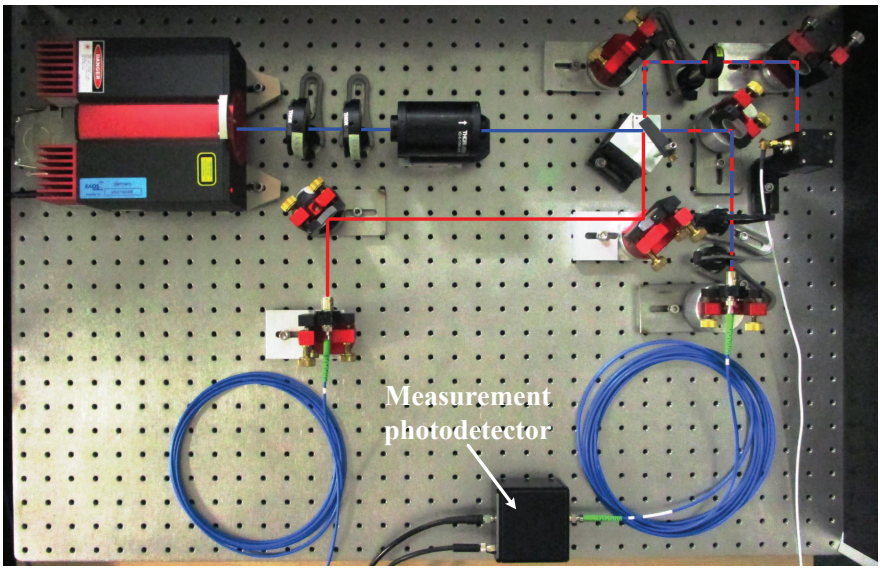

Figure 5.6: This picture shows the real setup used to test the frequency acquisition. Contrary to the schematic representation of Fig. 5.5, the superimposed beam is fiber coupled before reaching the measurement photodetector. The $\lambda/2$ wave plate shown on the path of the cavity stabilized laser of Fig. 5.5 is also here not present since it is placed in the optical setup of the cavity.

5.3.3 Frequency acquisition results

The frequency offset between the two lasers is generated biasing the temperature of the crystal of the free-running laser. The frequency scan covers an uncertainty area wide ±500 MHz and is implemented as a series of discrete steps which have an amplitude of 7 MHz and a length of 200 ms. These values return a scan rate of 35 MHz/s and an overall scan time of 1 min. In order to avoid that the frequency grows infinitely in case of a missed detection, the sign of the step function is inverted once the frequency control loop of the laser reaches the boundary of the frequency uncertainty. The discrete step function of the frequency scan is obtained combining the modulation of the piezo-electric input and the thermal input of the laser. Indeed, a steep edge of the stair function can be obtained only through the piezo-electric modulation, but since its tuning rate is limited (the piezo-electric control can change the frequency of the laser only up to 100 MHz) it cannot cover the whole width of the uncertainty region. For such a reason the thermal input is modulated using a linear ramp while the piezo-electric input is modulated with an inverse sawtooth function whose slope is opposite to the slope of the ramp of the thermal modulation. The time trend of the frequency modulation of the free-running laser is thus a step function (see Fig. 5.7).

Once the phasemeter locks, the band detection logic implemented in the FPGA stores the value of the beat frequency in a register and afterwards commands the piezo-electric driver to increase the laser frequency of 1 MHz using a step function. In order to prevent that the step command brings the beat frequency outside the bandwidth of the phasemeter, the frequency scan is stopped only if the beat frequency is between 3 MHz and 18 MHz. For 0.5 ms after the step command, the frequency value stored in the register is subtracted from the current beat frequency in order to evaluate if the beat frequency has increased or has decreased after the 1 MHz frequency step. Since the step command unlocks the main DPLL (because of its limited bandwidth), the phasemeter tracks the beat frequency using the Kalman filter until the

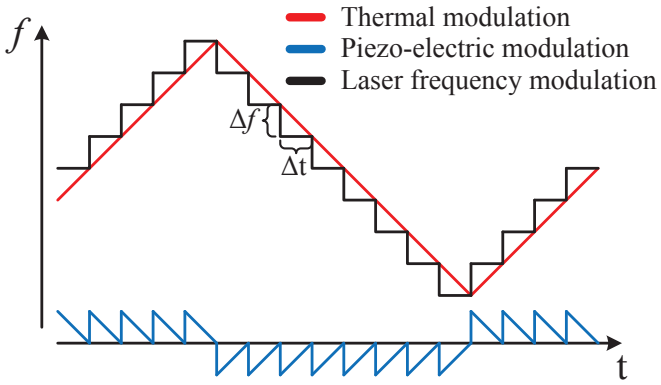

Figure 5.7: Representation of the time trend of the piezo-electric modulation, thermal modulation and their combination.

main DPLL locks again to the beat signal. Afterwards, the phasemeter waits 2 ms (it ensures that the link is stable) before activating the frequency control-loop which reduces/increases the frequency of the free-running laser in order to bring the beat frequency to 10 MHz.

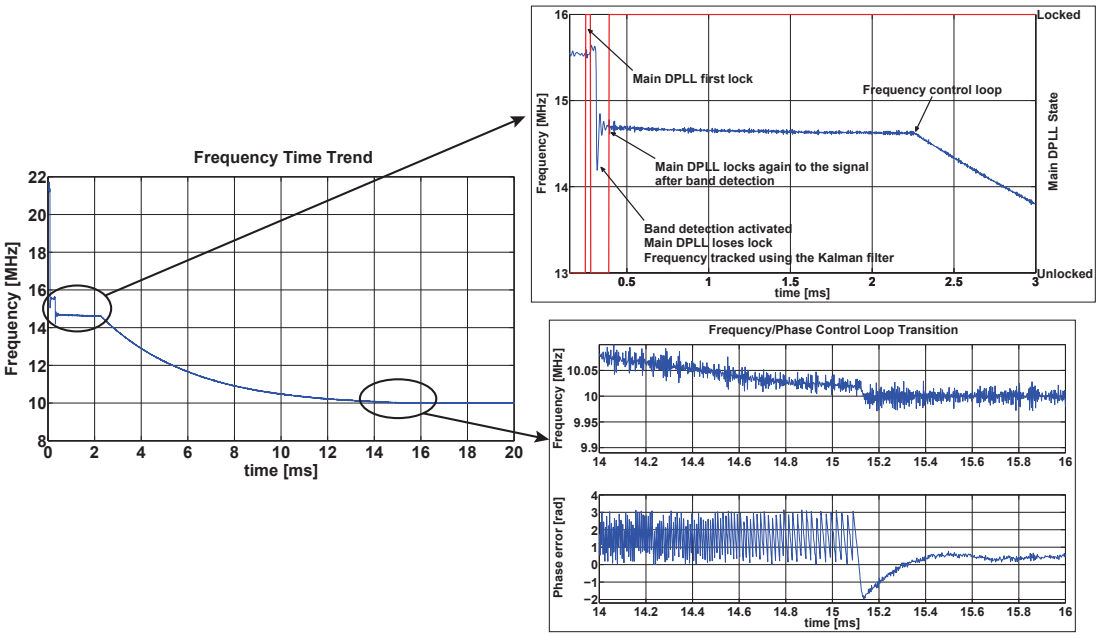

Figure 5.8: This picture depicts the frequency trend before and after the phasemeter acquires and phase-locks the two lasers. Since the beat frequency decreases after the step command, the frequency of the free-running laser is lower than the frequency of the cavity stabilized laser.

Figure 5.8, depicts the time trend of the heterodyne frequency as the phasemeters locks to the beat signal. Despite the lack of memory resources in the FPGA limit the amount of measurement data that can be stored (only 20 ms at the sampling frequency) these are sufficient to show the whole detection and lock process. In the close-up of the firs 3 ms it is possible to see all the logic phases implemented in the phasemeter in order to rapidly detect the correct sign of the frequency offset before activating the frequency control loop. Once the sign of the frequency offset is detected, the frequency control loop is activated in order to match the beat frequency to the reference frequency. As a result of the slow response of the laser crystal temperature, the frequency control loop uses both the thermal and the piezo-electric inputs. Once the frequency error is sufficiently small (after 14.83 ms in Fig. 5.8) the phase control loop

is activated and the free-running laser is phase-locked to the cavity stabilized one.

In order to estimate the time necessary to lock the phasemeter to the beat signal, the frequency acquisition test is repeated for a total of 9491 times. Once the phasemeter locks to the beat signal a random number generator is used to bias the temperature of the laser crystal (such that the frequency offset between the lasers is between −200 MHz and 200 MHz) and to reset all the states and parameters of the phasemeter (i.e. gain of the automatic gain controller). After that the temperature of the laser crystal stabilizes (this takes about 6 s) the frequency acquisition is re-started. Figure 5.9 depicts the distribution of the time necessary to acquire the signal during the 9491 signal acquisition attempts while table next to it summarises the measurement results. The linear sum of the measurement times is, also in this case, always below 500 µs.

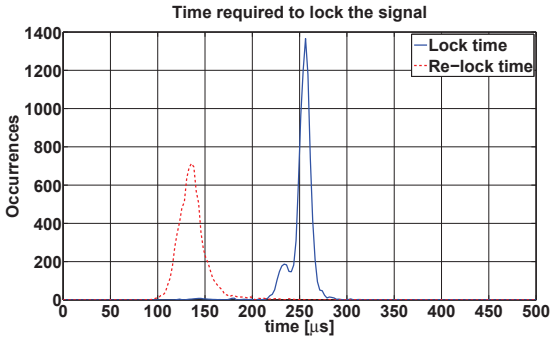

	μ [µs]	σ [µs]
Lock time	252.9	14.5
Re-lock time	140.6	18.3
Linear sum	**426.3**	

Figure 5.9: The picture on the left depicts the distribution of the locking time of the phasemeter. The solid line represents the time required by the phasemeter to lock the beat signal once this is within its bandwidth, while the dashed line is the time the phasemeter needs to relock the beat signal after that the band detection subsystem applies the 1 MHz step to the piezo-electric input. The total time the phasemeter needs to lock the beat signal is given by the sum of these two values. The table on the right summarises the result shown in the picture. μ and σ represent the mean locking time and its standard deviation.

5.4 Testing the SM close-loop control

The SM which has been used to perform the close-loop performance tests is an engineering model of the SM used for the first generation laser communication terminal. These tests are aimed to validate the SM model presented in chapter 3 and to evaluate its pointing accuracy when performing a bi-dimensional scan. The bandwidth of the controller designed for these tests is limited to 1 kHz. For higher frequencies the pointing performance of the SM deteriorate drastically because of its mechanical dynamics and because of limitations coming from its voice motor coils.

5.4.1 The experimental testbed

The test setup is realized in a ISO 14644-1 Class 5 laboratory. The SM is mounted on a 2 degrees of freedom turntable (Pitch and Yaw angles). Pitch rotations of the assembly are achieved using a Newport RV120HAT drive with a dedicated Newport ESP300 universal motion controller. The Yaw rotations of the turntable are performed using a Berger Lahr VRDM5910/50 stepper motor with a Heidenhain encoder for position feedback. The controller of the stepper motor is a Huber SMC9000. Both Yaw and Pitch angles are controlled in closed-loop in order to make sure that the exact position and inclination of the SM housing is known. The angular tilt of the mirror is evaluated using Kaman eddy-current sensors while the sensors electronics is from the Kaman KD-5100 series. The pointing commands are transmitted to the SM and

to the turntable using a Mathworks real-time system xPC target while the measurements from the sensors are acquired through a PCI-6052 card provided by National Instruments. A Newport LDS1000 autocollimator is placed in front of the housing of the SM and functions as an additional readout for evaluating the effective pointing of the SM. For the tests hereafter presented, the zero position of the mirror is chosen such that the autocollimator controller indicates that the actual tip-tilt angle of the mirror plane about its two rotating axes is zero.

The top left panel of Fig. 5.10 shows a SM similar to the one used to perform the tests (the picture shows the flight model of the SM of GRACE Follow-On) while the lower left panel of Fig. 5.10 shows the SM in its housing within the turntable. An overview of the whole setup is given in the right panel of Fig. 5.10. Figure 5.11 is a schematic representation of the experimental setup depicted in Fig. 5.10.

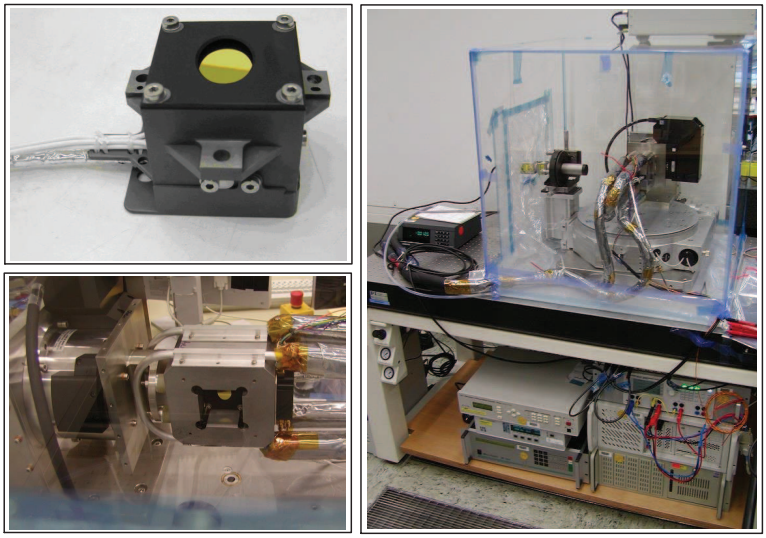

Figure 5.10: The pictures show a SM and the experimental setup used to test its pointing performance in close-loop. The SM shown in this figure is not the one used for the tests but is one of the three flight models of the LRI of GRACE Follow-On. Contrary to the flight model, the mirror of the engineering model used to conduct the tests has a silver coating rather than a gold coating.

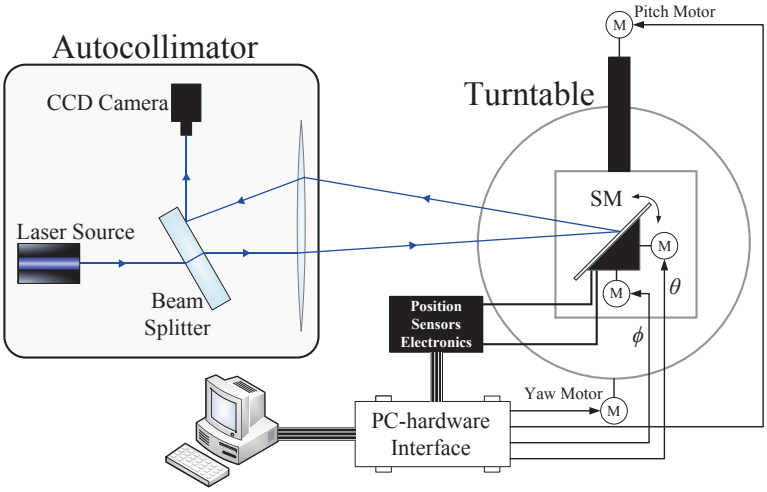

Figure 5.11: Schematic representation of the SM experimental setup.

5.4.2 Pointing performance results

The close-loop pointing accuracy of the mirror has been initially tested using a Lissajous pattern and a constant tangential velocity spiral. 5 ms and 1.4 mrad are, respectively, the dwell time and the amplitude of the bi-dimensional area used to tune the patterns equations. The trend of the constant tangential velocity spiral is inverted every time this pattern reaches the maximum distance from its center. As the plots of Fig. 5.12 show, with the selected dwell time, the mirror is capable of following the setpoint on both axes without introducing any distortion to the final pattern.

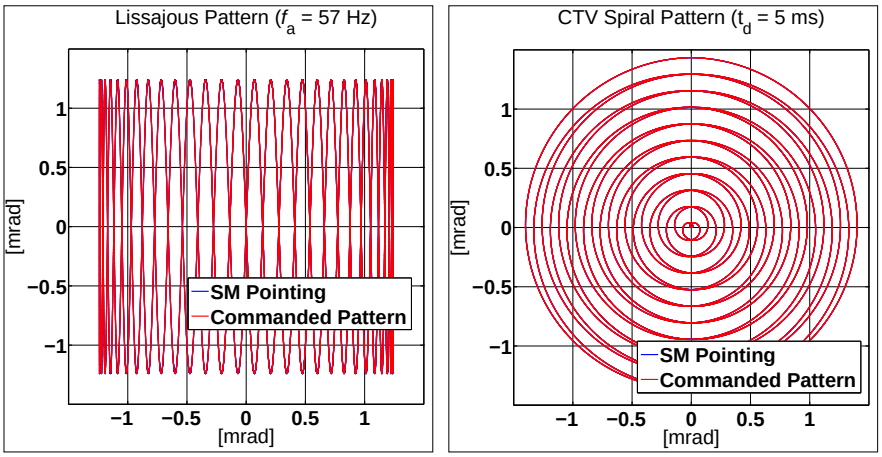

Figure 5.12: This figure depicts the pointing accuracy of the SM when this tracks a Lissajous pattern (left panel) and a constant tangential velocity (CTV) spiral. For both patterns the dwell time is set to 5 ms. The frequency of the Lissajous is calculated using Eq. 4.14 (or Eq. 4.15) and dividing the result by 2π.

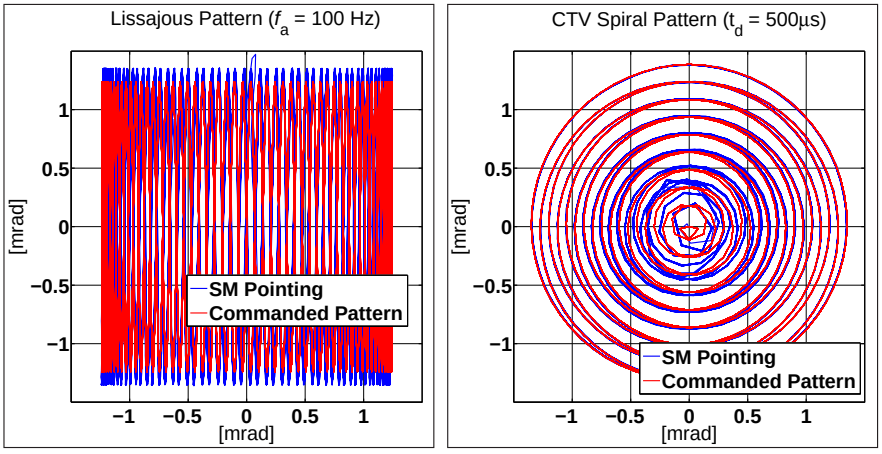

Figure 5.13: This figure shows the Lissajous pattern and constant tangential velocity (CTV) spiral commanded for the bi-dimensional area scan and the curves effectively followed by the SM.

The same test is repeated increasing the frequency of the fast axis of the Lissajous pattern to 100 Hz and reducing the dwell time of the spiral pattern from 5 ms to 0.5 ms. The Lissjous pattern designed by the SM (left panel of Fig. 5.13) is not anymore perfectly coincident with the commanded curve. Indeed, the mirror pointing is delayed with respect to the commanded angle and this causes an overshoot at the peak points of this guidance. Despite this error, the overall pattern is not significantly distorted and could be used for performing the initial acquisition if the peak overshoot is properly compensated by a reduction of the maximum

amplitude of the commanded angle.

The right panel of Fig. 5.13 compares the commanded spiral pattern with the one effectively drawn by the SM. As the picture shows, although in the outer boundary setpoint and mirror pointing overlap, the center presents an unacceptable distortion making this pattern unusable. A similar result is obtained replacing the constant tangential velocity spiral with a hybrid spiral. Indeed, the distortion is not caused by the pattern itself but by the fact that close to the center of the spiral, the setpoint in X and Y has a small amplitude and varies rapidly in time. Thus, even a small error/delay between setpoint and commanded angle distorts severely this family of patterns.

Unfortunately, because the time slot allocated in the cleanroom of Airbus for this test campaign was very limited (due to ongoing testing on the SM flight models of GRACE Follow-On), it was not possible to evaluate the pointing improvement introduced by the feedforward controller presented in chapter 3. For such a reason, further test are strongly recommended.

Chapter 6

On-Ground Calibration of the Laser Range Measurement

The laser ranging interferometer is designed to accurately measure the distance variation between the center of masses of the satellite pair along the longitudinal axis of the optical link. One of the noise sources that worsens the accuracy of the range measurement is the mechanism which couples the rotations of the laser instrument into an apparent longitudinal signal. This mechanism is commonly known as TPC noise. In Chapter 2, different sources of TPC noise are introduced and investigated. In this chapter, the term TPC noise is referred only to the noise mechanism caused by the misalignment between the measurement fiducial point of the instrument and the fiducial point of the accelerometer. Although the variations of the optical properties of the instrument (and therefore baseline changes of the fiducial point of the instrument) can be measured during the mission, their accuracies are often insufficient to mitigate the TPC to acceptable magnitudes.

The apparent longitudinal signal introduced in the range measurement by rotating one satellite of ϑ with respect to the longitudinal axis of the optical link is equivalent to the one introduced by multiplying ϑ with an appropriate scaling factor or *coupling coefficient*. Since the major spectral content of the attitude jitter of the satellites is in the measurement bandwidth of the instrument, the TPC noise cannot be removed by simple data filtering but requires a dedicated calibration procedure.

The TPC noise calibration consists in determining the coupling coefficient for each rotational degree of freedom of the two satellites. The coupling coefficients together with the pointing knowledge of the satellite can be used to correct, on ground, the range measurement. Since the pointing knowledge is at least one order of magnitude better than the pointing performance if, via calibration, the coupling coefficients are accurately determined, the on ground correction of the range measurement is an efficient way of mitigating the TPC noise.

The reminder of this chapter is organized as follows: paragraph 6.1 describes the calibration algorithm. In paragraph 6.2, the calibration algorithm is used to correct a simulated range measurement. In paragraph 6.3 and 6.4, the calibration process is applied using the range measurement data of the GRACE mission. The final paragraphs of this chapter discuss additional features that can enhance the calibration process and its applicability for future space missions.

6.1 Formulation of the calibration process

The TPC noise can be seen as a change of the phase of the light signal introduced when the instantaneous center of rotation of the optical wavefront is not coincident with its originating point. Geometrically this is equivalent to the distance variation between two points on two separate surfaces caused by the rotation of one of the two surfaces about a third point lying on it. According to this last definition, the total pathlength variation introduced by the lever

arm between the origin of the optical wavefront and its rotation point can be rewritten as a function of the magnitude of the rotation ϑ

$$n_{TPC} = \sum_{i=1}^{\infty} C_i \vartheta^i = C_1 \vartheta + \mathcal{O}^2 \tag{6.1}$$

where C_i are coefficients that couple attitude to noise. In agreement with the geometrical interpretation of the mechanism which generates TPC noise, rotations around the axis of symmetry of the laser beam do not introduce, at first order, apparent range changes ($C_1 \vartheta = 0$).

In order to measure the displacement between the two orbiting satellites, the ideal originating point of the wavefront of each laser interferometer has to be coincident with the fiducial point of the accelerometer. The angles responsible of the TPC noise are, therefore, the angles of Roll, Pitch and Yaw of the body frame with respect to the line of sight of the laser instrument. For the GRACE Follow-On mission, the pointing requirement for science operations is $\pm 10\,\text{mrad}$ (1σ) in Roll and $\pm 0.3\,\text{mrad}$ (1σ) in Yaw and Pitch [120]. Simulation studies (see paragraph 6.2.1) have shown that the magnitude of the coupling coefficients of the higher order terms (C_i with $i \geq 2$) never exceeds $10^{-3}\,\text{m/rad}$. According to Eq. 6.1, their contribution to the TPC noise is, in a worst case pointing condition, always below 0.1 nm. Future geodesy mission are expected to have attitude pointing performance equal or better than the ones of GRACE Follow-On while the requirement on the TPC noise is of a few tens of nanometers ($\approx 20\,\text{nm}$) [81]. A noise contribution of 0.1 nm can be considered negligible in the overall noise budget, therefore only the linear terms are considered hereafter relevant for the TPC noise.

The variation of the longitudinal distance between the CoMs of the two satellites measured by the instrument can be split in the gravity field contribution and the noises contribution. Among the noises, the longitudinal range error given by the TPC noise can be modelled as the sum of the six attitude signals (three rotational degrees of freedom per single satellite) each multiplied by a coupling coefficient. Separating the TPC noise from the other noises yields

$$s(t) = g_s(t) + \sum_{\text{master}} C_1^j \vartheta_j(t) + \sum_{\text{slave}} C_1^j \vartheta_j(t) + n(t) \quad \text{with } j = \text{Roll}, \text{Pitch}, \text{Yaw} \tag{6.2}$$

where $s(t)$ is the range measurement, $g_s(t)$ is the contribution of the gravity field to the range measurement, $n(t)$ is the residual range error affecting the range measurement, $\vartheta_j(t)$ is the j-th jitter source while C_1^j is the coupling coefficient associated to it. The attitude jitter along the three axis of each satellite can be determined either using star tracker data or using the measurement of the wavefront tilt at the photodiode (see paragraph 2.2). The objective of the calibration is instead to determine the coupling coefficients.

The calibration of the coupling coefficients hereby presented uses a set of external attitude stimuli which, together with the range measurement, are post-processed on ground by an appropriate algorithm. This procedure allows to determine a vector of coefficients only up to a one dimensional null space. Indeed, adding the null space vector multiplied by an arbitrary scale factor to the coupling coefficients vector returns a set of new coupling coefficients with the same properties of the original ones. This is not a problem if the coupling coefficients are used for on ground correction of the range data. However they are not, in general, representative of the physical phase center of the instruments and cannot be used for in-orbit calibration.

6.1.1 The calibration stimuli

The calibration of the TPC coefficients uses attitude stimuli which can be either deliberately induced pointing variations or the operational attitude jitter of the satellites. In the first case the calibration procedure is also known as *coherent calibration* while in the latter case as *incoherent calibration*.

With coherent calibration, the satellites are in turn oscillated along each of the sensitive

axis using a test signal (in general a sinusoid) which has an amplitude that exceeds the nominal pointing noise. By selecting a sufficiently long duration of the test signal, the energy of the TPC noise can be increased such that it becomes dominant with respect to the energy of the gravitational signal and the energy of the residual measurement noise. Moreover, knowing the oscillation frequency of the test signal it is possible to separate the TPC noise from the rest of the range measurement through data filtering. The drawback of this calibration procedure is the loss of measurement time as the science signal is unavailable. Moreover, coherent calibration requires a dedicated AOCS algorithm to perform the oscillating maneuver together with a considerable amount of thrust pulses (the calibration maneuver of the KBR of GRACE Follow-On requires about 1500 thrust pulses [136]).

With incoherent calibration, the coupling coefficients are derived using the operational attitude jitter of the satellites. Incoherent calibration does not interrupt the nominal science operation of the instrument and does not require additional thrust pulses, propellant or dedicated AOCS procedures to be carried out. Nevertheless, the energy of the TPC noise is much lower than the energy of the gravitational signal making the determination of the coupling coefficients non-trivial. Since the gravitational signal and the attitude jitter of the satellites are not fully uncorrelated it is necessary to find a region of the frequency domain where their correlation is minimized.

Coherent calibration is used to calibrate the CoM and the phase center of the KBR instrument for the GRACE mission [49] and is also foreseen as the baseline for calibrating the KBR instrument on GRACE Follow-On [136]. An approach similar to the coherent calibration is used to characterise the interferometer of LISA Pathfinder in order to ensure the achievement of the desired sensitivity for future gravitational waves observatories such as eLISA [137, 138]. Incoherent calibration, to knowledge, has never been used for performing the calibration of such instruments.

In the following sections, an algorithm optimized for recovering the coupling coefficients using incoherent calibration is presented. Nevertheless, the algorithm is sufficiently generic that it is capable of recovering the coupling coefficients also in case of coherent calibration. The algorithm is designed considering the gravity signal as the only source influencing both the range measurement and the attitude jitter. Common causes such as a temperature artifact which introduces errors both in the range and attitude measurements are neglected. This is a valid if the system design ensures that this coupling is minimized.

6.1.2 The data processing algorithm

If the generic operational attitude jitter ϑ of the satellites is considered as a wide-sense stationary process (of which we have a measurement), the problem of finding its associated coupling coefficient (C_1) can be formulated as the problem of finding the response of a Linear Time Invariant (LTI) system to the input ϑ. The output $\hat{y}$ of the filter $\mathbf{w}$ is the minimum mean square error estimate of a target process y which is wide sense stationary with ϑ. According to

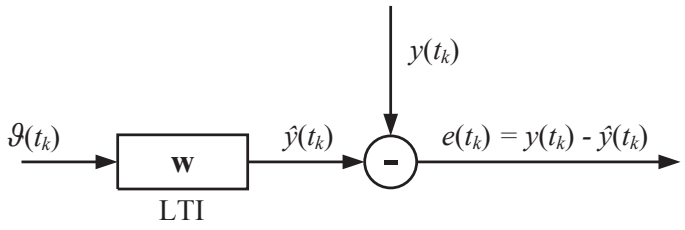

Figure 6.1: An LTI system which synthesizes the TPC noise produced by a generic input ϑ at the instant t_k.

the variables labelling of Fig. 6.1, the error signal at the time t_k is

$$e\left(t_k\right) = y\left(t_k\right) - \hat{y}\left(t_k\right) = y\left(t_k\right) - \mathbf{w}\vartheta\left(t_k\right) \tag{6.3}$$

where $\vartheta\left(t_k\right)$ is the satellite's attitude at the instant t_k. The expected value of the instantaneous squared error of Eq. 6.3 is

$$E\left[e^2\right] = E\left[y\right] + \mathbf{w}E\left[\vartheta^2\right]\mathbf{w} - 2E\left[\vartheta y\right]\mathbf{w} \tag{6.4}$$

The term $\left(t_k\right)$ is dropped for convenience. Letting $\mathbf{C} = E\left[\vartheta^2\right]$, $\mathbf{p} = E\left[\vartheta y\right]$ and $\xi = E\left[e^2\right]$ Eq. 6.4 can be rearranged as

$$\xi = E\left[y\right] + \mathbf{w}\mathbf{C}\mathbf{w} - 2\mathbf{p}\mathbf{w} \tag{6.5}$$

which represents the canonical expression of the mean square error. The goal of the algorithm is to find the filter response that minimizes the mean square error. Differentiating Eq. 6.5 with respect to $\mathbf{w}$ yields

$$\frac{\partial \xi}{\partial \mathbf{w}} = 2\mathbf{C}\mathbf{w} - 2\mathbf{p} \tag{6.6}$$

The minimum mean square error is obtained by matching the left term of Eq. 6.6 to zero. It follows that optimal filter response is given by

$$\begin{gathered} 2\mathbf{C}\mathbf{w} - 2\mathbf{p} = 0 \\ \downarrow \\ \mathbf{w}_{\text{opt}} = \mathbf{C}^{-1}\mathbf{p} \end{gathered} \tag{6.7}$$

and represents an expression of the Wiener-Hopf equation [139]. The optimal filter of Eq. 6.7 is also known in literature as Wiener filter. Although $\mathbf{C}$, $\mathbf{p}$ and $\mathbf{w}$ are 1×1 vectors, they have been written with bold letters in order to harmonize the previous formulation with the one commonly used in the literature related to this topic.

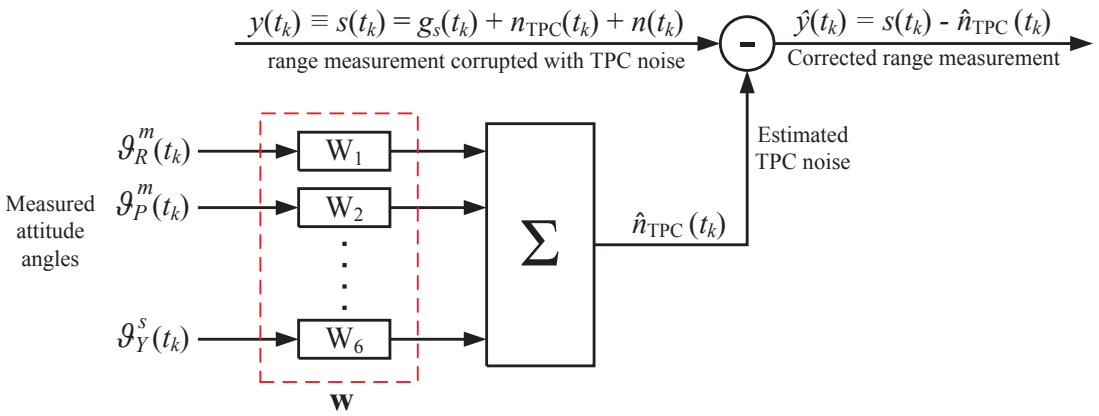

Figure 6.2: A multi-input linear combiner used for noise suppression. The coefficients W_i with $i = 1, \ldots, 6$ are equivalent to the coupling coefficients of Eq. 6.2. If correctly estimated, the multi-input linear combiner scheme can be used to remove the TPC noise from the range measurement.

The previous reasoning can be used to re-adapt the algorithm foreseen for canceling the noise of multiple sources [140, 141, 142, 143] in one used to suppress the TPC noise (see Fig. 6.2). The inputs of the filters W_i (with $i = 1, \ldots, 6$) are the time series of the six attitude jitters measured between t_0 and t_k ($\vartheta_j^h\left(t_k\right)$ in Fig. 6.2 with $j = R, P, Y$ and $h = m, s$) while the target process is the time series of the measured range in the same time interval ($y\left(t_k\right)$ in

Fig. 6.2). Yields,

$$\boldsymbol{\vartheta} = \begin{bmatrix} \vartheta_R^m(t_0) & \vartheta_R^m(t_1) & \cdots & \vartheta_R^m(t_k) \\ \vartheta_P^m(t_0) & \vartheta_P^m(t_1) & \cdots & \vartheta_P^m(t_k) \\ \vartheta_Y^m(t_0) & \vartheta_Y^m(t_1) & \cdots & \vartheta_Y^m(t_k) \\ \vartheta_R^s(t_0) & \vartheta_R^s(t_1) & \cdots & \vartheta_R^s(t_k) \\ \vartheta_P^s(t_0) & \vartheta_P^s(t_1) & \cdots & \vartheta_P^s(t_k) \\ \vartheta_Y^s(t_0) & \vartheta_Y^s(t_1) & \cdots & \vartheta_Y^s(t_k) \end{bmatrix} = \begin{bmatrix} \boldsymbol{\vartheta}_R^m(t_k) \\ \boldsymbol{\vartheta}_P^m(t_k) \\ \boldsymbol{\vartheta}_Y^m(t_k) \\ \boldsymbol{\vartheta}_R^s(t_k) \\ \boldsymbol{\vartheta}_P^s(t_k) \\ \boldsymbol{\vartheta}_Y^s(t_k) \end{bmatrix} \tag{6.8}$$

$$\mathbf{y} = \begin{bmatrix} s(t_0) & s(t_1) & \cdots & s(t_k) \end{bmatrix}$$

According to Eq. 6.8, the terms $\mathbf{C}$ and $\mathbf{p}$ can be rewritten as

$$\mathbf{C} = E\left[\boldsymbol{\vartheta}\boldsymbol{\vartheta}^T\right] = \begin{bmatrix} \boldsymbol{\vartheta}_R^m(\boldsymbol{\vartheta}_R^m)^T & \boldsymbol{\vartheta}_R^m(\boldsymbol{\vartheta}_P^m)^T & \cdots & \boldsymbol{\vartheta}_R^m(\boldsymbol{\vartheta}_Y^s)^T \\ \boldsymbol{\vartheta}_P^m(\boldsymbol{\vartheta}_R^m)^T & \boldsymbol{\vartheta}_P^m(\boldsymbol{\vartheta}_P^m)^T & \cdots & \boldsymbol{\vartheta}_P^m(\boldsymbol{\vartheta}_Y^s)^T \\ \vdots & \vdots & \vdots & \vdots \\ \boldsymbol{\vartheta}_Y^s(\boldsymbol{\vartheta}_R^m)^T & \boldsymbol{\vartheta}_Y^s(\boldsymbol{\vartheta}_P^m)^T & \cdots & \boldsymbol{\vartheta}_Y^s(\boldsymbol{\vartheta}_Y^s)^T \end{bmatrix} \tag{6.9}$$

$$\mathbf{p} = E\left[\boldsymbol{\vartheta}\mathbf{y}^T\right] = \begin{bmatrix} \boldsymbol{\vartheta}_R^m\mathbf{y}^T & \boldsymbol{\vartheta}_P^m\mathbf{y}^T & \cdots & \boldsymbol{\vartheta}_Y^s\mathbf{y}^T \end{bmatrix}^T$$

Once more, the term (t_k) is dropped for convenience. The matrix $\mathbf{C}$ is also know as the input correlation matrix. The main diagonal terms are the auto correlation of the attitude measurements, while the cross terms are the cross correlations among the attitude measurements. The vector $\mathbf{p}$ is the set of cross correlations between the measured range and the attitude measurements. Substituting Eq. 6.9 in Eq. 6.7 allows to determine the vector $\mathbf{w}_{\text{opt}} = [W_1, W_2, \ldots, W_6]^T$ whose elements are coincident with the six coupling coefficients C_1^j of Eq. 6.2. In particular, according to the order of the of the elements of $\mathbf{C}$ and $\mathbf{p}$

$$\mathbf{w}_{\text{opt}} = \begin{bmatrix} \hat{C}_1^{R_m} & \hat{C}_1^{P_m} & \hat{C}_1^{Y_m} & \hat{C}_1^{R_s} & \hat{C}_1^{P_s} & \hat{C}_1^{Y_s} \end{bmatrix}^T \tag{6.10}$$

The condition number of the input correlation matrix

The accuracy of the solution of Eq. 6.7 is widely influenced by the input correlation matrix $\mathbf{C}$, and in particular by the cross correlation and the auto correlation functions of the attitude jitter. If all the attitude jitters are uncorrelated, the off-diagonal terms of the matrix $\mathbf{C}$ are zero and the coupling coefficients are all uncoupled. Unfortunately, this is in general not the case due to common mode effects and measurement noise.

The input correlation matrix of multiple input sources (Eq. 6.9) is real, symmetric and positive semidefinite, therefore its corresponding eigenvalues are also non-negative and real. According to the perturbation theory, if the relative perturbations $\epsilon_{\mathbf{C}} = \| \delta\mathbf{C} \| / \| \mathbf{C} \|$ and $\epsilon_{\mathbf{p}} = \| \delta\mathbf{p} \| / \| \mathbf{p} \|$ of the matrix $\mathbf{C}$ and the vector $\mathbf{p}$ are of the same order of magnitude ($\epsilon_i \ll 1$ with $i = \mathbf{p}, \mathbf{C}$) [144], yields

$$\frac{\| \delta\mathbf{w} \|}{\| \mathbf{w} \|} \leq (\epsilon_{\mathbf{C}} + \epsilon_{\mathbf{p}})\, \kappa(\mathbf{C}) \tag{6.11}$$

where $\delta\mathbf{w}$ is the perturbation of the vector $\mathbf{w}$ resulting from a perturbation of the matrix $\mathbf{C}$ and the vector $\mathbf{p}$ while $\kappa(\mathbf{C})$ is the condition number of the matrix $\mathbf{C}$. Since the matrix $\mathbf{C}$ is

normal, its condition number is equal to the spread of the matrix

$$\kappa(\mathbf{C}) = \frac{\lambda_{\max}}{\lambda_{\min}} \tag{6.12}$$

where $\lambda_{\max}$ and $\lambda_{\min}$ are the biggest and the smallest eigenvalues of $\mathbf{C}$ respectively. The condition number is an indicator of the ill-conditioning of the matrix $\mathbf{C}$. If the input correlation matrix is ill-conditioned ($\kappa(\mathbf{C}) \gg 1$) small errors in $\mathbf{C}$ and $\mathbf{p}$ caused i.e. by measurement noise, causes the solution of Eq. 6.7 to diverge from the optimal one. The ill-conditioning of the input correlation matrix is therefore an indicator of the sensitivity of $\mathbf{w}_{\text{opt}}$ to noise. The condition number is used find the frequency region where the correlation between the six attitude jitters is minimized and the minimum measurement time for having a sufficient power of the calibration stimulus.

6.1.3 Range measurement correction

Once the coupling coefficients have been determined, the range measurement is corrected by subtracting the estimated TPC noise from it (as shown in Fig. 6.2). Post-processing correction of the range measurement is also used for the mission GRACE in order to remove ionosphere and geometric artifacts (range variations due to K-band antenna offsets) [145].

A perfect cancelation of the TPC noise though is not feasible since the estimated coupling coefficients and the measured attitude are affected by calibration error and measurement noise. Yields,

$$\begin{aligned} s_{\text{corr}}(t) &= g_s(t) + n_{\text{TPC}}(t) + n(t) - \overbrace{(\mathbf{w}_{\text{r}} + \Delta\mathbf{w})\left[\boldsymbol{\vartheta}_{\text{r}}(t) + \Delta\boldsymbol{\vartheta}(t)\right]^T}^{\mathbf{w}\boldsymbol{\vartheta}^T(t)} \\ &= g_s(t) + \cancel{n_{\text{TPC}}(t)} + n(t) - \cancel{\mathbf{w}_{\text{r}}\boldsymbol{\vartheta}_{\text{r}}^T(t)} - \Delta\mathbf{w}\boldsymbol{\vartheta}_{\text{r}}^T(t) - \mathbf{w}_{\text{r}}\Delta\boldsymbol{\vartheta}^T(t) - \cancel{\Delta\mathbf{w}\Delta\boldsymbol{\vartheta}^T(t)} \\ &= g_s(t) + n(t) - \left[\Delta\mathbf{w}\boldsymbol{\vartheta}_{\text{r}}^T(t) + \mathbf{w}_{\text{r}}\Delta\boldsymbol{\vartheta}^T(t)\right] \end{aligned} \tag{6.13}$$

where $s_{\text{corr}}(t)$ is the corrected range measurement, $\mathbf{w}_{\text{r}}$ and $\boldsymbol{\vartheta}_{\text{r}}(t)$ are the real coupling coefficients and the real attitude of the satellites respectively while $\Delta\mathbf{w}$ and $\Delta\boldsymbol{\vartheta}^T(t)$ represent the *calibration error* and the attitude measurement noise respectively (all the other terms have been defined in Eq. 6.2). The term $\Delta\mathbf{w}\Delta\boldsymbol{\vartheta}^T(t)$ is a second order error and therefore negligible. The last term in square brackets of Eq. 6.13 represents the *adjustment error* of the range measurement.

The magnitude of the calibration error $\Delta\mathbf{w}$ depends on the condition number of the input correlation matrix and on the signal-to-noise ratio between calibration stimuli and measurement signal. If the attitude signals are all uncorrelated, substituting Eq. 6.9 in Eq. 6.7 yields that the estimated coupling coefficient $\hat{C}_1^i$ (with $i = R_m, \ldots, Y_s$) of the generic attitude signal $\boldsymbol{\vartheta}_i$ is

$$\begin{gathered} \hat{C}_1^i\boldsymbol{\vartheta}_i\boldsymbol{\vartheta}_i^T = \left[\mathbf{g}_s + \mathbf{n} + \sum_j C_1^j\boldsymbol{\vartheta}_j\right]\boldsymbol{\vartheta}_i^T = \mathbf{N}\boldsymbol{\vartheta}_i^T + C_1^i\boldsymbol{\vartheta}\boldsymbol{\vartheta}_i^T \quad \text{with } i, j = R_m, P_m, \ldots, Y_s \\ \downarrow \\ \hat{C}_1^i = \frac{\mathbf{N}\boldsymbol{\vartheta}_i^T}{\boldsymbol{\vartheta}_i\boldsymbol{\vartheta}_i^T} + C_1^i \xrightarrow{\boldsymbol{\vartheta}_i\boldsymbol{\vartheta}_i^T \gg \mathbf{N}\boldsymbol{\vartheta}_i^T} \hat{C}_1^i \approx C_1^i \end{gathered} \tag{6.14}$$

where $\mathbf{N} = \mathbf{g}_s + \mathbf{n}$ since $\boldsymbol{\vartheta}_j\boldsymbol{\vartheta}_i^T = 0$ for $i \neq j$. The ratio $\mathbf{N}\boldsymbol{\vartheta}_i^T/\boldsymbol{\vartheta}_i\boldsymbol{\vartheta}_i^T$ is labelled as *algorithm noise*. The algorithm noise defines the applicability limit of incoherent calibration and the requirement on the test signal for the coherent one. If, for example, it is not possible to satisfy Eq. 6.14 using the natural jitter of the satellite than it is not possible to perform incoherent

calibration.

In reality it is not possible to directly measure the algorithm noise since it is not possible to separate the TPC noise from the rest of the range measurement. Nevertheless, through the usage of gravity models and noise models it is possible evaluate the extent of the algorithm noise. Moreover, if the algorithm noise is small, the ratio between the elements of the vector $\mathbf{p}$ and the corresponding diagonal elements of the matrix $\mathbf{C}$ has to be of the same order of magnitude of the expected coupling coefficients.[1]

6.2 Calibration of the range measurement of a GRACE Follow-On like mission

In this paragraph, the calibration process is used to adjust the simulated range measurement of a GRACE Follow-On like mission. Since the objective of the calibration is mitigating the TPC noise caused by the geometrical offset between the fiducial point of the instrument and the longitudinal line of sight of the satellites, the propagation of the laser beam using ray optics [84] is a valid approximation.

With ray optics, the far-field wavefront of the beam is treated as a perfect sphere. For a real laser interferometer this condition is not true due to wavefront errors on the transmit side. The higher the wavefront error, the higher will be the deviation of the far-field wavefront from a perfect sphere. With a non-spherical wavefront, any movement of the receive aperture of the instrument and the jittering of the laser beam around it introduces an apparent displacement (TPC noise) in the range measurement. Since the receiving aperture is around 1 m away from the rotation point of the satellite, with the noise jitter of GRACE Follow-On, the aperture moves at maximum of 300 µm (Roll rotation do not introduce TPC noise). With such a small displacement, the wavefront error is negligible. Nevertheless, the TPC noise introduced by the far-field wavefront is approximately equal to the magnitude of the displacement of the receive aperture times a scaling factor [124]. Hence the calibration algorithm determines coupling coefficients that account also for this additional noise effect ($C_1^j = C_{\mathrm{PCO}}^j + C_{\mathrm{WFE}}^j$).[2] Therefore, neglecting this noise mechanism while simulating the range measurement does not invalidate the calibration results.

The wavefront error also introduces TPC noise due to the jitter of the TX beam. The jitter of the TX beam in the far field is given by the jitter of the steering mirror since this removes any pointing error caused by the jitter of the satellite via the DWS signal. Since the jitter of the steering mirror is not correlated to the attitude jitter of the satellites, this mechanism of TPC noise can be treated as instrument noise.[3]

The measurement principle of the instrument is the same as the one of the LRI of GRACE Follow-On; that is, measuring the round-trip pathlength. The instrument and the satellite are designed such that under ideal science operations, the body frame of the satellite and the science reference frame are aligned and centered, together with the phase center of the optical instrument, at the fiducial point of the accelerometer assembly (see paragraph 2.1). The angles which induce TPC noise are the ones between the science reference frame and the body frame. Since the optical axis of the transmitted and received beam is parallel to the X-axis of the body frame of the satellite, Roll rotations do not linearly couple with the lever arm mechanism of the TPC noise but via other mechanisms (i.e. beam co-alignment). Hence, the contribution of

[1] If the magnitude of the coupling coefficient is expected to be 10^{-3} m/rad and this ratio is equal to 1, than the algorithm noise is significantly high and the incoherent calibration is not applicable. If the ratio is smaller or equal to 10^{-3} than it is not possible to infer anything regarding the algorithm noise by just looking at this ratio.

[2] C_1^j is written as the sum of two coefficients for the sake of clarity. In reality it is not possible to distinguish the contribution of the phase center offset (C_{PCO}^j) from the contribution of the wave-front error (C_{WFE}^j)

[3] Eventually this noise can be calibrated either via incoherent calibration or simply applying a test signal on the steering mirror (coherent calibration).

the Roll to the TPC noise is primarily related to the layout of the instrument. Moreover, Roll rotations can only be measured with the STR and not by means of the DWS signal (as it will be showed in paragraph 6.2.2, the STRs are not sufficiently accurate for mitigating the TPC noise). For these reasons, the Roll contribution is hereafter neglected (although the algorithm can account for it) and Eq. 6.8 is equal to

$$\mathbf{C} = E\left[\boldsymbol{\vartheta}\boldsymbol{\vartheta}^T\right] = \begin{bmatrix} \boldsymbol{\vartheta}_P^m\left(\boldsymbol{\vartheta}_P^m\right)^T & \boldsymbol{\vartheta}_P^m\left(\boldsymbol{\vartheta}_Y^m\right)^T & \boldsymbol{\vartheta}_P^m\left(\boldsymbol{\vartheta}_P^s\right)^T & \boldsymbol{\vartheta}_P^m\left(\boldsymbol{\vartheta}_Y^s\right)^T \\ \boldsymbol{\vartheta}_Y^m\left(\boldsymbol{\vartheta}_P^m\right)^T & \boldsymbol{\vartheta}_Y^m\left(\boldsymbol{\vartheta}_Y^m\right)^T & \boldsymbol{\vartheta}_Y^m\left(\boldsymbol{\vartheta}_P^s\right)^T & \boldsymbol{\vartheta}_Y^m\left(\boldsymbol{\vartheta}_Y^s\right)^T \\ \boldsymbol{\vartheta}_P^s\left(\boldsymbol{\vartheta}_P^m\right)^T & \boldsymbol{\vartheta}_P^s\left(\boldsymbol{\vartheta}_Y^m\right)^T & \boldsymbol{\vartheta}_P^s\left(\boldsymbol{\vartheta}_P^s\right)^T & \boldsymbol{\vartheta}_P^s\left(\boldsymbol{\vartheta}_Y^s\right)^T \\ \boldsymbol{\vartheta}_Y^s\left(\boldsymbol{\vartheta}_P^m\right)^T & \boldsymbol{\vartheta}_Y^s\left(\boldsymbol{\vartheta}_Y^m\right)^T & \boldsymbol{\vartheta}_Y^s\left(\boldsymbol{\vartheta}_P^s\right)^T & \boldsymbol{\vartheta}_Y^s\left(\boldsymbol{\vartheta}_Y^s\right)^T \end{bmatrix} \tag{6.15}$$

$$\mathbf{p} = E\left[\boldsymbol{\vartheta}\mathbf{y}^T\right] = \begin{bmatrix} \boldsymbol{\vartheta}_P^m\mathbf{y}^T & \boldsymbol{\vartheta}_Y^m\mathbf{y}^T & \boldsymbol{\vartheta}_P^s\mathbf{y}^T & \boldsymbol{\vartheta}_Y^s\mathbf{Y}^T \end{bmatrix}^T$$

Thus, the total number of coupling coefficients that need to be determined reduces to four $\mathbf{w}_{\text{opt}} = \left[\hat{C}_1^{P_m}, \hat{C}_1^{Y_m}, \hat{C}_1^{P_s}, \hat{C}_1^{Y_s}\right]^T$. Despite this simplification, the calibration algorithm is independent from the geometry of the optical link and from the layout of the instrument. The results presented in the following sections are, therefore, representative of the algorithm performance.

6.2.1 The optical link simulator

The simulator is a simplified version of the one described in chapter 3 and includes only the models of the optical and of the optoelectronic components which are relevant for evaluating the range between the satellites, generating the TPC noise, and applying the calibration. Since the propagation of the laser beam is evaluated using ray optics, beam diffraction, optical abberation, and ghost beams cannot be simulated, but are taken into account by adding noise to the range measurement. A block diagram of the simulator used to performing the range measurement is depicted in Fig. 6.3.

Due to the nature of the simulator, the overall optical pathlength difference between the RX beam and the LO beam is evaluated summing the distance travelled by the RX beam over its measurement path. The noise level of the measurement branch and the optical noise are added to the simulated range measurement using a noise shape filter. The final range measurement has an accuracy which is representative of the one expected from the instrument.

The DWS measurement, used to keep the alignment between the RX beam and the LO beam, is evaluated by calculating the in-plane and out-of-plane angles between the unit vector of the RX beam and the one of the LO beam (see paragraph 2.2). The resulting angles are summed with the output of two noise shape filters designed using the NSF of the GRACE Follow-On mission (see appendix A.6). The DWS signal is used to command the steering mirror in order to keep the RX an TX beams aligned, maximizing the amplitude of the beat note on the photodiodes. The accuracy of the alignment between the TX and RX beam is affected by the DWS noise and by the jitter of the steering mirror although the in-band spectral density of the DWS noise ($\approx 10\,\text{nrad}/\sqrt{\text{Hz}}$) is negligible with respect to the in-band residual jitter of the steering mirror ($\approx 10\,\mu\text{rad}/\sqrt{\text{Hz}}$).

The jitter of the steering mirror produces TPC noise via the wavefront error in the far-field. Indeed, it translates into an apparent jitter of the receiving aperture of the trailing/following spacecraft with respect to the beam's axis. Since the jitter of the steering mirror is not correlated with the jitter of the satellite, its induced TPC noise does not influence directly the calibration but increases the noise on the range measurement. Accordingly, the component of TPC noise introduced by the steering mirror is replaced, without loss of generality, by an increased noise level of the range measurement.

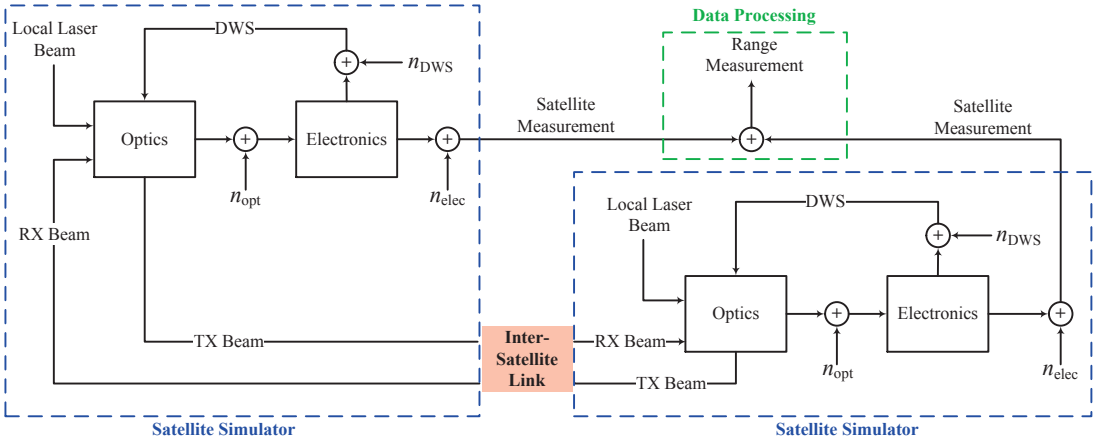

Figure 6.3: Block diagram of the simulator used to reproduce the range measurement. The simulator is divided in four sections. The satellite simulators reproduce the instrument measurement and the satellite behavior along the orbit. The intra-satellite simulator reproduces the propagation of the laser beam on the far-field while the data processing block evaluates the total round trip range measurement. TPC noise is not artificially added like the optical noise and the optoelectronic noise but is introduced through the misalignment of the optical components in the "Optics" blocks.

The position of both instruments and their orientation along the orbit is evaluated with respect to the CRS J2000 frame (see appendix C.1) and are updated with a frequency of 2 Hz. The orbit ephemeris of the satellites and their attitudes are reproduced using the gravitational model (up to J_{10}) and the models of the non-gravitational disturbances described in paragraph 3.1. Any effect that changes the relative orientation of the fundamental reference frames of the satellite over time (i.e. thermal drifts due to the sun/eclipse transitions during one orbit) is neglected for these simulations.

The non-ideality of the optical instrument is introduced by applying random misalignments to its optical components. The angular and spatial alignment accuracies are equal to ± 2 mrad and ± 100 µm respectively and are generated according to a uniform distribution. The angular misalignment is applied by rotating the component with respect to its local frame (in its local frame the ideal normal of the optical component is $\vec{v} = [0\,0\,1]^T$) while the spatial misalignment is applied by moving the reference plane of the component with respect to the body frame of the satellite. The coupling coefficients resulting from the misalignment of the optical components are not known beforehand, and are determined by performing test simulations.

Recovery of the coupling coefficients with test simulations

The coupling coefficients are evaluated by maintaining the satellites at a fixed distance and oscillating them with respect to the body axes which introduce TPC noise. The satellites are oscillated using four sinusoids which are separated in time in order to distinguish the contribution of each oscillatory movement in the induced TPC noise. Each oscillation lasts for a Δt equal to the orbital period of GRACE Follow-On while the oscillation frequency is double with respect to the orbital one ($f = 2/\Delta t$). For each time interval Δt, the measurement signal is equal to the fixed satellite separation plus the TPC noise induced by oscillatory motion (all the other noise sources are set to zero). The linear and quadratic coupling coefficients can be, therefore, estimated as

$$s(t) = d + C_1^j \vartheta_j(t) + C_2^j \vartheta_j^2(t) \;\longrightarrow\; \frac{\partial s(t)}{\partial \vartheta_j} = C_1^j + C_2^j \vartheta_j(t) \quad \text{with } j = P_m, Y_m, P_s, Y_s \tag{6.16}$$

where d is the fixed distance between the satellites. In order to minimize the numerical noise of the simulator, d is equal to 4 m. A schematic representation of the logic used to recover the

coupling coefficients is depicted in Fig. 6.4.

The first and second order coupling coefficients are determined using a curve fitting of the partial derivative of the range measurement and are listed in Tab. 6.1. The quadratic coupling coefficients are reported only to show that their contribution (as the one of higher order terms) is negligible in the TPC noise mechanism when nanometer precision is required by the instrument.

Master	C_1 (m/rad)	C_2 (m/rad^2)	Slave	C_1 (m/rad)	C_2 (m/rad^2)
ϑ_P	$2,25 \times 10^{-3}$	$0,14 \times 10^{-3}$	ϑ_P	$-0,39 \times 10^{-3}$	$-0,01 \times 10^{-3}$
ϑ_Y	$0,63 \times 10^{-3}$	$1,07 \times 10^{-3}$	ϑ_Y	$1,88 \times 10^{-3}$	$0,48 \times 10^{-3}$

Table 6.1: First and second order coupling coefficients of the TPC noise. These coupling coefficients are the result of a random misalignment of the optical components of the instrument.

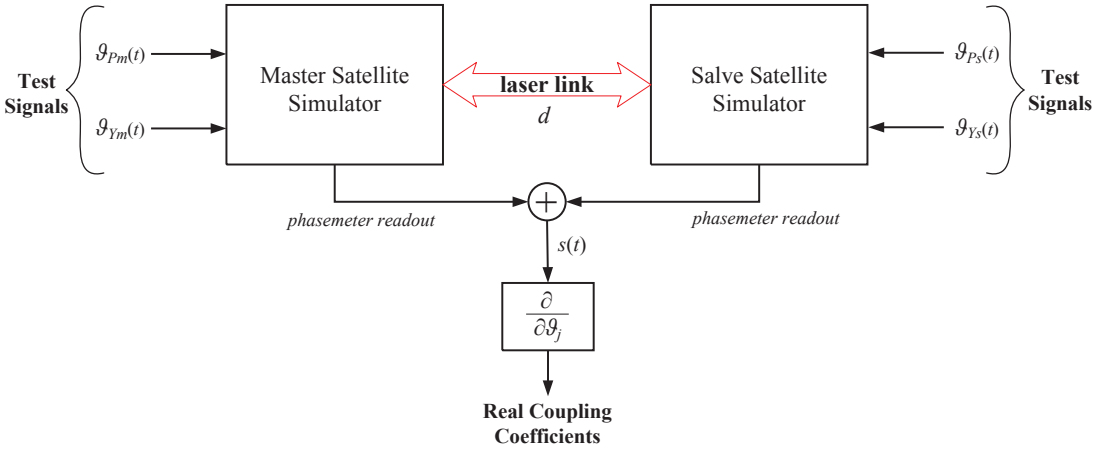

Figure 6.4: Representation of the process adopted to recover the coupling coefficients. The distance between the satellites is kept constant and equal to d.

6.2.2 Calibration process applied to the simulated range measurement

The TPC noise calibration discussed in this paragraph is applied to an interferometer whose coupling coefficients, after misalignment of its optical components, are identical to the ones listed in Tab. 6.1. Additional simulations with different magnitudes of the coupling coefficients have shown that the results presented here are representative of the performance of the calibration process.

The accuracy of the range measurement is given by the sum of the TPC noise and the other noise sources. In particular, $45\,\mathrm{nm}/\sqrt{\mathrm{Hz}}$ (RSS value) are allocated for the other noise sources. Study on future geodesy missions [81] have been performed using a requirement on the TPC noise, after the calibration, equal to

$$n_{\mathrm{TPC}} \leq 20\,\mathrm{nm}/\sqrt{\mathrm{Hz}} \sqrt{1 + \left(\frac{f}{2\mathrm{mHz}}\right)^{-2}} \times \sqrt{1 + \left(\frac{f}{10\mathrm{mHz}}\right)^{-2}} \tag{6.17}$$

Equation 6.17 is used in this chapter to define the requirement curve of the TPC noise. The combination of TPC noise and the other noise sources returns, in a worst case condition, $50\,\mathrm{nm}/\sqrt{\mathrm{Hz}}$ (RSS value) as instrument noise. All the noise sources, except for the TPC noise, are modelled either as white Gaussian noise or as non-white Gaussian noise. The non-white

Gaussian noise are generated using noise shaping filters whose frequency response is equal to the NSF(f) of the LRI of GRACE Follow-On (see appendix A.6). Reduced accuracies of the range measurement have also been studied and are discussed further in this paragraph. Figure 6.4 shows the requirement curves of the TPC noise and the instrument noise and compares them with the nominal performance of the GRACE accelerometer and the dominant noise source of the GRACE KBR system (thermal noise).

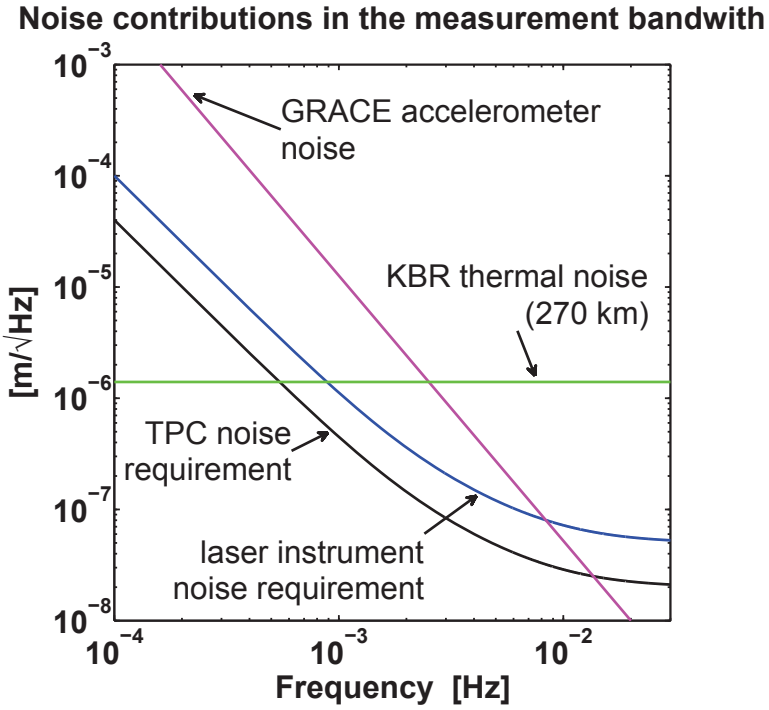

Figure 6.5: This figure compares the requirement curves of the TPC noise and the displacement noise of the laser instrument with the major noise contributors of the GRACE mission [40]. The KBR noise is evaluated for the worst case satellite separation. The requirement of the LRI of GRACE Follow-On is not included in this plot since it is identical to the requirement of the laser instrument.

Figure 6.6 shows the separation between the satellites (left panel) and the time series of the operational attitude of the master satellite (right panel) over a 24 hour time span (these time series are the ones generated for AOCS simulation studies of GRACE Follow-On - see paragraph 3.1). Roll, Pitch and Yaw are the angles between the body frame of the satellite and the science reference frame. The left panel of Fig. 6.7 depicts the ASD of the real range (range trend over time) and the ASD of the real pointing jitter of one of the two satellites in both Pitch and Yaw, while the right panel of Fig. 6.7 shows the comparison between the ASD of the real range and the ASD of the TPC noise. Figure 6.8 depicts the spectral coherence between the real range and the Pitch and Yaw operational attitudes of the master satellite (the same plots are obtained using the attitude of the slave satellite). The analysis of the coherence plots shows that attitude signals and range measurement are strongly correlated at the orbital frequency and also at its multiples because of the gravity gradient which affects both range measurement and indirectly, the attitude of the satellites (the AOCS is designed to keep the body frame of the satellite aligned to the LoS which varies, as intra-satellite distance, along the orbit). For frequencies between 0.1 mHz and 1 mHz the condition number of the input correlation matrix is ≈ 80 and the ratio between the elements of the vector $\mathbf{p}$ and the diagonal elements of the matrix $\mathbf{C}$ is $\approx 10^2$. This means that the operational jitter of the satellite is not capable of reducing the algorithm noise to acceptable levels. Therefore, it is not possible to apply incoherent calibration if the data used by the calibration algorithm are not pre-processed.

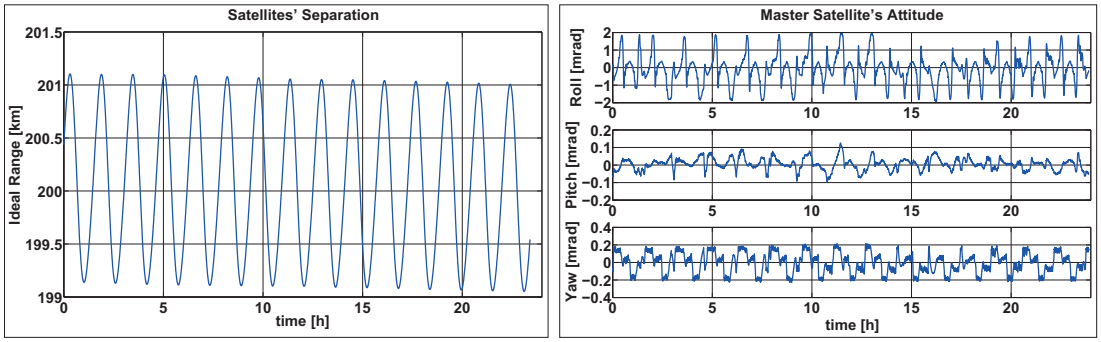

Figure 6.6: The oscillatory effect of the satellites' separation (left panel) is given by the eccentricity of the GRACE-Follow On orbit while the slope of the curve is given by the drift of the orbit. The operational attitude of one of the two satellites is depicted in the right panel of this figure. The Roll drift is one order of magnitude bigger than the drift along the other two body axis. This derives from the negligible measurement noise induced by Roll rotations.

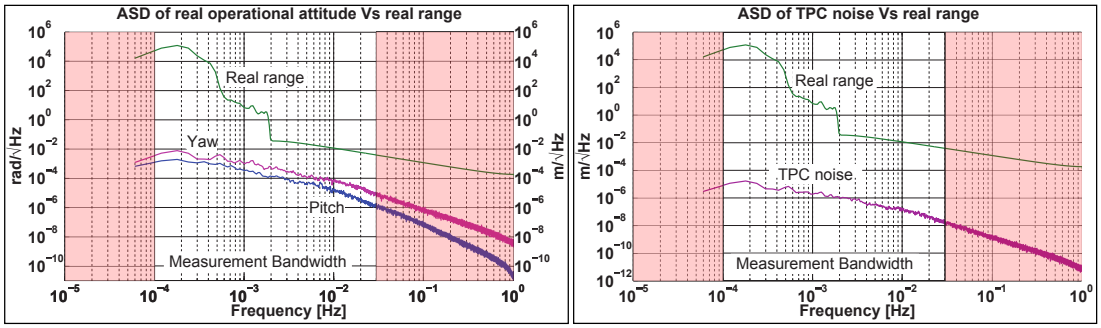

Figure 6.7: The ASD of the range between the satellites shows a sudden jump at a frequency of $\approx 2\,\mathrm{mHz}$. This behavior is caused by the limited number of spherical harmonics used to generate the orbit ephemerides used by the simulator. The ASD of the real Pitch and Yaw angles (left panel) exploit a $1/f^2$ behavior because the attitude of the satellites is calculated integrating the angular acceleration around the axis of the body frame. Therefore the plant model of the satellite is equal to $G = 1/js^2$. The ASD of the TPC noise (right panel) exploits the same trend of the real attitude angles. This is an expected behavior since the TPC noise is a scaled linear sum of the attitude angles.

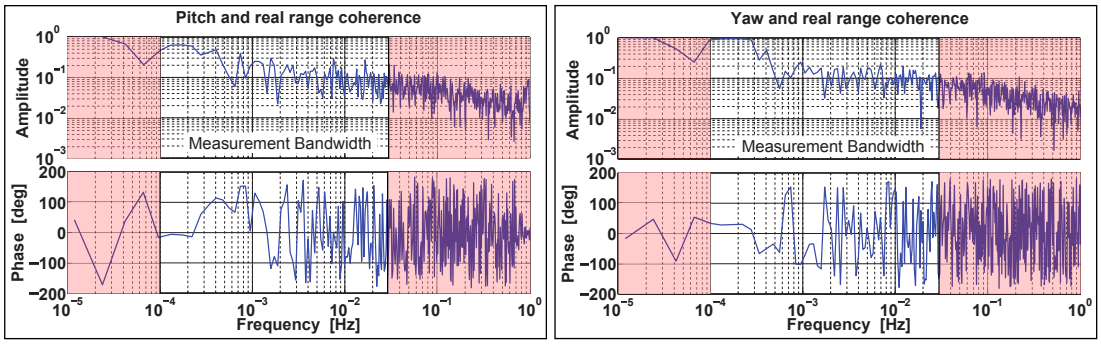

Figure 6.8: The left panel of this picture depicts the spectral coherence between the Pitch angle and the real satellite's range while the right panel depicts the spectral coherence between the Yaw angle and the real satellite's range. Both plots show a correlation between the signals at the orbital frequency (the coherence between the signals at this frequency is $\mathrm{C}_{xy}(f) \approx 1$). At multiples of the orbital frequency this relation is less evident. For frequencies above 10 mHz both plots show absence of coherence between the signals (noisy behaviour of both amplitude and phase signal). Here the gravity gradient is null due to the limited usage of spherical harmonics.

In order to reduce the algorithm noise, the range calculated using precise satellite orbit ephemerides is subtracted from the measured one. Yields,

$$\Delta s\,(t) = s\,(t) - \hat{s}\,(t) = n_{TPC}\,(t) + n\,(t) \tag{6.18}$$

where $\Delta s\,(t)$ is the residual range, $s\,(t)$ is the simulated range measurement, $\hat{s}\,(t)$ is the one calculated with the orbit ephemerides, while $n_{TPC}\,(t)$ and $n\,(t)$ are the TPC noise and the residual measurement noise respectively. The result of Eq. 6.18 implies a perfect knowledge of the spherical harmonics of the gravity field and a perfect modeling of the disturbances acting on the satellites. In reality, this perfect subtraction is practically not feasible. Since this paragraph wants to demonstrate the feasibility of the incoherent calibration, the contribution of the gravitational potential to the residual range measurement is neglected (the subtraction is considered perfect as in Eq. 6.18). It is going to be considered in the next paragraph when the calibration is applied to the flight data of GRACE.

The attitude data and the range data exploit correlation mainly at the orbital frequency. The range measurement noise and the DWS noise are generated using a noise shape filter whose trend is equal to the NSF(f) used for the LRI of the GRACE Follow-On mission. These noises are not uncorrelated for frequencies below 10 mHz. The data are therefore pre-filtered with a an elliptic high-pass filter [125] with a cut-off frequency of 30 mHz, a stop-band attenuation of 80 dB and a pass-band ripple of 0.01 dB. Since filtering is used to de-correlate the attitude and the range data, the filter is labelled as *de-correlating filter*. According to Fig. 6.7, in this frequency range, the attitude signal is expected to be three order of magnitudes bigger than the measurement noise ($50\,\mathrm{nm}/\sqrt{\mathrm{Hz}}$). Figure 6.9 is a schematic representation of the calibration process applied to the range measurement.

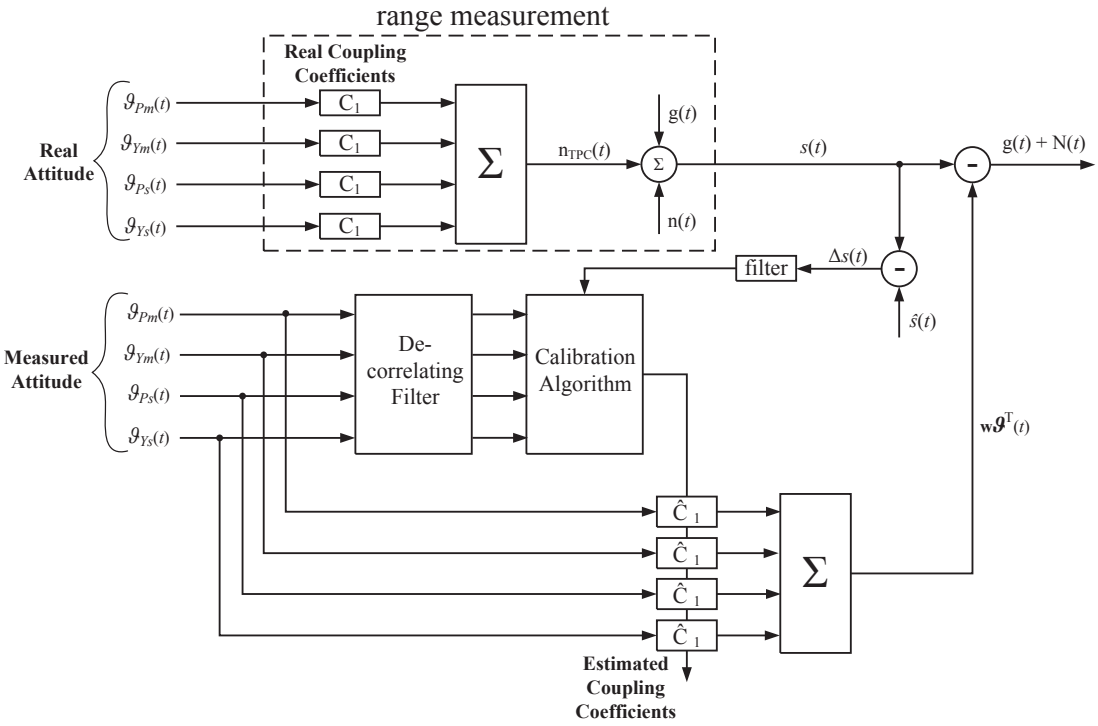

Figure 6.9: This picture shows a scheme of the calibration process applied to the range measurement for reducing the TPC noise.

The TPC noise and the residual error after the calibration process are evaluate using the ASD and are compared to the requirement provided by Eq. 6.17.

Calibration of the coupling coefficients using a high-pass filter as de-correlating filter

The calibration process is applied using the real attitude data, the STR measurement and the DWS measurement. With the real attitude data, the adjustment error is only given by the term $\Delta\mathbf{w}\boldsymbol{\vartheta}_{\mathrm{r}}^{T}(t)$ (Eq. 6.13) and is, therefore, representative of the performance of the calibration algorithm. The calibration processes using the DWS measurement and the STR measurement takes into account both contributions of the adjustment error and is, therefore, representative of the performance of the calibration process.

The coupling coefficients, estimated using the three different time series of the attitude signal are listed in Tab. 6.2. Figure 6.10 depicts the noise level of the TPC noise before and after applying the calibration process.

Attitude data	Master	$\hat{C}_1$ (m/rad)	ϵ	Slave	$\hat{C}_1$ (m/rad)	ϵ
real	ϑ_P	2.22×10^{-3}	-4.17%	ϑ_P	-0.35×10^{-3}	-13.53%
	ϑ_Y	0.63×10^{-3}	0.15%	ϑ_Y	1.85×10^{-3}	-1.90%
	$\kappa(\mathbf{C}) = 8.6$					
DWS	ϑ_P	2.22×10^{-3}	-4.18%	ϑ_P	-0.34×10^{-3}	-13.55%
	ϑ_Y	0.63×10^{-3}	0.15%	ϑ_Y	1.85×10^{-3}	-1.90%
	$\kappa(\mathbf{C}) = 8.6$					
STR	ϑ_P	2.21×10^{-3}	-4.85%	ϑ_P	-0.78×10^{-3}	95.3%
	ϑ_Y	0.65×10^{-3}	3.41%	ϑ_Y	1.80×10^{-3}	-3.94%
	$\kappa(\mathbf{C}) = 13$					

Table 6.2: Estimated coupling coefficients using the calibration algorithm. ϵ is the estimation error between the real linear coupling coefficient reported in Tab. 6.1 and the estimated ones. For each application of the calibration algorithm the condition number of input correlation matrix $\kappa(\mathbf{C})$ is specified.

The adjustment of the range measurement allows to reduce of almost two orders of magnitude the TPC noise within the measurement bandwidth. The incoherent calibration process, under the hypothesis of a having only noise in the residual range, is therefore applicable if the contribution of the gravitational potential and any other correlation effect is removed from the processed data. The curve labelled "calibration limit" is about parallel to the TPC noise curve. Since the spectral content of the attitude signals is almost the same, the calibration error introduces a residual TPC noise which is a scaled version of the initial one.

The calibration process using the DWS data returns a solution comparable to the one obtained using the real attitude time series. Indeed, the $\Delta\boldsymbol{\vartheta}$ contribution to the adjustment error is negligible compared to the calibration error $\Delta\mathbf{w}$.[4] Therefore the range measurement correction using the DWS measurement, within the measurement bandwidth, is mainly limited by the performance of the calibration process. For frequencies above 0.1 Hz the adjustment of the range measurement is limited by the accuracy of the DWS measurement.

Figure 6.10 shows that the range measurement adjustment is not feasible if the operational attitude of the satellites is measured using the modelled STRs. According to Tab. 6.2, the condition number of the input correlation matrix increases with respect to the other two cases. The noise of the attitude measurement increases the cross-correlation among the operational attitude jitters and both condition number of the input correlation matrix and algorithm error result worsened. Despite the calibration error, the measurement noise of the star trackers itself is not compatible with the requirement on the TPC noise. In Fig. 6.11, the effect of the

[4]The contribution to the adjustment error given by the measurement error is $\mathbf{w}_{\mathrm{r}}\Delta\boldsymbol{\vartheta} \approx 10^{-3}\mathrm{m/rad}\times 10^{-8}\mathrm{rad}/\sqrt{\mathrm{Hz}} \approx 10\mathrm{pm}/\sqrt{\mathrm{Hz}}$ while the contribution to the adjustment error given by the calibration error is $\Delta\mathbf{w}_{\mathrm{r}}\boldsymbol{\vartheta} \approx 10^{-5}\mathrm{m/rad}\times 10^{-4}\mathrm{rad}/\sqrt{\mathrm{Hz}} \approx 1\mathrm{nm}/\sqrt{\mathrm{Hz}}$.

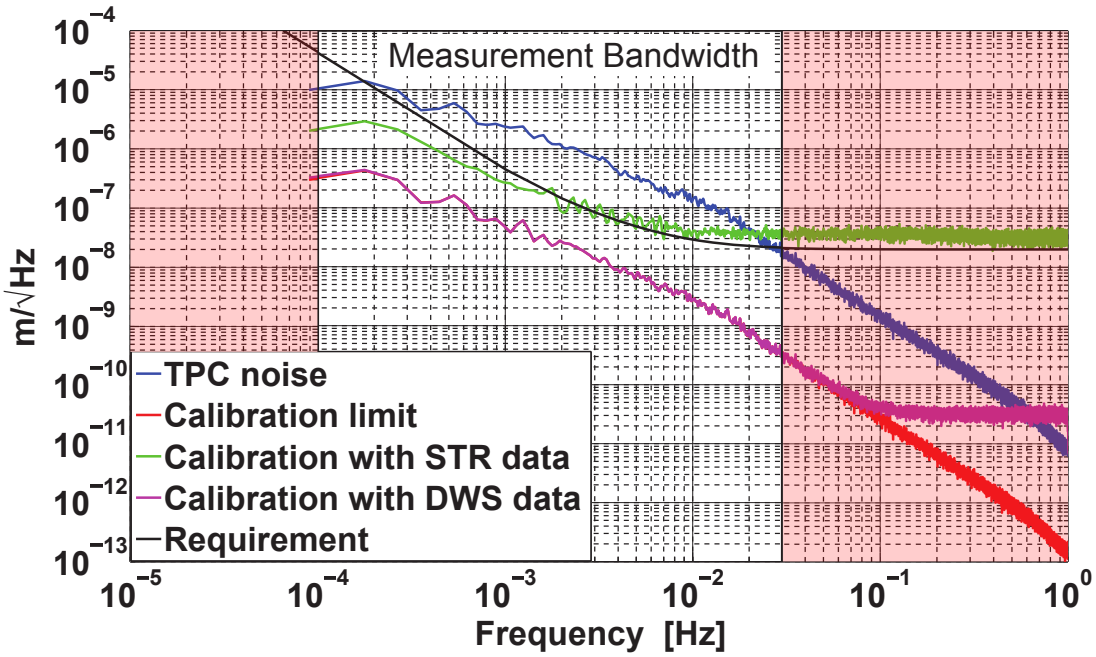

Figure 6.10: ASD of the TPC noise before (blue curve) and after applying the adjustment of the range measurement (except for the requirement line). The calibration process, described in paragraph 6.1, is in turn applied using the real attitude of the satellite (red curve labelled calibration limit), the STR measurement (green curve labelled as calibration with STR data) and the DWS measurement (violet curve labelled as calibration with DWS data). The requirement curve is calculated according to Eq. 6.17.

calibration error is separated from the attitude measurement error. Within the measurement bandwidth, the calibration error is compatible with the requirement on the TPC noise while the measurement noise is not.

The performance of the sensors used to model the readouts of the STRs (see paragraph 3.2) represent the actual state of art. Therefore, if the noise level of the instrument and the environmental conditions are comparable to the ones adopted in this paragraph, the usage of STRs, to date, does not allow to perform incoherent calibration.

Calibration of the coupling coefficients using different noise levels of the instrument

Previously, the residual instrument noise is kept constant and equal to $45\,\mathrm{nm}/\sqrt{\mathrm{Hz}}$ (RSS value). Here this noise is gradually increased in order to evaluate which is the applicability limit of the calibration process. The reduced accuracy of the range measurement has to be interpreted as a relaxation on the requirements of the instrument (i.e. increased noise due to diffraction, increased shot noise etc.) since the noise sources are once more modeled as white and non-white Gaussian noise source. The noise modeling adopted excludes again the possibility of taking into account, within the term $n(t)$ of Eq. 6.18, the range error introduced by subtracting the real range measurement from the calculated one since the power spectral density of this error is not white nor equal to the one generated using a noise shape filter. The coupling coefficient are once more estimated filtering the residual range measurement and the DWS measurement with a high-pass filter. The STR measurement is not considered because it is not capable of fulfilling the requirement on the TPC noise.

Figure 6.12 depicts the TPC noise before and after applying the calibration process for measurement noise ($n(t)$ in Eq. 6.18) which increases from $45\,\mathrm{nm}/\sqrt{\mathrm{Hz}}$ to $1\,\mu\mathrm{m}/\sqrt{\mathrm{Hz}}$. As the instrument noise increases, the solution of Eq. 6.7 is every time less accurate. With a noise of

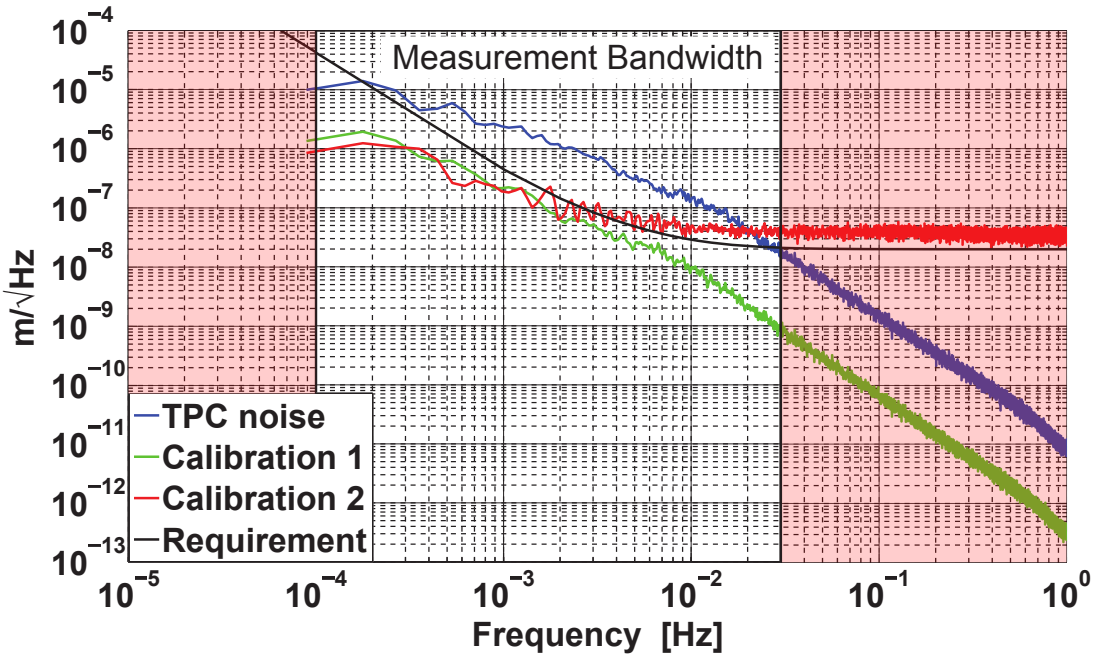

Figure 6.11: This figure depicts the TPC noise and the result of two calibration processes. In calibration 1, the coupling coefficients are estimated using the STR attitude measurement. The range correction is performed multiplying these coefficients with the real attitude of the satellite. In calibration 2, the coupling coefficients are estimated using the real attitude of the satellites while the range correction is performed multiplying these coefficients with the attitude measurement of the STR.

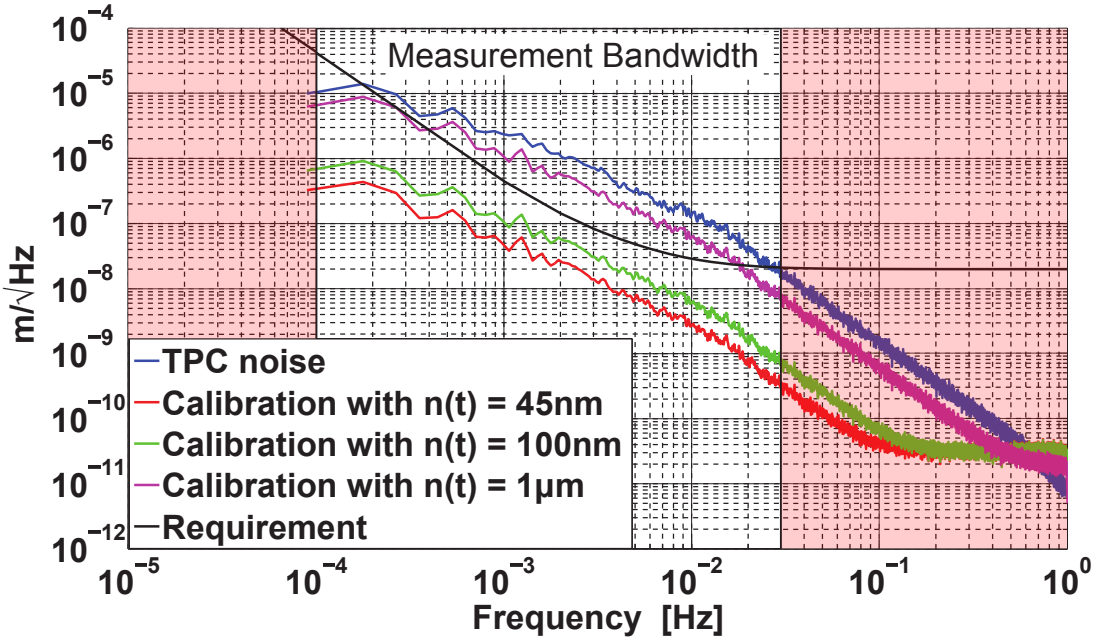

Figure 6.12: Initial TPC noise and residual TPC noise after applying the calibration process. The coupling coefficients are estimated using the DWS attitude data and the range measurement with different levels of noise. With a noise level above 1µm/$\sqrt{\text{Hz}}$ the calibration process is not capable of fulfilling the requirement on the TPC noise.

1 µm/$\sqrt{\text{Hz}}$ the estimation of the coupling coefficients becomes arbitrary because the result of Eq. 6.7 is dominated by the algorithm error of Eq. 6.14.

The coupling coefficients estimated after each application of the calibration algorithm are listed in Tab. 6.3. The table also shows the condition number of the input correlation matrix for each application. As expected, the lower estimation accuracy is caused by the increasing algorithm noise and is independent from $\kappa(\mathbf{C})$.

Instrument noise	Master	$\hat{C}_1$ (m/rad)	ϵ	Slave	$\hat{C}_1$ (m/rad)	ϵ
45 nm	ϑ_P	2.22×10^{-3}	-4.18%	ϑ_P	-0.34×10^{-3}	-13.55%
	ϑ_Y	0.63×10^{-3}	0.15%	ϑ_Y	1.85×10^{-3}	-1.90%
	$\kappa(\mathbf{C}) = 8.6$					
100 nm	ϑ_P	2.05×10^{-3}	-9.21%	ϑ_P	-0.29×10^{-3}	-27.35%
	ϑ_Y	0.63×10^{-3}	0.33%	ϑ_Y	1.80×10^{-3}	-4.27%
	$\kappa(\mathbf{C}) = 8.6$					
1 µm	ϑ_P	0.19×10^{-3}	-92%	ϑ_P	0.61×10^{-3}	-253%
	ϑ_Y	0.65×10^{-3}	3.22%	ϑ_Y	1.10×10^{-3}	-43%
	$\kappa(\mathbf{C}) = 8.6$					

Table 6.3: Estimated coupling coefficients using different noise levels of the instrument. ϵ is the estimation error between the real linear coupling coefficient reported in Tab. 6.1 and the estimated ones. The table also reports the condition number $\kappa(\mathbf{C})$. Since the attitude measurement is always the same, the condition number of the input correlation matrix does not change. What worsens the performance of the calibration process is, as expected, the algorithm error.

In this paragraph, the feasibility of performing incoherent calibration is studied using simulated data comparable with the ones expected for the GRACE Follow-On mission. The results have shown that incoherent calibration (under the hypothesis of having only noise in the residual range) allows to reduce up to two orders of magnitude the TPC noise within the measurement bandwidth. According to the previous results, with an instrument noise level of about $500\,\mathrm{nm}/\sqrt{\mathrm{Hz}}$ it would be still possible to reduce the TPC noise below the $20\,\mathrm{nm}/\sqrt{\mathrm{Hz}}$ requirement without the aid of a dedicated maneuver.

These results, though, are not fully representative of a real calibration scenario. Indeed, the residual range is not made of only noise but includes the error of the range estimation. Moreover, the instrument noise may be in part correlated with the attitude jitter. In order to take into account these additional disturbances, the calibration process is applied using real measurement data from the GRACE mission.

6.3 Calibration of the range measurement using GRACE data products

In this paragraph, the range measurement from the optical interferometer is replaced with the range measurement from the GRACE K-band instrument. The TPC noise is calculated separately and added to this range measurement. Attitude measurements and orbit ephemerides are also replaced with the ones of the GRACE mission. The pointing requirement for the science operations mode of the GRACE mission along the TPC sensitive axes [146, 147] is less demanding than the one of GRACE Follow-On or future geodesy missions [148] thanks to the wider field of view of the KBR instrument. The increased energy level of the calibration stimuli is nevertheless compensated by a comparable increase of measurement noise from the K-band instrument. In particular, the pointing performance are worsen by a factor of 10 while the range measurement accuracy is worsen by a factor of 20. The increased magnitude of the attitude jitter has, therefore, no significant benefit for the incoherent calibration.

The time series of the GRACE data used to test the calibration process are obtained after ground processing the telemetry coming from the science instruments on board the two satellites. They are labelled as Level-1 B data products in the GRACE science data system [145, 85]. The data products used here are the K-Band Ranging Data Product (KBR1B), the Star Camera Data Product (SCA1B) and the GPS Navigation Data Product (GNV1B).

The KBR1B data provide the biased range (true range variation plus an unknown bias) between the antenna phase centers of the two GRACE satellites and the correction factors required for estimating the range measurement with respect to the centers of mass of the satellites [149]. The KBR measurement is affected by phase breaks either in the K or in the Ka phase. If the time interval between the corrupted data and the valid phase observation before and after the data outliers is below a certain threshold, the faulty data are discarded and the gap is filled using linear or quadratic interpolation. If the threshold is exceeded, the faulty data are discarded and a temporal gap in the data stream is introduced. The calibration process is tested using the data products from June 20, 2009 to June 28, 2009 since the KBR measurement does not have temporal gaps in this time interval.

The SCA1B data are obtained after combining the attitude measurements from the two star cameras mounted on board each GRACE spacecraft. They provide the inertial orientation of the science reference frame of each satellite in the form of a quaternion. The science reference frame used for the GRACE mission is different than the one defined in this thesis. Nevertheless, since this reference frame has a static offset with respect to the body frame defined in this thesis, the SCA1B data are used here to define the inertial orientation of the body frames of the satellite pair. The SCA1B data have often gaps in their time series. The missing values of this time series are here calculated using the spherical linear interpolation of the quaternion [150] and introduced in the original time series.

The GNV1B data provide the precise orbit ephemerides for the two satellites in the Earth Fixed frame. The ephemerides are on ground estimated using the GPS tracking data (CA, L1 and L2). In order to properly process together the different data provided by the Level-1 B products, the timetags of the data streams are corrected to GPS time using GPS clock solutions.

The MWI does not generate TPC noise, therefore this needs to be added to the range measurement in order to apply the calibration process. This can be done either using the optical simulator described beforehand (in this case orbit ephemerides and attitude information are taken from the GNV1B and SCA1B data respectively) or by simply multiplying the attitude jitter with scaling factors and adding the result to the KBR1B data. The latter solution is here used since it is an easier choice for calculating the performance of the calibration process using different coupling coefficients (the recovery of the coupling coefficients through test simulations is avoided). The four coefficients used to test the calibration process are listed in Tab. 6.4. Also in this case, the calibration algorithm has been applied using different coupling coefficients and the results here presented are representative of the calibration performance.

Master	C_1 (m/rad)	Slave	C_1 (m/rad)
ϑ_P	20×10^{-3}	ϑ_P	-0.5×10^{-3}
ϑ_Y	-3×10^{-3}	ϑ_Y	-6×10^{-3}

Table 6.4: Coupling coefficients used to generate the TPC noise added to the range measurement of the K-band instrument.

In order to generate the TPC noise, the jitters of the spacecrafts orthogonal to the longitudinal line of sight have to be multiplied with the intended coupling coefficients. SCA1B data provide the inertial orientation of the body frame of the satellites while the orientation of the science reference frame is evaluated using the orbit ephemerides of the GRACE constellation. Since these are defined in the Earth Fixed frame, the transformation sequence depicted in Fig.

6.13 is mandatory for evaluating the orbit ephemerides in the CRS J2000 frame. The position and the velocity of each satellite along the orbit is

$$\mathbf{r}_{\mathrm{J}} = \mathbf{r}_{\mathrm{JE0}} + \mathbf{R}_{\mathrm{JE0}}\mathbf{r}_{\mathrm{E0}}$$

$$\mathbf{v}_{\mathrm{J}} = \mathbf{R}_{\mathrm{JE0}}\left(\mathbf{v}_{\mathrm{E0}} + \begin{bmatrix} 0 \\ 0 \\ \omega_{\mathrm{E}} \end{bmatrix} \times \mathbf{r}_{\mathrm{E0}}\right) \tag{6.19}$$

where $\mathbf{R}_{\mathrm{JE0}}$ is the transformation matrix from Earth Fixed frame to CRS J2000 frame, ω_{E} is the mean Earth rotation rate (excluding the Earth's precession), $\mathbf{r}_{\mathrm{E0}}$ and $\mathbf{v}_{\mathrm{E0}}$ are the position and velocity vector in the Earth Fixed frame respectively while $\mathbf{r}_{\mathrm{J}}$ and $\mathbf{v}_{\mathrm{J}}$ are the same vectors expressed in the CRS J2000 frame (see appendix C.3). The vector $\mathbf{r}_{\mathrm{JE0}}$ defining the origin offset between CRS J2000 frame and Earth Fixed frame is null since both frames have their origin at the center of the Earth. The rotation matrix $\mathbf{R}_{\mathrm{JS}}$ is converted to a quaternion and than

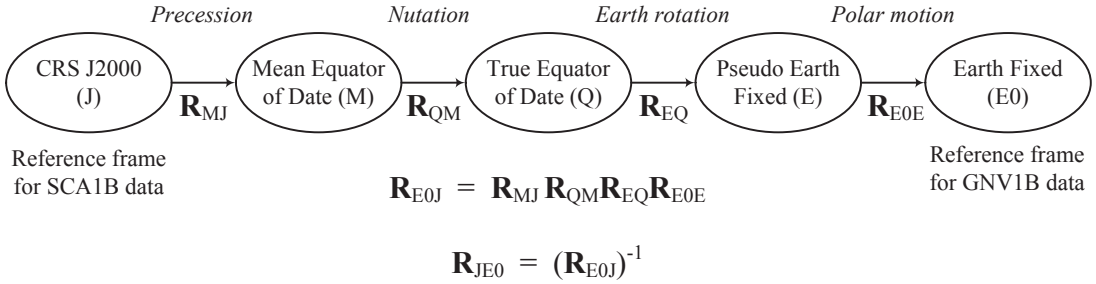

Figure 6.13: This figure shows the sequence of transformations required in order to evaluate the orbit ephemerides in the inertial frame.

multiplied with the quaternion specified in the SCA1B data (see appendix C.4). The resulting quaternion provides the orientation of the body frame with respect to the science reference frame (see appendix A.5). By converting this quaternion into Tait-Bryan angles (Roll, Pitch and Yaw) and multiplying these angles with the coupling coefficients listed in Tab. 6.4, it is possible to generate the TPC noise which is added to the KBR1B data. The resulting range measurement is equivalent to the one of Eq. 6.2.

The time trend of the range measurement between the satellites and the residual range is depicted in the left panel of Fig. 6.14 while the time trend of the operational attitude of one of the two satellites is depicted in the right panel of Fig. 6.14. Once more, the amplitude of the gravity signal is orders of magnitude bigger with respect to the operational jitter of the satellite and, without pre-processing the measurement data, incoherent calibration would not allow to reduce the algorithm error to acceptable values. Therefore the residual range is used for estimating the coupling coefficients. The residual range is calculated subtracting the K-band range measurement with the one calculated using the orbit ephemerides provided by the GNV1B data products. This time though, the residual range includes all the errors introduced by telemetry post-processing, imperfect modeling of the forces acting on the satellites, residual gravitational potential and measurement noise.

The left panel of Fig. 6.15 depicts the ASD of the range measurement and of the residual range while the right panel of Fig. 6.15 shows the ASD of the operational jitter of the satellite along the three body axis. Since the ASD is calculated using 8 days data (instead of the 24 hours data used in the previous paragraph) the contribution of the harmonics of the gravity field to the range and the attitude measurement is emphasized. Together with the main peak at the orbital frequency, also the peaks at multiples of the orbital frequency are now evident. This high correlation between range measurement and attitude measurements at multiples of the orbital frequency is confirmed by the coherence plots of Fig. 6.16.

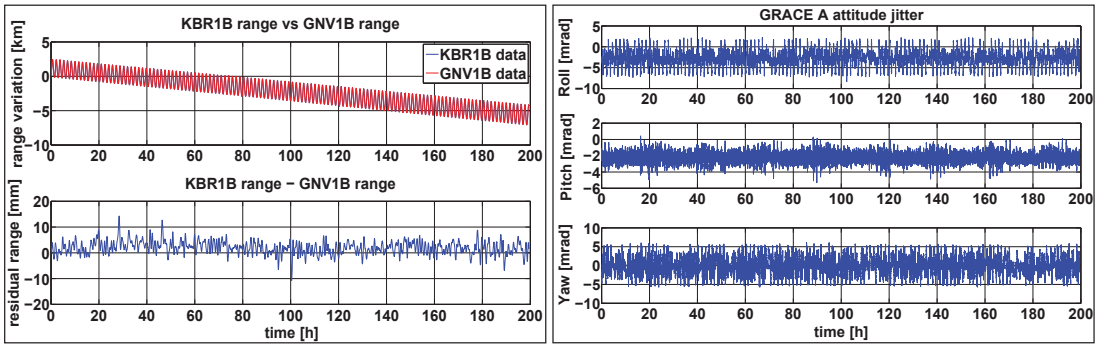

Figure 6.14: The left panel shows the time trend of the range variation between the satellites measured with the K-band instrument and with the GPS. Also in the left panel is depicted the residual range measurement obtained by subtracting the two range signals showed above. The right panel depicts the time trend of the attitude signal of one of the two satellites over a 200 hours time span. The two satellites have been labelled so far as master and slave due to the operation mode of the laser instrument (cavity stabilized or phase-locked). For the GRACE mission, this distinction is not possible and the two satellites are known as GRACE A and GRACE B. Since the calibration process is intended for the measurement of an laser instrument, the attitude data of GRACE A are appointed to the master satellite while the ones of GRACE B to the slave satellite.

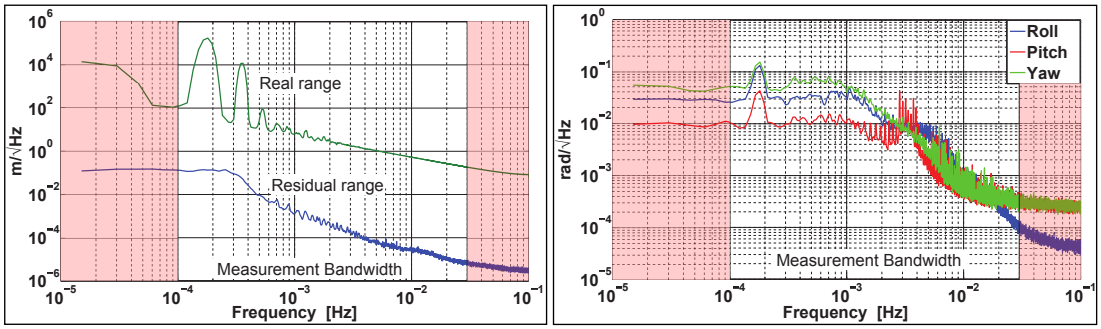

Figure 6.15: The left panel shows the ASD of the range measurement retrieved with the K-band instrument and the ASD of the residual range. The contribution of the gravitational potential to the separation between the satellites is highlighted by the peaks around the orbital frequency and its multiples. When subtracting the range given by the GNV1B data, only the contribution of the lower harmonics of the gravity field is removed. In the region between 0.6 mHz and 40 mHz the contribution of the high order harmonics is still evident in the residual range data. For frequencies higher than 40 mHz, the measurement is dominated by the noise of the MWI. The ASD of the attitude data shows a major peak at the orbital frequency and ancillary peaks at multiples of the orbital frequency. The time span of the measurement emphasizes the contribution of the higher harmonics of the gravity field (between ≈ 2 mHz and ≈ 20 mHz) with respect to the lower ones. Increasing the measurement time span would define better also the peaks of the lower harmonics.

For frequencies below the orbital one, the residual range is mainly affected by the inaccuracies in estimating the satellite orbits [151] and the magnitude of this error is in the millimeter range. This requires long measurement periods before the energy content of the attitude jitter is sufficient for reducing the algorithm noise to acceptable levels. Since the range measurements are affected by phase breaks, long measurement periods without outliers are difficult to achieve. Using measurements with temporal gaps introduce peaks in the pre-filtered data which increase the algorithm noise to unacceptable levels.

For frequencies above 30 mHz the MWI instrument and the antenna phase center correction noise are the major noise sources (the instrument noise is the dominant one) [152]. This region of the frequency spectrum is used to test the calibration process since the correlation between the instrument noise and the attitude measurement noise is expected to be minimized.

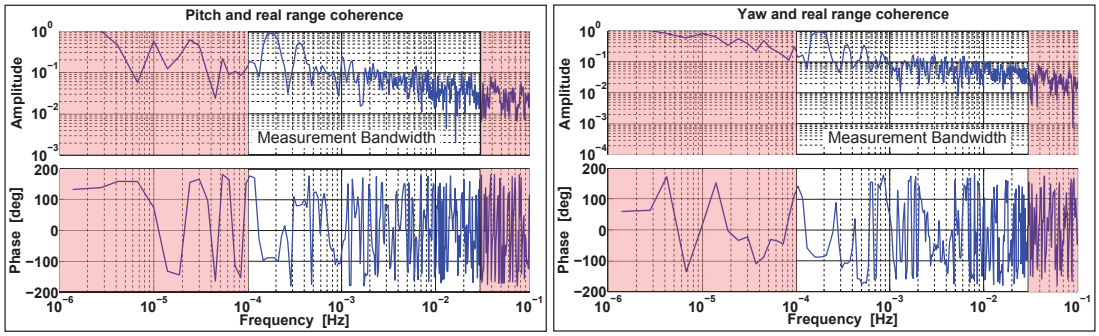

Figure 6.16: The coherence plots highlight how range measurement and satellites' pointing are both affected by the gravity field. Between 20 and 30 Mhz the noise sources start to become dominant. The coherence also approaches one for very low frequencies because of some drift in the SCA1B measurement data. If the KBR1B data are not corrected for the phase center offset, this relation is not present.

6.3.1 Calibration process applied to the GRACE range measurement

The calibration process is applied to the Level-1 B data products on top of which the TPC noise and the noise of the attitude measurement are artificially added

$$\begin{aligned} \Delta s\,(t) &= [s_{\mathrm{KBR1B}}\,(t) - \hat{s}_{\mathrm{GNV1B}}\,(t)] + \sum_j C_1^j \vartheta_j^{\mathrm{SCA1B}}\,(t) \\ \vartheta_j\,(t) &= \vartheta_j^{\mathrm{SCA1B}}\,(t) + n_{\mathrm{DWS}}\,(t) \end{aligned} \qquad \text{with } j = P_m\,, Y_m\,, P_s\,, Y_s \quad (6.20)$$

The TPC noise is generated using the Pitch and Yaw angles between body frame and science reference frame recovered from the SCA1B data. These angles are summed to the DWS noise (generated using the DWS noise shape filter) for simulating attitude measurements using the laser instrument. The range measurement of the K-band instrument is not corrected for the antenna phase center offset in order to minimize attitude related artifacts.

Calibration of the coupling coefficients using a high-pass filter as de-correlating filter

For comparison with the results of the previous paragraph, the calibration algorithm is once more applied pre-filtering the residual range and the attitude data with an elliptic high-pass filter. The cutoff frequency of the high-pass filter is 30 mHz, the stop-band attenuation is 80 dB and the pass-band ripple is 0.01 dB. The coupling coefficients estimated using this calibration method are listed in Tab. 6.5 while the ASD of the TPC noise after applying the range measurement adjustment is depicted in Fig. 6.17.

Calibration of the coupling coefficients using N band-pass filters as de-correlating filters

In Eq. 6.14 the estimated coupling coefficient is divided in the real value plus a delta contribution labelled as calibration error. Since the calibration error at high frequencies is principally caused by the instrument noise, the estimated coupling coefficient can be treated as the real coupling coefficient summed to a random variable. Indeed if there is no artefact that correlates the noise sources at different frequencies, the calibration noise resulting from the calibration process applied to the same set of data using two different filters is uncorrelated. Therefore, instead of using a single high-pass filter, the calibration algorithm can be applied N-times by pre-filtering the data with N different band-pass filters. The coupling coefficients can be

estimated afterwards as

$$\hat{C}_1^j = \frac{1}{N}\sum_{i=1}^{N}\hat{C}_{1,i}^j \quad \text{with } j = P_m\,,\, Y_m\,,\, P_s\,,\, Y_s \tag{6.21}$$

The band-pass filters used here are elliptic filters with a pass band width of 100 µHz and are distributed within the frequency spectrum that goes from 30 mHz to 90 mHz. Adjacent filters are separated by 50 µHz which return a band overlap of $\sim$ 50%. Also for these filters, the stop-band attenuation is 80 dB and the pass-band ripple is set to 0.01 dB.

The final estimate of the coupling coefficients can be further improved taking into account only the solutions of Eq. 6.7 where the condition number of the input correlation matrix is below a prefixed threshold. This expedient is referred hereafter as *optimization*. The optimization removes the high frequencies in which the attitude signals exploit correlation. Here, the threshold is set to $\kappa(\mathbf{C}) \leq 4$. The estimated coupling coefficients using and not using the optimization device are also listed in Tab. 6.5 while the ASD of the residual TPC noise is depicted in Fig. 6.17.

Analysis of the calibration results

When the range and attitude data are pre-processed with a high-pass filter the total TPC is reduced of one order of magnitude within most of the measurement bandwidth (exception made for some peaks at multiples of the orbital frequency). The error in estimating the coupling coefficients is about or below 10% except for the smallest one. The TPC noise induced by the Pitch jitter of the slave satellite is in the order of $\sim$ 0.1µm (the Pitch jitter is in the order of milliradians). This value is one order of magnitude below the MWI instrument noise. Since the coupling coefficients are recovered trying to separate the attitude noise from the K-band instrument noise (above 30 mHz the gravitational potential in KBR1B and SCA1B data is negligible) the noise introduced by this jitter stimulus is not clearly distinguishable from the background noise. The opposite result is achieved with the biggest of the coupling coefficients ($\hat{C}_1^P$ of the master satellite). In this case the estimation is highly accurate since the Pitch jitter stimulus of the master satellite introduces noise which is one order of magnitude higher than the background noise.

Data Pre-processing	Master			Slave		
	angle	$\hat{C}_1$ (m/rad)	ϵ	angle	$\hat{C}_1$ (m/rad)	ϵ
31 mHz HPF	ϑ_P	20.60×10^{-3}	3.04%	ϑ_P	-0.92×10^{-3}	84.98%
	ϑ_Y	-3.33×10^{-3}	10.88%	ϑ_Y	-5.91×10^{-3}	−1.42%
1201-BPFs	ϑ_P	19.99×10^{-3}	−0.04%	ϑ_P	-0.55×10^{-3}	10.40%
	ϑ_Y	-3.04×10^{-3}	1.32%	ϑ_Y	-5.92×10^{-3}	−1.21%
1201-BPFs + Optimization	ϑ_P	20.01×10^{-3}	0.07%	ϑ_P	-0.52×10^{-3}	2.91%
	ϑ_Y	-3.01×10^{-3}	0.37%	ϑ_Y	-5.95×10^{-3}	−0.74%

Table 6.5: The coupling coefficients recovered using different expedients when pre-processing the range and attitude data. ϵ is the estimation error between the real linear coupling coefficient reported in Tab. 6.4 and the estimated ones.

The range measurement adjustment can be further improved of one order of magnitude when the data are pre-processed using multiple band-pass filters. In this case, the estimation error is mitigated by calculating the mean coupling coefficients over 1201 estimated values. The optimization expedient further reduces the residual TPC noise. With the optimization, the total number of averages reduces from 1201 to 1062. The mitigation of the TPC noise, in this latter case, is not as evident as the one achieved switching from a single filtering to

multiple filtering (the residual TPC noise is on average reduce by a factor of 2). When using the optimization method, the estimate of the coupling coefficients is always improved except for the biggest one. Usually, the spread of the matrix **C** reduces the accuracy of the estimate. In the case of $\hat{C}_1^P$ of the master satellite even with a higher condition number of the input correlation matrix, the estimate is sufficiently good (due to the higher energy content of this attitude stimulus in the measured range) that reducing the total number of averages in Eq. 6.21 worsens the estimated value.

Although the estimation error using multiple band-pass filters is better than the estimation error achieved with the simulated range measurement (see paragraph 6.2.2) the residual TPC noise is not capable of fulfilling the $20\,\mathrm{nm}/\sqrt{\mathrm{Hz}}$ requirement. The cause is the magnitude of the operational jitter of the satellite which is at least one order of magnitude bigger than the one expected for future geodesy missions. In fact, when the data are pre-processed with multiple band-pass filters and only the optimal solutions are used for estimating the coupling coefficients, the TPC noise is reduced up to three orders of magnitude within the measurement bandwidth.

The residual TPC noise resembles a scaled version of the original one. This is due to the spectral content of the attitude jitter which is the same independently of the angle considered.

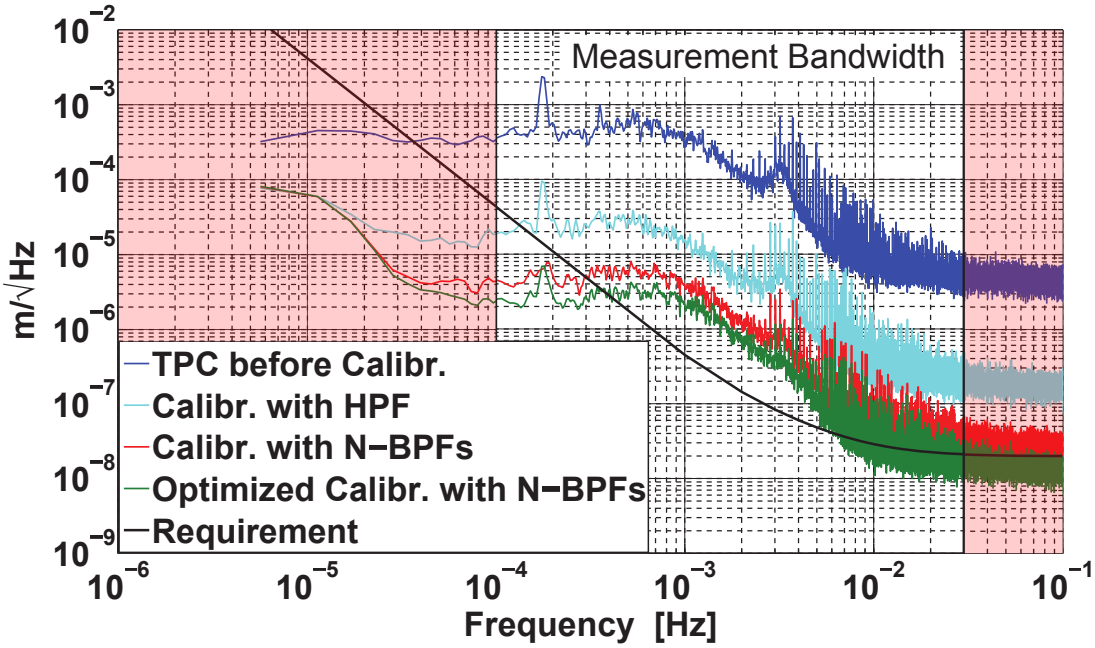

Figure 6.17: The TPC noise artificially added to the GRACE K-band range measurement is here depicted (blue line). The picture also shows the residual TPC noise (cyan, red and green curves) after applying the range measurement correction using the three different data processing techniques.

Analysis of algorithm noise and data filtering

The result presented in Tab. 6.5 is somehow contradictory with what one would expect. Indeed, within the bandwidth of the high-pass filter the energy content of the calibration signal should be higher than the one within the bandwidth of one of the 1201 band-pass filters. According to this reasoning, the estimated coupling coefficients should be more accurate with the first pre-filtering process. One of the causes of this discrepancy is the correlation between the calibration signals within the bandwidth of the high-pass filter (indeed, in absence of such correlation the optimization should not further improve the estimated coupling coefficients).

Another noise contribution that can nullify the outcome of the calibration algorithm is the correlation between the calibration stimulus and the range measurement. Indeed, mechanisms

which influence both the range measurement and the attitude readout significantly increase the algorithm noise (in this cases the term $\mathbf{N}\boldsymbol{\vartheta}_i^T$ of Eq. 6.14 is, most likely, not approximately zero or significantly smaller than $\boldsymbol{\vartheta}_i\boldsymbol{\vartheta}_i^T$). Without a deep analysis of all the noise sources that influence the accuracy of the range measurement, the magnitude of the algorithm noise can be estimated calculating the standard deviation of the N coupling coefficients calculated using N different de-correlating filters (indeed, if there would be no algorithm noise, the outcome of the calibration process is always the same independently from the de-correlating filters).

In order to estimate the algorithm noises in the high frequency region ($f > 30\,\text{mHz}$), the calibration algorithm is applied more than once. For each application, the high frequency bandwidth is subdivided evenly with N pass-band filters (in particular the algorithm is executed 5 times with N respectively equal to 13, 121, 601, 1201 and 2401). For each application, the mean coupling coefficient is recovered through Eq. 6.21 after applying the optimization. Figure 6.18 shows the normalized estimation error and the standard deviation of the estimated coupling coefficients. As the plot shows, the estimation error decreases as the number of filter increases (contrary to expectation since the energy of the calibration signal should decrease with the number of filters employed). The explanation of such a behaviour is in the trend of the magnitude of the standard deviation. Indeed, this is quasi-constant independently of the number of filters used (thus, measurement noise and the calibration stimuli both increase with time). The relation between estimation accuracy and number of filters is, in this case, independent form the energy content of the calibration stimulus but reflects Bernoulli's theorem. The coefficient calculated with Eq. 6.21 is more accurate as the number of estimates increases.

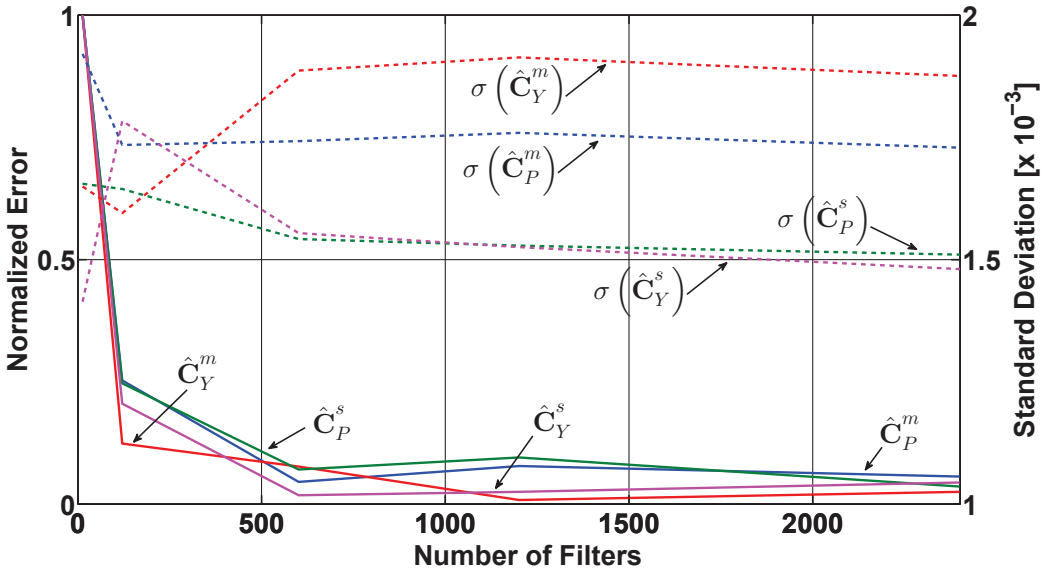

Figure 6.18: The picture depicts the trend of the normalized estimation error (solid line) and of the standard deviation of the estimated coupling coefficients (dashed line) as a function of the number of filters used during data pre-processing.

The standard deviation of $\hat{C}_P^m$ and $\hat{C}_P^s$ decreases as the number of filters increases. This unexpected behavior is most likely given by some short-term mechanism that affects both the range measurement and the Pitch angle. $\hat{C}_Y^m$ and $\hat{C}_Y^s$ instead, behave as expected since their standard deviation increases as the bandwidth of the filter decreases. Such "asymmetric" performance would require further investigation.

The outcome of the calibration simulations of Fig. 6.18 is listed in Tab. 6.6. About 500 averages would be already sufficient for a good estimation of the coupling coefficients. Increasing the number of averages (and thus of runs of the calibration algorithm) does not significantly

improve the result but increases the computation time. 1201 filters are here identified as a good compromise between accuracy and computation time. Nevertheless, with a better understanding of how the range measurement and attitude jitter are correlated in the frequency spectrum above 30 mHz it could be possible to design optimal band-pass filters which contemporary improve the algorithm accuracy and reduce the computation time.

Filters & angles		Master			Slave		
		$\hat{C}_1$ (m/rad)	ϵ (%)	σ (m/rad)	$\hat{C}_1$ (m/rad)	ϵ (%)	σ (m/rad)
13	ϑ_P	19.47×10^{-3}	-2.7	1.9×10^{-3}	0.21×10^{-3}	-141.6	1.7×10^{-3}
	ϑ_Y	-2.43×10^{-3}	-19.1	1.6×10^{-3}	-5.26×10^{-3}	-12.31	1.4×10^{-3}
121	ϑ_P	19.87×10^{-3}	-0.67	1.7×10^{-3}	-0.33×10^{-3}	-34.97	1.6×10^{-3}
	ϑ_Y	-2.93×10^{-3}	-2.37	1.6×10^{-3}	-5.85×10^{-3}	-2.53	1.8×10^{-3}
601	ϑ_P	19.98×10^{-3}	-0.12	1.7×10^{-3}	-0.55×10^{-3}	10.02	1.5×10^{-3}
	ϑ_Y	-3.04×10^{-3}	1.47	1.9×10^{-3}	-5.99×10^{-3}	-0.22	1.6×10^{-3}
1201	ϑ_P	20.01×10^{-3}	0.07	1.8×10^{-3}	-0.52×10^{-3}	2.91	1.5×10^{-3}
	ϑ_Y	-3.01×10^{-3}	0.37	1.9×10^{-3}	-5.95×10^{-3}	-0.74	1.5×10^{-3}
2401	ϑ_P	19.97×10^{-3}	-0.15	1.7×10^{-3}	-0.53×10^{-3}	5.08	1.5×10^{-3}
	ϑ_Y	-3.02×10^{-3}	0.48	1.9×10^{-3}	-5.96×10^{-3}	-0.55	1.5×10^{-3}

Table 6.6: This table lists the results of the calibration process when the high frequency bandwidth is subdivided into smaller bandwidths whose dimensions depend on the number of filters used. ϵ is the estimation error between the real linear coupling coefficient reported in Tab. 6.4 and the estimated ones.

6.3.2 Minimum measurement time for incoherent calibration

In the previous applications, the full length of the available data is used for estimating the coupling coefficients. One could to think that, the longer the measurement time, the higher is the energy accumulated by the calibration stimulus and thus more accurate is the estimate of the coupling coefficient. In reality, since the data are high-pass filtered, a good reconstruction of the incoherent calibration stimulus is reached with a finite number of observations and adding more measurements to the attitude and range data does not bring any significant improvement to the outcome of the calibration algorithm.

In order to evaluate the minimum measurement time required by the calibration algorithm for converging to an optimal solution, the calibration algorithm is executed increasing the measurement time from 1 hour to 200 hours using steps of 1 hour. The variable monitored for evaluating the convergence of the algorithm is the condition number of the input correlation matrix. Its trend over time is depicted in Fig. 6.19. As the plot shows, the condition number after ~ 50 hours reaches a steady state condition. From this point on, the estimation error of the coupling coefficients is not expected to vary significantly. In order to prof this statement, the calibration algorithm is executed using the first 60 hours of the attitude and range measurement data. The data are pre-processed using N band-pass filters and applying the optimization. The estimated coupling coefficients are listed in Tab. 6.7.

Figure 6.20 depicts the ASD of the residual TPC noise after adjusting the range measurement. This residual TPC noise is compared to the one obtained applying the same data pre-processing to the total length of the measurement data. The solution using 60 hours data is slightly worse than the one obtained using the full time series of the range and attitude measurements. This is caused by a bigger error in the estimation of $\hat{C}_1^P$ of the master satel-

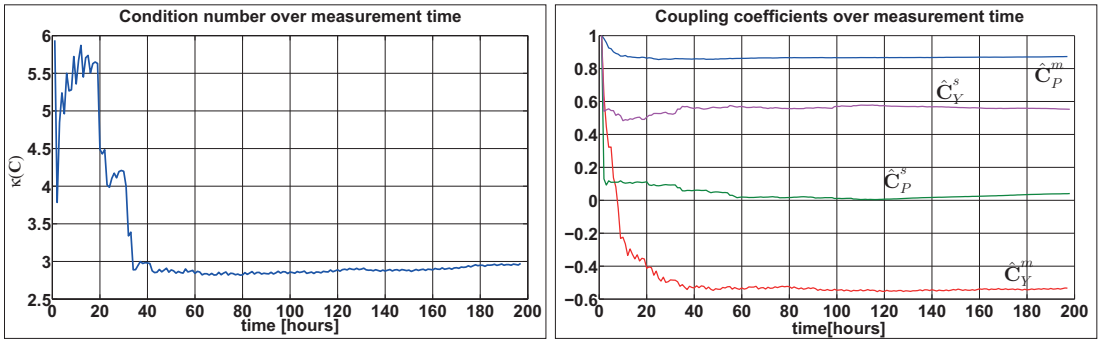

Figure 6.19: The left panel depicts the trend of the condition number of the input correlation matrix over a 200 hours time span. The right panel shows the normalized values of the four coupling coefficients over the same time interval. After ≈ 60 hours the coefficients do not change significantly over time.

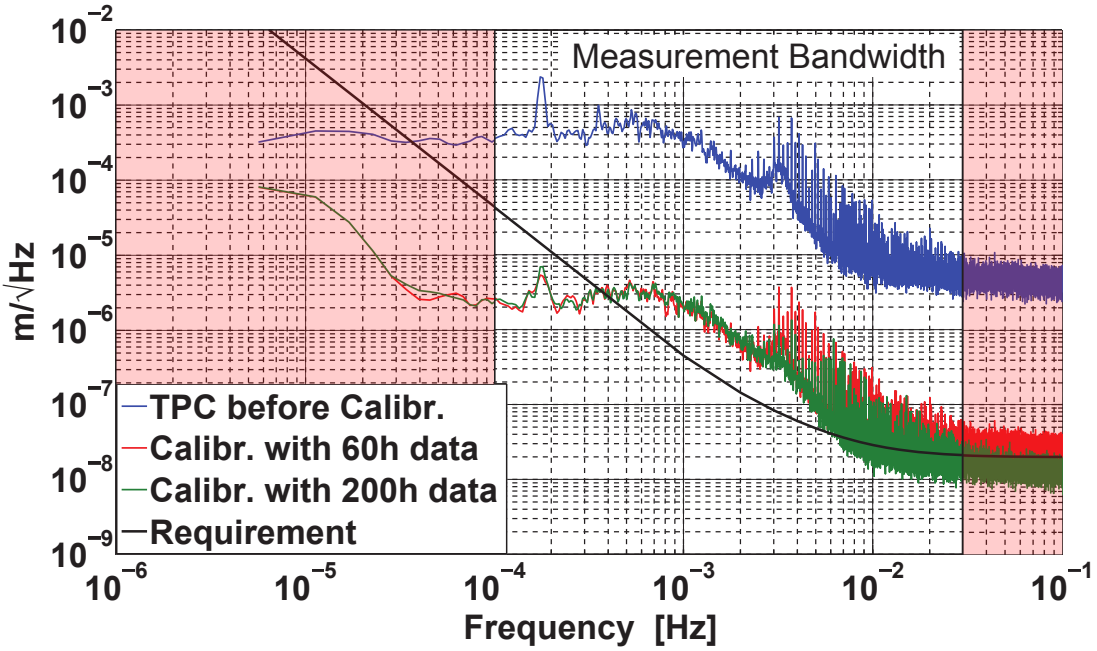

Figure 6.20: Residual TPC noise when the coupling coefficients are estimated using 60 and 200 hours of range and attitude measurements. The two residual noises are comparable.

lite. Since this factor is the major contributor to the TPC noise, small errors in its estimation translate into higher residual noise. Despite this, the difference between these two calibration process is fairly negligible.

Although the calibration process is capable, in some regions of the measurement bandwidth, of reducing the TPC noise of three orders of magnitude, the residual noise level is not compatible with the one of a future geodesy mission. The operational jitter is such that even a small error in the estimation of coupling coefficients translates into a non-negligible TPC noise.

6.4 Recovery of the coupling coefficients using coherent calibration

The range measurement of the K-band instrument of the GRACE mission does not measure the distance between the CoMs of the two satellites but between the phase centers of the K-band horns [149]. Each satellite is designed such that the line joining the phase center of

Measurement length	Master			Slave		
	angle	$\hat{C}_1$ (m/rad)	ϵ	angle	$\hat{C}_1$ (m/rad)	ϵ
200 hours	ϑ_P	20.01×10^{-3}	0.07%	ϑ_P	-0.52×10^{-3}	2.91%
	ϑ_Y	-3.01×10^{-3}	0.37%	ϑ_Y	-5.95×10^{-3}	−0.74%
60 hours	ϑ_P	19.89×10^{-3}	−0.51%	ϑ_P	-0.48×10^{-3}	−3.49%
	ϑ_Y	-3.02×10^{-3}	0.63%	ϑ_Y	-5.96×10^{-3}	−0.65%

Table 6.7: Coupling coefficients estimated with 60 hours of measurement data and with 200 hours of measurement data. ϵ is the estimation error between the real linear coupling coefficient reported in Tab. 6.4 and the estimated ones. This error is about the same order of magnitude for the two calibration processes.

the K-band horn to the fiducial point of the accelerometer is coincident with the LoS of the instrument. In reality, perfect alignments are not feasible and the phase centers of the K-band horns may change after undergoing lunch vibrations. The KBR1B range measurement is therefore corrected during on ground processing of the K-band range data in order to take into account this offset. The magnitude of the phase center offset of each K-band horn is recovered after performing a KBR calibration maneuver [49].

The KBR calibration maneuver consist of applying a static offset (ϑ_0) to the satellite's pointing with respect to the line of sight and, on top of that, applying a periodic oscillation. Because of the indirect reflection of the microwave signals around the antenna horn during the calibration maneuver the multipath noise of the instrument is significantly high and the contribution of the antenna phase center offset cannot be isolated. For such a reason, the KBR calibration is performed applying two mirrored maneuvers. Indeed, for each calibration maneuver, the multipath noise is expected to have the same magnitude and opposite sign. The KBR calibration maneuvers for GRACE B were executed on February 10, 2003, February 11, 2003 and February 20, 2003. The KBR calibration maneuvers for GRACE A were executed on March 12, 2003, March 19, 2003 and March 20, 2003. Figure 6.21 depicts the time trend of the attitude measurement during two of the calibration maneuvers and the residual range in the same time frame.

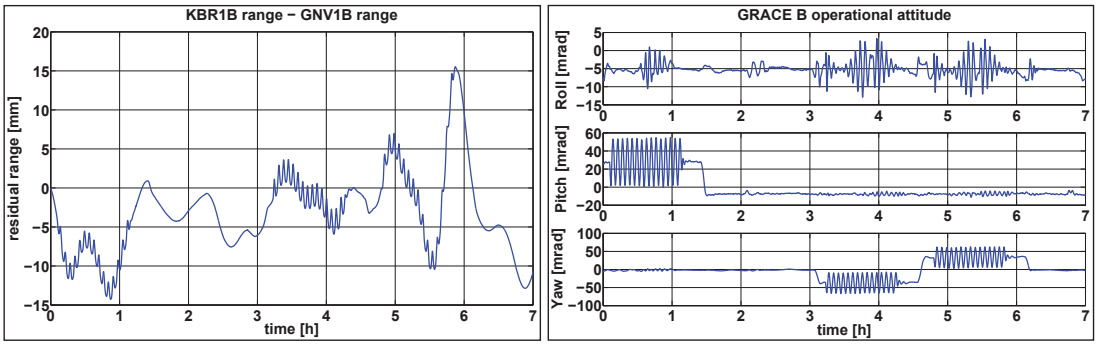

Figure 6.21: The right panel shows the time trend of the attitude of GRACE B on February 20, 2003. It is possible to clearly distinguish the calibration maneuver performed oscillating the satellite around the Y axis of the body frame and the two (mirrored) maneuvers applied rotating the satellite about the Z axis of the body frame. The left panel shows the time trend of the residual range on the same date.

The calibration maneuvers together with the calibration algorithm described in paragraph 6.1.2 are used in this paragraph to estimate the coupling coefficients responsible of the TPC noise. Since the sinusoidal signal used to oscillate the satellites is wide sense stationary (see appendix C.5), the calibration algorithm is expected to return valid results. Since each maneuver

is used to recover its associated coupling coefficient (the calibration process can be reduced to the LTI system of Fig. 6.1) the calibration algorithm needs to be applied separately for each axis on which the calibration maneuver is performed.

The TPC noise and the attitude measurement noise are once more artificially added to the KBR1B data (once more neglecting the antenna phase center correction) and to the SCA1B data as described in Eq. 6.20. The coefficients used to generate the TPC noise are the ones listed in Tab. 6.4.

The amplitude of the satellite oscillation during the calibration maneuver of the KBR is about one degree. A maneuver with such amplitude is unrealistic for an LRI like interferometer due to the limited field of view of the instrument. Therefore, the following paragraphs are just intended to demonstrate the flexibility of the proposed calibration algorithm in estimating the coupling coefficients using either incoherent or coherent stimuli.

6.4.1 Calibration process using the KBR calibration maneuver

The range measurement of the KBR antenna is affected by an error given by the multipath effect which can be modelled as $\Delta r = \pm\mu\vartheta$. With a positive static pointing offset ($\vartheta_0 > 0$), the multipath takes a positive sign while with a negative static pointing offset ($\vartheta_0 < 0$) the multipath takes a negative sign. In order to find these constant errors and subtract them from the estimated coupling coefficients, the calibration algorithm is first applied using the range and attitude data which have not been artificially corrupted by noise (C_1^j and $n_{\mathrm{DWS}}(t)$ of Eq. 6.20 are set to zero). Once these values are determined, the noises (TPC and DWS) are added to the data and the calibration algorithm is once more executed.

Calibration of the coupling coefficients band-pass filtering attitude and range data

The oscillating part of each calibration maneuver consists 15 cycles each of which lasts 250 seconds and can be isolated from the rest of the measurement using a band-pass filter centered on the fundamental frequency of the oscillation. The filter employed has the lower cut-off frequency at 2 mHz and the higher at 6 mHz. The pass-band ripple is 0.01 dB while the attenuation in the stop-band is 80 dB.

When the calibration algorithm is applied to the range and attitude data, it returns a positive constant value for the calibration maneuver with a positive static offset and a negative value for the mirrored one. These constants are subtracted from the estimated coupling coefficients since their translation into the phase center offset has already been studied in the past [49] and is beyond the scope of this thesis.

The four coupling coefficients are estimated using the eight KBR calibration maneuvers of GRACE. Since each coupling coefficient is calculated twice, the final coefficient is estimated as the mean value of the two. The coupling coefficients recovered after applying coherent calibration are listed in Tab. 6.8.

The ASD of the residual TPC noise after adjusting the range measurement is compared to the best result achieved using incoherent calibration and is depicted in Fig. 6.22. The result shows that there is no significant improvement in the residual range with respect to the case of incoherent calibration. As in the previous paragraph, because of the high magnitude of the operational jitter even a small calibration error introduces non-negligible adjustment error to the range measurement. The cause of the calibration error is mainly ascribable to the correlation between the attitude signals and between the attitude signals and the range measurement in the spectrum that goes from 2 mHz to 6 mHz. Here 21 harmonics of the orbital frequency are present and all the three attitudes are strongly influenced by them (the ASDs of the attitude measurements, depicted in the right panel of Fig. 6.15, have a considerable amount of spikes in the pass-band region of the filter).

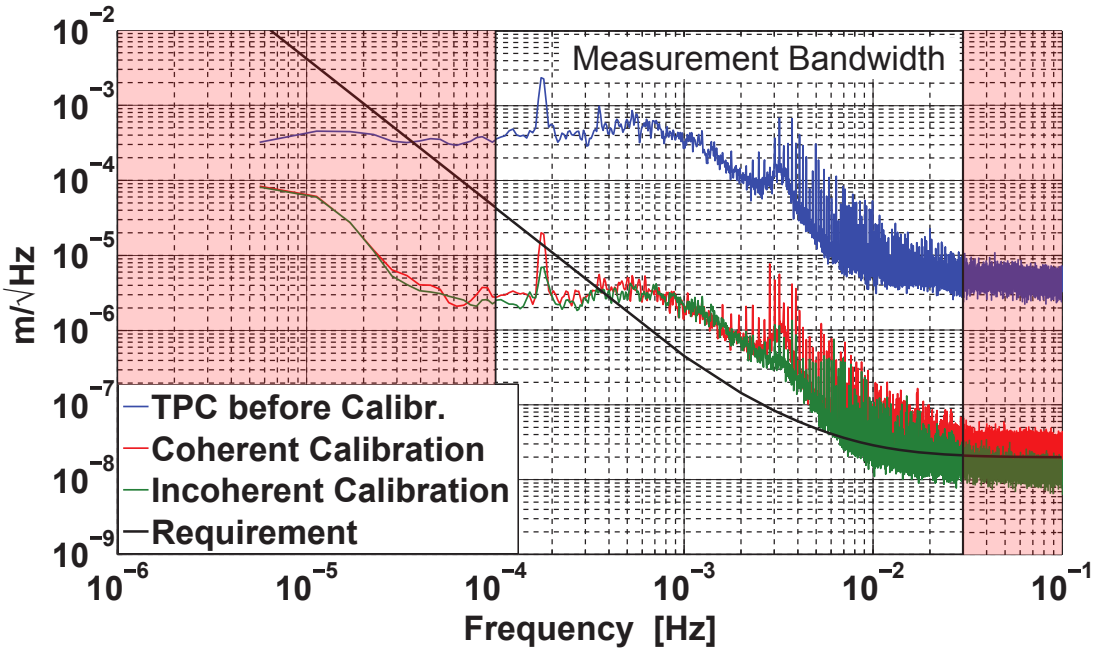

Figure 6.22: The magnitude of the residual range measurement applying the coherent calibration or the incoherent calibration is, in this case, comparable. For some frequencies within the measurement bandwidth the incoherent calibration performs even better.

Calibration method	Master			Slave		
	angle	$\hat{C}_1$ (m/rad)	ϵ	angle	$\hat{C}_1$ (m/rad)	ϵ
Incoherent Calibration	ϑ_P	20.01×10^{-3}	0.07%	ϑ_P	-0.52×10^{-3}	2.91%
multiple filters	ϑ_Y	-3.01×10^{-3}	0.37%	ϑ_Y	-5.95×10^{-3}	−0.74%
Coherent Calibration	ϑ_P	20.01×10^{-3}	0.07%	ϑ_P	-0.4×10^{-3}	−20.96%
single filter	ϑ_Y	-2.96×10^{-3}	−1.44%	ϑ_Y	-5.99×10^{-3}	−0.22%

Table 6.8: Estimated coupling coefficients using coherent and incoherent calibration. ϵ is the estimation error between the real linear coupling coefficient reported in Tab. 6.4 and the estimated ones. Since the magnitude of the calibration error is comparable, no advantage is taken, in this case, in performing a calibration maneuver.

Calibration of the coupling coefficients using multiple band-pass filters for filtering attitude and range data

The fundamental frequency of the oscillation maneuver is in the measurement bandwidth and the result of the calibration algorithm is strongly influenced by the harmonics of the orbital frequency. A solution for mitigating this effect is to execute the calibration algorithm multiple times and for each execution pre-filter the data with a different band-pass filter. The filters are not necessarily centered at 4 mHz, but all include this frequency within their pass-band. The final coupling coefficients are calculated as in Eq. 6.21. 18 filters are used to pre-process the data for each of the 8 calibration maneuver. The total number of averages for each coefficient is therefore 36. Table 6.9 lists the new estimated coupling coefficients while Fig. 6.23 compares the residual TPC noise after adjusting the range measurement with these new coefficients with the best calibration result achieved using incoherent calibration. In this second application, the coherent calibration estimates the coupling coefficients with a negligible calibration error. The residual TPC noise is mainly given by the DWS measurement noise which has been artificially added to the attitude measurement and is below the 20 nm$\sqrt{\text{Hz}}$ requirement. Also in this

Calibration method	Master			Slave		
	angle	$\hat{C}_1$ (m/rad)	ϵ	angle	$\hat{C}_1$ (m/rad)	ϵ
Incoherent Calibration	ϑ_P	20.01×10^{-3}	0.07%	ϑ_P	-0.52×10^{-3}	2.91%
multiple filters	ϑ_Y	-3.01×10^{-3}	0.37%	ϑ_Y	-5.95×10^{-3}	−0.74%
Coherent Calibration	ϑ_P	20×10^{-3}	$< 10^{-5}$%	ϑ_P	-0.50×10^{-3}	$< 10^{-5}$%
multiple filters	ϑ_Y	-3×10^{-3}	$< 10^{-5}$%	ϑ_Y	-6×10^{-3}	$< 10^{-5}$%

Table 6.9: Estimated coupling coefficients using coherent and incoherent calibration. ϵ is the estimation error between the real linear coupling coefficient reported in Tab. 6.4 and the estimated ones.

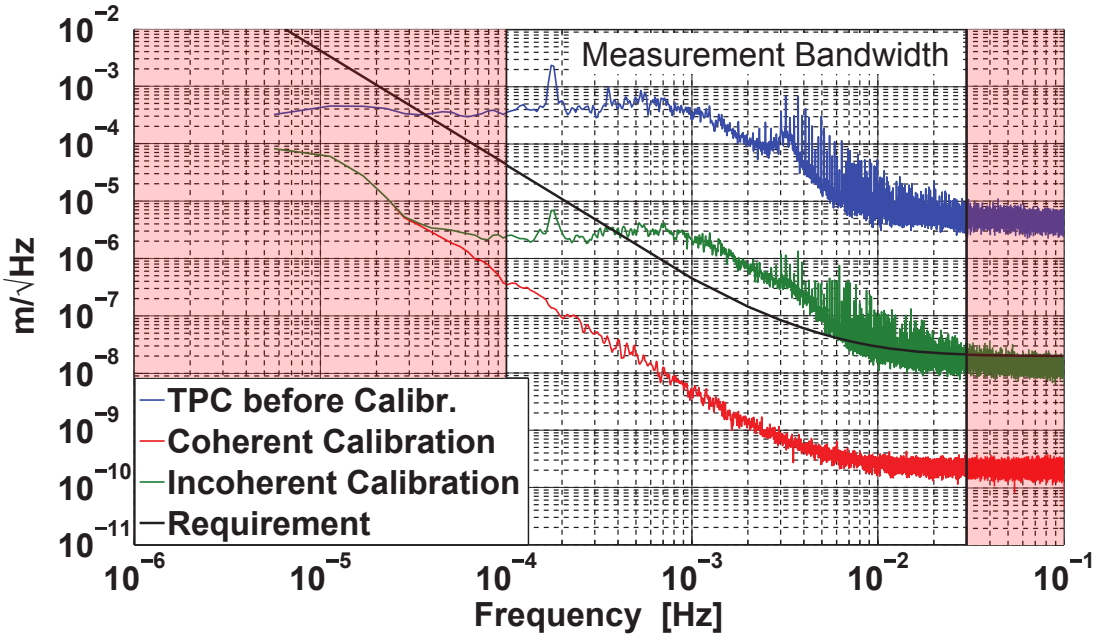

Figure 6.23: The magnitude of the residual range measurement applying the coherent calibration and the incoherent calibration is depicted. In this application, coherent calibration is capable of reducing the TPC noise below the requirement curve.

case, using multiple filters for pre-processing the attitude and range data is an efficient way of improving the calibration process.

6.5 Calibration process using adaptive filtering

In the previous paragraphs, the calibration process is applied considering the coupling coefficients constant over time. In reality the measurement fiducial of the instrument might change over the mission lifetime. Thermal deformations and moisture release are among the main causes of this variation. In case of coherent calibration, calibration maneuvers over the lifetime of the mission would be required to keep track of the changes of the coupling coefficients. This implies interruption of the science operations, significative consumption of propellant and, most important, a high number thrust pulses (just the calibration maneuver of the K-band instrument requires almost 1500 thrust pulses while the average over the mission lifetime of thrust pulses per day is 810). Since this is not a feasible solution, tight requirements are set on the maximum allowable excursion of the phase center of the instrument.

With incoherent calibration, the coupling coefficients can be estimated on regular basis

without interrupting science operations and without affecting the lifetime of the mission. This can be done either executing the calibration algorithm on a regular schedule or tuning the algorithm according to the adaptive filter theory. Different algorithms are available in literature [139] and can be applied for tracking changes of the coupling coefficients.

The adaptive process though has a limitation on the time scales with which changes of the coupling coefficients can be tracked. As shown in the subparagraph 6.3.2, there is a minimum measurement time below which the result of Eq. 6.7 is non-optimal. Therefore, extending the calibration algorithm with the adaptive filter theory, it is possible to track variations of the phase center of the instrument with a time scale of days. Variations due to thermal deformation caused by illumination-eclipse transition over one single orbit are, in general, not feasible. The noise introduced by these deformations has to be taken into account when defining the requirement on the TPC noise.

6.6 Applicability of the incoherent calibration to eLISA and GRACE Follow-On

The GRACE Follow-On mission mounts the first intra-spacecraft laser interferometer as a technology demonstrator. For such a reason, the calibration maneuvers are intended only for the K-band instrument while the TPC noise of the LRI is included in the noise budget of the instrument and is expected to be a non-negligible noise source when compared to the other noise sources.

A possible solution for mitigating TPC noise and improve the range measurement could be applying incoherent calibration. The calibration algorithm could use the residual range measurement given by subtracting the biased range of the K-band instrument with the measurement of the LRI. In this case, any correlation caused by the gravitational potential would be minimized and the only noise sources would be the ones of the instruments. Calibrating the coupling coefficients could also give information about the in-orbit performance of instrument components such as the TMA. Tracking the trend of the coupling coefficients over the mission lifetime could give an indication on the stability of this optical component aiding its design for future gravity missions.

The goal of the eLISA measurement setup is to measure the distance variation between two drag-free proof masses [153, 154, 155]. In reality, the proof mass to proof mass measurement is synthesized combining the measurement of the distance variation between the optical benches on board two separate spacecraft and the local distance variation between the optical benches and the associated proof masses. Under ideal circumstances, the line of sight of the telescope is aligned to the incoming beam while the reference surface of the proof mass is oriented orthogonal to the line of sight and centered in its housing.

The non ideality of the system are such that rotations of the proof masses, rotations of the optical bench versus the proof mass or versus the inertial reference frame compromise the proof mass to proof mass measurement accuracy via TPC noise. This noise is distinguishable from cross talk effects caused by electrical or gravitational fields (which cause an acceleration of the proof mass along the measurement axis) since its effect is dominating at frequencies higher than 5 mHz.

The calibration of the long arm interferometry measurements can be performed using the external stimuli. In this case, the execution of an induced movement of the spacecraft does not change the system behavior. Each spacecraft can be rotated in turn around the two sensitive axes with a sinusoidal signal. In principle, the position of the proof mass relative to the optical bench could be measured in the same way. The proof mass would be rotated and shifted along the sensitive axes of the system. The difficulty of this approach is avoiding that torques and forces employed for generating the test signal accelerate the proof mass along other directions except for the desired one. Indeed with the excitation of more than one degree of freedom, the

calibration of the purely rotational/translational effects along the sensitive axes would not be possible.

The alternative is to use the jitter of the proof mass to remove on ground the TPC effect due to its motion. In this case, no actuation is involved and the contribution of the rotational/translational effect along each axis can be isolated. For such a reason, incoherent calibration can be considered as a possible baseline for the interface calibration of the proof mass relative to the optical bench. With the improvement of the noise models acting on the test masses (thanks also to the results of the LISA Pathfinder mission) a deep analysis of this calibration procedure would be feasible and thus recommended.

Chapter 7

Conclusions

In the initial part of this work, three possible layouts of an interferometer for future geodesy missions are analyzed together with their measurement principle. Two of the three layouts are a modification of the interferometer design used for the LRI of GRACE Follow-On; precisely, the TMA configuration is an improvement of the LRI design whilst the compact corner cube configuration is conceptually identical to the LRI despite the fact that the TMA is replaced by a classical corner cube retroreflector in order to minimize the size of the instrument. The on-axis system is conceived for minimizing both attitude dependant disturbances and dimensional constraints.

Together with the three interferometers, the principal equations for identifying their displacement noise are also presented. These equations are used later to calculate the measurement performance of each design and compare it with the requirement of the GRACE Follow-On mission. The three interferometers address the $50\,\mathrm{nm}\sqrt{\mathrm{Hz}}$ mission requirement and, most interesting, the measurement performance are practically layout independent. Indeed, the principal noise terms have roughly always the same magnitude. Thus, according to this analysis, the on-axis interferometer and the layout with the compact corner cube would be the best candidates for a future geodesy mission since the dimensions, the manufacturing complexity and the costs of the instrument would be contained.

Herein, the noise budget is used to calculate the measurement accuracy of the instrument given its design parameters. Nevertheless, this can be also used in the other direction; given the desired measurement accuracy, the equations of the noise budget can be used to calculate the design parameters of the instrument (i.e. the alignment of the optical components).

In the second chapter, a phasemeter with a novel frequency estimation stage is described. The logic elements and the implementation choices adopted for the frequency estimation stage minimize the usage of computational resources of an FPGA when compared to a frequency estimation stage based on a DFFT algorithm. Simulation and experimental results have demonstrated that this phasemeter is capable of acquiring a signal which is buried into noise and whose frequency can vary in a band 24 MHz wide. Using signal generators, the phasemeter locks a time varying signal with an SNR of $-11\,\mathrm{dB}$ in less than $500\,\mu\mathrm{s}$ and its main DPLL fulfills the requirement of the eLISA mission in terms of phase measurement accuracy.

The phasemeter is also tested with an experimental setup which reproduces the frequency acquisition process of two lasers (one cavity stabilized and one free-running). The outcome of this experiment confirmed the robustness of the signal processing logic of the frequency estimation stage and the capability of the system in switching to frequency control mode in less than $500\,\mu\mathrm{s}$.

Together with a new phasemeter design, also a new solution for the beam pointing control is discussed. The possibility of rapidly steering the laser beam depends on the layout of pointing controller of the SM and on its closed-loop performance. Simulation and experimental analysis show that the feedback controller limits the capability of the SM to track a setpoint with a frequency of $80 - 100\,\mathrm{Hz}$ unless its close-loop bandwidth is above $4\,\mathrm{kHz}$. Since the SM of the

LRI has a maximum close-loop bandwidth of 1 kHz the feedback controller is, herein, replaced by a feedforward controller. This significantly enhances the pointing capabilities of the SM without influencing its close-loop bandwidth. Nevertheless this new controller is much more sensitive to process variations and, unlike the feedback controller, can be fully optimized only for a specific time series of setpoint commands. A SM capable of tracking a high frequency setpoint is extremely important especially during the initial signal acquisition phase. Indeed, by introducing the concept of feedforward control to the initial acquisition algorithm of the GRACE Follow-On mission, it could be possible to reduce its execution time of $\approx 73\%$.

In the fourth chapter of this thesis, the problem of the initial signal acquisition has been tackled. Here two possible strategies are considered for conducting the signal acquisition; namely the split acquisition and the direct acquisition. According to simulations, the split acquisition strategy has a lower probability of acquiring the signal (only 90% of acquisition attempts are successful) when compared to the direct acquisition strategy (97% of acquisition attempts are successful after only one trial) since this latter strategy does not rely on high platform stability, low laser frequency noise, low pointing noise and it avoids the satellite-to-ground data transfer. In case of a missed acquisition, the telemetry of both laser instruments can be used to evaluate the cause of the miss-detection, re-calibrate the instrument and perform a second acquisition attempt (similarly to what is done for the split acquisition). For these reasons the direct acquisition represents the best acquisition strategy since it is the most straight forward solution for establishing the optical link and because it intrinsically allows to execute the acquisition algorithm also according to the split acquisition.

Beside four continuous patterns, also random patterns are considered as possible beam guidance laws. A random pattern allows to loosen the rigid hierarchy of the acquisition algorithm as if the instrument would include a dedicated acquisition sensor. However, no additional hardware or refinement of the on-board software of the instrument is needed. Acquisition algorithms that implement random patterns usually acquire the signal sooner, compared to algorithms that use continuous patterns, (in some cases, the mean acquisition time is about 1 hour lower) with a success rate bigger than 96% over 400 simulated acquisition attempts. Hence, if the instrument and the boundary constraints of a future geodesy mission are compatible with the ones of GRACE Follow-On, random patterns can be an economic alternative to the usage of an acquisition sensor.

The calibration algorithm used to reduce, during data postprocessing, the TPC noise is derived from the studies on adaptive filters used for suppressing environmental noise. This device allows to determine the attitude-to-noise coupling coefficients availing of dedicated calibration stimuli (coherent calibration) or using the residual attitude jitter of the satellite (incoherent calibration). The incoherent calibration process, applied using both simulated measurements of the GRACE Follow-On orbit and the Level-1B data products of GRACE, proved itself capable of recovering the coupling coefficients only if the input data are conveniently pre-processed. ASD plots and coherence plots of the measured attitude and range time series suggest that the optimal frequency range for recovering the coupling coefficients is above 31 mHz (outside the measurement bandwidth). De-correlating the signals processed by the calibration algorithm with a high-pass filter (whose cutoff frequency is 31 mHz) allows to recover the coupling coefficients with an estimation error around 10%. Such error is reduced below 1% when multiple band-pass filters are used to de-correlate range measurement and attitude measurements.

The coherent calibration process is applied using the Level-1B data products of the calibration maneuver of GRACE. In this case, the relevant signals need to be pre-processed with pass-band filters matched to the frequency of the calibration stimulus. When using a single pass-band filter centered at the oscillating frequency of the maneuver, the estimation error is below 1% (similar to the case of incoherent calibration) while using multiple band-pass filters (which include the fundamental oscillating frequency of the satellite) allows to reduce the estimation error below 10^{-5} %.

Although coherent calibration returns more accurate results, the actuation of the satellite

along a single axis for the duration of the calibration maneuver requires as many thrust pulses as the ones required by the satellite in two days. Thus, for reducing the TPC noise of about one order of magnitude or for tracking the variation of the coupling coefficients with time, the usage of incoherent calibration is a valid option.

Appendix A

A.1 Point-ahead angles

Since the satellites have a relative motion while orbiting around the Earth, an angular offset occurs between the sending direction and receiving direction of the laser beam. This angle is know as the point-ahead angle. In order to estimate this point-ahead angle, the equations are expressed in a reference frame whose axes are parallel to the ones of the geocentric frame, but centered on the barycenter of the slave satellite. Hence, knowing the position and velocity of both satellites in the geocentric inertial frame, it is possible to calculate their relative position and velocity in the new reference frame

$$\begin{aligned} \mathbf{v}_2 &= \mathbf{v}_{2,\mathrm{If}} - \mathbf{v}_{1,\mathrm{If}} \\ \mathbf{r}_2 &= \mathbf{r}_{2,\mathrm{If}} - \mathbf{r}_{1,\mathrm{If}} \end{aligned} \tag{a.1}$$

The motion of the master satellite is evaluated as

$$\mathbf{x}_{\mathrm{send}} = \mathbf{r}_2 + \mathbf{v}_2 t_{\mathrm{send}} \tag{a.2}$$

Through Eq. a.2 it is possible to calculate the wavefront emitted from the slave satellite

$$\left(ct_{\mathrm{send}}\right)^2 = \mathbf{x}_{\mathrm{send}}^T \mathbf{x}_{\mathrm{send}} \tag{a.3}$$

The intersection of Eq. a.2 and Eq. a.3 returns the time required for the laser beam to reach i.e. the master satellite

$$t_{\mathrm{send}} = \frac{1}{c^2 - \mathbf{v}_2^T \mathbf{v}_2} \left[\mathbf{r}_2^T \mathbf{v}_2 + \sqrt{\left(\mathbf{r}_2^T \mathbf{v}_2\right)^2 + \mathbf{r}_2^T \mathbf{r}_2 \left(c^2 - \mathbf{v}_2^T \mathbf{v}_2\right)} \right] \tag{a.4}$$

where c represents the speed of light. Reversing the sign of the relative velocity it is possible to find the receiving direction of the slave satellite

$$\mathbf{x}_{\mathrm{rec}} = \mathbf{r}_2 - \mathbf{v}_2 t_{\mathrm{rec}} \tag{a.5}$$

The wavefront emitted from the master spacecraft, can be evaluated as in Eq. a.3 by replacing $\mathbf{x}_{\mathrm{send}}$ with $\mathbf{x}_{\mathrm{rec}}$. Combining this equation with Eq. a.5 returns the time required for the laser beam to reach the slave satellite

$$t_{\mathrm{rec}} = \frac{1}{c^2 - \mathbf{v}_2^T \mathbf{v}_2} \left[-\mathbf{r}_2^T \mathbf{v}_2 + \sqrt{\left(\mathbf{r}_2^T \mathbf{v}_2\right)^2 + \mathbf{r}_2^T \mathbf{r}_2 \left(c^2 - \mathbf{v}_2^T \mathbf{v}_2\right)} \right] \tag{a.6}$$

where c is once more the speed of light.

Based on the light-travel times, the unit vectors for the sending and receiving directions

(calculated in the geocentric frame) are estimated as

$$\begin{aligned} \mathbf{u}_{\text{send}} &= \frac{\mathbf{r}_2 + \mathbf{v}_2 t_{\text{send}}}{\|\mathbf{r}_2 + \mathbf{v}_2 t_{\text{send}}\|} \\ \mathbf{u}_{\text{rec}} &= \frac{\mathbf{r}_2 - \mathbf{v}_2 t_{\text{rec}}}{\|\mathbf{r}_2 - \mathbf{v}_2 t_{\text{rec}}\|} \end{aligned} \tag{a.7}$$

This yields the point-ahead angle

$$\theta_{\text{pa}} = \sin^{-1}\left(\frac{\mathbf{u}_{\text{send}} \times \mathbf{u}_{\text{rec}}}{\|\mathbf{u}_{\text{send}} \times \mathbf{u}_{\text{rec}}\|}\right) \tag{a.8}$$

Figure a.1 depicts the estimation of the point ahead angle which results from the orbit of the GRACE Follow-On mission. This angle is calculated using orbit simulated data.

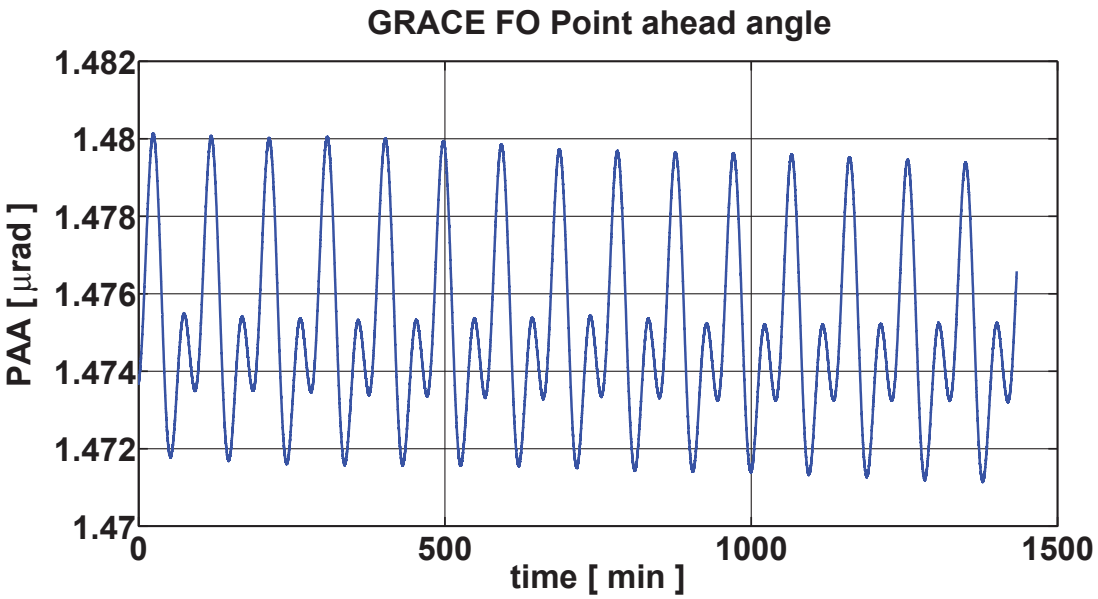

Figure a.1: This figure shows the trend of the point ahead angle (PAA) of the orbit of GRACE Follow-On over 24 hours.

A.2 Amplitude Noise Model for RIN

The relative intensity noise is herein modelled as a noise source which adds to the sinusoidal beat note of the measurement signal. Indeed, as the beat note is tracked by a DPLL, any amplitude variation would be interpreted, without loss of generality, as a phase variation given by the slope of the beat signal at the lock point. This introduces a change in the phase which can be considered identical to the relative amplitude variation. The phase variation introduced by the RIN noise at the heterodyne frequency can be calculated as

$$\delta\varphi = \sqrt{\frac{\mathrm{P}_n}{\mathrm{P}_s}} \tag{a.9}$$

where P_n and P_s are, respectively, the noise and signal power.

In heterodyne detection, the power of the electrical signal is proportional to the square of the photocurrent generated by the beat note (RMS value)

$$I_{\mathrm{beat}} = \eta_{\mathrm{resp}}\sqrt{2\eta_{\mathrm{het}}\eta_{\mathrm{opt}}P_{\mathrm{LO}}P_{\mathrm{RX}}} \tag{a.10}$$

The noise power in the electrical domain is proportional to the variation of the optical power squared. Hence,

$$\delta\varphi_{\mathrm{RIN}} = \sqrt{\frac{\delta P_{\mathrm{tot}}^2}{2\eta_{\mathrm{het}}\eta_{\mathrm{opt}}P_{\mathrm{LO}}P_{\mathrm{RX}}}} = \sqrt{\frac{(\mathrm{RIN}\,P_{\mathrm{tot}})^2}{2\eta_{\mathrm{het}}\eta_{\mathrm{opt}}P_{\mathrm{LO}}P_{\mathrm{RX}}}} \tag{a.11}$$

which is expressed in rad/$\sqrt{\mathrm{Hz}}$. This formulation is valid considering a good SNR while its validity for signals buried into noise is unknown.

A.3 Geometrical properties of the TMA

The TMA is a triad of mirrors in a corner cube arrangement. Hence this assembly inherits all the properties of a CCR. The coordinates of the vertex of the TMA can be obtained as

$$\mathbf{v} = \frac{\det(\mathbf{M}_i)}{\det(\mathbf{Mn})} \quad \text{where } i = x, y, z \tag{a.12}$$

where the matrices $\mathbf{M}_i$ and $\mathbf{Mn}$ are defined as

$$\begin{aligned} \mathbf{M}_x &= \begin{bmatrix} -\mathrm{d}_1 & \mathrm{n}_{1y} & \mathrm{n}_{1z} \\ -\mathrm{d}_2 & \mathrm{n}_{2y} & \mathrm{n}_{2z} \\ -\mathrm{d}_3 & \mathrm{n}_{3y} & \mathrm{n}_{3z} \end{bmatrix}, \quad \mathbf{M}_y = \begin{bmatrix} \mathrm{n}_{1x} & -\mathrm{d}_1 & \mathrm{n}_{1z} \\ \mathrm{n}_{2x} & -\mathrm{d}_2 & \mathrm{n}_{2z} \\ \mathrm{n}_{3x} & -\mathrm{d}_3 & \mathrm{n}_{3z} \end{bmatrix} \\ \mathbf{M}_z &= \begin{bmatrix} \mathrm{n}_{1x} & \mathrm{n}_{1y} & -\mathrm{d}_1 \\ \mathrm{n}_{2x} & \mathrm{n}_{2y} & -\mathrm{d}_2 \\ \mathrm{n}_{3x} & \mathrm{n}_{3y} & -\mathrm{d}_3 \end{bmatrix}, \quad \mathbf{Mn} = \begin{bmatrix} \mathrm{n}_{1x} & \mathrm{n}_{1y} & \mathrm{n}_{1z} \\ \mathrm{n}_{2x} & \mathrm{n}_{2y} & \mathrm{n}_{2z} \\ \mathrm{n}_{3x} & \mathrm{n}_{3y} & \mathrm{n}_{3z} \end{bmatrix} \end{aligned} \tag{a.13}$$

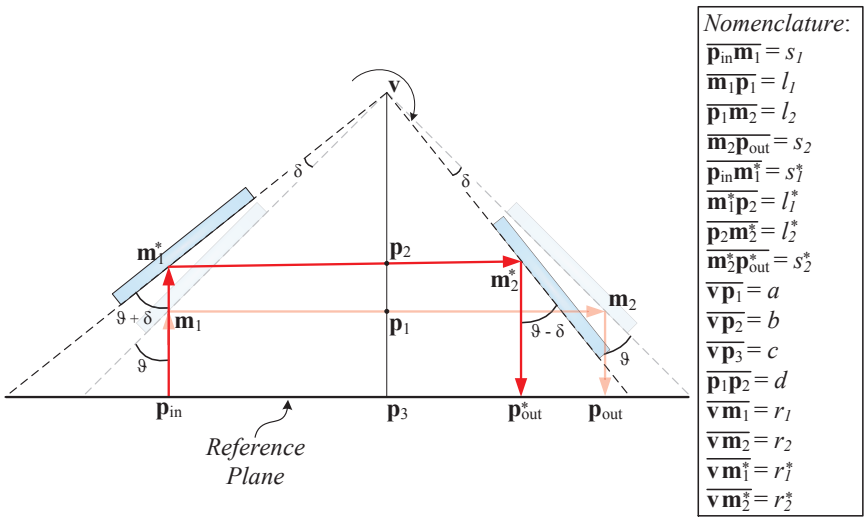

Figure a.2: This figure depicts an ideal bi-dimensional TMA and how the propagation of a beam changes through this subsystem when it is rotated about its vertex.

The vertex of the TMA is an important feature of the system since rotations around this point do not linearly couple into an apparent displacement of the optical path. According to the bi-dimensional representation of the TMA of Fig. a.2, the optical pathlength accrued by the laser beam is equal to

$$\mathrm{OPL} = s_1 + l_1 + l_2 + s_2 = 2c \tag{a.14}$$

since $\vartheta = \pi/4$. If the TMA is now rotated about its vertex of the (small) angle δ, the optical path difference is equal to

$$\begin{aligned} \mathrm{OPD} &= (s_1^* + l_1^* + l_2^* + s_2^*) - (s_1 + l_1 + l_2 + s_2) \\ &= (s_1^* - s_1) + (s_2^* - s_2) + r_1^* \sin(\vartheta + \delta) + r_2^* \sin(\vartheta - \delta)\, r_1 \sin(\vartheta) + r_2 \sin(\vartheta) \\ &= r_1^* [\sin(\vartheta + \delta) - \cos(\vartheta + \delta)] + r_2^* [\sin(\vartheta - \delta) - \cos(\vartheta - \delta)] \end{aligned} \tag{a.15}$$

because $(s_1^* - s_1) = r_1 \cos(\vartheta) - r_1^* \cos(\vartheta + \delta)$, $(s_2^* - s_2) = r_2 \cos(\vartheta) - r_2^* \cos(\vartheta - \delta)$ and $\cos(\vartheta) = \sin(\vartheta)$.

Using the trigonometric angle sum and difference identities together with the small angle approximation, Eq. a.15 can be reduced to

$$\begin{aligned}\mathrm{OPD} \approx & r_1^* \sin(\vartheta) + r_1^* \sin(\vartheta)\,\delta - r_1^* \sin(\vartheta) + r_1^* \sin(\vartheta)\,\delta + r_2^* \sin(\vartheta) - r_2^* \sin(\vartheta)\,\delta + \\ & - r_2^* \sin(\vartheta) - r_2^* \sin(\vartheta)\,\delta \\ \approx & 2\sin(\vartheta)\,(r_1^*\delta - r_2^*\delta)\end{aligned} \tag{a.16}$$

Since the rotation δ is small, $(s_1^* - s_1) \approx (s_2^* - s_2)$ thus $r_2^* \cos(\vartheta - \delta) \approx r_1^* \cos(\vartheta + \delta)$. According to this approximation, Eq. a.16 can be further simplified

$$\begin{aligned}\mathrm{OPD} \approx & 2\sin(\vartheta)\,[r_1^*\delta\cos(\vartheta - \delta) - r_1^*\delta\cos(\vartheta + \delta)] \\ \approx & 2\sin(\vartheta)\,r_1^*\,[\cos(\vartheta) + \sin(\vartheta)\,\delta - \cos(\vartheta) + \sin(\vartheta)\,\delta] \\ \approx & 2\sin^2(\vartheta)\,r_1^*\delta^2\end{aligned} \tag{a.17}$$

which shows that the pathlength variation is a quadratic function of the magnitude of the rotation around the vertex of the TMA. Although this property has been demonstrated for a bi-dimensional assembly, it can be extended also for the case of a three-dimensional TMA.

The quadratic relation between TMA rotation and optical path difference holds only when the alignment of the mirrors form a perfect corner cube. Indeed, a misalignment of even one mirror introduces a linear coupling which is proportional to the magnitude of the misalignment. If the second mirror of Fig. a.2 is now tilted of $\vartheta_2 = \vartheta + \epsilon$, from Eq. a.15 yields

$$\begin{aligned}\mathrm{OPD} = & -r_2\sin(\vartheta_2) - r_1^*\cos(\vartheta + \delta) + r_2\sin(\vartheta_2) - r_2^*\sin(\vartheta - \delta) + \\ & + r_1^*\sin(\vartheta + \delta) + r_2^*\cos(\vartheta + \delta)\end{aligned} \tag{a.18}$$

Using again the small angle approximation and substituting ϑ_2 with $\vartheta + \epsilon$ the optical path difference is

$$\begin{aligned}\mathrm{OPD} \approx & 2r_1^*\sin(\vartheta)\,\delta - 2r_2\sin(\vartheta)\,\epsilon + 2r_2^*\sin(\vartheta)\,\epsilon - 2r_2^*\sin(\vartheta)\,\delta \\ \approx & 2\sin(\vartheta)\,(r_1^*\delta - r_2^*\delta) + 2\sin(\vartheta)\,\epsilon\,(r_2^* - r_2)\end{aligned} \tag{a.19}$$

The first term of Eq. a.19 is identical to Eq. a.16 and represents the quadratic coupling of the optical path difference with the rotation of the TMA while the second term represents an additional error given by the non-ideality of the TMA. If the rotation δ is small, the variation of the points in which the reflection occurs is very small, and the magnitude r_2^* can be approximated to the magnitude of r_2 after undergoing the rotation around the vertex (considering the origin of the reference frame coincident with the vertex of the TMA)

$$\begin{aligned}r_2^* - r_2 = & \left[(x\cos\delta - y\sin\delta - x)^2 + (y\cos\delta - x\sin\delta - y)^2\right]^{0.5} \\ \approx & \left[(y + x)^2\,\delta^2\right]^{0.5} \\ \approx & r_2\delta\end{aligned} \tag{a.20}$$

Substituting Eq. a.20 in Eq. a.19

$$\mathrm{OPD} \approx \mathrm{OPD}_{\mathrm{id}} + 2\sin(\vartheta)\,r_2\epsilon\delta \tag{a.21}$$

where $\mathrm{OPD}_{\mathrm{id}}$ is the optical path difference introduced by an ideal TMA when rotated about its vertex. The non-ideality of the TMA introduces a linear coupling between the optical path difference and the rotation of the assembly proportional to the magnitude of the misalignment of the mirror. Although the demonstration is once more performed with a bi-dimensional TMA, this result can be extended also to the three-dimensional TMA.

A.4 Relation between TMA vertex offset and TPC noise

When the vertex of the TMA is not coincident with the reference point of the accelerometer, any rotation around this point introduces displacement noise. Using the nomenclature of Fig. a.3, the coordinates of the vertex of the TMA after rotating the assembly with respect to the accelerometer (in Roll, Pitch and Yaw) are

$$\begin{bmatrix} \mathrm{v}_{rx} \\ \mathrm{v}_{ry} \\ \mathrm{v}_{rz} \end{bmatrix} = \begin{bmatrix} c(\mathrm{Y})c(\mathrm{P}) & c(\mathrm{R})s(\mathrm{Y}) + c(\mathrm{Y})s(\mathrm{P})s(\mathrm{R}) & s(\mathrm{Y})s(\mathrm{R}) - c(\mathrm{Y})c(\mathrm{R})s(\mathrm{P}) \\ -c(\mathrm{P})s(\mathrm{Y}) & c(\mathrm{Y})c(\mathrm{R}) - s(\mathrm{Y})s(\mathrm{P})s(\mathrm{R}) & c(\mathrm{Y})s(\mathrm{R}) + c(\mathrm{R})s(\mathrm{Y})s(\mathrm{P}) \\ s(\mathrm{P}) & -c(\mathrm{P})s(\mathrm{Y}) & c(\mathrm{P})c(\mathrm{R}) \end{bmatrix} \cdot \begin{bmatrix} \mathrm{v}_x \\ \mathrm{v}_y \\ \mathrm{v}_x \end{bmatrix} \tag{a.22}$$

since the origin of the coordinate system is coincident with the accelerometer. R, P and Y are the acronyms of Roll, Pitch and Yaw while the letters c and s are used as abbreviations of cosine and sine.

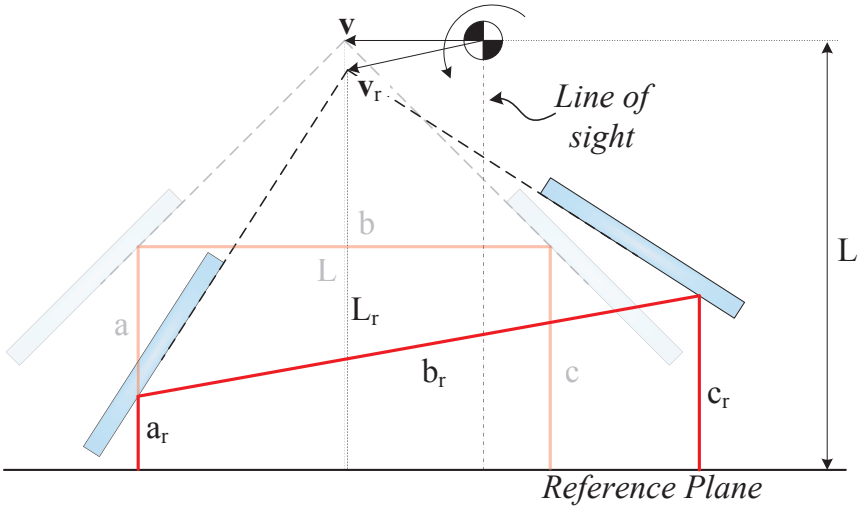

Figure a.3: Graphical representation of the lever arm effect that introduces the TPC noise.

Since the measurement of interest is along the longitudinal axis of the line of sight, the coordinate change which is relevant for the TPC noise is given by the first row of Eq. a.22. Substituting the cosine and sine with a second order Taylor expansion, Eq. a.22 returns

$$\mathrm{v}_{rx} = -\frac{1}{2}\left(\mathrm{Y}^2 + \mathrm{P}^2 - 1\right)\mathrm{v}_x + \left(\mathrm{Y} + \mathrm{P}\cdot\mathrm{R}\right)\mathrm{v}_y + \left(\mathrm{Y}\cdot\mathrm{R} - \mathrm{P}\right)\mathrm{v}_z \tag{a.23}$$

The variation of the longitudinal coordinate is thus

$$\delta\mathrm{v}_x = \mathrm{v}_{rx} - \mathrm{v}_x = -\frac{1}{2}\left(\mathrm{Y}^2 + \mathrm{P}^2\right)\mathrm{v}_x + \left(\mathrm{Y} + \mathrm{P}\cdot\mathrm{R}\right)\mathrm{v}_y + \left(\mathrm{Y}\cdot\mathrm{R} - \mathrm{P}\right)\mathrm{v}_z \tag{a.24}$$

The properties of the TMA are such that the distance travelled by the beam from and to the reference plane throughout the assembly is always twice the distance from the vertex of the TMA to the reference plane. Therefore,

$$\begin{gathered} 2\mathrm{L} = \mathrm{a} + \mathrm{b} + \mathrm{c} \\ 2\mathrm{L}_r = 2\left(\mathrm{L} - \delta\mathrm{v}_x\right) = \mathrm{a}_r + \mathrm{b}_r + \mathrm{c}_r \\ \downarrow \\ \Delta\mathrm{L} = 2\mathrm{L}_r - 2\mathrm{L} = 2\delta\mathrm{v}_x \end{gathered} \tag{a.25}$$

Deriving the last term of Eq. a.25 with respect to the angles of Roll, Pitch and Yaw yields the sensitivity of the measurement to rotations

$$\mathbf{s_v}\left(\mathrm{P},\mathrm{Y},\mathbf{v}\right) = \begin{bmatrix} \dfrac{\partial \Delta \mathrm{L}}{\partial \mathrm{R}} \\ \dfrac{\partial \Delta \mathrm{L}}{\partial \mathrm{P}} \\ \dfrac{\partial \Delta \mathrm{L}}{\partial \mathrm{Y}} \end{bmatrix} = 2 \begin{bmatrix} 0 & \mathrm{P} & \mathrm{Y} \\ -\mathrm{P} & \mathrm{R} & -1 \\ -\mathrm{Y} & 1 & \mathrm{R} \end{bmatrix} \cdot \begin{bmatrix} \mathrm{v_x} \\ \mathrm{v_y} \\ \mathrm{v_z} \end{bmatrix} \tag{a.26}$$

A.5 Instrument reference frames

Body frame or satellite frame

The body frame is centered in the fiducial point of the accelerometer. The X-axis points in the direction of the trailing/following satellite and is orthogonal to the front panel of the satellite structure. The Z-axis points towards the Earth and is orthogonal to the satellite platform. The Y-axis is chosen to form a right handed triad. The propagation of the laser beam through the components of the interferometer is generally evaluated in this frame.

Science frame

The science frame is centered in the fiducial point of the accelerometer. The X-axis is coincident with the LoS and points towards the trailing/following satellite. The Z-axis points towards the Earth. The Y-axis is chosen to form a right handed triad. The range measurement is, unless specified, evaluated in this frame.

Mirror frame

The mirror frame is principally used throughout this thesis to apply misalignments to the mirrors of the interferometer or to evaluate the tip-tilt angles of the SM. The Z-axis of this reference frame is directed like the normal vector of the mirror while the X-axis and the Y-axis lie on the surface of the mirror forming a right handed triad. The rotation matrix between the mirror reference frame and the reference frame in which the normal vector $\mathbf{n}$ of the mirror is defined (i.e. body frame) can be calculated, if the first element of $\mathbf{n}$ (n_x) is > 0.5, as

$$\begin{aligned} \mathbf{r}_y &= \frac{\widehat{j} \times \mathbf{n}}{\|\widehat{j} \times \mathbf{n}\|} \\ \mathbf{r}_x &= \frac{\mathbf{n} \times \mathbf{r}_y}{\|\mathbf{n} \times \mathbf{r}_y\|} \end{aligned} \tag{a.27}$$

where $\widehat{j} = [\,0\,,\,1\,,\,0]^{\mathrm{T}}$. If the first element of $\mathbf{n}$ (n_x) is < 0.5

$$\begin{aligned} \mathbf{r}_y &= \frac{\mathbf{n} \times \widehat{i}}{\|\mathbf{n} \times \widehat{i}\|} \\ \mathbf{r}_x &= \frac{\mathbf{r}_y \times \mathbf{n}}{\|\mathbf{r}_y \times \mathbf{n}\|} \end{aligned} \tag{a.28}$$

where $\widehat{i} = [\,1\,,\,0\,,\,0]^{\mathrm{T}}$. The rotation matrix is therefore equal to

$$\mathbf{R} = \begin{bmatrix} \mathrm{r}_x^1 & \mathrm{r}_y^1 & 0 \\ \mathrm{r}_x^2 & \mathrm{r}_y^2 & 0 \\ \mathrm{r}_x^3 & \mathrm{r}_y^3 & 1 \end{bmatrix} \tag{a.29}$$

Motors frame and Sensors frame

The motors frame is used to properly calculate the torque that the voice coil motors have to generate in order to rotate the SM of the desired angle. The sensors frame is used to properly evaluate the inclination of the SM in order to feed this information to the SM controller. Indeed, both motors and sensors might not be placed along the axes of rotation of the SM for manufacturing reasons.

The origin of these reference frames and their Z-axis are coincident with the origin and the Z-axis of the SM reference frame. The X-axis and Y-axis both lie on the surface of the SM and form an angle θ with the X-axis and the Y-axis of the SM frame. The magnitude of θ is equal to the angular offset between the axis of rotation of the mirror and the position of the motor/sensor. The relation between this reference frame an the mirror frame of the SM is thus

$$\begin{bmatrix} \mathrm{X_{mf\text{-}sf}} \\ \mathrm{Y_{mf\text{-}sf}} \\ \mathrm{Z_{mf\text{-}sf}} \end{bmatrix} = \begin{bmatrix} \cos(\theta) & -\sin(\theta) & 0 \\ \sin(\theta) & \cos(\theta) & 0 \\ 0 & 0 & 1 \end{bmatrix} \begin{bmatrix} \mathrm{X_{SMf}} \\ \mathrm{Y_{SMf}} \\ \mathrm{Z_{SMf}} \end{bmatrix} \tag{a.30}$$

where $X_{\mathrm{mf\text{-}sf}}$ is the generic X coordinate in the motor frame or in the sensor frame while $\mathrm{X_{Mf}}$ is the same coordinate expressed in the frame of the SM.

QPD frame

The QPD frame is principally used to calculate the offset between the RX beam and the LO beam and retrieve their relative angles. This information is used afterwards to derive the DWS signal. The origin of this reference frame is coincident with the center of the QPD's sensitive surface. The Z-axis is orthogonal of the surface of the QPD and points towards its back. The Y-axis lies on the surface of the QPD and points towards the upper quadrants. The X-axis is chosen to form a right handed triad.

STR frame

The STR frame is used only for generating the STR noise. The Z-axis of this frame is aligned to the line of sight of the STR while the X-axis and the Y-axis are aligned with its optical plane forming a right handed triad. Since the GNC data used in most of the calibration simulations are derived from the orbit simulator of GRACE Follow-On, the STRs noise is generated using the data of three STRs whose orientations, with respect to the body frame of the satellite, are listed in Tab. a.1.

Parameter	**STR 1**	**STR 2**	**STR 3**
$\mathbf{r}_{\mathrm{STRf\text{-}Bf}}$ [m]	$\begin{bmatrix} -0.326 \\ 0.025 \\ -0.089 \end{bmatrix}$	$\begin{bmatrix} -0.272 \\ 0.132 \\ -0.134 \end{bmatrix}$	$\begin{bmatrix} -0.373 \\ -0.135 \\ -0.137 \end{bmatrix}$
q_0	-0.1830	0.2420	-0.4627
$\boldsymbol{q}$	$\begin{bmatrix} 0.6830 \\ 0.6830 \\ 0.1830 \end{bmatrix}$	$\begin{bmatrix} -0.0456 \\ 0.8515 \\ 0.4627 \end{bmatrix}$	$\begin{bmatrix} 0.8515 \\ -0.0456 \\ -0.2420 \end{bmatrix}$

Table a.1: Orientation of the STRs reference frames.

The vector $\mathbf{r}_{\mathrm{STRf\text{-}Bf}}$ is the distance from the origin of the body frame to the origin of the STR frame and $Q_{\mathrm{Bf\text{-}STRf}} = \left[q_0\, \boldsymbol{q}^{\mathrm{T}}\right]^{\mathrm{T}}$ is the rotation matrix from the STR frame to the body frame expressed as a quaternion (see appendix C.4).

A.6 Noise shape filtering

The noise of those sources which cannot be modelled as white Gaussian noise are generated using a noise shape filter. A noise shape filter is capable of producing noise whose spectral density has the same trend of the frequency response of the filter. The requirement on the noise is usually given by a minimum noise level times a NSF. The NSF used to define the noise shape filters used in these thesis is the one of the LRI of GRACE Follow-On

$$NSF\left(f\right) = \sqrt{1 + \left(\frac{f}{2\text{mHz}}\right)^{-2}} \times \sqrt{1 + \left(\frac{f}{10\text{mHz}}\right)^{-2}} \tag{a.31}$$

The transfer function of the noise shape filter is obtained fitting the frequency response of the filter to Eq. a.31. In the Laplace domain, the transfer function of the noise shape filter is

$$H\left(s\right) = \frac{h_1 s^3 + h_2 s^2 + h_3 s + h_4}{h_5 s^3 + h_6 s^2 + h_7 s + h_8} \tag{a.32}$$

The coefficients h_i (with $i = 1 \ldots 8$) of Eq. a.32 are listed in Tab. a.2. The noise floor of the noise shape filter is set to $10^{-8} \times 1/\sqrt{\text{Hz}}$.

Filter Coefficients							
h_1	h_2	h_3	h_4	h_5	h_6	h_7	h_8
7.452e^{-6}	9.365e^{-3}	5.416e^{-4}	7.832e^{-6}	2827	8.883e^{5}	37.12	3.896e^{-4}

Table a.2: Coefficients of the noise shape filter.

In order to generate the desired noise level, the output of the noise shape filter has to be multiplied by an appropriate scaling factor. For example, a noise floor of $20^{-9} \times 1/\sqrt{\text{Hz}}$ is generated multiplying the output of the noise shape filter by 2.

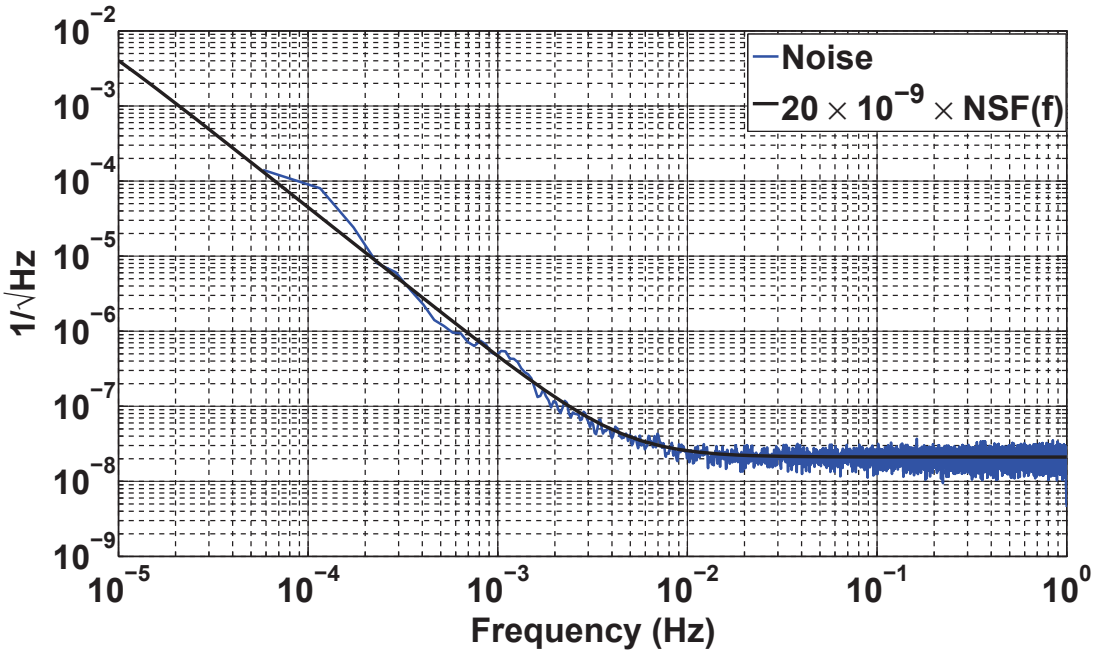

Figure a.4: ASD of the noise produce by the filter.

A.7 The state space equations of the steering mirror

For a rigid body j, the Newton-Euler equations are the simplest set of equations which describe its motion. Indeed Newton's equations are used to describe the translation of the center of mass of the body while the Euler's equations are used to describe its rotation. Hence, combining these equations yield the six equations of motion of an unconstrained rigid body j

$$\underbrace{\begin{bmatrix} m_i\mathbf{I} & \mathbf{0} \\ \mathbf{0} & \mathbf{J} \end{bmatrix}}_{\mathbf{M}_j} \underbrace{\begin{Bmatrix} \ddot{\mathbf{r}} \\ \dot{\boldsymbol{\omega}} \end{Bmatrix}}_{\dot{\boldsymbol{\nu}}_j} = \underbrace{\begin{Bmatrix} \mathbf{f} \\ \boldsymbol{\Omega} - \tilde{\boldsymbol{\omega}}\mathbf{J}\boldsymbol{\omega} \end{Bmatrix}}_{\mathbf{g}_j} \tag{a.33}$$

where m_i is the mass of the body along the i^{th} axis, $\mathbf{J}$ is the rotational inertia matrix, $\mathbf{f}$ is the vector of forces acting on the body while $\boldsymbol{\Omega}$ the vector of the torques. The matrix $\tilde{\boldsymbol{\omega}}$ is the skew matrix of the vector $\boldsymbol{\omega}$. If the body is constrained, the right side of Eq. a.33 has to include the reaction force-momentum matrix $\mathbf{H}_j$.

If two bodies j and k are connected to each other, the reaction force-momentum matrix $\mathbf{H}$ has to include the kinematic properties of the joint. Thus, for a two body system, Eq. a.33 can be rearranges such that

$$\underbrace{\begin{bmatrix} \mathbf{M}_j & 0 \\ 0 & \mathbf{M}_k \end{bmatrix}}_{\mathbf{M}} \underbrace{\begin{Bmatrix} \dot{\boldsymbol{\nu}}_j \\ \dot{\boldsymbol{\nu}}_k \end{Bmatrix}}_{\dot{\boldsymbol{\nu}}} = \underbrace{\begin{Bmatrix} \mathbf{g}_j \\ \mathbf{g}_k \end{Bmatrix}}_{\mathbf{g}} + \underbrace{\begin{bmatrix} \mathbf{H}_j^{\mathrm{T}} \\ \mathbf{H}_k^{\mathrm{T}} \end{bmatrix}}_{\mathbf{H}} \boldsymbol{\lambda} \tag{a.34}$$

where $\boldsymbol{\lambda}$ is a vector of Lagrange multipliers which contains as many elements as the constraints which are used to describe the joint.

The moving part of a SM is, in general, an assembly of more elements rather than a single body. These have to be capable of rapidly rotating with respect to two degrees of freedom. For such a reason, the multi-body formulation is a valid approach for modelling a SM as non-ideality of the rotating assembly can be also taken into account. In this formulation, the SM is considered build from two gimballed bodies although this is not a strict requirement. The equations of the multi-body problem can be simplified applying a proper coordinate transformation aimed to reduce the total number of equations that need to be solved and to cancel the constraints matrix $\mathbf{H}$. A suitable solution is given through the joint-coordinate formulation [94] where the new coordinates are associated with the kinematic joints that connect the bodies (see the left panel of Fig. a.5). Since the two bodies of the SM have to rotate about the same point as a single structure, the open-chain system is made of two coincident bodies connected by a revolute joint (see the right panel of Fig. a.5). By moving one of the two bodies or the revolute joint it is possible to simulate a non ideal assembly. Nevertheless, this possibility is here neglected and the rotating assembly of the mirror is considered ideal.

Applying the coordinate transformation of a revolute joint to Eq. a.34, the equations of the multi-body problem become

$$\begin{gathered} \boldsymbol{\nu} = \mathbf{R}\dot{\boldsymbol{\vartheta}} \quad \Rightarrow \quad \dot{\boldsymbol{\nu}} = \mathbf{R}\ddot{\boldsymbol{\vartheta}} + \dot{\mathbf{R}}\dot{\boldsymbol{\vartheta}} \\ \downarrow \\ \mathbf{M}\mathbf{R}\ddot{\boldsymbol{\vartheta}} + \mathbf{M}\dot{\mathbf{R}}\dot{\boldsymbol{\vartheta}} = \mathbf{g} + \mathbf{H}\boldsymbol{\lambda} \\ \downarrow \\ \mathbf{R}^{\mathrm{T}}\mathbf{M}\mathbf{R}\ddot{\boldsymbol{\vartheta}} + \mathbf{R}^{\mathrm{T}}\mathbf{M}\dot{\mathbf{R}}\dot{\boldsymbol{\vartheta}} = \mathbf{R}^{\mathrm{T}}\mathbf{g} + \underbrace{\mathbf{R}^{\mathrm{T}}\mathbf{H}}_{=0}\boldsymbol{\lambda} \\ \downarrow \\ \mathbf{R}^{\mathrm{T}}\mathbf{M}\mathbf{R}\ddot{\boldsymbol{\vartheta}} = \mathbf{R}^{\mathrm{T}}\left(\mathbf{g} - \mathbf{M}\dot{\mathbf{R}}\dot{\boldsymbol{\vartheta}}\right) \end{gathered} \tag{a.35}$$

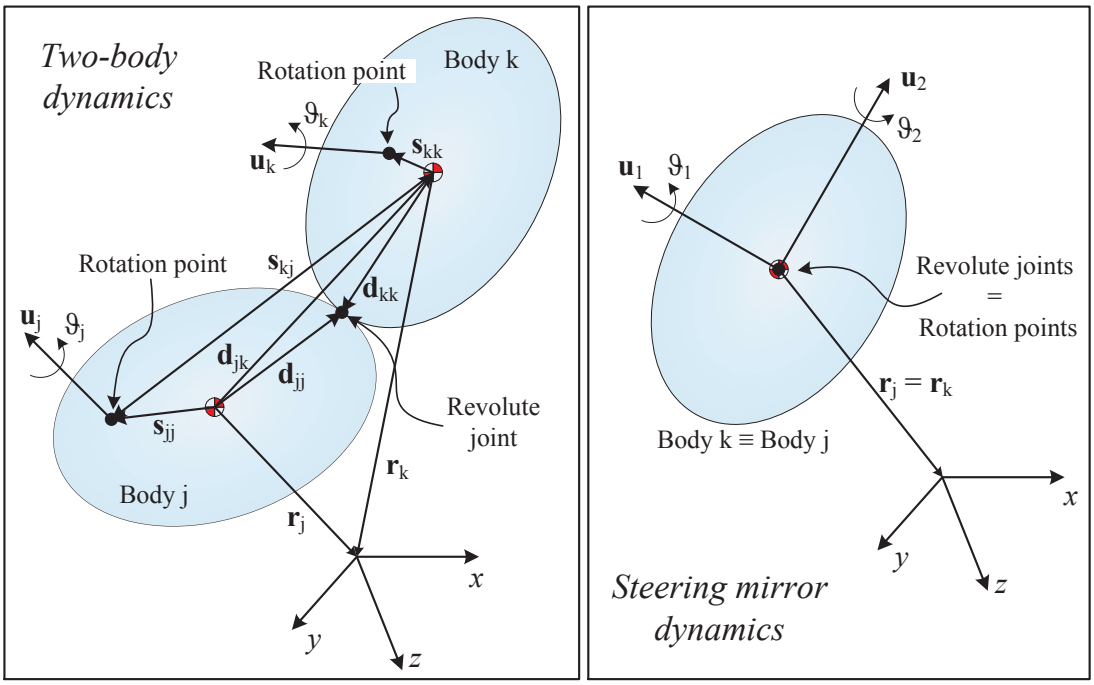

Figure a.5: The left panel of this figure shows a generic open-chain system connected by a revolute joint. The right panel instead depicts equivalence between the steering mirror dynamics and the dynamics of a open-chain system adopted for modeling the SM.

Since the number of degrees of freedom N_{dof} is coincident with the number of variables of the coordinate transformation ($\boldsymbol{\vartheta}$ is a $N_{\text{dof}} \times 1$ vector) the product $\mathbf{R}^{\mathrm{T}}\mathbf{H} = 0$ [156]. For a revolute joint, the transformation vector $\mathbf{t}_{i,b}$ is equal to

$$\mathbf{t}_{i,b} = \begin{bmatrix} -\tilde{\mathbf{d}}_{i,b}\mathbf{u}_b \\ \mathbf{u}_b \end{bmatrix} \quad \Rightarrow \quad \dot{\mathbf{t}}_{i,b} = \begin{bmatrix} -\left(\dot{\tilde{\mathbf{d}}}_{i,b} + \tilde{\mathbf{d}}_{i,b}\tilde{\boldsymbol{\omega}}_b\right)\mathbf{u}_b \\ \tilde{\boldsymbol{\omega}}_b\mathbf{u}_b \end{bmatrix} \tag{a.36}$$

where $\tilde{\mathbf{d}}_{i,b}$ and $\tilde{\boldsymbol{\omega}}_b$ with $i, b = j, k$ are the skew matrices of the vectors $\mathbf{d}_{i,b}$ and $\boldsymbol{\omega}_b$. The transformation matrix $\mathbf{R}$ is calculated through the transformation vector $\mathbf{t}_{i,b}$ as

$$\begin{bmatrix} \boldsymbol{\nu}_j \\ \boldsymbol{\nu}_k \end{bmatrix} = \underbrace{\begin{bmatrix} \mathbf{t}_{jj} & \mathbf{0} \\ \mathbf{t}_{jk} & \mathbf{t}_{kk} \end{bmatrix}}_{\mathbf{R}} \begin{bmatrix} \dot{\vartheta}_j \\ \dot{\vartheta}_k \end{bmatrix} \tag{a.37}$$

Using the nomenclature of Fig. a.5, the angular velocity of the body k is calculated as

$$\boldsymbol{\omega}_k = \boldsymbol{\omega}_j + \dot{\vartheta}_k\mathbf{u}_k \tag{a.38}$$

In order to simplify the formulation, the origin of the reference frame is chosen coincident with the center of mass of the mirror assembly and the axes X and Y are directed like the vectors $\mathbf{u}_1$ and $\mathbf{u}_2$. According to the position of the center of mass of the bodies, the position of the revolute joint and the rotation point shown in the right panel of Fig. a.5 and remembering that the bodies of the mirror can only rotate and not shift,

$$\begin{gathered} \mathbf{s}_{jj} = \mathbf{d}_{jj} = \mathbf{s}_{kj} = \mathbf{d}_{jk} = \mathbf{s}_{kk} = \mathbf{d}_{kk} = \mathbf{r}_j = \mathbf{r}_k = \mathbf{0} \\ \vartheta_j = \vartheta_1 = \vartheta \quad ; \quad \vartheta_k = \vartheta_2 = \phi \end{gathered} \tag{a.39}$$

Substituting Eq. a.39 in Eq. a.36

$$\mathbf{R} = \begin{bmatrix} \mathbf{0} & \mathbf{0} \\ \mathbf{u}_1 & \mathbf{0} \\ \mathbf{0} & \mathbf{0} \\ \mathbf{u}_1 & \mathbf{u}_2 \end{bmatrix} \quad , \quad \dot{\mathbf{R}} = \begin{bmatrix} \mathbf{0} & \mathbf{0} \\ \tilde{\boldsymbol{\omega}}_1\mathbf{u}_1 & \mathbf{0} \\ \mathbf{0} & \mathbf{0} \\ \tilde{\boldsymbol{\omega}}_1\mathbf{u}_1 & \tilde{\boldsymbol{\omega}}_2\mathbf{u}_2 \end{bmatrix} \tag{a.40}$$

where $\boldsymbol{\omega}_1 = \dot{\vartheta}\mathbf{u}_1$ and $\boldsymbol{\omega}_2 = \boldsymbol{\omega}_1 + \dot{\phi}\mathbf{u}_2$.

The pivots which are used to connect the rotating structure of the mirror to its external caging contrast the torque applied by the motors and can be modelled as a torsion spring combined with a rotary damper. Hence, labeling as $\boldsymbol{\tau}_i$ the torque applied by the voice coil motors to the i^{th} body (with $i = j\,,\,k$), the total torque $\boldsymbol{\Omega}$ acting on the rotating axes of the mirrors is

$$\boldsymbol{\Omega}_i = \boldsymbol{\tau}_i - \mathbf{K}_i\boldsymbol{\Theta}_i - \mathbf{C}_i\boldsymbol{\omega}_b \quad \text{with} \quad \begin{cases} b = 1 \text{ if } i = j \\ b = 2 \text{ if } i = k \end{cases} \tag{a.41}$$

where $\mathbf{K}_i$ and $\mathbf{C}_i$ are the matrices of the spring constants and damping constants while $\boldsymbol{\tau}_i$ is the vector of the torques applied by the voice coil motors. Without loss of generality, it is possible to assume that $\boldsymbol{\tau}_j = [\,\tau_x\,,\,0\,,\,0\,]^{\mathrm{T}}$ and $\boldsymbol{\tau}_k = [\,0\,,\,\tau_y\,,\,0\,]^{\mathrm{T}}$. Substituting Eq. a.40 and Eq. a.41 in Eq. a.35 and solving for $\ddot{\boldsymbol{\vartheta}}$

$$\begin{aligned} \ddot{\vartheta} &= -\frac{C_x}{J_x}\omega_{1,x} - \frac{K_x}{J_x}\Theta_{j,x} + \frac{\tau_x}{J_x} \\ \ddot{\phi} &= -\frac{C_y}{J_y}\omega_{2,y} - \frac{K_y}{J_y}\Theta_{k,y} + \frac{\tau_y}{J_y} \end{aligned} \tag{a.42}$$

where $\omega_{1,x}$ is the first element of the vector $\boldsymbol{\omega}_1$ and is equal to $\dot{\vartheta}$. Similarly $\omega_{2,y} = \dot{\phi}$. The terms $\Theta_{j,x}$ and $\Theta_{k,y}$ are equal to

$$\begin{aligned} \boldsymbol{\Theta}_j &= \int \mathbf{u}_1\dot{\vartheta}_x\mathrm{dt} \quad \rightarrow \quad \Theta_{j,x} = \int \dot{\vartheta}\mathrm{dt} = \vartheta \\ \boldsymbol{\Theta}_k &= \int \mathbf{u}_2\dot{\vartheta}_y\mathrm{dt} \quad \rightarrow \quad \Theta_{k,y} = \int \dot{\phi}\mathrm{dt} = \phi \end{aligned} \tag{a.43}$$

In order to obtain the result of Eq. a.42, the axes X and Y are also the principal axes of inertia of the two bodies and $J_x = J_{j,x} + J_{k,x}$ and $J_y = J_{k,y}$.

Introducing the state space vector $\mathbf{x} = \left[\,\vartheta\,,\,\phi\,,\,\dot{\vartheta}\,,\,\dot{\phi}\,\right]^{\mathrm{T}}$ it is possible to derive the state space equations of the steering mirror.

$$\begin{aligned} \dot{\mathbf{x}} &= \begin{bmatrix} 0 & 0 & 1 & 0 \\ 0 & 0 & 0 & 1 \\ -\dfrac{K_x}{J_x} & 0 & -\dfrac{S_x}{J_x} & 0 \\ 0 & -\dfrac{K_y}{J_y} & 0 & -\dfrac{S_y}{J_y} \end{bmatrix} \begin{bmatrix} \vartheta \\ \phi \\ \dot{\vartheta} \\ \dot{\phi} \end{bmatrix} + \begin{bmatrix} 0 & 0 \\ 0 & 0 \\ -\dfrac{1}{J_x} & 0 \\ 0 & -\dfrac{1}{J_y} \end{bmatrix} \begin{bmatrix} \tau_x \\ \tau_y \end{bmatrix} \\ \mathbf{y} &= \begin{bmatrix} 1 & 0 & 0 & 0 \\ 0 & 1 & 0 & 0 \end{bmatrix} \begin{bmatrix} \vartheta \\ \phi \\ \dot{\vartheta} \\ \dot{\phi} \end{bmatrix} + \mathbf{0}_{2\times 2}\,\boldsymbol{\tau} \end{aligned} \tag{a.44}$$

where $\mathbf{0}_{2\times 2}$ is the 2×2 null matrix while $\boldsymbol{\tau} = [\,\tau_x\,,\,\tau_y\,]^{\mathrm{T}}$.

A.8 The GA-PSO routine

The flow diagram of the genetic algorithm (GA) - particle swarm optimization (PSO) routine is depicted in Fig. 3.5. This paragraph describes the actions taken during the execution of this optimization tool. When the algorithm is executed, the first optimization routine is the genetic algorithm which performs the following actions:

- The algorithm generates the population of 100 individuals which is going to be processed by the genetic algorithm. The population is a vector containing the parameters of the controller which have to be optimized. For each individual, its parameters are randomly generated within the predefined search interval.
- The algorithm calculates the closed-loop performance of the feedback control loop for each of the 100 settings of the controller. The individuals (controller settings) which do not satisfy the stability criterion (unstable control loop) or the robustness constraints are discarded. If none of the individuals of the populations satisfies these criterions, the algorithm is re-initialized and a new population is generated.
- The routine calculates the fitness function of the individuals which satisfy the stability and robustness criterions. Afterwards, the individuals are arranged within a matrix according to an ascending order which depends on the magnitude of their fitness function. The first 20 individuals are selected for generating the new population. If the matrix has less than 20 individuals, the empty rows are filled with new random generated individuals.
- The individuals fit for the crossbreed are randomly chosen from the best 20. The point of crossover is also randomly chosen. The crossbred, generates two new individuals which are going to form a new population if 100 individuals.
- The individuals are mutated in order to avoid that the algorithm remains stuck in a local minima. Nevertheless, the level of mutation cannot be too high otherwise the optimization becomes a random search within the search space. For the first 50 individuals of the new population generated through the crossbreed, the mutation factor permitted is below 10%. From element 51 to 60 the factor is increased of 10% and so forth for the following 10 individuals. Thus the last 10 individuals of the new population have a mutation factor of 50%.
- Once the new population is generated the algorithm is repeated starting from point 2.

The genetic algorithm stops either when the maximum number of iterations is reached, or when the algorithm converges. The algorithm is considered to have reach convergence when the value of the best fitness function of the last 10 iterations is below a threshold. For this application, the threshold is set to 10^{-3}.

Once the genetic algorithm is terminated, the best solution is used to generate the new search space of the particle swarm optimization. In particular, the new limits of the search space are generated dividing an multiplying the genes of the best individual by a factor 2. Defined the interval, a swarm of 100 particles is randomly generated using the new boundaries of the search space. The velocity and the trajectory of the i^{th} particle are calculated as

$$\begin{aligned} v_i(t) =& w v_i(t-1) + c_1\eta_1\left[p^i_{\text{best}}(t-1) - x_i(t-1)\right] \\ &+ c_2\eta_2\left[g_{\text{best}}(t-1) - x_i(t-1)\right] \\ x_i(t) =& x_i(t-1) + v_i(t) \end{aligned} \tag{a.45}$$

where v_i and x_i are the velocity and the trajectory of the particle. The term w is an inertial weight that keeps the particle in its current trajectory (usually decreases linearly from 0.9 to 0.4 as the number of iterations increases). p^i_{best} is the best solution achieved by the particle

while g_{best} is the global best of the swarm. The constants c_1 and c_2 are used to (eventually) weight differently the personal experience and the swarm experience while the coefficients η_1 and η_2 are random factors $\epsilon\,[\,0\,,\,1\,]$ which change these weighting at each simulations. The boundary of the search space is restricted (the particles cannot cross it) and three boundary conditions are implemented, namely absorbing, reflecting and damping [157].

The number of individuals of the population, the number of particles of the swarm or i.e. the maximum mutation factors are all values which provided good controller settings. Nevertheless, these could be changed for further optimizing the GA-PSO routine.

A.9 Feedforward control of the SM

The feedforward control enables the SM to execute patterns (see chapter 4) which are precluded using a feedback controller. Indeed the finite close-loop bandwidth of the feedback controller represents a limitation to the pointing performance of this component. An example of the limited pointing performance of the feedback controller is given in the left panel of Fig. a.6. In this picture, the SM is repointed according to a hybrid spiral (see paragraph 4.3.1) whose dwell time is 500 µs. In order to properly draw this spiral, the setpoint commands on both the X and Y axis of the mirror frame rapidly vary in time and the feedback controller is not capable of reacting accordingly. The pattern drawn by the mirror is a distorted version of the original pattern.

When the same pattern is executed using a feedforward controller, the setpoint information is directly forwarded to the SM which rotates accordingly. The feedback controller in this case takes care of suppressing the noise. The right panel of Fig. a.6 shows the pointing performance of the SM when this is commanded using the feedforward controller. Although the patter is identical to the one of the previous example, the mirror is capable of tracking it without introducing distortions. This picture also shows that, despite the noise level of the sensors and of the electronics is higher than in the previous example (by a factor of 10) this does not compromise the pointing accuracy of the mirror since the noise is suppressed by the feedback controller.

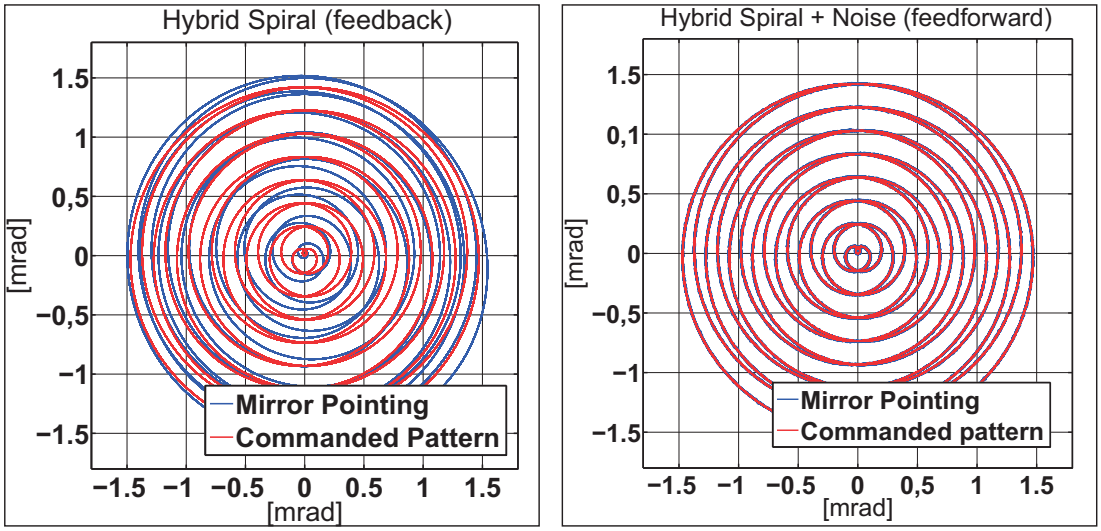

Figure a.6: A hybrid spiral with a dwell time of 500 µs executed using a feedback controller (left panel) and a feedforward controller (right panel)

Appendix B

B.1 The relative ratio of the Lissajous pattern

In order to cover the uncertainty cone without leaving gaps, the maximum distance between two consecutive peaks of the Lissajous profile has to be always smaller than $2K\delta$. Choosing $\omega_a > \omega_b$ and the ratio $\omega_a/\omega_b \, \epsilon \, \mathbb{N}^+$ the guidance will show a finite number of peaks equal to $\omega_a/\omega_b = \omega_r$ along the X-axis (if the oscillation along the Y-axis is faster than the one along the X-axis). At every quarter of the repetition period the faster sinusoidal motion has a phase shift of $\pi/2$ and the trend of the curve is mirrored with respect to the one just drawn (see dashed line in Fig. b.1). The inequality that has to be satisfied in order to cover the uncertainty cone without gaps, expressed in polar coordinates, is equal to

$$\Theta = \rho_{unc} \sin(\omega_b t_2) - \rho_{unc} \sin(\omega_b t_1) \leq 2K\delta \tag{b.1}$$

The maximum separation occurs between the two consecutive peaks close to the fast axis. Since the angular velocity of the slow axis (ω_b) can be expressed as a function of the angular velocity of the fast axis (ω_a), the time instants t_1 and t_2 (corresponding to the points P_1 and P_2 of Fig. b.1) are

$$\begin{aligned} t_1 &= \frac{T_a}{4} \\ t_2 &= \frac{T_b}{2} - \frac{3}{4}T_a = \frac{T_a}{2}\left(\omega_r - \frac{3}{2}\right) \end{aligned} \tag{b.2}$$

where T_a is the oscillation period of the fast axis while T_b is the oscillation period of the slow axis. Substituting Eq. b.2 in Eq. b.1 and ω_b with ω_a/ω_r, yields

$$\Theta = \sin\left\{\frac{2\pi}{\omega_r T_a}\left[\frac{T_a}{2}\left(\omega_r - \frac{3}{2}\right)\right]\right\} - \sin\left\{\frac{2\pi}{\omega_r T_a}\frac{T_a}{4}\right\} \leq \frac{2K\delta}{\rho_{unc}}$$

$$\downarrow$$

$$\Theta = \sin\left(\pi - \frac{3\pi}{2\omega_r}\right) - \sin\left(\frac{\pi}{2\omega_r}\right) \leq \frac{2K\delta}{\rho_{unc}}$$

$$\downarrow$$

$$\Theta = \sin(\pi)\cos\left(\frac{3\pi}{2\omega_r}\right) - \cos(\pi)\sin\left(\frac{3\pi}{2\omega_r}\right) - \sin\left(\frac{\pi}{2\omega_r}\right) \leq \frac{2K\delta}{\rho_{unc}}$$

$$\downarrow$$

$$\Theta = \sin\left(\frac{3\pi}{2\omega_r}\right) - \sin\left(\frac{\pi}{2\omega_r}\right) \leq \frac{2K\delta}{\rho_{unc}}$$

$$\downarrow$$

$$\Theta = 2\cos\left(\frac{\frac{3\pi}{2\omega_r}+\frac{\pi}{2\omega_r}}{2}\right)\sin\left(\frac{\frac{3\pi}{2\omega_r}-\frac{\pi}{2\omega_r}}{2}\right) \leq \frac{2K\delta}{\rho_{unc}} \tag{b.3}$$

$$\downarrow$$

$$\Theta = \cos\left(\frac{\pi}{\omega_r}\right)\sin\left(\frac{\pi}{2\omega_r}\right) \leq \frac{K\delta}{\rho_{unc}}$$

Therefore, if $\exists\, \omega_r \,\epsilon\, \mathbb{N}^+$ that fulfills Eq. b.3, the uncertainty cone is covered without leaving gaps.

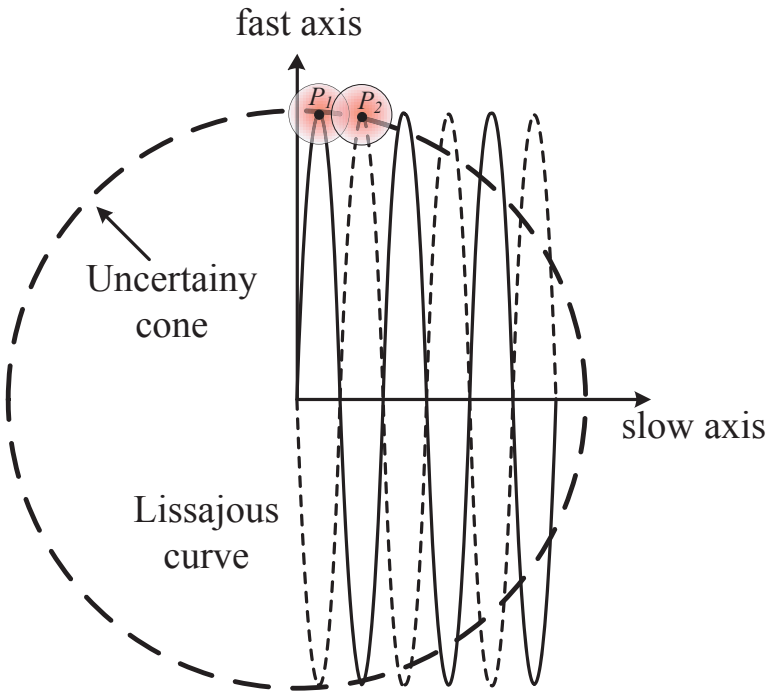

Figure b.1: Coverage of the uncertainty cone using a Lissajous pattern after $t = T_b/2$.

B.2 The shape parameter of the rhodonea pattern

Similarly to the case of the Lissajous curve, the distance between the tips of two consecutive petals has to fulfill the inequality

$$\Theta = \rho_{unc}\sqrt{\left[\cos\left(\zeta_1\right)\sin\left(\chi_1\right) - \cos\left(\zeta_2\right)\sin\left(\chi_2\right)\right]^2 + \left[\cos\left(\zeta_1\right)\cos\left(\chi_1\right) - \cos\left(\zeta_2\right)\cos\left(\chi_2\right)\right]^2} \leq 2K\delta \tag{b.4}$$

where the terms $\zeta_1 = \Upsilon\omega_{rho}t_1$, $\chi_1 = \omega_{rho}t_1$, $\zeta_2 = \Upsilon\omega_{rho}t_2$ and $\chi_2 = \omega_{rho}t_2$. The times t_1 and t_2 correspond to the points P_1 and P_2 of Fig. b.2.

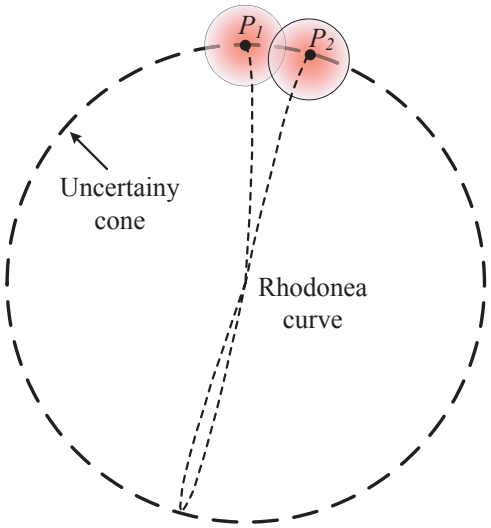

Figure b.2: The figure shows the coverage of the rhodonea pattern in the time interval $[\,0\,,\,T_{rho}/\Upsilon\,]$ when Υ is odd.

Case 1 - Υ is odd

When the shape parameter is odd, the points P_1 and P_2 are obtained at $t_1 = 0$ and $t_2 = T/\Upsilon$ where T is the repetition time of the rhodonea pattern (one should notice that when Υ is odd, the pattern repeats itself two time in the period T). Yields that $\zeta_1 = \chi_1 = 0$ and that $\zeta_2 = 2\pi$ while $\chi_2 = 2\pi/\Upsilon$. Substituting these values in Eq. b.4 returns,

$$\sqrt{\sin^2\left(\frac{2\pi}{\Upsilon}\right) + 1 - 2\cos\left(\frac{2\pi}{\Upsilon}\right) + \cos^2\left(\frac{2\pi}{\Upsilon}\right)} \leq \frac{2K\delta}{\rho_{unc}} \tag{b.5}$$

Remembering that $\sin^2(x) + \cos^2(x) = 1$, Eq. b.5 returns Eq. 4.16.

Case 2 - Υ is even

When the shape parameter is even, the points P_1 and P_2 are obtained at $t_1 = 0$ and $t_2 = (\Upsilon + 1)\,T/2$ where T is the repetition time of the rhodonea pattern. Yields that $\zeta_1 = \chi_1 = 0$ and that $\zeta_2 = \pi\,(1 + \Upsilon)$ while $\chi_2 = \pi\,(1 + \Upsilon)\,/\Upsilon$. Substituting these values in Eq. b.4 returns,

$$\sqrt{\sin^2\left(\frac{\Upsilon+1}{\Upsilon}\pi\right) + 1 - 2\cos\left(\frac{\Upsilon+1}{\Upsilon}\pi\right) + \cos^2\left(\frac{\Upsilon+1}{\Upsilon}\pi\right)} \leq \frac{2K\delta}{\rho_{unc}} \tag{b.6}$$

Since $\sin^2(x) + \cos^2(x) = 1$, Eq. b.5 returns Eq. 4.16.

B.3 Continuity of the equations of a pattern

Initially, the hybrid spiral was designed combining a constant angular velocity spiral with a constant tangential velocity spiral without taking into account the continuity of the first and second derivative of the angular coordinate (polar coordinates) of the curve. Subsequent laboratory tests performed with a steering mirror testbed (see paragraph 5.4) highlighted how these derivatives are important in order to have a bumpless transition from one pattern equation to another. Figure b.3 depicts the outcome of one of these tests. The center of the spiral results distorted although the commanded curve results, apparently, continuous.

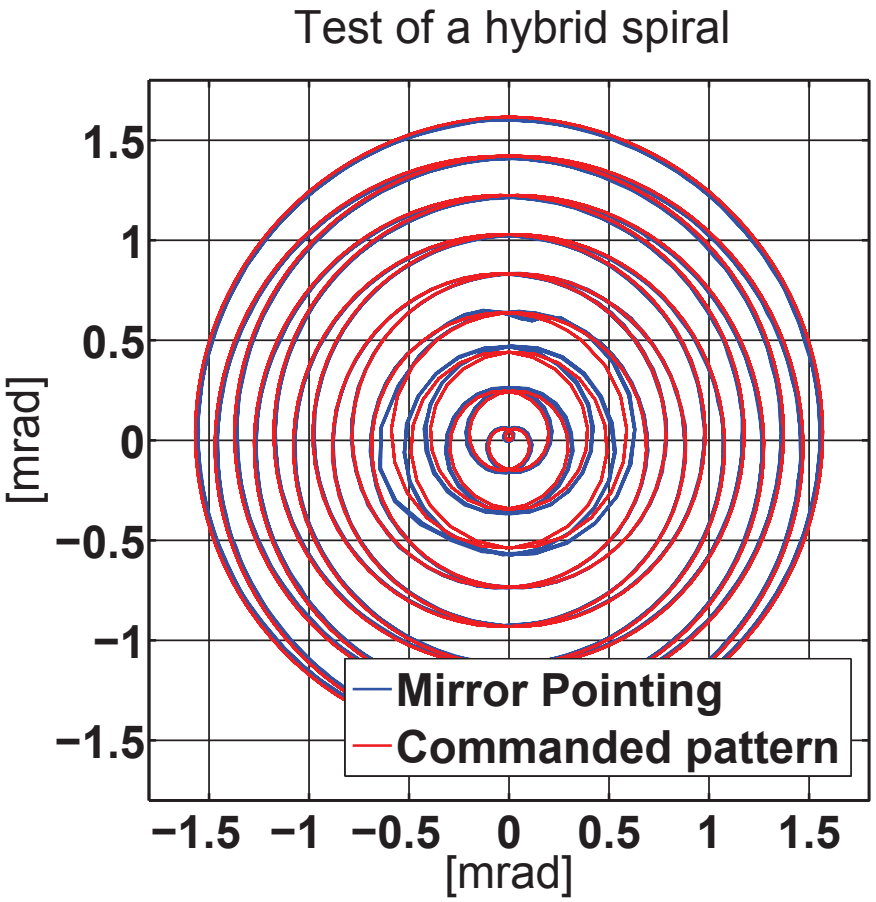

Figure b.3: The discontinuity in the first and second order derivative of the angular coordinate of this pattern introduces a distortion when transiting from constant angular velocity spiral to constant tangential velocity spiral.

B.4 Detection probability of a Gaussian pattern

When using a normally distributed random pattern, the probability P of solving the spatial acquisition problem can be evaluated using the random variables theory. Since the two satellites may not exploit synchronous detections, for the following formulation, the satellite that is detecting the signal is labelled as *receiver* while the other one as *sender*. In this section, bold lower case letters denote random variables and not vectors.

From a geometrical point of view the four degrees of freedom of the spatial acquisition are solved when the distance $\mathbf{z}(\xi)$ between the pointing coordinates of the laser beam of the receiver and pointing coordinates of the laser beam of the sender is smaller (or equal) to δ. Contemporarily the distance $\mathbf{v}(\xi)$ between the pointing coordinates of the laser beam of the sender and the receiving aperture of the receiver has to be also smaller or equal to δ. Accordingly, the spatial acquisition problem can be split into two subproblems which are solved separately.

In real operational conditions, together with the initial pointing offsets, long term pointing drifts and satellite attitude jitters influence the estimate of the line of sight. Considering a generic plane between the two satellites with its origin coincident with the nominal line of sight and labelling as $\mathbf{x}_{gui}$ and $\mathbf{y}_{gui}$ the pointing direction of the laser beam of the receiver and as $\mathbf{r}_{gui}$ and $\mathbf{s}_{gui}$ the pointing direction of the laser beam of the sender, the separation of the scanning cones can be expressed as

$$\begin{aligned}\mathbf{z} = \Big[&\left\{ [\mathbf{x}_{gui} + (x_0 + \epsilon_x)] - [\mathbf{r}_{gui} + (r_0 + \epsilon_r)] \right\}^2 + \\ &+ \left\{ \left[\mathbf{y}_{gui} + (y_0 + \epsilon_y)\right] - [\mathbf{s}_{gui} + (s_0 + \epsilon_s)] \right\}^2 \Big]^{\frac{1}{2}}\end{aligned} \tag{b.7}$$

where x_0, y_0, r_0 and s_0 are the coordinates of the centers of the uncertainty cones. ϵ_x, ϵ_y, ϵ_r and ϵ_s are time dependant pointing errors which represent the sum of long term pointing drifts and pointing noise (i.e. attitude jitter). From the first term between square brackets of Eq. b.7 one gets

$$\mathbf{x} = \mathbf{x}_{gui} + [x_0 + \epsilon_x(t)] \;\rightarrow\; E\{\mathbf{x}\} = E\{\mathbf{x}_i\} + [x_0 + \epsilon_x(t)] \tag{b.8}$$

The random variable $\mathbf{x}$ is normally distributed with standard deviation $\sigma_x^2 = \sigma_{x_{gui}}^2$ and mean $\mu_x = x_0 + \epsilon_x(t)$. Applying the same reasoning to all terms between square brackets, Eq. b.7 reduces to

$$\mathbf{z} = \sqrt{(\mathbf{x} - \mathbf{r})^2 + (\mathbf{y} - \mathbf{s})^2} \tag{b.9}$$

and can be split into 3 sub-problems

$$\begin{gathered}\mathbf{w} = g_1(\mathbf{x}, \mathbf{r}) = \mathbf{x} - \mathbf{r} \;\; ; \;\; \mathbf{h} = g_2(\mathbf{y}, \mathbf{s}) = \mathbf{y} - \mathbf{s} \\ \downarrow \\ \mathbf{z} = g_3(\mathbf{w}, \mathbf{h}) = \sqrt{\mathbf{w}^2 + \mathbf{h}^2}\end{gathered} \tag{b.10}$$

which are all widely discussed in literature [91]. In particular, sub-problems g_1 and g_2 return two normally distributed random variables ($\mathbf{w}$ and $\mathbf{h}$) whose mean and standard deviation are respectively $\mu_w = x_0 + r_0 + \epsilon_x(t) + \epsilon_r(t)$, $\mu_h = y_0 + s_0 + \epsilon_y(t) + \epsilon_s(t)$, $\sigma_w^2 = \sigma_x^2 + \sigma_y^2$ and $\sigma_h^2 = \sigma_y^2 + \sigma_s^2$. The random variable $\mathbf{z}$ instead has PDF equal to

$$f_z(z,t) = \frac{z e^{-\frac{\left[z^2 + \mu_z^2(t)\right]}{2\sigma_z^2}}}{\sigma_z^2} \mathrm{I}_0\left[\frac{z\mu_z(t)}{\sigma_z^2}\right] \tag{b.11}$$

which also known in literature as Rician distribution [91]. The term $\mu_z = \sqrt{\mu_w^2(t) + \mu_h^2(t)}$ while $\sigma_z^2 = \sigma_w^2 = \sigma_h^2$. The Cumulative Distribution Function (CDF) of the Rician distribution

is

$$F_z(z,t) = 1 - \mathrm{Q}_1\left[\frac{\mu_z(t)}{\sigma_z}, \frac{z}{\sigma_z}\right] \tag{b.12}$$

where Q_1 is the Marcum Q-function of first order.

With the same reasoning, the distance between the scanning cone of the sender and the receiving aperture of the receiver is equal to

$$\mathbf{v} = \sqrt{\left\{\left[\mathbf{x}_{gui} + (x_0 + \epsilon_x)\right] - x_a\right\}^2 + \left\{\left[\mathbf{y}_{gui} + (y_0 + \epsilon_y)\right] - y_a\right\}^2} \tag{b.13}$$

where $\mathbf{x}_{gui}$ and $\mathbf{y}_{gui}$ is the position of the scanning cone of the sender at a generic instant t, x_0 and y_0 the coordinates of the center of the uncertainty cone of the sender, ϵ_x and ϵ_y the time dependant disturbances while x_a and y_a the coordinates of the incoming aperture of the receiver. Using the same reasoning applied to Eq. b.7, Eq. b.13 returns that the random variable $\mathbf{v}$ has PDF

$$f_v(v,t) = \frac{v e^{-\frac{\left[v^2 + \mu_v^2(t)\right]}{2\sigma_v^2}}}{\sigma_v^2} \mathrm{I}_0\left[\frac{v\mu_v(t)}{\sigma_v^2}\right] \tag{b.14}$$

and CDF equal to

$$F_v(v,t) = 1 - \mathrm{Q}_1\left[\frac{\mu_v(t)}{\sigma_v}, \frac{v}{\sigma_v}\right] \tag{b.15}$$

where $\sigma_v^2 = \sigma_x^2 = \sigma_y^2$ and $\mu_v = \sqrt{\left[x_0 + \epsilon_x(t) - x_a\right]^2 + \left[y_0 + \epsilon_x(t) - y_a\right]^2}$.

The random variables $\mathbf{z}$ and $\mathbf{v}$ can be combined such that

$$\begin{aligned} \mathbf{k} &= \mathcal{G}(\mathbf{z}, \mathbf{v}) = a\mathbf{z} + b\mathbf{v} \\ \mathbf{u} &= \mathcal{H}(\mathbf{z}, \mathbf{v}) = c\mathbf{z} + d\mathbf{v} \end{aligned} \tag{b.16}$$

The join density of the random variables $\mathbf{k}$ and $\mathbf{u}$ can be expressed as

$$f_{ku}(k,u) = \sum_i \frac{1}{|J(z_i, v_i)|} f_{zv}(z_i, v_i) \tag{b.17}$$

where the determinant $J(z_i, v_i)$ represents the Jacobian of the original transformation. Letting $b = c = 0$ and $a = d = 1$, follows that $J(z_i, v_i) = 1$ [158]. Treating the random variables $\mathbf{z}$ and $\mathbf{v}$ as independent

$$\begin{aligned} f_{ku}(k,u) = f_{zv}(k,u) = f_z(k) f_v(u) = \\ = \frac{k e^{-\frac{\left(k^2 + \mu_k^2\right)}{2\sigma_k^2}}}{\sigma_k^2} \mathrm{I}_0\left(\frac{k\mu_k}{\sigma_k^2}\right) \frac{u e^{-\frac{\left(u^2 + \mu_u^2\right)}{2\sigma_u^2}}}{\sigma_u^2} \mathrm{I}_0\left(\frac{u\mu_u}{\sigma_u^2}\right) \quad 0 < k\,,\, u < \infty \end{aligned} \tag{b.18}$$

Yields,

$$f_k(k) = \int_0^\infty f_{ku}(k,u)\,\mathrm{d}u = -\frac{k e^{-\frac{\left(k^2 + \mu_k^2\right)}{2\sigma_k^2}}}{\sigma_k^2} \mathrm{I}_0\left(\frac{k\mu_k}{\sigma_k^2}\right) \tag{b.19}$$

since $Q_1(a,0) = 1$ and $Q_1(a,\infty) = 0$. Similarly

$$f_u(u) = \int_0^\infty f_{ku}(k,u)\,\mathrm{d}k = -\frac{u e^{-\frac{\left(u^2 + \mu_u^2\right)}{2\sigma_u^2}}}{\sigma_u^2} \mathrm{I}_0\left(\frac{u\mu_u}{\sigma_u^2}\right) \tag{b.20}$$

Therefore,

$$f_{ku}\left(k,u\right)=f_k(k)f_u(u) \tag{b.21}$$

As the PDF $f_{ku}\left(k,u\right)=f_{zv}\left(z,v\right)$, the probability that the two laser beams are overlapped after one trial can be calculated as

$$\begin{aligned}\mathrm{P}\{\mathbf{z}\leq\delta\,,\,\mathbf{v}\leq\delta,t\}&=1-\int_z^{\delta}\int_v^{\delta}f_{zv}\left(z,v,t\right)\mathrm{d}z\mathrm{d}v=\\&=\left\{1-\mathrm{Q}_1\left[\frac{\mu_z\left(t\right)}{\sigma_z},\frac{\delta}{\sigma_z}\right]\right\}\left\{1-\mathrm{Q}_1\left[\frac{\mu_v\left(t\right)}{\sigma_v},\frac{\delta}{\sigma_v}\right]\right\}\end{aligned} \tag{b.22}$$

which is a function of time and of the initial conditions.

B.5 The time optimal slew maneuver

When designing the optimal slew maneuver, the time t_{acc} (see the right panel of Fig. b.4) is calculated limiting the angular velocity of the steering mirror

$$\omega = \alpha t_{acc} \longrightarrow t_{acc} = \frac{\omega}{\alpha} \tag{b.23}$$

Yields

$$\begin{aligned} \rho_1 &= \rho_i + \frac{1}{2}\alpha t_{acc}^2 \\ &= \rho_i + \frac{\omega^2}{2\alpha} \end{aligned} \tag{b.24}$$

Due to the symmetry of the accelerating and decelerating phase, the position ρ_2 shown in the right panel of Fig. b.4 is equal to

$$\begin{aligned} \rho_2 &= \rho_f - (\rho_1 - \rho_i) \\ &= \rho_f - \frac{\omega^2}{2\alpha} \end{aligned} \tag{b.25}$$

In the time interval between t_{acc} and t_{cost}, the repointing is performed at a constant angular velocity. Therefore,

$$\rho_2 - \rho_1 = \omega \frac{\Delta\rho}{|\Delta\rho|} (t_{acc} - t_{cost}) \tag{b.26}$$

where $\Delta\rho = \rho_f - \rho_i$. Substituting Eq. b.24 and Eq. b.25 in Eq. b.26 yields

$$t_{cost} = \frac{\Delta\rho - \frac{\omega^2}{\alpha}}{\omega} + t_{acc} = \frac{|\Delta\rho|}{\omega} \tag{b.27}$$

The equation for calculating the time t_{dec} is given by solving $\omega - \alpha (t_{dec} - t_{cost}) = 0$ with respect to t_{dec} and remembering that $t_{acc} = \omega/\alpha$.

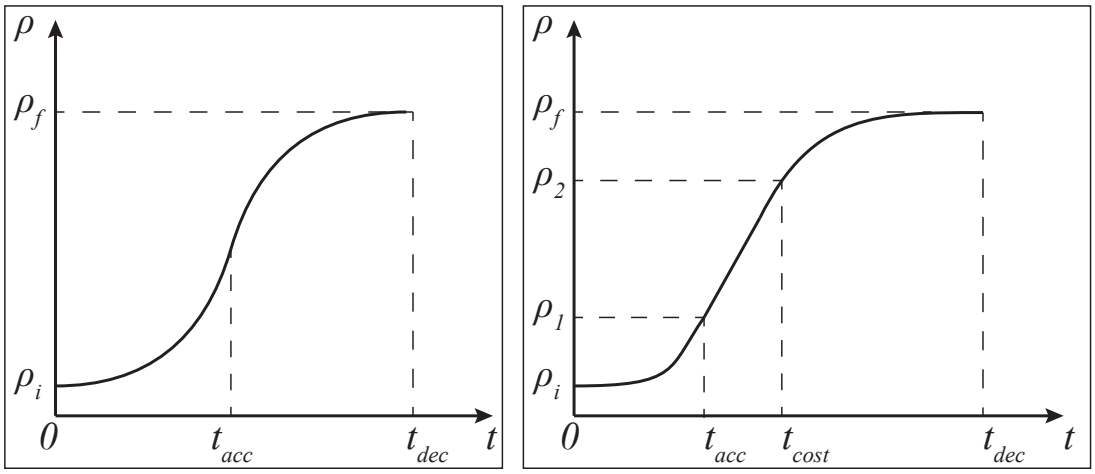

Figure b.4: The left panel shows the repointing trend when a slew maneuver is executed with a constant torque while the right panel depicts the time optimal maneuver with constant torque and limited maximum angular velocity.

B.6 Beam pointing using on-board measurement data

As discussed in paragraph 3.3.2, when the phasemeter has not yet acquired the signal (no DWS information), the beam pointing has to be controlled using the measurements coming from the GPS receiver and from the attitude control system. During the initial acquisition, the tip-tilt angles provided to the steering mirror (in order to draw the desired pattern) have to be properly corrected in order to take into account the drift of the satellite in terms of pointing and orbit position. Labelling as $\mathbf{d}_{\mathrm{gui}}$ the unit vector of the direction of the laser beam in the intra-satellite medium (which corresponds to a point of the desired pattern) and $\hat{\mathbf{d}}_{\mathrm{L}}$ (see Eq. 3.11) the unit vector that takes into account the drift of the satellite, the effective pointing direction of the TX beam is given by $\mathbf{d}_{\mathrm{gui}} - \hat{\mathbf{d}}_{\mathrm{L}}$.

When performing the initial acquisition using a random pattern, the pointing correction can be neglected since it does not affect the distribution of the dwell spots within the uncertainty cone. If the execution time of the continuous pattern is below the cut-off frequency of the filter used to remove the AOCS measurement noise, then the pattern is not going to be distorted by the pointing correction noise.

For the simulations presented in paragraph 4.6, the execution time of the fast spiral is below the cut-off frequency of the filters used to remove the AOCS noise (0.5 Hz) while the slower spiral is not. Figure b.5 depicts the coverage of the uncertainty area given by the slow pattern of the guidance algorithm. As the picture shows, although the area coverage is not uniform as in Fig. 4.7, there are no gaps within the uncertainty cone. Thus the superimposition between adjacent cones is sufficient to guarantee a proper coverage of the uncertainty area.

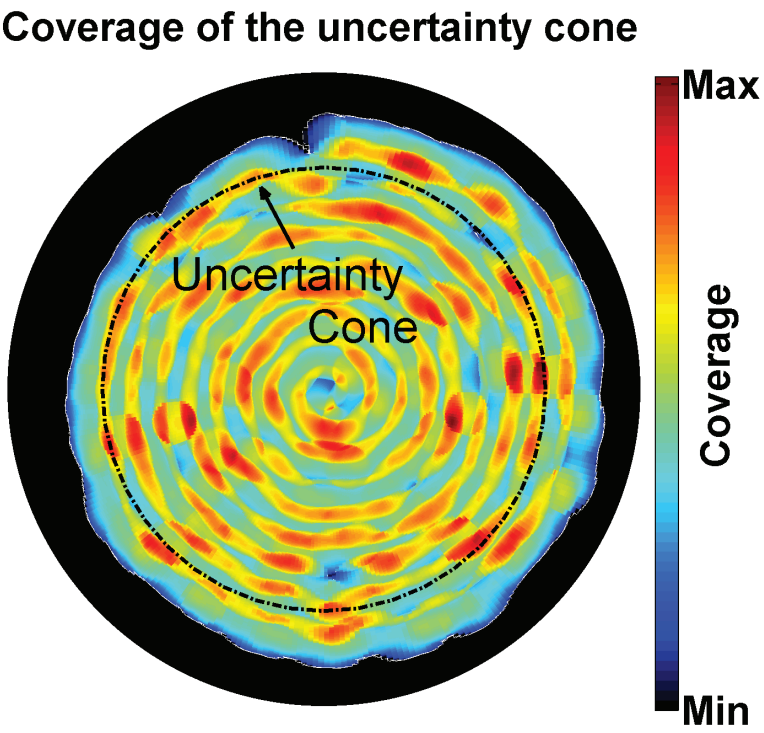

Figure b.5: This figure shows the temporal coverage of the uncertainty cone give by the slowest of the two scan patterns. This plot is obtained when the guidance algorithm is executed according to the direct acquisition mode. Indeed, in this case, one of the two laser beams has to be firmly pointed for a longer time when compared to the split acquisition mode.

Appendix C

C.1 Orbital coordinate frames

The orbital coordinate frames, the transformation matrices between the different orbital frames and the time standards (the latter defied in appendix C.2) are derived from the Astronomical almanac for the year 2013 [159].

CRS J2000

The CRS J2000 is used as inertial frame. The origin of this coordinate system is at the center of the Earth. The X-axis lies along the intersection of the mean equatorial and elliptic planes and points towards the mean vernal equinox as defined at 12:00 on 1 January 2000 Terrestrial Time. The Z-axis is the mean rotation axis of the Earth and points to the celestial pole while the Y-axis completes the right-handed system.

Mean Equator of Date

The Mean Equator of Date coordinate system includes the precession of the Earth's spin axis and is used as alternative inertial frame to the CRS J2000. The origin of this coordinate system is at the center of the Earth. The X-axis lies along the intersection of the mean equatorial and elliptic planes and points towards the mean vernal equinox as defined by the specified or current date. The Z-axis is the mean rotation axis of the Earth and points to the celestial pole while the Y-axis completes the right handed system.

The rotation matrix from the CRS J2000 (labelled as J) to the Mean Equator of Date coordinate system (labelled as M) is

$$\begin{aligned}\mathbf{R}_{\mathrm{MJ}} &= \mathbf{R}_3\left(-z\right)\mathbf{R}_2\left(\vartheta\right)\mathbf{R}_3\left(-\zeta\right)\\ &= \begin{bmatrix} -\sin z\sin\zeta+\cos z\cos\vartheta\cos\zeta & -\sin z\cos\zeta-\cos z\cos\vartheta\sin\zeta & -\cos z\sin\vartheta \\ \cos z\sin\zeta+\sin z\cos\vartheta\cos\zeta & \cos z\cos\zeta-\sin z\cos\vartheta\sin\zeta & -\sin z\sin\vartheta \\ \sin\vartheta\cos\zeta & -\sin\vartheta\sin\zeta & \cos\vartheta \end{bmatrix}\end{aligned} \tag{c.1}$$

where z, ϑ and ζ are the precession angles and are computed as

$$z = \left(23060.9097T + 109.5270T^2 + 18.2667T^3 - 0.2821T^4 - 0.0301T^5 - 0.0001T^6\right)\frac{\pi}{180\cdot 3600}$$

$$\vartheta = \left(20042.0207T - 42.6566T^2 - 41.8238T^3 - 0.0731T^4 - 0.0127T^5 - 0.0004T^6\right)\frac{\pi}{180\cdot 3600}$$

$$\zeta = \left(23060.9097T + 30.2226T^2 + 18.0183T^3 - 0.0583T^4 - 0.0285T^5 - 0.0002T^6\right)\frac{\pi}{180\cdot 3600}$$

T are the Julian millenniums since 1 January 2000, 12:00 computed using terrestrial time (see appendix C.2)

$$T = \frac{JD\,(TT) - 2451545}{365250}$$

True Equator of Date

The True Equator of Date coordinate system includes the nutation of the Earth's spin axis and can be used as an alternative inertial frame to the Mean Equator of Date.

The origin of this coordinate system is at the center of the Earth. The X-axis lies along the intersection of the true equatorial and elliptic planes and points towards the mean vernal equinox as defined by the specified or current date. The Z-axis is the true rotation axis of the Earth and points to the celestial pole while the Y-axis completes the right handed system.

The rotation matrix from the Mean Equator of Date reference frame to the True Equator of Date coordinate system (labelled as Q) is

$$\begin{aligned}\mathbf{R}_{\mathrm{QM}} &= \mathbf{R}_1\,(-\epsilon')\,\mathbf{R}_3\,(-\Delta\psi)\,\mathbf{R}_1\,(\epsilon) \qquad \text{(c.2)}\\ &= \begin{bmatrix} \cos\Delta\psi & -\sin z - \sin\Delta\psi\cos\epsilon & -\sin\Delta\psi\sin\epsilon \\ \sin\Delta\psi\cos\epsilon' & \cos\Delta\psi\cos\epsilon'\cos\epsilon + \sin\epsilon'\sin\epsilon & \cos\Delta\psi\cos\epsilon'\sin\epsilon - \sin\epsilon'\cos\epsilon \\ \sin\Delta\psi\sin\epsilon' & \cos\Delta\psi\sin\epsilon'\cos\epsilon - \cos\epsilon'\sin\epsilon & \cos\Delta\psi\sin\epsilon'\sin\epsilon + \cos\epsilon'\cos\epsilon \end{bmatrix}\end{aligned}$$

where ϵ and $\epsilon' = \epsilon + \Delta\epsilon$ are the mean and true obliquity of the elliptic respectively. The mean obliquity of the elliptic is calculated as

$$\epsilon = (84381''.488 - 46''.8150T)\,\frac{\pi}{180\cdot 3600}$$

The nutation angles are calculated considering only the terms $> 0.1''$

$$\begin{aligned}\Delta\psi &= \{-17.1996\sin(\Omega) - 1.3187\sin[2\,(F - D + \Omega)]\\ &\quad -0.2274\sin[2\,(F+\Omega)] + 0.2062\sin(2\Omega) + 0.1426\sin(\ell)\}\,\frac{\pi}{180\cdot 3600}\\ \Delta\epsilon &= \{9.2025\cos(\Omega) + 0.5736\cos[2\,(F - D + \Omega)]\\ &\quad +0.0977\cos[2\,(F+\Omega)] - 0.0895\cos(2\Omega) + \cos(\ell)\}\,\frac{\pi}{180\cdot 3600}\end{aligned}$$

where ℓ is the mean anomaly of the sun, F is the mean distance of the moon from the ascending node, D is the difference between the mean longitudes of the sun and the moon and Ω is the ascending node of the lunar orbit. These terms are given by

$$\begin{aligned}\ell &= (1287099''.804 + 129596581''.224T)\,\frac{\pi}{180\cdot 3600}\\ F &= (335778''.877 + 1739527263''.137T)\,\frac{\pi}{180\cdot 3600}\\ D &= (1072261''.307 + 1602961601''.328T)\,\frac{\pi}{180\cdot 3600}\\ \Omega &= (450160''.280 - 6962890''.539T)\,\frac{\pi}{180\cdot 3600}\end{aligned}$$

T is the number of Julian centuries since the 1 January 2000 at 12:00 computed using terrestrial time (see appendix C.2)

$$T = \frac{JD\,(TT) - 2451545}{36525}$$

Pseudo Earth Fixed

The Pseudo Earth Fixed coordinate system is used to specify the position and velocity of a spacecraft relative to the surface of the Earth.

The origin of this coordinate system is at the center of the Earth. The X-axis lies along the intersection of the true equator and the Greenwich meridian time and rotates with the Earth. The Z-axis is the rotation axis of the Earth and points to the celestial pole while the Y-axis completes the right handed system.

The rotation matrix from the True Equator of Date reference frame to the Pseudo Earth Fixed coordinate system (labelled as E) is

$$\mathbf{R}_{\mathrm{EQ}} = \mathbf{R}_3\left(\vartheta_{\mathrm{GAST}}\right) = \begin{bmatrix} \cos\vartheta_{\mathrm{GAST}} & \sin\vartheta_{\mathrm{GAST}} & 0 \\ -\sin\vartheta_{\mathrm{GAST}} & \cos\vartheta_{\mathrm{GAST}} & 0 \\ 0 & 0 & 1 \end{bmatrix} \tag{c.3}$$

where $\vartheta_{\mathrm{GAST}}$ is the Greenwich apparent sidereal time which is defined as the angle between the true vernal equinox and the Greenwich meridian. The Greenwich mean sidereal time is computed as

$$\begin{aligned} \vartheta_{\mathrm{GMST}} = &(24110.54841 + 8640184.812866T_0 + 1.002737909350795UT1 \\ &+0.03104T^2 - 0.0000062T^3)\,\frac{2\pi}{86400} \end{aligned}$$

where T_0 is the number of Julian centuries that have elapsed from 1 January 2000 12:00 at the beginning of the day computed using the universal time. T_0 is expressed as (see appendix C.2)

$$T_0 = \frac{JD\left(UT1_0\right) - 2451545}{36525}$$

T is the number of Julian centuries that have elapsed since 1 January 2000 12:00 computed using the universal time (see appendix C.2)

$$T = \frac{JD\left(UT1\right) - 2451545}{36525}$$

$UT1$ is the number of seconds elapsed since the beginning of the day expressed using universal time. The Greenwich apparent sidereal time is computed as

$$\vartheta_{\mathrm{GAST}} = \vartheta_{\mathrm{GMST}} + \Delta\psi\cos\epsilon$$

$\Delta\psi$ and ϵ are the nutation angles defined beforehand.

Earth Fixed

The Earth Fixed coordinate system accounts for the motion of the Earth's spin axis relative to the crust (polar motion). The origin of this coordinate system is at the center of the Earth. The X-axis lies along the intersection of the instantaneous equator and the Greenwich meridian and rotates with the Earth. The Z-axis is the instantaneous rotation axis of the Earth and points to the celestial pole while the Y-axis completes the right handed system.

The rotation matrix from the Pseudo Earth Fixed coordinate system to the Earth Fixed coordinate system (labelled as E0) is

$$\mathbf{R}_{\mathrm{E0E}} = \mathbf{R}_2\left(-x_p\right)\mathbf{R}_1\left(-y_p\right)$$

$$= \begin{bmatrix} \cos x_p & \sin x_p \sin y_p & \sin x_p \cos y_p \\ 0 & \cos y_p & -\sin y_p \\ -\sin x_p & \cos x_p \sin y_p & \cos x_p \cos y_p \end{bmatrix} \approx \begin{bmatrix} 1 & 0 & x_p \\ 0 & 1 & -y_p \\ -x_p & y_p & 1 \end{bmatrix} \tag{c.4}$$

where the angles x_p and y_p, describing the polar motion, are sufficiently small that it is possible to apply the small-angles approximation. The motion of the Earth's spin axis relative to the crust can be neglected if ground tracking is not required. Therefore, the rotation matrix $\mathbf{R}_{\mathrm{E0E}} = \mathbf{I}$.

C.2 Time standards and Julian calendar

Universal Time

In this thesis, universal time $UT1$ is used as the principal form of Universal Time. $UT1$ is proportional to the rotation angle of the Earth with respect to the distant quasars defined by the International Celestial Reference Frame.

Terrestrial Time

The terrestrial time (TT) is a time standard primarily used for time-measurements of astronomical observations made from the surface of the Earth. TT runs a little ahead of $UT1$ by an amount ΔT which is equal to 65.7768 seconds. The relation between TT and $UT1$ is therefore

$$UT1 = TT - \Delta T$$

Julian Day Number

The Julian Day Number (JDN) is the integer assigned to a whole solar day in the Julian day count. The Julian day count starts from noon of the Greenwich Mean Time. The Julian day number 0 is assigned to January 1, 4713 BC at noon time. The Julian Date (JD) of any instant within a day is given by the JDN of the date plus the time elapsed until the desired instant.

In order to compute the JDN, the number of years (y) and months (m) since March 1, 4800 BC have to be calculated

$$a = \left\lfloor \frac{14 - \text{month}}{12} \right\rfloor$$
$$y = \text{year} + 4800 - a$$
$$m = \text{mont} + 12a - 3$$

If a date of the Gregorian calendar is used, the JDN is computed as

$$JDN = \text{day} + \left\lfloor \frac{153m + 2}{5} \right\rfloor + 365y + \left\lfloor \frac{y}{4} \right\rfloor - \left\lfloor \frac{y}{100} \right\rfloor + \left\lfloor \frac{y}{400} \right\rfloor - 32045$$

Otherwise, if starting from a Julian calendar date, the JDN is computed as above neglecting the terms $y/100$ and $y/400$ and by replacing the constant value 32045 with 32083.

Given the JDN, the JD is calculated as

$$JD = JDN + \frac{\text{hour} - 12}{24} + \frac{\text{minutes}}{1440} + \frac{\text{seconds}}{86400}$$

C.3 From Earth Fixed frame to CRS J2000

The transformation of position and velocity from the Earth Fixed coordinate system to the CRS J2000 is needed to transform the orbit state vector provided by the Global Navigation Satellite System.

According to the reference frame transformations defined previously, the position vector defined in the Earth Fixed frame can be expressed in the CRS J2000 according to the transformation

$$\mathbf{r}_{\mathrm{J}} = \mathbf{r}_{\mathrm{JE0}} + \mathbf{R}_{\mathrm{JE0}}\mathbf{r}_{\mathrm{E0}} \tag{c.5}$$

where $\mathbf{R}_{\mathrm{JE0}}$ is the transformation matrix from Earth fixed frame to CRS J2000, $\mathbf{r}_{\mathrm{E0}}$is the position vector defined in the Earth fixed frame, $\mathbf{r}_{\mathrm{J}}$ is the position vector defined in CRS J2000 and $\mathbf{r}_{\mathrm{JE0}}$ is the vector defining the origin offset between CRS J2000 and Earth Fixed frame. Since both origins are at the center of the Earth this last vector is equal to the null vector. The matrix $\mathbf{R}_{\mathrm{JE0}}$ is defined as

$$\begin{aligned}\mathbf{R}_{\mathrm{JE0}} &= \mathbf{R}_{\mathrm{JM}}\mathbf{R}_{\mathrm{MQ}}\mathbf{R}_{\mathrm{QE}}\mathbf{R}_{\mathrm{EE0}} \\ &= \mathbf{R}_{\mathrm{MJ}}^{T}\mathbf{R}_{\mathrm{QM}}^{T}\mathbf{R}_{\mathrm{EQ}}^{T}\mathbf{R}_{\mathrm{E0E}}^{T}\end{aligned} \tag{c.6}$$

where $\mathbf{R}_{\mathrm{JM}}$, $\mathbf{R}_{\mathrm{MQ}}$, $\mathbf{R}_{\mathrm{QE}}$ and $\mathbf{R}_{\mathrm{EE0}}$ have been defined in appendix C.1 (respectively, in Eq. c.1, Eq. c.2, Eq. c.3 and Eq. c.4).

The transformation of the velocity vector is retrieved differentiating the equation defining the transformation of the position vector from the Earth Fixed frame to the CRS J2000. Considering the matrices $\mathbf{R}_{\mathrm{JM}}$, $\mathbf{R}_{\mathrm{MQ}}$ and $\mathbf{R}_{\mathrm{EE0}}$ as constants, yields

$$\mathbf{v}_{\mathrm{J}} = \mathbf{R}_{\mathrm{JE0}}\mathbf{v}_{\mathrm{E0}} + \frac{d}{dt}\left(\mathbf{R}_{\mathrm{JE0}}\right)\mathbf{r}_{\mathrm{E0}}$$

$$\frac{d}{dt}\left(\mathbf{R}_{\mathrm{JE0}}\right) = \mathbf{R}_{\mathrm{JM}}\mathbf{R}_{\mathrm{MQ}}\frac{d}{dt}\left(\mathbf{R}_{\mathrm{QE}}\right)\mathbf{R}_{\mathrm{EE0}}$$

$$\frac{d}{dt}\left(\mathbf{R}_{\mathrm{QE}}\right) = \frac{d}{dt}\left(\vartheta_{\mathrm{GAST}}\right)\begin{bmatrix}0 & -1 & 0\\ 1 & 0 & 0\\ 0 & 0 & 0\end{bmatrix}\mathbf{R}_{\mathrm{QE}}$$

where $\mathbf{v}_{\mathrm{J}}$ and $\mathbf{v}_{\mathrm{E0}}$ are the velocity vectors of the satellite expressed in the CRS J2000 and in the Earth fixed frame respectively. If the Earth's precession is neglected, the mean Earth rotation rate can be expressed as

$$\frac{d}{dt}\left(\vartheta_{\mathrm{GAST}}\right) \approx \omega_{\mathrm{E}} = 7.2921158553 \times 10^{-5}\frac{rad}{s}$$

According to this definition of the Earth rotation rate, the equation for transforming the velocity vector in the CRS J2000 can be rewritten as

$$\begin{aligned}\mathbf{v}_{\mathrm{J}} &= \mathbf{R}_{\mathrm{JE0}}\mathbf{v}_{\mathrm{E0}} + \mathbf{R}_{\mathrm{JM}}\mathbf{R}_{\mathrm{MQ}}\omega_{\mathrm{E}}\begin{bmatrix}0 & -1 & 0\\ 1 & 0 & 0\\ 0 & 0 & 0\end{bmatrix}\mathbf{R}_{\mathrm{QE}}\mathbf{R}_{\mathrm{EE0}}\mathbf{r}_{\mathrm{E0}} \\ &= \mathbf{R}_{\mathrm{JE0}}\mathbf{v}_{\mathrm{E0}} + \mathbf{R}_{\mathrm{JM}}\mathbf{R}_{\mathrm{MQ}}\left\{\begin{bmatrix}0\\ 0\\ \omega_{\mathrm{E}}\end{bmatrix} \times \left(\mathbf{R}_{\mathrm{QE}}\mathbf{R}_{\mathrm{EE0}}\mathbf{r}_{\mathrm{E0}}\right)\right\}\end{aligned}$$

If the polar motion is neglected ($\mathbf{R}_{\mathrm{E0E}} = \mathbf{I}$), the previous equation can be further simplified

$$\begin{aligned}\mathbf{v}_{\mathrm{J}} &= \mathbf{R}_{\mathrm{JE0}}\mathbf{v}_{\mathrm{E0}} + \mathbf{R}_{\mathrm{JM}}\mathbf{R}_{\mathrm{MQ}}\left\{\begin{bmatrix} 0 \\ 0 \\ \omega_{\mathrm{E}} \end{bmatrix} \times (\mathbf{R}_{\mathrm{QE}}\mathbf{I}\mathbf{r}_{\mathrm{E0}})\right\} \\ &= \mathbf{R}_{\mathrm{JE0}}\left(\mathbf{v}_{\mathrm{E0}} + \begin{bmatrix} 0 \\ 0 \\ \omega_{\mathrm{E}} \end{bmatrix} \times \mathbf{r}_{\mathrm{E0}}\right)\end{aligned}$$

C.4 Quaternion operations

Rotation of a vector by a quaternion

The rotation of a vector $\mathbf{v}$ by a quaternion Q is

$$Q\mathbf{v} = \left(q_0^2 - 1\right)\mathbf{v} + (2\boldsymbol{q}\cdot\mathbf{v}) - 2q_0\,(\boldsymbol{q}\times\mathbf{v})$$

where the quaternion $Q = (q_0\ q_1\ q_2\ q_3) = (q_0\ \boldsymbol{q})$.

Product of two quaternions

Let $Q_{\mathrm{B,A}}$ the quaternion that rotates the reference frame A into B and $P_{\mathrm{C,B}}$ the quaternion that rotates the reference frame B into C. The quaternion $R_{\mathrm{C,A}}$ which rotates the reference frame A into C can be obtained from the quaternions $Q_{\mathrm{B,A}}$ and $P_{\mathrm{C,B}}$ as

$$R_{\mathrm{C,A}} = Q_{\mathrm{B,A}}P_{\mathrm{C,B}} = \begin{bmatrix} q_0 & -q_1 & -q_2 & -q_3 \\ q_1 & q_0 & -q_3 & q_2 \\ q_3 & -q_2 & q_0 & -q_1 \\ q_3 & -q_2 & q_1 & q_0 \end{bmatrix} \begin{pmatrix} p_0 \\ p_1 \\ p_2 \\ p_3 \end{pmatrix}$$

$$= \begin{bmatrix} p_0 & -p_1 & -p_2 & -p_3 \\ p_1 & p_0 & -p_3 & p_2 \\ p_3 & -p_2 & p_0 & -p_1 \\ p_3 & -p_2 & p_1 & p_0 \end{bmatrix} \begin{pmatrix} q_0 \\ q_1 \\ q_2 \\ q_3 \end{pmatrix}$$

Inverse of a quaternion

The inverse of a quaternion rotates a vector of the same magnitude of the original quaternion but in the opposite direction. It is calculated as

$$Q^{-1} = (q_0\ -q_1\ -q_2\ -q_3) = (-q_0\ q_1\ q_2\ q_3)$$

Difference between two quaternions

If $Q_{\mathrm{B,A}}$ and $P_{\mathrm{B,A}}$ are two quaternions rotating defining the rotation from reference frame A to reference frame B, then the difference between these two quaternions in the reference frame B is expressed as

$$\Delta_{\mathrm{B,A}} = Q_{\mathrm{B,A}}^{-1}P_{\mathrm{B,A}}$$

Relation between Tait-Bryan angles and quaternion components

The rotation represented by a quaternion can be decomposed into the rotation angles of Roll,Pitch and Yaw. The rotation angles with respect to the quaternion components are

$$\phi = \tan^{-1}\left[\frac{2\,(q_0q_1 + q_2q_3)}{q_0^2 - q_1^2 - q_2^2 + q_3^2}\right]\ ,\ \begin{cases} \text{if } q_0^2 + q_3^2 > q_1^2 + q_2^2\ ,\ 0 < \phi < \pi/2 \text{ or } 3\pi/2 < \phi < 2\pi \\ \text{if } q_0^2 + q_3^2 < q_1^2 + q_2^2\ ,\ \pi/2 < \phi < 3\pi/2 \end{cases}$$

$$\theta = \sin^{-1}\left[2\,(q_0q_2 - q_1q_2)\right]\ ,\ -\pi/2 < \theta < \pi/2$$

$$\psi = \tan^{-1}\left[\frac{2\,(q_1q_2 + q_0q_3)}{q_0^2 + q_1^2 - q_2^2 - q_3^2}\right]\ ,\ \begin{cases} \text{if } q_0^2 + q_1^2 > q_2^2 + q_3^2\ ,\ 0 < \psi < \pi/2 \text{ or } 3\pi/2 < \psi < 2\pi \\ \text{if } q_0^2 + q_3^2 < q_1^2 + q_2^2\ ,\ \pi/2 < \psi < 3\pi/2 \end{cases}$$

Rotation matrix from quaternion elements

A matrix which transforms a reference frame A into B can be expressed through the components of the quaternion $Q_{\mathrm{B,A}}$ as

$$\mathbf{R}_{\mathrm{BA}} = \begin{bmatrix} q_0^2 + q_1^2 - q_2^2 - q_3^2 & 2\,(q_1 q_2 + q_0 q_3) & 2\,(q_1 q_3 - q_0 q_2) \\ 2\,(q_1 q_2 - q_0 q_3) & q_0^2 - q_1^2 + q_2^2 - q_3^2 & 2\,(q_2 q_3 + q_0 q_1) \\ 2\,(q_1 q_3 + q_0 q_2) & 2\,(q_2 q_3 - q_0 q_1) & q_0^2 - q_1^2 - q_2^2 + q_3^2 \end{bmatrix}$$

Vice versa, if the matrix $\mathbf{R}_{\mathrm{BA}}$ is known, it is possible to determine the elements of the quaternion $Q_{\mathrm{B,A}}$ combining the elements of the matrix $\mathbf{R}_{\mathrm{BA}}$

$$\mathbf{R}_{\mathrm{BA}} = \begin{bmatrix} r_{1,1} & r_{1,2} & r_{1,3} \\ r_{2,1} & r_{2,2} & r_{2,3} \\ r_{3,1} & r_{3,2} & r_{3,3} \end{bmatrix} \longrightarrow \begin{aligned} q_0 &= \pm\frac{1}{2}\sqrt{1 + r_{1,1} + r_{2,2} + r_{3,3}} \\ q_1 &= \frac{(r_{2,3} - r_{3,2})}{4q_0} \\ q_2 &= \frac{(r_{3,1} - r_{1,3})}{4q_0} \\ q_3 &= \frac{(r_{1,2} - r_{2,1})}{4q_0} \end{aligned}$$

C.5 Statistics of a sinusoidal signal

The sinusoidal process

$$X(t) = A\sin(\omega t - \varphi) \quad \text{with} \quad \varphi \,\epsilon\, [-\pi\,,\,\pi] \tag{c.7}$$

where A, ω and φ are random and independent. The expected value of Eq. c.7 is equal to

$$\begin{aligned} E[X(t)] &= A\{E[\sin(\omega t - \varphi)]\} = A\{E[\sin(\omega t)\cos(\varphi) - \cos(\omega t)\sin(\varphi)]\} \\ &= A\{E[\sin(\omega t)]\,E[\cos(\varphi)] - E[\cos(\omega t)]\,E[\sin(\varphi)]\} \end{aligned} \tag{c.8}$$

For a complete sinusoidal oscillation

$$E[\sin(\varphi)] = \int_{-\pi}^{\pi} \frac{1}{2\pi}\sin(\varphi)\,\mathrm{d}\varphi = 0$$

Likewise, the term $E[\cos(\varphi)]$ of Eq. c.8 is also null. Yields, $E[X(t)] = 0$.

The autocorrelation function of Eq. c.7 is equal to

$$\begin{aligned} &R_X(t+\tau, t) = E[X(t+\tau)\,X(t)] = A^2\{E[\sin(\omega t + \omega\tau - \varphi)]\,E[\sin(\omega t - \varphi)]\} = \\ &= \frac{A^2}{2}E[\sin(\omega\tau) + \sin(2\omega t + \omega\tau - 2\varphi)] = \\ &= \frac{A^2}{2}E[\sin(\omega\tau)] + \frac{A^2}{2}\underbrace{\{E[\sin(2\omega t + \omega\tau)\cos(2\varphi)] - E[\cos(2\omega t + \omega\tau)\sin(2\varphi)]\}}_{0} = \\ &= \frac{A^2}{2}E[\sin(\omega\tau)] \end{aligned} \tag{c.9}$$

where the zero term is obtained due to the independence of the expected values $E[\sin(2\varphi)] = E[\cos(2\varphi)] = 0$. Since the expected value of the sinusoidal process is null and its autocorrelation is constant, the sinusoidal process is wide sense stationary.

Bibliography

1. Z. Sodnik, B. Furch, and H. Lutz. Free-Space Laser Communication Activities in Europe: SILEX and beyond. In *IEEE* 19^{th} *Annual Meeting of the Lasers and Electro-Optics Society*, pages 78–79, 2006.

2. B. Smutny et al. In-orbit verification of optical inter-satellite communication links based on homodyne BPSK. In *Proceedings of SPIE,*, volume 6877, pages 687702–687702–6, 2008.

3. M. Gregory, F. Heine, H. Kaempfner, R. Meyer, R. Fields, and C. Lunde. TESAT Laser Communication Terminal Performance Results On 5.6 GBIT Coherent Inter Satellite And Satellite Ground Links. In *International Conference on Space Optics (ICSO)*, Rhodes, Greece, 2010.

4. D.M. Boroson, J.J. Scozzafava, D.V. Murphy, B.S. Robinson, and H. Shaw. The Lunar Laser Communications Demonstration (LLCD). In 3^{rd} *IEEE International Space Mission Challenges for Information Technology (SMC-IT)*, pages 23–28, 2009.

5. M. Witting et al. Status of the European Data Relay Satellite System. In *Proceedings of the International Conference on Space Optical Systems and Applications (ICSOS)*, Ajaccio, Corsica, France, 2012.

6. L.E. Bernard, D. Israel, K. Wilson, J.D. Moores, and A.S. Fletcher. The Laser Communications Relay Demonstration. In *Proceedings of the International Conference on Space Optical Systems and Applications (ICSOS)*, Ajaccio, Corsica, France, 2012.

7. K.S. Thorne. Gravitational radiation. In *Three Hundred Years of Gravitation*, pages 330–459. Cambridge University Press, 1987.

8. A. Abramovici et al. LIGO: The Laser Interferometer Gravitational-Wave Observatory. *Science*, 256(5055):325–333, 1992.

9. B. P. Abbott et al. Observation of Gravitational Waves from a Binary Black Hole Merger. *Physics Review Letters*, 116:061102, 2016.

10. C. Bradaschia et al. The VIRGO Project: A wide band antenna for gravitational wave detection. *Nuclear Instruments and Methods in Physics Research Section A: Accelerators, Spectrometers, Detectors and Associated Equipment*, 289(3):518–525, 1990.

11. B. Willke et al. The GEO 600 gravitational wave detector. *Classical and Quantum Gravity*, 19(7):1377, 2002.

12. P. Aufmuth. eLISA - Hunting waves in space. *Einstein Online,*, 04:(viewed on–line 02.2014), 2010.

13. S. Kawamura et al. The Japanese space gravitational wave antenna - DECIGO. *Classical and Quantum Gravity*, 23:125, 2006.

14. P. Amaro-Seoane et al. Low-frequency gravitational-wave science with eLISA/NGO. *Classical and Quantum Gravity*, 29(12):124016, 2012.

15. N. Wei-Tou. ASTROD-GW: Overview and Progress. *International Journal of Modern Physics D*, 22:1341004, 2013.

16. S. Vitale. Space-borne Gravitational Waves Observatories. *arXiv:1404.3136 [gr-qc]*, 2014.

17. P. Amaro-Seoane et al. eLISA: Astrophysics and cosmology in the millihertz regime. *arXiv:1201.3621 [astro-ph.CO]*, 2012.

18. O. Jennrich et al. NGO assessment study report (Yellow Book). Technical Report ESA/SRE(2011)19, ESA, 2012.

19. M. Tinto and S.V. Dhurandhar. Time-delay interferometry. *Living Reviews in Relativity*, 8(4), 2005.

20. G. de Vine, B. Ware, K. McKenzie, R.E. Spero, W.M. Klipstein, and D.A. Shaddock. Experimental Demonstration of Time-Delay Interferometry for the Laser Interferometer Space Antenna. *Physics Review Letters*, 104:211103, 2010.

21. M. Armano et al. LISA Pathfinder: the experiment and the route to LISA. *Classical and Quantum Gravity*, 26(9):094001, 2009.

22. P.W. McNamara. The LISA Pathfinder Mission. *International Journal of Modern Physics D*, 22(01):1341001, 2013.

23. S. Anza et al. The LTP experiment on the LISA Pathfinder mission. *Classical and Quantum Gravity*, 22(10):S125, 2005.

24. W. Fichter, P. Gath, S. Vitale, and D. Bortoluzzi. LISA Pathfinder drag-free control and system implications. *Classical and Quantum Gravity*, 22(10):S139, 2005.

25. H. Audley et al. The LISA Pathfinder interferometry—hardware and system testing. *Classical and Quantum Gravity*, 28(9):094003, 2011.

26. D.I. Robertson et al. Construction and testing of the optical bench for LISA Pathfinder. *Classical and Quantum Gravity*, 30(8):085006, 2013.

27. G. Matticari, G. Noci, P. Siciliano, G. Colangelo, and R. Schmidt. Cold Gas Micro Propulsion Prototype for Very Fine Spacecraft Attitude/Position Control. In *42nd AIAA/ASME/SAE/ASEE Joint Propulsion Conference & Exhibit*, Sacramento, California, USA, 2006.

28. B.D. Tapley, S. Bettadpur, M. Watkins, and C. Reigber. The gravity recovery and climate experiment: Mission overview and early results. *Geophysical Research Letters*, 31(9), 2004.

29. http://www.csr.utexas.edu/grace/.

30. A. Albertella, F. Migliaccio, and F. Sanso. GOCE: The Earth gravity field by space gradiometry. *Celestial mechanics and dynamical astronomy*, 83(1-4):1–15, 2002.

31. M.R. Drinkwater, R. Floberghagen, R. Haagmans, D. Muzi, and A. Popescu. GOCE: ESA's first Earth Explorer Core mission. In *Earth Gravity Field from Space - from Sensors to Earth Science*, volume 18 of *Space Science Series of ISSI*, pages 419–432. Kluwer Academic Publishers, 2003.

32. A. Cazenave and J. Chen. Time-variable gravity from space and present-day mass redistribution in theEarth system. *Earth and Planetary Science Letters*, 298(3):263–274, 2010.

33. F.G. Almeida et al. Time-variations of equivalent water heights' from Grace Mission and in-situ river stages in the Amazon basin. *Acta Amazonica*, 42(1):125–134, 2012.

34. G. Ramillien, F. Frappart, and L. Seoane. Application of the regional water mass variations from GRACE Satellite Gravimetry to large-scale water management in Africa. *Remote Sensing*, 6(8):7379–7405, 2014.

35. B.D. Loomis, R.S. Nerem, and S.B. Luthcke. Simulation study of a follow-on gravity mission to GRACE. *Journal of Geodesy*, 86(5):319–335, 2012.

36. T.M. Niebauer, G.S. Sasagawa, J.E. Faller, R. Hilt, and F. Klopping. A new generation of absolute gravimeters. *Metrologia*, 32(3):159, 1995.

37. N. Sneeuw, J. Flury, and R. Rummel. Science requirements on future missions and simulated mission scenarios. In *Future Satellite Gravimetry and Earth Dynamics*, pages 113–142. Springer, 2005.

38. S. Cesare and G. Sechi. Next generation gravity mission. In *Distributed Space Missions for Earth System Monitoring*, pages 575–598. Springer, 2013.

39. W.M. Folkner et al. Laser Frequency Stabilization for GRACE-II. In *Proceedings of the 2010 Earth Science Technology Forum*, pages 1–8, Arlington, VA, USA, 2010.

40. B.S. Sheard, G. Heinzel, K. Danzmann, D.A. Shaddok, Klipstein W.M., and Folkner W.M. Intersatellite laser ranging instrument for the GRACE follow-on mission. *Journal of Geodesy*, 86(12):1083–1095, 2012.

41. F. Flechtner, P. Morton, M. Watkins, and F. Webb. Status of the GRACE follow-on mission. In *Gravity, Geoid and Height Systems*, pages 117–121. Springer, 2014.

42. P.D. Welch. The Use of Fast Fourier Transform for the Estimation of Power Spectra: A Method Based on Time Averaging Over Short, Modified Periodograms. *IEEE Transactions Audio Electroacustics*, 15:70–73, 1967.

43. F.J. Harris. On the Use of Windows for Harmonic Analysis with the Discrete Fourier Transform. In *Proceeding of IEEE*, volume 66, pages 51–83, 1978.

44. D. Schütze et al. LISA-like Laser Ranging for GRACE Follow-on. In *9th LISA Symposium*, volume 467 of *Astronomical Socitey of the Pacific Conference Series*, pages 285–289, Paris, France, 2013.

45. K. Abich et al. GRACE Follow-On Laser Ranging Interferometer: German Contribution. *Journal of Physics: Conference Series*, 601:012010, 2015.

46. R. L. Ward et al. The design and construction of a prototype lateral-transfer retro-reflector for inter-satellite laser ranging. *Classical and Quantum Gravity*, 31(9):095015, 2014.

47. R. Fledderman et al. Testing the GRACE follow-on triple mirror assembly. *Class. Quantum Grav.*, 31:195004, 2014.

48. B. F. Oreb, J. Burke, R. P. Netterfield, J. A. Seckold, A. Leistner, M. Gross, and S. Dligatch. Development of precision double corner cubes for the space interferometer mission. In *Proceedings of SPIE, Interferometry XIII: Techniques and Analysis*, volume 6292, pages 629202–629202–13, 2006.

49. F. Wang. *Study on Center of Mass Calibration and K-band Ranging System Calibration of the GRACE Mission*. PhD thesis, Faculty of the Graduate School of The University of Texas at Austin, Austin, Texas, USA, December 2003.

50. E. Morrison, B. J. Meers, D. I. Robertson, and H. Ward. Experimental demonstration of an automatic alignment system for optical interferometers. *Applied Optics*, 33(22):5037–5040, 1994.

51. E. Morrison, B. J. Meers, D. I. Robertson, and H. Ward. Automatic allignemnt of optical interferometers. *Applied Optics*, 33(22):5041–5049, 1994.

52. G. Hechenblaikner. Measurement of the Absolute Wavefront Curvature Radius in a Heterodyne Interferometer. *Journal of the Optical Society of America (JOSA) A*, 9(27):2078–2083, 2010.

53. O. Jennrich, R. T. Stebbinis, P.L. Bender, and S. Pollack. Demonstration of the LISA phase measurement principle. *Classical and Quantum Gravity*, 18:4159–4164, 2001.

54. S. Pollack, O. Jennrich, R. T. Stebbinis, and P.L. Bender. Status of LISA phase measurement work in US. *Classical and Quantum Gravity*, 20:S193–S199, 2003.

55. S. Pollack and R. T. Stebbinis. Demonstration of the Zero-Crossing Phasemeter with a LISA Test-bed Interferometer. *Classical and Quantum Gravity*, 23:4189–4200, 2006.

56. B. Ware et al. Phase Measurement System for Inter-Spacecraft Laser Metrology. In *Earth Science Technology Conference*, College Park, MD, USA, 2006.

57. D. Shaddock, B. Ware, P. Halverson, R.E. Spero, and B. Klipstein. Overview of the LISA Phasemeter. In *AIP Conference Proceedings*, volume 873, pages 654–660, Greenbelt, MD, USA, 2006.

58. V. Wand, F. Guzman, G. Heinzel, and K. Danzmann. LISA phasemeter development. In *AIP Conference Proceedings*, volume 873, pages 689–696, Greenbelt, MD, USA, 2006.

59. I. Bykov, J.J. Esteban Delgado, A.F. Garcia Marin, G. Heinzel, and K. Danzmann. LISA phasemeter development: Advanced prototyping. In 7^{th} *LISA Symposium, Journal of Physics: Conference Series*, volume 154, Barcellona, Spain, 2008.

60. O. Gerberding et al. Phasemeter core for intersatellite laser heterodyne interferomtry: modelling, simulations and experiments. *Classical and Quantum Gravity*, 30:235029, 2013.

61. R. E. Best. *Phase-Locked Loops: Design, Simulation, & Applications*. Mc-Graw-Hill Professional, 6th edition, 2007.

62. D. Abramovitch. Phase-locked loops: a control centric tutorial. In *Proceedings of the 2002 American Control Conference*, volume 1, pages 1–15, Anchorage, AK, USA, 2002.

63. Christoph Mahrdt. *Laser Link Acquisition for the GRACE Follow-On Laser Ranging Interferometer*. PhD thesis, Der Fakultät für Mathematik und Physik der Gottfried Wilhelm Universität Hannover, Hannover, Germany, January 2014.

64. D.M.R. Wuchenich et al. Laser link acquisition demonstration for the GRACE Follow-On mission. *Optics Express*, 22(9), 2014.

65. T.S. Schwarze et al. Advanced phasemeter for deep phase modulation interferometry. *Optics Express*, 22(15), 2014.

66. D. F. Walnut. *An Introduction to Wavelet Analysis*. Birkhäuser, 2001.

67. P. Lian. Improving Tracking Performance of PLL in High Dinamic Applications. Diploma thesis, University of Calgary, Department of Geomatics Engineering, Calgary, Alberta, Canada, 2004.

68. Y.Y. Li, X.S. Xu, and T. Zhang. Improving Tracking Performance of PLL Based on Wavelet Packet De-noising Technology. In *Advances in Computer Science, Environment, Ecoinformatics, and Education*, volume 214, pages 449–456. Springer Berlin Heidelberg, 2011.

69. M.R. Mosavi and I. EmamGholipour. De-noising of GPS Receivers Positioning Data Using Wavelet Transform and Bilateral Filtering. *Wireless Personal Communications*, 71(3):2295–2312, 2013.

70. F. Langford-Smith, editor. *Radiotron Designer's Handbook*. RCA, 4th edition, 1953.

71. E.B. Hogenauer. An Economical Class of Digital Filters for Decimation and Interpolation. *IEEE Transactions on Acoustics, Speech, and Signal Processing*, ASSP-29(2):155–162, 1981.

72. V. Müller. Simulations for lisa & grace-follow-on: Satellite constellations at lagrangian points for lisa-like missions and interferometer simulations for the grace follow-on mission. Master's thesis, Max-Planck-Institute for Gravitational Physics (Albert-Einstein-Institute), Gottfried Wilhelm Universität Hannover, Hannover, Germany, 2013.

73. J.B. Thomas. An Analysis of Gravity-Field Estimation Based on Intersatellite Dueal-1-Way Biased Ranging. Technical Report 98-15, pp. B-2, JPL, 1999.

74. E.D. Fitzsimons, M. Perreur-Lioyd, M. Tröbs, S. Sönke, and G. Fernandez Barranco. Detailed Design of Tilt-to-Piston Invesigation. Technical Report LOB-TN-14-01-ASD, Airbus Defence and Space, 2015.

75. K. Nicklaus, K. Voss, and F. Gilles. Triple Mirror Assembly Mirror Assembly Specification. Technical Report LRI-STI-SP-010, Rev. 2, Space Tech GmbH, 2012.

76. D. Schütze et al. Retroreflector for GRACE follow-on: Vertex vs. point of minimal coupling. *Opt. Expr.*, 22(8), 2014.

77. P.L. Bender, D.N. Wiese, and R.S. Nerem. A possible dual-GRACE mission with 90 degree and 63 degree inclination orbits. In *Proceedings of the 3rd International Symposium on Formation Flying, Missions and Technologies*, pages 23–25, 2008.

78. B. Elsaka. Feasible Multiple Satellite Mission Scenarios Flying in a Constellation for Refinement of the Gravity Field Recovery. *International Journal of Geosciences*, 5:267–273, 2014.

79. A. Bacchetta et al. The Results of the AOCS Solutions and Technologies study for the Next Generation Gravity Mission. In *AIAA Guidance, Navigation and Control Conference, part of AIAA SciTech 2015*, Orlando, FL, USA, 2015.

80. G. Heinzel and B. Sheard. The GRACE-C interferometer. Technical Report GR-AEI-TN-1002, version 5, AEI Hannover, 2011.

81. e^2.motion Earth System Mass Transport Mission (Square), Final Report, Munich 2014. ISBN 978-3-7696-8597-8, http://dgk.badw.de/fileadmin/docs/b-318.pdf.

82. M. Herper et al. High stability single-frequency Yb fiber amplifier for next generation gravity missions. In *Proceedings of SPIE*, volume 9344, pages 93440B–93440B–8, 2015.

83. J. Sanjuan, M. Gohlke, S. Rasch, K. Abich, A. Görth, G. Heinzel, and C. Braxmaier. Interspacecraft link simulator for the laser ranging interferometer onboard GRACE Follow-On. *Applied Optics*, 54(22):6682–6689, 2015.

84. E. Hecht. *Optics*. Addison-Wesley, 2nd edition, 1987.

85. S. Bettadpur. Product Specification Document. Technical Report GRACE 327-720, CSR-GR-03-02, Rev. 4.6, University of Texas at Austin, 2012.

86. B. D. Tapley et al. The Joint Gravity Model 3. *Journal of Geophysical Research: Solid Earth*, 101(B12):28029–28049, 1996.

87. C. C. Finlay, S. Maus, D. C. Beggan, M. Hamoudi, J. F. Lowes, N. Olsen, and E. Thébault. Evaluation of candidate geomagnetic field models for IGRF-11. *Earth, Planets and Space*, 62(10):787–804, 2010.

88. A. E. Hedin. Extension of the MSIS Thermosphere Model into the middle and lower atmosphere. *Journal of Geophysical Research: Space Physics*, 96(A2):1159–1172, 1991.

89. Stars sensors terminology and performance specification. Technical Report ECSS-E-ST-60-20C Rev. 1, ESA-ESTEC, 2008.

90. Quang Lam, C. Woodruff, S. Ashton, and D. Martin. Noise estimation for star tracker calibration and enhanced precision attitude determination. In *Proceedings of the Fifth International Conference on Information Fusion*, volume 1, pages 235–242, 2002.

91. A. Papoulis and S.U. Pillai. *Probability, Random Variables and Stochastic Processes*. McGraw-Hill Europe, fourth edition, 2002.

92. Data Sheet ASTRO 10, June 2007.

93. Data Sheet ASTRO 15, June 2007.

94. P.E. Nikravesh and H.A. Affifi. Construction of the Equations of Motion for Multibody Dynamics Using Point and Joint Coordinates. *Computer-Aided Analysis of Rigid and Flexible Mechanichal Systems, NATO ASI Series E: Applied Scienece*, 268:31–60, 1994.

95. J. G. Ziegler, N. B. Nichols, and N.Y. Rochester. Optimum Settings for Automatic Controllers. *ASME Transactions*, 64:759–765, 1942.

96. K.J. Åström and R.M. Murray. *Feedback Systems: An Introduction for Scientist and Engineers*. Priceton University Press, 2.11b edition, 2012.

97. D. Xue, Y. Chen, and D.P. Atherton. *Linear Feedback Control: Analysis and Design with MATLAB*. Advances in Design and Control. Society for Industrial and Apllied Mathematics, 1st edition, 2008.

98. L. Davis. *Handbook Of Genetic Algorithms*. Van Nostrand Reinhold, 1st edition, 1991.

99. J. Kennedy and R. Eberhart. Particle Swarm Optimization. In *Proceedings of the IEEE International Conference on Neural Networks*, volume IV, pages 1942–1948, 1995.

100. M. Vajta. Some remarks on Padé-approximations. In *Proceedings of the 3rd TEMPUS-INTCOM Symposium*, 2000.

101. T. Marlin. *Process Control: Designing Processes and Control Systems for Dynamic Performance*. Mc-Graw Hill Science/Engineering/Math, 2nd edition, 2000.

102. C.J. Livas, J.I. Thorpe, K. Numata, S. Mitryk, G. Mueller, and V. Wand. Frequency-tunable pre-stabilized laser for LISA via sideband locking. *Classical and Quantum Gravity*, 26(9):094016, 2009.

103. G. Picchi, G. Prati, and D. Santerini. Algorithms for Spatial Laser Beacon Acquisition. *IEEE Transactions on Aerospace and Electronics Systems*, AES-22(1):106–113, 1986.

104. J.E. Kaufmann and E.A. Swanson. Laser Intersatellite Transmission Experiment Spatial Acquisition, Tracking and Pointing System. Technical Report SC-80, Lincoln Laboratory, Massachusetts Institute of Technology, 1989.

105. V.A. Skormin, C.R. Herman, M.A. Tascillo, and D.J. Nicholson. Mathematical modeling and simulation analysis of a pointing, acquisition, and tracking system for laser-based intersatellite communication. *Optical Engineering*, 32(11):2749–2763, 1993.

106. P.R. Chakravarthi and C. Chen. Spatial Acquisition in the Presence of Satellite Vibrations for Free-Space Optical Communication Link. In *Proceedings of SPIE*, volume 2221, Orlando, FL, USA, 1994.

107. T. Jono et al. Acquisition, tracking and pointing system of OICETS for free space laser communications. In *Proceedings of SPIE*, volume 3692, Orlando, FL, USA, 1999.

108. G. Griseri. SILEX Pointing Acquisition and Tracking: ground tests and flight performances. In *Proceedings of the* 4^{th} *International Conference on Spacecraft Guidance, Navigation and Control Systems*, volume SP-425, Noordwijk, The Netherlands, 1999.

109. J.J. Kim, T. Sands, and B.N. Agrawal. Acquisition, Tracking and Pointing Technology Development for Bifocal Relay Mirror Spacecraft. In *Proceedings of SPIE*, volume 6569, Orlando, FL, USA, 2007.

110. C. Hindman and L. Robertson. Beaconless Satellite Laser Acquisition - Modeling and Feasability. In *Proceedings of the IEEE Military Communications Conference (MILCOM)*, volume 1, Monteray, CA, USA, 2004.

111. F. Cirillo and P.F. Gath. Control System Design for the Constellation Acquisition Phase of the LISA Mission. *Journal of Physics: Conference Sereries*, 154:012014, 2009.

112. H. Langenbach and M. Schmid. Fast Steering Mirror for Laser Communication. In *Proceedings of the European Space Mechanisms And Tribology Symposium (ESMATS)*, Lucerne, Switzerland, 2005.

113. M. Scheinfeild, N.S. Kopeika, and S. Arnon. Acquisition Time Calculation and Influence of Vibrations for Micro Satellite Laser Communications in Space. In *Proceedings of SPIE*, volume 4365, Orlando, FL, USA, 2001.

114. J. Wang, J.M. Kahn, and K.Y. Lau. Minimization of acquisition time in short range free-space optical communication. *Applied Optics*, 41(36):7592–7602, 2002.

115. R.C. Yates. *A Handbook on Curves and Their Properties.* Ann Arbor, J.W. Edwards, 1947.

116. H.M. Cundy and A.P. Rollett. *Mathematical Models.* Tarquin Publications, 3rd edition, 1981.

117. J.D. Lawrence. *A Catalog of Special Plane Curves.* Dover Books on Mathematics. Dover Publications, 1st edition, 2014.

118. S. Arnon and E. Gill. The optical communication link outage probability in satellite formation flying. *Acta Astronautica*, 95:133–140, 2014.

119. X. Li, S. Yu, J. Ma, and L. Tan. Analytical expression and optimization of spatial acquisition for intersatellite optical communications. *Optics Express*, 19(3):2381–2390, 2011.

120. D. Fischer, T. Usbeck, and P. Gath. Science Mode Reference Pointing. Technical Report GFO.TN.ASTR.SY.00010703, Issue 4, Airbus Defence and Space, 2014.

121. S. V. Dhurandhar, K. Rajesh Nayak, S. Koshti, and J-Y. Vinet. Fundamentals of the LISA stable flight formation. *Classical and Quantum Gravity*, 22(3), 2005.

122. C. Diekmann, F. Steier, B. Sheard, G. Heinzel, and K. Danzmann. Analog phase lock between two lasers at LISA power levels. In *Journal of Physics: Conference Series*, volume 154, page 12020, 2009.

123. F. Guzmán Cervantes, J. Livas, R. Silverberg, E. Buchanan, and R. Stebbins. Characterization of Photoreceivers for LISA. *Classical and Quantum Gravity*, 28(9), 2011.

124. G. Heinzel et al. Laser Ranging Interferometer for GRACE Follow-On. In *Proceedings of the International Conference on Space Optics (ICSO)*, Ajaccio, Corsica, France, 2012.

125. D. Schlichthärle. *Digital Filters, Basics and Design.* Springer, 2nd edition, 2011.

126. Altera®. FFT MegaCore Function - User Guide 9.1, 2009.

127. R.H. Walden. Analog-to-Digital Converter Survey and Analysis. *IEEE Journal on Selected Areas in Communication*, 17(4):539–550, 1999.

128. H. Kobayashi, M. Morimura, K. Kobayashi, and Y. Onaya. Aperture Jitter Effects in Wideband ADC Systems. In *Proceedings of the 6th IEEE International Conference on Electronics, Circuits and Systems (ICECS)*, pages 1705–1708, Pafos, Cyprus, 1999.

129. C.M. Burnett. Development of an ultra-precise digital phasemeter for the lisa gravitational wave detector. M. eng. thesis, Lulea University of Technology, Kiruna, Sweden, September 2010.

130. W. Koechner. *Solid State Laser Engineering.* Springer series in optical science. Springer-Verlag Berlin Heidelberg, 2nd edition, 1996.

131. Coherent. Ultra-Low Noise and Narrow Linewidth, White Paper, 2007.

132. G. Holz. Laser-frequenzstabilisierung zweier nd:yag-lasersysteme auf optische hoch-finesse resonatoren für die präzisionsinterferometrie. Master's thesis, Hochschule für Technik, Wirtschaft und Gestaltung Konstanz (HTWG-Konstanz), Konstanz, Germany, February 2011.

133. J. Schwab. Laser frequency stabilization to optical high-finesse resonators for precision interferometry. Master's thesis, University of Applied Sciences Konstanz, Department of Electrical Engineering and Computer Science, Konstanz, Germany, 2011.

134. R. W. P. Drever, J. L. Hall, F. V. Kowalski, J. Hough, G. M. Ford, A. J. Munley, and H. Ward. Laser phase and frequency stabilization using an optical resonator. *Applied Physics B*, 31(2):97–105, 1983.

135. H. Kögel. HSL - Testbed Calibration Report. Technical Report HSL-ASD-TN-001, Airbus Defence and Space, 2014.

136. N. Duske and D. Fischer. K-band Phase Center Calibration Maneuver. Technical Report GFO.TN.AO.00016748, Issue 1, EADS Astrium, 2013.

137. M. Armano et al. Bayesian statistics for the calibratiom of the LISA Pathfinder experiment. *Journal of Physics: Conference Series*, 601:012027, 2015.

138. M. Nofrarias et al. Optimal design of calibration signals in space borne gravitational wave detectors. *ArXiv:1511.09198*, 2015.

139. B. Widrow and S.D. Stearns. *Adaptive Signal Processing.* Prentice-Hall, 1985.

140. S.J. Elliott, J.M. Stothers, and P.A. Nelson. A Multiple Error LMS Algorithm and Its Application to the Active Control of Sound and Vibration. *IEEE Transactions on Acustics, Speech, and Signal Processing*, ASSP-35(10):1423–1434, 1987.

141. S.J. Elliott, C.C. Boucher, and P.A. Nelson. The Behavior of a Multiple Channel Active Control System. *IEEE Transactions on Signal Processing*, 40(5):1041–1052, 1992.

142. M.H. Hayes. *Statistical Digital Signal Processing and Modeling.* John Wiley and Sons, Inc., 1996.

143. J.W. Leis. *Digital Signal Processing using MATLAB for Students and Researchers.* John Wiley and Sons, Inc., 2011.

144. S. Chandrasekaran and I. Ipsen. Perturbation Theory for the Solution of Systems of Linear Equations. Technical Report YALEU/DOCS/RR-866, Department of Computer Science, Yale University, 1991.

145. K. Case, G. Kruizinga, and S. Wu. *GRACE Level 1B Data Product User Handbook.* Jet Propulsion Laboratory, March 2010. JPL D-22027.

146. R. Stanton, S. Bettadpur, C. Dunn, K.P. Renner, and M. Watkind. Gravity Recovery and Cliamte Experiemnt (GRACE): Science Mission & Requirements Document. Technical Report 327-200, JPL, University of Texas at Austin and GFZ Postdam, 1998.

147. C. Arbinger, S. D'Amico, U. Feucht, and A. Finzi. The GRACE Formation: Science Mode Pointing Performance Analysis. In *Third International Workshop on Satellite Constellations and Formation Flying*, Pisa, Italy, 2003.

148. B. Schlepp, M. Kirschner, T.H. Sweetser, W.M. Klipstein, and S. Dubovitsky. Flight Dynamics Challenges for the GRACE Follow-On Mission. In 25^{th} *International Symposium on Space Flight Dynamics (ISSFD)*, Munich, Germany, 2015.

149. J. Kim. *Simulation Study of a Low-Low Satellite to Satellite Tracking Mission.* PhD thesis, Faculty of the Graduate School of The University of Texas at Austin, Austin, Texas, USA, May 2000.

150. K. Shoemake. Animating Rotation with Quaternion Curves. *SIGGRAPH Computer Graphics*, 19(3):245–245, 1985.

151. P. Ditmar, J. Teixweira da Encarnacao, and H. Hashemi Farahani. Understanding data noise in gravity field recovery on the basis of inter-satellite ranging measurements acquired by the satellite gravimetry mission GRACE. *Journal of Geodesy*, 86:441–465, 2012.

152. U. Ko, B.D. Tapley, J.C. Ries, and S.V. Bettadpur. Analysis of High Frequency Noise in the GRACE Intersatellite Ranging System. *Journal of Spacecraft and Rockets*, 49(6):1163–1173, 2012.

153. M. Sallusti, P. Gath, D. Weise, M. Berger, and H.R. Schulte. LISA system design highlights. *Classical and Quantum Gravity*, 26(9):094015, 2009.

154. J.I. Thorpe. LISA long-arm interferometry. *Classical and Quantum Gravity*, 27(8):084008, 2010.

155. L. d'Arcio et al. Optical Bench Development for LISA. In *International Conference on Space Optics (ICSO)*, Rhodes, Greece, 2010.

156. P. E. Nikravesh. *Product Engineering: Eco-Design, Technologies and Green Energy*, chapter An Overview of Several Formulations for Multibody Dynamics, pages 189–226. Springer Netherlands, Dordrecht, 2005.

157. S. Xu and Y. Rahmat-Samii. Boundary Conditions in Particle Swarm Optimization Revisited. *IEEE Transactions on Antennas and Propagation*, 55(3):760–765, 2007.

158. M. Abramowitz and I.A. Stegun. *Handbook of Mathematical Functions*. Dover Books on Mathematics. Dover Pubblications, 1965.

159. *The Astronomical Almanac for the year 2013*. United States Naval Observatory/Nautical Almanac Office, 2013.

Acknowledgements

It is a pleasure for me to thank all the people who supported me during these last years and contributed in making this work possible.

I am very grateful to Professor Claus Braxmaier, for giving me the opportunity to undertake my PhD studies at the University of Bremen and for kindly supporting and promoting me and my work within the scientific community.

I would like to thank also Professor Gerhard Heinzel for reviewing my thesis and for the fruitful discussions about laser interferometry.

A heartfelt thanks to Dr. Peter Gath, for giving me the chance of working in a leading company like Airbus and for sharing with me his knowledge about control theory, programming and many other different fields. I have gratefully appreciated your advices and friendship.

I would like to express my gratitude to Dr. Ewan Fitzsimons. If today I have an idea of what an interferometer is, it is thanks to you.

My sincere appreciation goes Dr. Ulrich Johann, for keeping me always motivated during the years of my PhD. I am thankful for the dedication you put when it was most necessary for me.

Many thanks to all the colleagues of Airbus, ZARM and DLR, for the nice working atmosphere and good collaboration. It have really enjoyed the time spent with you people.

I am grateful to the students I have supervised in these years: Oliver Mandel and Johannes Kuhner-Roca. It was a great pleasure for me working together. I hope it was the same for you.

Many thanks to Harald and Ruven for turning hard working days in amusement times.

Thank you to the IC (Arturo, Vincenzo, Marianna, Francesca, Domenico, Federico and Ivonne). You guys are simply the best.

Thank you to my family, who has always helped and encouraged me during these years. I hope that all your sacrifices have been rewarded.

Finally a special THANK YOU goes to my wife Marica, for her patience and comprehension. If today I am here is thanks to your active support during my studies, my thesis, and my life. Without your help I would have not been able to achieve all this.

List of Publications

Peer-reviewed publications

F. Ales, O. Mandel, P.F. Gath, U. Johann and C. Braxmaier, *A Phasemeter Concept for Space Application that Integrates an Autonomous Signal Acquisition Stage Based on the Discrete Wavelet Transform*, Review of Scientific Instruments, Vol.86, 084502 (2015).

F. Ales, P.F. Gath, U.Johann and C. Braxmaier, *Modeling and Simulation of a Laser Ranging Interferometer Acquisition and Guidance Algorithm*, Journal of Spacecraft and Rockets, Vol.51 No.1, pp.226-238 (2014).

Conference proceedings

F. Ales, P.F. Gath, U. Johann and C. Braxmaier, *Line of Sight Alignment Algorithms for Future Gravity Missions*, Proceedings of the AIAA Guidance Navigation and Control Conference, Kissimmee (FL), USA (2015).

F. Ales, O. Mandel, P.F. Gath, U. Johann and C. Braxmaier, *Design and Development of a Laser Fine Pointing Sensor*, Proceedings of the AIAA Guidance Navigation and Control Conference, Kissimmee (FL), USA (2015).

F. Ales, P.F. Gath, U.Johann and C. Braxmaier, *Modeling and Simulation of a Laser Ranging Interferometer Acquisition and Guidance Algorithm*, Proceedings of the AIAA Guidance Navigation and Control Conference, Boston (MA), USA (2013).

Patents

F. Ales, O. Mandel and P.F. Gath, *A digital phase measurement unit that integrates an automated signal acquisition stage for signals buried into noise*, Patent filed November 2014; Pending.

Supervision

In this thesis are included the results coming from the supervision of the following students (6 months, full time):

Oliver Mandel,
Testing the Frequency Acquisition of an Optical Beat Signal using a Laser Interferometer, 2015.